

**Design, Development, and Validation of a Rapid Modal Testing System for the  
Efficient Structural Identification of Highway Bridges**

A Thesis

Submitted to the Faculty

of

Drexel University

by

John Louis DeVitis

in partial fulfillment of the

requirements for the degree

of

Doctor of Philosophy

December 2015





## Acknowledgements

I would like to extend my sincere gratitude to my advisors, Dr. Frank Moon and Dr. A. Emin Aktan. You have both been tremendous sources of knowledge and support throughout my time at Drexel. Thank you for the opportunity to experience such a challenging, rewarding journey. And thank you for sharing it with me.

I would like to thank my committee, led by Dr. Moon, who guided me throughout my research and provided valuable insight and review. Thank you Dr. Moon, Dr. Aktan, Dr. Tien-Min Tan, Dr. Ivan Bartoli, Dr. Yared Shifferaw.

I'd like to thank my friends and colleagues who, without, none of this could have been possible. Thank you, Dave Masceri, John Braley, and Nick Romano. Whether we were wet, tired, and hungry in the field, or laughing over a beer, we always have a good time together. And thank you to the old timers for helping me come up through the ranks - John Prader, Matt Yarnold, Nate Dubbs, and (especially) Jeff Weidner.

The research presented within this thesis would not have been possible without the support and funding by The National Institute of Standards and Technology, Pennoni Associates Inc. The findings and conclusions reported herein are those of my own and do not necessarily represent the opinions, conclusions, or recommendations of the National Institute of Standards and Technology Pennoni Associates Inc.

I would like to thank my parents, Louis and Donna, my sister, Sarah, my brother and sister-in-law, David and Mariedel, my grandfather, Earl, and the rest of my family. You have provided me with so much love and support and are the best family a guy can ask for.

Finally, I would like to thank my best friend and loving fiancé, Miss Van Tu. We've had a hell of a ride so far, and I can't wait to start the next step of our lives together.

**TABLE OF CONTENTS**

List of Tables .....	xi
List of Figures .....	xiii
Abstract.....	xxv
CHAPTER 1: INTRODUCTION .....	1
1.1 Vision.....	1
1.2 Summary of Current Bridge Assessment Practice within the U.S.....	1
1.3 Discussion of Current Structural Assessment Practice .....	3
1.4 Summary of Research Objectives and Scope .....	5
1.5 Research Approach .....	6
1.6 Overview of Thesis Structure.....	7
CHAPTER 2: CONCEPT EXPLORATION, CONCEPT OF OPERATIONS, AND SYSTEM REQUIREMENTS.....	10
2.1 Problem Statement .....	10
2.2 System Goals .....	11
2.3 Limitations of Existing Technologies.....	11
2.3.1 Truck Load Tests.....	12

2.3.2 Vibration Tests .....	14
2.3.3 Summary of Constraints .....	17
2.4 Concept of Operations.....	18
2.5 System Requirements.....	19
2.6 System Validation Plan .....	20
CHAPTER 3: EXPERIMENTAL MODAL ANALYSIS CONCEPTS .....	21
3.1 Modal Measurement & Identification .....	21
3.1.1 Frequency Response Function Method .....	22
3.1.2 Analytical Modal Models .....	26
3.1.3 Parameter Estimation of Modal Models .....	28
3.2 Numerical Example – 5DOF Lumped Mass Beam .....	36
3.2.1 Description of Beam.....	36
3.2.2 Eigenanalysis .....	37
3.2.3 Simulated FRF Measurements .....	40
3.2.4 Mode Interaction .....	46
3.2.5 SDOF Shape Estimates .....	51
3.2.6 SDOF Pole Estimates .....	54

3.2.7 Use of Multiple References .....	56
3.3 Conclusions.....	60
CHAPTER 4: TEST METHODOLOGY .....	61
4.1 Background .....	61
4.2 General Approach .....	62
4.3 FRF Measurements .....	63
4.3.1 Roving Measurements.....	65
4.3.2 Global Measurements.....	67
4.3.1 Combination of Measurements.....	69
4.4 Parameter Identification Considerations.....	70
4.4.1 Shape Estimation.....	72
4.4.2 Pole Estimation .....	75
4.4.3 Conclusions.....	77
4.5 Comparison to MRIT .....	78
CHAPTER 5: DESIGN & DEVELOPMENT OF THMPER SYSTEM .....	80
5.1 Overview of System Design.....	80
5.2 Excitation Source .....	81

5.2.1 Review of Impact from Falling Mass .....	81
5.2.2 Review of Impact Devices .....	84
5.2.3 Development & Component Testing .....	92
5.3 Response Measurements .....	103
5.3.1 Mobile Sensor Array .....	103
5.3.2 Wireless Stationary Reference Sensors .....	115
5.4 Software Systems .....	120
5.4.1 Data Acquisition & Controls .....	121
5.4.2 Modal Analysis Tools .....	122
5.5 Summary of Completed System.....	129
CHAPTER 6: Overview of Field Validation Case Study .....	131
6.1 Introduction.....	131
6.2 Description of Bridge.....	132
6.3 On-site Observations .....	136
6.4 A Priori Modeling .....	139
6.4.1 RAMPS Overview .....	139
6.4.2 FE Model Creation .....	140

CHAPTER 7: MOSSY INTERCHANGE BRIDGE TESTS .....	141
7.1 Forced Vibration Tests .....	141
7.1.1 MRIT Benchmark .....	141
7.1.2 THMPER System.....	157
7.1.3 Comparison of Modal Parameters .....	172
7.2 Static Truck Load Test.....	175
7.2.1 Instrumentation Plan .....	176
7.2.2 Test Execution.....	178
7.2.3 Summary of Results .....	182
7.2.4 Summary of Constraints.....	190
7.2.5 Additional Measurements.....	192
CHAPTER 8: Model-Experiment Correlation .....	193
8.1 Modal Properties .....	194
8.2 Displacement Predictions.....	195
8.3 Load Rating.....	200
CHAPTER 9: SUMMARY OF MID-ATLANTIC CLUSTER THMPER TESTS .....	202
9.1 Overview of THMPER Tests .....	202

9.1.1 Traffic Control .....	202
9.1.2 Test Execution.....	203
9.2 Overview of Results .....	204
9.2.1 Data Quality .....	204
9.2.2 Parameter Estimation .....	204
9.3 Summary of Constraints.....	211
9.4 Summary of System Limitations .....	212
CHAPTER 10: CONCLUSIONS, RECOMMENDATIONS AND FUTURE WORK .....	214
10.1 Summary of Research Objectives and Scope .....	214
10.2 Conclusions.....	215
10.2.1 Conclusions Related to Objective 1 – Development of Rapid Structural Assessment Concept.....	216
10.2.2 Conclusions Related to Objective 2 – Theoretical Development.....	217
10.2.3 Conclusions Related to Objective 3 - System Design, Development and Integration .....	219
10.2.4 Conclusions Related to Objective 4a - Component Validation.....	220
10.2.5 Conclusions Related to Objective 4b - System Validation .....	221
10.2.6 Conclusions Related to Objective 4c - Field Implementation.....	222

10.3 Future Work .....	223
List of References .....	224
Vita .....	229

## List of Tables

Table 2-1: Comparison of Experimental Approaches .....	17
Table 3-1: Modal Properties.....	37
Table 3-2: MAC Comparison of SDOF Column Residue Estimation .....	52
Table 3-3: Residue Damping Estimation .....	55
Table 3-4: Residue Damped Natural Frequencies Estimation .....	55
Table 3-5: Comparison of Mode shape solution as a function of column reference .....	56
Table 3-6: Best to Worst Ranking of MAC Correlations .....	57
Table 3-7: Damping Estimations – Percent Error.....	59
Table 3-8: Natural Frequency – Percent Error by Input Pairs .....	59
Table 5-1: Impact Numerical Analysis Variable Definitions .....	83
Table 5-2: Summary of Impact Device Comparison .....	100
Table 5-3: Accelerometer Benchmark – Root Mean Square Comparison.....	112
Table 7-1: Sledge MRIT – MAC Values .....	151
Table 7-2: Sledge MRIT – Natural Frequencies and Damping .....	152
Table 7-3: Sledge MRIT – Natural Frequencies and Damping .....	168
Table 7-4: THMPER vs. Sledge – MAC Values .....	173

Table 7-5: THMPER vs. Sledge – MAC Value Statistics .....	173
Table 7-6: Pole Estimation Percent Error.....	175
Table 7-7: Pole Estimation Comparison – Statistics .....	175
Table 7-8: Truck Test Instrumentation Schedule .....	177
Table 7-9: Load Test – Truck Configurations & Applied Loads.....	179
Table 7-10: Peak Strain and Displacement.....	185
Table 7-11: Neutral Axis Locations .....	188
Table 8-1: Comparison of Experimental and Predicted Natural Frequencies .....	194
Table 8-2: Comparison of Experimental and Predicted Natural Frequencies - Percent Error.....	194
Table 8-3: Displacement Predictions – Percent Error .....	195
Table 8-4: Displacement Predictions – Percent Error Statistics .....	196
Table 8-5: LRFR Load Rating Factors.....	200
Table 9-1: Overview of THMPER Mid-Atlantic Cluster Tests.....	202

## List of Figures

Figure 1-1: Systems Engineering “V” Model (National ITS Architecture Team, 2007) .....	7
Figure 2-1: Strain Gauge Installation .....	13
Figure 2-2: Challenges of Underside Instrumentation.....	14
Figure 2-3: Rapid Modal Test System .....	18
Figure 2-4: Global Modal Parameter Integration .....	19
Figure 3-1: Measurement of the FRF (Allemang R. J., Vibrations III: Experimental Modal Analysis, 1999) .....	22
Figure 3-2: Frequency Response Function and Characteristic Space .....	24
Figure 3-3: 5DOF Discrete System .....	37
Figure 3-4: Eigenvector – Mode 1 .....	38
Figure 3-5: Eigenvector – Mode 2 .....	38
Figure 3-6: Eigenvector – Mode 3 .....	39
Figure 3-7: Eigenvector – Mode 4 .....	39
Figure 3-8: Eigenvector – Mode 5 .....	40
Figure 3-9: 5DOF – Numerical Example – Mode Contributions .....	41
Figure 3-10: FRF Magnitude – H33.....	42

Figure 3-11: Phase Angle – H33 .....	42
Figure 3-12: IRF – H33.....	43
Figure 3-13: SIMO - Column Measurement – Input at DOF 1 .....	44
Figure 3-14: MISO – Row Measurement – Output at DOF 1 .....	44
Figure 3-15: Driving Point Comparison H11 vs H33.....	45
Figure 3-16: FRF Magnitude – H11.....	47
Figure 3-17: Phase Angle – H11 .....	47
Figure 3-18: FRF Magnitude – H51.....	48
Figure 3-19: Phase Angle – H51 .....	48
Figure 3-20: FRF Magnitude – H22.....	49
Figure 3-21: Phase Angle – H22 .....	49
Figure 3-22: FRF Magnitude – H42.....	50
Figure 3-23: Phase Angle – H42 .....	50
Figure 3-24: SDOF Residue Estimation – Mode 4 – Input at DOF 1 .....	53
Figure 3-25: SDOF Residue Estimation – Mode 5 – Input at DOF 1 .....	53
Figure 3-26: SDOF Residue Estimation – Mode 5 – Input at DOF 3 .....	54
Figure 3-27: Mode 5 – Eigenvector vs Mode Shape from References 1 & 2 .....	58

Figure 4-1: THMPER System – Typical Test Configuration .....	63
Figure 4-2: THMPER Measurement Example .....	65
Figure 4-3: 5DOF Beam – Roving Measurement.....	65
Figure 4-4: 5DOF Beam – Global Measurement Example.....	68
Figure 4-5: 5DOF Beam - Global DOF – CMIF .....	71
Figure 4-6: 5DOF Beam – Roving DOF – CMIF.....	71
Figure 4-7: 5DOF Beam – Combined DOF - CMIF .....	72
Figure 4-8: 5DOF Beam – Global DOF – Mode 1 - Shape .....	73
Figure 4-9: 5DOF Beam – Roving DOF – Mode 1 - Shape .....	73
Figure 4-10: 5DOF Beam – Combined DOF – Mode 1 - Shape .....	74
Figure 4-11: 5DOF Beam – Global DOF – Mode 2 - Shape .....	74
Figure 4-12: 5DOF Beam – Roving DOF – Mode 2 – Shape.....	75
Figure 4-13: 5DOF Beam – Combined DOF – Mode 2 - Shape .....	75
Figure 4-14: 5DOF Beam – Global DOF – Mode 1 – Pole Fit.....	76
Figure 4-15: 5DOF Beam – Roving DOF – Mode 1 – Pole Fit.....	77
Figure 4-16: 5DOF – Combined DOF – Mode 1 – Pole Fit .....	77
Figure 4-17: Characteristic Space –Traditional MRIT (Left) vs. THMPER Approach (Right)....	79

Figure 5-1: Overview of THMPER System .....	80
Figure 5-2: Impact Numerical Analysis .....	82
Figure 5-3: Impact Numerical Analysis Results.....	84
Figure 5-4: Impact Devices used for PCB Tests .....	85
Figure 5-5: Pennsauken Creek Bridge in Palmyra, New Jersey – Elevation View.....	85
Figure 5-6: Impact Force Characteristics – Instrumented Sledge .....	86
Figure 5-7: Impact Force Characteristics – Damped Drop Hammer .....	87
Figure 5-8: Impact Force Characteristics – Drexel Drop Hammer Proto1 .....	88
Figure 5-9: Drexel Drop Hammer with Rebound Control.....	90
Figure 5-10: Impact Force Characteristics – Drexel Drop Hammer Proto2 .....	91
Figure 5-11: Original FWD Trailer Purchased in June, 2011.....	92
Figure 5-12: Excitation Source - A Modified FWD Impact Device .....	94
Figure 5-13: Falling Weight Deflectometer Load Cell Installation .....	95
Figure 5-14: Force Ring Load Cell .....	95
Figure 5-15: Load Cell Assembly – Benchmark Test .....	96
Figure 5-16: Load Cell Assembly – Benchmark Test – Load Cell Individual Force Record .....	97
Figure 5-17: Load Cell Assembly – Benchmark – Comparison of Forces – Time Domain .....	97

Figure 5-18: Load Cell Assembly Laboratory Benchmark – Frequency Comparison .....	98
Figure 5-19: Rebound Mitigation System .....	99
Figure 5-20: Impact Carriage Schematic.....	99
Figure 5-21: Comparison of Impact Devices – Time Domain.....	101
Figure 5-22: Comparison of Impact Devices – Frequency Domain .....	101
Figure 5-23: THMPER vs Sledge – FRF Comparison in Traffic .....	103
Figure 5-24: THMPER System Sensor Footprint.....	104
Figure 5-25: Mobile Sensor Array – Pneumatic Deployment & Sensor Housing Details .....	105
Figure 5-26: Sensor Housing Prototypes.....	106
Figure 5-27: Numerical Benchmark Model.....	107
Figure 5-28: Numerical Benchmark – Acceleration Record .....	107
Figure 5-29: Numerical Benchmark – Frequency Content.....	108
Figure 5-30: Accelerometer Housing – Experimental Benchmark Setup .....	109
Figure 5-31: Experimental Benchmark – Time Domain Comparison .....	109
Figure 5-32: Experimental Benchmark – Frequency Domain Comparison 1 .....	110
Figure 5-33: Experimental Benchmark – Frequency Domain Comparison 2 .....	110
Figure 5-34: Filter Design.....	111

Figure 5-35: Driving Point Comparison – Post Filter.....	112
Figure 5-36: THMPER Driving Point Benchmark – Filtered Vs. Non-Filtered Response .....	113
Figure 5-37: Trailer Mounted Data Acquisition & Control.....	114
Figure 5-38: Data Acquisition & Control Schematic .....	115
Figure 5-39: Distributed Data Acquisition Module.....	116
Figure 5-40: GPS Synchronization Concept .....	117
Figure 5-41: GPS Synchronization – Signal Comparison .....	118
Figure 5-42: GPS Synchronization – Zoomed Signal Comparison .....	119
Figure 5-43: GPS Synchronization – Relative Drift.....	120
Figure 5-44: Data Acquisition & Control User Interface Panel.....	122
Figure 5-45: Matlab/Strand7 API Panel.....	123
Figure 5-46: VMA File IO Panel .....	124
Figure 5-47: VMA – Pre-Processing Panel .....	125
Figure 5-48: Modal Parameter Identification – CMIF – Shape Selection Panel.....	127
Figure 5-49: Modal Parameter Identification – CMIF / eFRF – Pole Selection .....	128
Figure 5-50: THMPER System – Trailer Subsystem Components.....	130
Figure 6-1: Load Posting.....	133

Figure 6-2: Regional Location of Test Site .....	134
Figure 6-3: Position of Test Structure and Staging Zones .....	134
Figure 6-4: Bridge Topsides .....	135
Figure 6-5: Bridge Underside.....	135
Figure 6-6: Center Span Deck Deterioration.....	136
Figure 6-7: Expansion Bearing at Interior Girder – Pier 1 .....	137
Figure 6-8: Deterioration of Exterior Expansion Bearings at Pier 1 .....	138
Figure 6-9: Center Span (Far) and Side Span (Near) Exterior Expansion Bearings at Pier 2 .....	138
Figure 6-10: Repairs at Pinned Bearing Pier .....	139
Figure 6-11: Schematic of FEM Bridge Model Developed with RAMPS.....	140
Figure 7-1: Benchmark MRIT – Instrumentation Plan.....	142
Figure 7-2: Sledge MRIT – FRF – Driving Point at DOF 13 .....	143
Figure 7-3: Sledge MRIT – FRF – Driving Point at DOF 22 .....	143
Figure 7-4: Sledge MRIT – Reciprocity – DOF 9 & 17 .....	144
Figure 7-5: Sledge MRIT – Reciprocity – DOF 4 & 22 .....	145
Figure 7-6: Sledge – MRIT – CMIF .....	146
Figure 7-7: Sledge MRIT – Mode 1 .....	147

Figure 7-8: Sledge MRIT – Mode 2.....	147
Figure 7-9: Sledge MRIT - Mode 3.....	148
Figure 7-10: Sledge MRIT – Mode 4.....	148
Figure 7-11: Sledge MRIT - Mode 5.....	149
Figure 7-12: Sledge MRIT – Mode 6.....	149
Figure 7-13: Sledge MRIT – Mode 7.....	150
Figure 7-14: Sledge – MRIT – Mode 8.....	150
Figure 7-15: Sledge MRIT – MAC Values .....	151
Figure 7-16: Sledge MRIT – eFRF Estimates for Modes 1 - 4.....	153
Figure 7-17: Sledge MRIT – eFRF Fit – Mode 1 .....	154
Figure 7-18: Sledge MRIT – eFRF Fit – Mode 2 .....	154
Figure 7-19: Sledge MRIT – eFRF Fit – Mode 3 .....	155
Figure 7-20: Sledge MRIT – eFRF Fit – Mode 4 .....	155
Figure 7-21: Sledge MRIT – FRF Synthesis – Input at DOF 17, Output at DOF 9.....	156
Figure 7-22: Sledge MRIT - FRF Synthesis – Input at DOF 22, Output at DOF 4 .....	157
Figure 7-23: THMPER System Test on Mossy Interchange Bridge.....	158
Figure 7-24: THMPER Instrumentation Plan.....	159

Figure 7-25: THMPER – Force – Time Signal .....	160
Figure 7-26: THMPER – Force – Frequency Content.....	160
Figure 7-27: THMPER – Typical Driving Point Acceleration .....	161
Figure 7-28: THMPER – FRF Measurement and Coherence.....	162
Figure 7-29: THMPER – CMIF.....	163
Figure 7-30: THMPER – Mode 1 .....	164
Figure 7-31: THMPER – Mode 2 .....	165
Figure 7-32: THMPER – Mode 3 .....	165
Figure 7-33: THMPER – Mode 4 .....	166
Figure 7-34: THMPER – Mode 5 .....	166
Figure 7-35: THMPER – Mode 6 .....	167
Figure 7-36: THMPER – Mode 7 .....	167
Figure 7-37: THMPER – Mode 8 .....	168
Figure 7-38:THMPER – eFRF Fit – Mode 1 .....	170
Figure 7-39: THMPER – eFRF Fit – Mode 2 .....	170
Figure 7-40: THMPER – eFRF Fit – Mode 3 .....	171
Figure 7-41: THMPER – eFRF Fit – Mode 4 .....	171

Figure 7-42: THMPER vs. Sledge – Mode Shape Comparison – MAC Values.....	172
Figure 7-43: Mode Superposition Errors – Mode 1.....	174
Figure 7-44: mode Superposition Errors – Mode 2 .....	174
Figure 7-45: Superstructure Instrumentation Layout.....	176
Figure 7-46: Strain Gage Position .....	178
Figure 7-47: String Pot Position.....	178
Figure 7-48: Diaphragm Strain Gage Position .....	178
Figure 7-49: Typical String Pot Installation .....	180
Figure 7-50: Installation of String Pot Displacement Sensors .....	180
Figure 7-51: Strain Gauge Web Installation – Web .....	182
Figure 7-52: Positioning Trucks during Proof Loading.....	183
Figure 7-53: Proof Load Truck Positions.....	183
Figure 7-54: Proof Load Test – Peak Displacements .....	184
Figure 7-55: Proof Load Test – Strain Responses .....	184
Figure 7-56: Midspan Displacement vs Quarterspan Load .....	186
Figure 7-57: Midspan Displacement vs Midspan Load .....	187
Figure 7-58: Midspan Displacement vs Three-Quarterspan Load .....	187

Figure 7-59: Variability of Neutral Axis Due to Load Levels.....	190
Figure 7-60: Underside Installation with Hydra Platform .....	191
Figure 8-1: Comparison of Predicted Displacements – Elevation View.....	197
Figure 8-2: Cross-section Displacement – Proof Load Test – Quarter Span .....	198
Figure 8-3: Cross-section Displacement – Proof Load Test – Mid Span.....	198
Figure 8-4: Cross-section Displacement – Proof Load Test – Three-Quarter Span.....	199
Figure 9-1: Two Span Example – Plans .....	206
Figure 9-2: Two Span Example – Bearing Details .....	206
Figure 9-3: CMIF of NJ Bridge.....	207
Figure 9-4: CMIF – Low Frequency Band.....	208
Figure 9-5: Mode 1 .....	209
Figure 9-6: Mode 2 .....	209
Figure 9-7: Mode 3 .....	209
Figure 9-8: Mode 4 .....	209
Figure 9-9: CMIF – Frequency Band 2 .....	210
Figure 9-10: Mode 10 .....	211
Figure 9-11: Mode 11 .....	211

Figure 9-12: Mode 12 .....	211
Figure 9-13: Mode 13 .....	211
Figure 10-1: Systems Engineering “V” Model (National ITS Architecture Team, 2007) .....	215
Figure 10-2: The Targeted Hits for Modal Parameter Estimation and Rating (THMPER) System .....	219
Figure 10-3: THMPER System Test Methodology .....	220

## Abstract

### **Design, Development and Validation of a Rapid Modal Testing System for the Efficient Structural Identification of Highway Bridges**

John L. DeVitis

A rapid modal testing system for highway bridges was designed, developed, and validated. The motivation for the work stemmed from the lack of quantitative, experimental evaluations in current highway bridge condition assessment practice. Modern applications of St-Id can provide an accurate assessment of the load carrying capacity of a highway bridge but are too costly for widespread application. The developed system aims to supplement perform modal impact tests on common highway bridges in a rapid, low-cost, and repeatable manner.

The experimental approach utilizes a mobile driving point (input/output source) that is equipped with a local array of accelerometers and a reduced set of stationary sensors. The stationary sensors are installed out of the way of traffic and are used as a modal scaling and phase reference. This allows independent subsets of local single-input-multiple-output (SIMO) measurements to be sequentially integrated into a full multiple-input-multiple-output (MIMO) data set. The result is a mobile, adaptable testing system that can quickly and efficiently obtain reliable FRF measurements of a structure.

As part of this research, the physical prototype of the test system was developed using a systems engineering approach. Through a series of numerical examples, laboratory benchmarks, and field tests, the prototype system and general experimental and analytical methodology is developed. The system performance is evaluated by comparisons between two field tests on a typical highway bridge: a multi-reference impact test (MRIT) and a static truck load test. The research concluded that the prototype system is capable of performing a modal impact test that is

equivalent to a traditional MRIT but with reductions in both time and cost of the evaluation. The research also found good agreement between displacement predictions made by a finite element (FE) model that was calibrated with the dynamic results from the prototype system and the “ground truth” displacement measurements obtained by truck load testing.



## CHAPTER 1: INTRODUCTION

### 1.1 Vision

The research reported herein aims to develop a quantitative bridge structural assessment tool which disrupts the current cost/benefit trade-offs of conventional approaches. While ‘best practices’ field testing approaches are more than capable of providing an objective and quantitative understanding of bridge performance, they are costly and require significant traffic disruptions, and thus are very rarely used. As a result, bridge structural assessment practice is forced to rely on excessively conservative approaches that distort true bridge performance and hamper the ability to effectively allocate resources to preserve and renew the U.S. bridge population. By relaxing the costs and access constraints associated with field testing approaches, the envisioned tool will provide owners, for the first time, with the ability to rapidly and cost-effectively obtain quantitative structural performance data across broad populations of bridges.

### 1.2 Summary of Current Bridge Assessment Practice within the U.S.

The practice of bridge assessment in the U.S. can be traced to the 1967 collapse of the Silver Bridge between West Virginia and Ohio. This event led to the Federal Highway Aid Bill of 1968, which required the U.S. Secretary of Transportation to develop a standardized approach for bridge inspection. The National Bridge Inspection Standard (NBIS, 1970) followed and provided guidance related to bridge inspector qualifications, inspection and load rating procedures, and the coding of bridge data (descriptive and condition-related) for compliance with the National Bridge Inventory (NBI) database. While the general approach to bridge assessment remains unchanged from its inception, an evolution of these procedures occurred due to bridge failures that brought “new” vulnerabilities to light (e.g. definition of “fracture-critical” and “scour-critical” bridges and associated additional inspection requirements) as well as the desire to use inspection data to better

inform bridge management practices (which has prompted visual inspections to adopt a higher spatial resolution).

Today, bridge assessment practice in the U.S. requires the collection/calculation and reporting of four types of information. The first is the development of condition ratings based on visual inspection. This falls under the purview of FHWA's Office of Infrastructure, Bridges and Structures Office which issues and maintains the National Bridge Inspection Standards (NBIS, 2004). While these procedures have evolved over the last four decades as described above, they remain inherently qualitative in nature and are conditioned by an inspector's education, experience, vision, hearing, and safe climbing-reaching skills. More quantitative surveying and scanning with non-destructive evaluation (NDE) tools are referenced when conditions warrant, but their actual use is optional and their deployment is rare.

In addition, during regular inspections, more than 100 inventory items are collected either from past inspection reports, design/as-built plans, or field survey. These items describe both the attributes of a bridge as well some demands. For example, this information includes bridge type and material, overall dimensions, number of spans, average daily traffic (ADT) and average daily truck traffic (ADTT), among others. Inventory items of particular importance are related to the scour and fracture criticality of the bridge, which can influence the type and frequency of required visual inspections.

The third item required is the calculation and reporting of a “load rating” for each bridge, that reflects its capacity to carry live loads. Operating and Inventory ratings are generally based on the analysis of a simple line-girder idealization following allowable stress, load factor or load and resistance factor approaches (Hearn 2014). While the representative nature of such simplified models is debatable (as discussed further below), load ratings are noteworthy as they remain the

only assessment activity to attempt to quantitatively assess a safety-related limit state based on principles of physics.

The final activity associated with assessment is the calculation and reporting of indices and designations that combine information from the other three sources to aide in decision-making and resource allocation. These historically have taken the form of Structurally Deficient and Functionally Obsolete designations as well as the computation of the Sufficiency Rating. With the increased popularity (and now requirement) for element-level inspections, the development of indices that combine element-level condition ratings are now becoming more relevant. Examples include the California Health Index and the AASHTO Health Index.

### **1.3 Discussion of Current Structural Assessment Practice**

The process outlined by the American Association of State Highway Transportation Officials (AASHTO) (2011) for computing load rating factors is organized into a hierarchy of methods that essentially present a trade-off between accuracy and cost. That is, the lowest levels of the hierarchy are the least expensive, but tend to under-estimate the actual capacity of a bridge. As you move up through the hierarchy, the methods become both more expensive and more accurate in terms of capacity estimation.

The most common approach to perform load ratings of bridges makes use of simple analytical models and is typically referred to as the single-line girder method. In this approach, the bridge is typically idealized as a single, static beam through the use of live load distribution factors (which approximate the percentage of a lane-load carried by each girder), skew correction factors, and dynamic load allowance factors. A recent NCHRP study investigated current bridge load rating and posting practices within the U.S. (Hearn, 2014) and found that over 80% of bridges are rated using this approach, which accounted for over 95% of all load ratings reported (as the study also

found that 16% of bridges received no load rating). Although this simple method is convenient and thus quite popular, it has been shown to systematically under-estimate the true safe load-carrying capacity of many types of bridges and to incorrectly identify critical members and or behavioral mechanisms (Masceri 2015).

The next level of the hierarchy involves refined simulation modeling approaches. In this method, more accurate finite element (FE) simulation models are used to better estimate the stresses and deflections that may result from various truck configurations and weights. While this approach is more accurate than the single-line girder approach, it requires a more explicit representation of the bridge and thus the user must make a number of modeling assumptions related to the performance/participation of diaphragms/cross-frames, boundaries, barriers and sidewalks, etc. Without some direct measurements from a bridge that may help inform such modeling decisions, it is difficult to justify such decisions, especially considering that the results obtained from the FE model simulations may be far less conservative than the single-line girder approach. Given these challenges and the higher cost associated with such methods, it is no surprise that they are rarely implemented (Hearn 2014).

The top level of the hierarchy focuses on the use of field testing to take actual measurements from the bridge in question. This is typically done by placing sensors on the bridge and measuring responses (strains and deflections) caused by trucks of known weight. These measurements may either be used directly to compute a rating factor (termed proof-level load testing) or used in conjunction with either an FE model or a single-line girder model to estimate rating factors (termed diagnostic-level load testing). Although such methods are not without their technical problems (Weidner 2012), they are inherently superior to other approaches as they include direct observations of the performance of the bridge in question. That is, these are the only methods that establish a direct link to the bridge through observed responses, and thus have the ability to more

accurately estimate load carrying capacity and other structural characteristics (which may be needed to properly diagnose durability and other performance problems).

Given the clear benefits of field testing approaches, it is somewhat surprising that in practice such approaches are rarely ever used. Consider that over 61,000 bridges are currently posted for less than legal loads, but fewer than 600 bridges nationwide have been rated using load testing procedures (Hearn 2014). It is clear that owners do not consider current load testing approaches to be an attractive proposition in terms of value. This no doubt stems from the relatively high cost associated with such tests as well as the required closures during the preparation and execution of the test that imposes significant traffic disruptions.

#### **1.4 Summary of Research Objectives and Scope**

As stated previously, the research reported herein aimed to develop a quantitative bridge structural assessment tool which disrupts the conventional cost/benefit paradigm, and offers a rapid and cost-effective approach to informing decisions that require a reliable and quantitative understanding of structural performance. To meet this overarching goal and help structure the entire research effort, the following four specific research objectives were defined and adopted.

- (1) Develop a rapid structural assessment concept and establish its feasibility through (a) documenting logistical constraints associated with the field testing of bridges, (b) examining a suite of candidate assessment approaches and mapping their technical requirements against the identified logistical constraints, (c) establishing the feasibility of each candidate assessment approach to support rapid structural assessment, and (d) selection of the most promising technique and development of both a concept of operations and a set of system requirements.

- (2) Develop and validate a theoretical basis capable of extending the selected candidate approach to serve as the basis for the envisioned rapid structural assessment tool, which entails accommodating the identified logistical and technical constraints, and updating the concept of operations and system requirements accordingly.
- (3) Design, develop, and integrate the necessary hardware and software systems required to realize the concept of operations and meet the identified system requirements
- (4) Establish the performance of the developed systems through (a) validation of the system components through comparison of performance with the identified requirements, (b) validation of the system performance through comparison with best practice structural assessment approaches, and (c) implementation on a suite of operating bridges to validate and/or refine the concept of operations.

## **1.5 Research Approach**

The research program carried out to satisfy the objectives list above is firmly rooted within the systems engineering paradigm. The International Council on Systems Engineering (INCOSE) defines systems engineering as an interdisciplinary approach and means to enable the realization of successful systems. The general approach to systems design focuses first on identifying the end-state expectations of the system, describing expectations and functionality in high-level terms, before any choices are made regarding the specific technology used and before the system is implemented.

A common process model used to describe the general steps of the system engineering approach is referred to as the “V” model (National ITS Architecture Team, 2007) and is shown in Figure 1-1. The “V” model is used as a framework to manage the system throughout its life-cycle. It provides a structure that facilitates focused development throughout the projects life-cycle and

aids to maintain a series of documented baselines which support each subsequent step of the process.

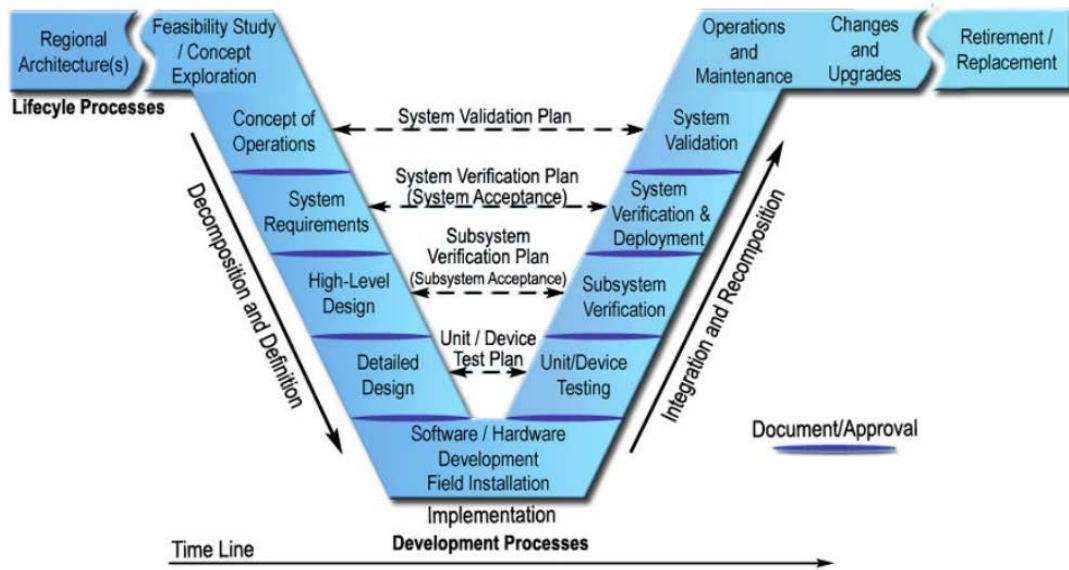


**Figure 1-1: Systems Engineering “V” Model (National ITS Architecture Team, 2007)**

As may be apparent to the readers, the objectives presented in the previous section were defined in a consistent manner with the systems engineering approach. Specifically, Objectives 1 and 2 focus on *Decomposition and Definition*, Objective 3 focuses on the *Development Process*, and Objective 4 focuses on *Integration and Recomposition*.

## 1.6 Overview of Thesis Structure

The thesis is structured as follows:

Chapter 1 presents an overview of the current condition assessment practices as well as the motivation, objectives and structure of the research presented in this paper.

Chapter 2 explores the concept of rapid condition assessment and establishes the Concept of Operations and System Requirements. The Concept of Operations identifies the stakeholder's needs, describes the goals, vision, and scope of the system, and provides a general overview of the system's functionality and operation, and the System Requirements are a high level set of specifications that the system is designed to achieve.

Chapter 3 presents Experimental Modal Analysis (EMA) concepts and theory. Using a lumped mass beam as an illustrative example, the Frequency Response Function (FRF) method and accompanying modal parameter identification techniques are presented.

Chapter 4 presents the development of the experimental approach. Typical test scenarios and constraints encountered in EMA applications on civil structures are discussed and, together with theoretical and practical considerations, a general experimental strategy is developed and illustrated through numerical examples.

Chapter 5 presents the development of the hardware and software systems developed for the THMPER system. The component design requirements and unit/device testing and verification of the subsystem are presented as well.

Chapter 6 presents an overview of the case study bridge used in the field validation effort for the THMPER system. A description of the bridge, summary of observations from a field visit, and development of the a priori FE model are described.

Chapter 7 presents the experimental design and results of the testing performed on the Mossy Interchange Bridge. The dynamic tests (sledge MRIT and THMPER system) are described and the modal parameters are compared between the two tests. The static truck load testing is also described and the live load results presented.

Chapter 8 presents the finite element model calibration effort and comparisons of model predictions. The model calibration results and comparisons between the measured displacements and those simulated with the updated modes are shown.

Chapter 9 presents a summary of the Long Term Bridge Performance (LTBP) Mid Atlantic Cluster NDE effort. Eleven bridges within the Mid-Atlantic cluster were tested using the THMPER system. An example of a two-span analysis is presented as well as an evaluation of system performance.

Chapter 10 presents a summary of the research objectives and scope as well as the overarching conclusions regarding the four primary objectives.

## **CHAPTER 2: CONCEPT EXPLORATION, CONCEPT OF OPERATIONS, AND SYSTEM REQUIREMENTS**

This chapter describes the concept exploration, the Concept of Operation (ConOps), and the system requirements that guided the development of the THMPER system. As described in Chapter 1, the development of a ConOps is a critical, initial step within the Systems Engineering process as it is used to reach a shared understanding of the system to be developed and how it will be operated and maintained (National ITS Architecture Team, 2007). The ConOps identifies the stakeholder's needs, describes the goals, vision, and scope of the system, and provides a general overview of the systems functionality and operation. It outlines the key concepts of the system's capabilities and conveys how those capabilities meet the stakeholder's needs in high level terms. The ConOps also identifies system success criteria which are used to form a plan for system validation.

### **2.1 Problem Statement**

Modern applications of St-Id can provide an accurate assessment of the load carrying capacity of a highway bridge but are too costly for widespread application. As a result, experimental evaluations are seldom used in practice - a recent NCHRP Synthesis report (Hearn 2014) reviewed state DOT load rating practices and reported less than 1% of load ratings were determined via truck load testing. Instead, owners routinely opt for simplified analytical methods, which are often excessively conservative. This practice has resulted in over 60,000 bridges nationwide being posted, which limits mobility, commerce, and the movement of emergency vehicles. Although it is impossible to say how many of these bridges actually require such load postings, applications of load testing routinely result in higher load ratings and the removal of posting suggesting that the widespread practice of posting may have more to do with the simplified analysis method employed than the actual safe load-carrying capacity of the bridge.

## 2.2 System Goals

The envisioned system aims to break the cost/benefit compromise currently encountered in traditional assessment practices. The goal of the THMPER system is to provide an economical and logically feasible means of obtaining modal parameters to error screen and calibrate FE models that may in turn be used to produce more reliable load ratings. It is envisioned that this system will:

- Complement the qualitative and semi-qualitative assessment metrics with quantitative metrics
- Improve accuracy and reduce uncertainty of load rating estimations
- Improve resource allocation
- Reduce the number of structural deficient bridges caused by overly conservative analytical load ratings
- Remove unnecessary load postings caused by overly conservative analytical load ratings

## 2.3 Limitations of Existing Technologies

State of the art bridge evaluation utilizes the Structural-Identification (St-Id) paradigm as a means of interpreting experimental measurements into actionable metrics, such as a load rating. Experiments are designed to capture global characteristics related to load carrying mechanisms of the in situ structure and, within the context of St-Id, are used for comparisons to predictions made by simulation models (i.e. finite element model). The experiment/model comparison serves two purposes. Model uncertainties are an inherent reality when a complex, physical system is reduced to an idealized analytical model, and the inclusion of an experiment allows for an objective

verification that the physical mechanisms driving global behavior are represented. Once the analytical model and measured behavior are consistent, conservative bounds regarding modelling assumptions can be developed and loading simulations, such as a load rating, can be made with relative confidence. If the specific goal(s) of the St-Id application requires reducing the level of uncertainty further, several attributes of the model may also be calibrated to better represent the observed behavior. The ideal result of the St-Id process is to quantify and reduce the level of uncertainty of the predictions and decisions made with the refined model.

The high costs are typically accrued within the controlled experimentation, data reduction, and result interpretation phases of the paradigm. Experimentation involves the design, preparation, installation, and execution of a physical test, all of which are subjected to various bridge specific constraints. Once the experiment is completed, the raw data must be processed and reduced to actionable metrics which are interpreted and used for decision making, both of which require specific expertise.

### **2.3.1 Truck Load Tests**

Static truck load tests directly measure structural responses of a bridge due to live load and in some cases are able to measure specific characteristics explicitly (distribution factor, etc.). As a result, the measurements can be easily interpreted and understood within the context of the common simplified analytical rating procedure. However, truck load tests can be restrictive as heavy loaded trucks must be acquired, weighed, and coordinated in a series of loading patterns. This can be logically difficult to manage and requires complete closure to traffic and pedestrians during the loading phases of the experiment.

Truck load tests also require extensive access to the underside of the structure. Proper static tests involve the acquisition of local (e.g. strains, curvatures) and global (e.g. displacements, rotations)

response quantities. Installation of a standard strain gauge on a steel girder, for example, is a lengthy process that requires use of power-tools to remove paint and a micro-dot welder or epoxy to bond the gauge (Figure 2-1). This necessitates that an AC power source be accessible during underside installation. Displacement measurements are relative measurements which require an external reference below the bridge. This requires underside access which can be quite restricting. If the bridge spans over a roadway, additional traffic closures are needed which causes more disruption to traffic. If the bridge spans over a waterway additional access equipment such as a Hydra platform or snooper is needed (Figure 2-2) which can significantly lengthen installation times.



**Figure 2-1: Strain Gauge Installation**

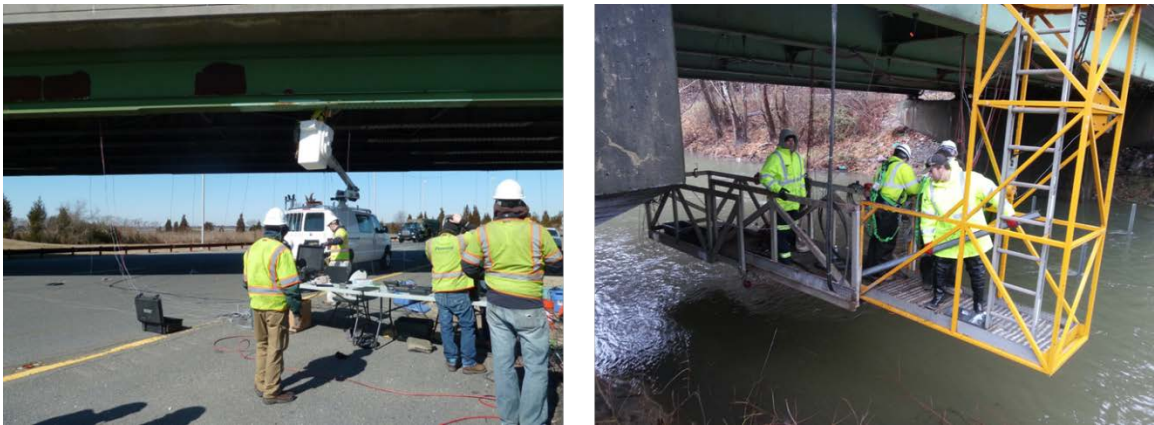


**Figure 2-2: Challenges of Underside Instrumentation**

### 2.3.2 Vibration Tests

The goal of vibration tests, or modal tests, is to identify the structure's in-situ modal parameters (e.g. frequencies, mode shapes). Modal parameters are directly related to the structure's in-situ mass and stiffness distributions and are estimated through multi-stage curve fits of the discrete FRF measurements. The modal model can be used directly (i.e. modal flexibility) or used to update an FE model.

Dynamic tests offer several advantages when compared to static tests – both the excitation and the response measurement are often significantly easier to acquire. Vibrations are measured with accelerometers which do not need an external reference and are relatively fast to install. This relieves many of the access and installation constraints associated with static measurements. The type of excitation source used can vary but is typically easier to use and transport compared to coordinating dump trucks.

### 2.3.2.1 Types of Vibration Tests

Vibration tests are categorized by the source of excitation to the system and fall into one of two categories, Operational Modal Analysis (OMA) or Experimental Modal Analysis (EMA). OMA is perhaps the most common method as it relies solely on the responses due to service operation level excitation (i.e. wind load and traffic load). EMA is the general approach of estimating the modal parameters of a structure using a controlled excitation source. EMA both provides and measures the forcing functions to the system.

OMA is particularly useful for larger, signature bridges where ambient excitation levels are too large to realistically overcome with shakers or impact devices. But in the context of testing short to medium span highway bridges, OMA approaches offer no real advantage when compared to EMA techniques. The excitation is assumed as white noise which may not always be an appropriate assumption, and because the excitation is not measured modal scaling (i.e. modal mass) cannot be estimated. OMA also offers no significant advantage in terms of the desirable location and number of sensors for highway bridge tests. Measurement degrees of freedom are determined by the system's structural characteristics, and, because the techniques used for EMA and OMA modal parameter estimation are essentially the same, the set of ideal measurements are the same as well. The only time an OMA approach may prove more useful than an EMA approach is when erroneous noise from the structure's operating conditions overwhelm the EMA excitation source. In this way, the OMA approach is used as a contingency plan.

EMA has the additional benefit of an observable input. This allows for modal scaling and a quantification of the linearity of the system. All systems have some degree of nonlinearity and deterministic input signals result in FRF estimations that are dependent on the signal level and type. Varied force levels during a field test can be used to identify and quantify nonlinearities (Allemand R. J., Vibrations III: Experimental Modal Analysis, 1999).

### 2.3.2.2 Excitation Sources

The two most common excitation approaches for modal testing of highway bridges are shaker testing and impact testing. Shaker tests use an oscillating mass to excite the structure throughout a frequency bandwidth of interest. The shaker is either placed onto the bridge deck or rigidly fixed to the structure if the system response is desired to reach +1g's. This is often necessary for bridges tested in the presence of traffic and makes spatially varying the inputs to the system a time consuming task. Typically a select few input locations are chosen and either a fixed grid or roving accelerometers are used to acquire the response. Shaker vibration testing has seen successful field use (Douglas and Reid 1982; Buckle et al. 1986; Richardson and Douglas 1993), however, generally requires testing times of approximately 20-30 minutes per input location.

In general, impact tests leverage input/output measurements from a roving excitation source (e.g. instrumented sledge, drop hammer, etc.) and a fixed array of accelerometers to determine the structure's discrete FRF (Raghavendrachar and Aktan 1992; Aktan et al. 1993; Aktan et al. 1995; Aktan et al 1996; Farhey et al. 1997; Lenett et al. 1997; Catbas et al. 1997; Turer et al. 1998, Prader 2012). The usefulness of the impulse technique lies in the fact that the energy in an impulse is distributed across a broad band within the frequency domain rather than occurring at discrete spectral lines as in the case of periodic signals (Halvorsen & Brown, 1977). A large amount of energy is imparted into the system, which results in large amplitude responses. Compared to the relatively low amplitude responses induced by the shaker, the larger responses resulting from an impact can be acquired more reliably, are less likely to be polluted with ambient excitation, and thus do not require long time-series for averaging. Only short periods of the structure's free-decay are needed to obtain good estimates of the systems modal parameters. The frequency content of the excitation can be configured by changing the mass and stiffness of the impact device and the force levels can be varied by adjusting the impact height. Broadband

excitation and short measurement windows make the impact method the most efficient and versatile experimental technique available.

### 2.3.3 Summary of Constraints

Comparisons of preparation and execution time, access equipment and requirements, as well as the extent and duration of traffic closures between the commonly used experimental approaches discussed above are shown in Table 2-1. The table is based upon the authors' experience and implementation of these technologies, and the ranges reflect bounds based on the bridge type, complexity, and ease of access. The relaxed time and execution constraints of dynamic testing most often renders these tests slightly more economical than truck load tests. However, despite the advantages, more user-expertise is generally required to interpret vibration data into actionable metrics due to the level of abstraction between the measured acceleration and afield calibrated FE model for load rating estimation.

**Table 2-1: Comparison of Experimental Approaches**

	Technology/ Approach	Cost	Prep. Time	Testing Time	Report Time	Access Equip	Bridge Closure	Overall Quality
Quasi-Static	Ambient monitoring w/ displacement transducers	\$30-50K	5-10 days	2-5 day	3-5 days	Yes	Only under-side	Mod
	Load testing w/ strain and displacement transducers	\$30-50K	5-10 days	1 day	3-5 days	Yes	Partial to Full	High
Dynamic	Ambient vibration monitoring	\$20-30K	1-3 days	2-5 days	5-7 days	Yes	Only under-side	Mod
	MIMO Impact Testing	\$30-40K	1-3 days	1-2 day	5- 7 days	Yes	Partial to Full	High/ Mod

## 2.4 Concept of Operations

To mitigate the constraints of conventional experimental approaches, the envisioned system is a self-contained modal impact testing trailer that is equipped with a broad banded impact source and local, distributed accelerometer array (Figure 2-3). At the start of the test, a fixed grid of accelerometers is installed along any available shoulders or sidewalks. These stationary measurements are installed out of the way of traffic and remain throughout the test. The system is towed by a vehicle outfitted with a mobile workstation and performs impact tests at several locations along each traffic lane during brief traffic slow-downs or single lane closures. The stationary measurements are used as a global reference to sequentially integrate the roving measurements into a full set of modal parameters (Figure 2-4).

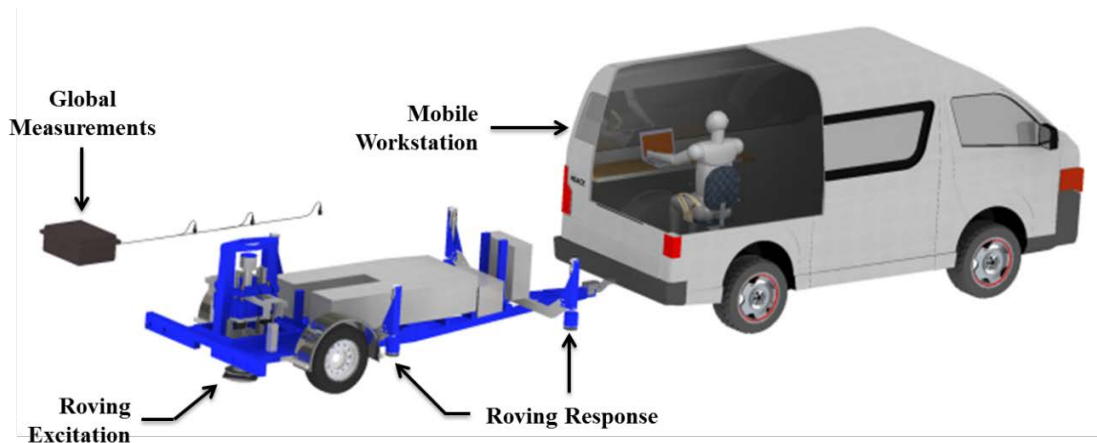
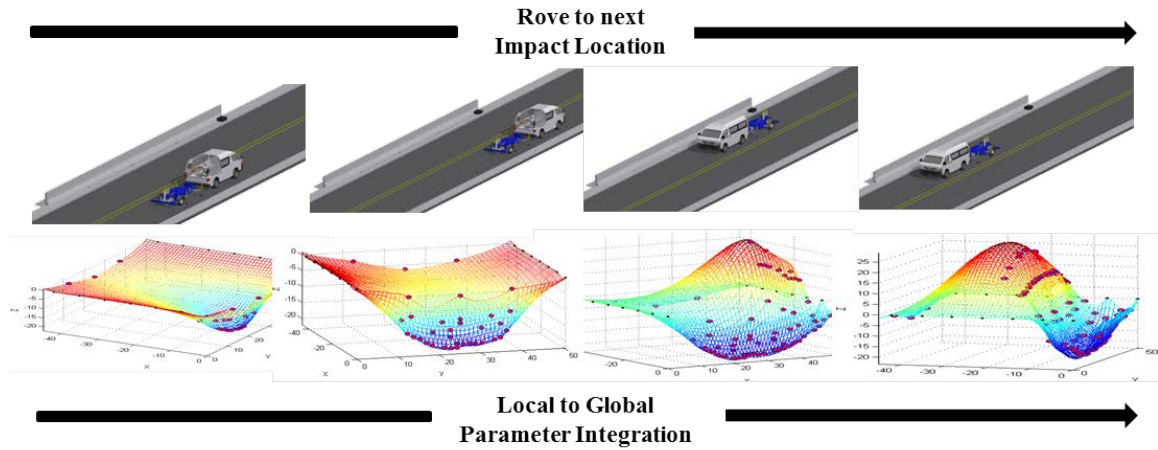


Figure 2-3: Rapid Modal Test System



**Figure 2-4: Global Modal Parameter Integration**

## 2.5 System Requirements

Given the constraints of the existing technologies, the functional objectives of the envisioned system are to minimize cost and effort of field test preparation, installation, and execution while streamlining data acquisition, data reduction and analysis, and result interpretation. The method must minimally disrupt daily operation of the bridge, and the system must ultimately be flexible as each experiment presents a specific set of constraints. Therefore, the system requirements are:

- Rapid execution – The speed of test execution determines the duration of the traffic control.
- Self-contained – The excitation source must be able to drive on to the bridge, excite the structure, measure the global response, and drive off while staying contained within a single traffic lane. A self-contained system also reduces the time required to prepare for each test.

- Test in the presence of traffic – This alleviates the need for extensive traffic control. Using a minimized traffic control reduces the impact the surrounding environment.
- Mobile & Rugged – The envisioned system will need to travel to each test bridge safely and efficiently and thus must be appropriately suited to withstand the fatigue of continuous travel.

## 2.6 System Validation Plan

System validation is necessary to confirm that the system meets the user's needs and effectively meets the intended purpose of the system. The effectiveness of the developed system and test methodology will be determined through benchmark field tests using a typical highway bridge as a case study. The developed impact trailer and experimental approach of the THMPER system will be compared to a conventional "best practices" MRIT using the following success criteria:

- Natural Frequencies within +/-5%
- Mode Shapes Modal Assurance Criterion (MAC) value above .9

The case study will also be used to evaluate the system level design goals.

In addition to directly comparing modal results, the vibration tests will also be used to update several FE models. The FE models are used to predict truck load displacements and field calibrated load ratings which compared to ground truth displacement measurements. The results from the correlated FE model predictions will be assessed using the following success criteria:

- Displacement predictions within +/-15%
- Load Rating estimations within +/-25%

## CHAPTER 3: EXPERIMENTAL MODAL ANALYSIS CONCEPTS

This chapter presents an overview of Experimental Modal Analysis (EMA) concepts and theory. The Frequency Response Function (FRF) method and accompanying modal parameter identification techniques are presented. A simple beam is used as an illustrative example throughout.

### 3.1 Modal Measurement & Identification

EMA is an inverse process where system response information is used to estimate system state information of the structure (e.g. mass and stiffness distributions). This is different than the forward analysis where the state information is known and the desired attribute is system response. With modern computing hardware and software, the solution space for the forward analysis is typically not limited by practical constraints and can be considered essentially infinite. For the experimental case, the models used to estimate modal parameters are affected by physical constraints of the experiment, which limit the spatial resolution of the data. The solution space is then determined by the DOF able to be physically measured. When performing an experiment on a large constructed facility such as a bridge, access and logistics often present significant challenges. This limits the solution space to DOF that are able to be practically measured and also limits the effectiveness of the modal parameter identification algorithms used to recover the system state information. In practice, a compromise is ultimately made which balances the accuracy and completeness of the estimated modal model with the required effort and cost of the experiment. Nevertheless, the effects of the experimental constraints on the models used for parameter estimation must be understood in order to produce meaningful modal models that are representative of the actual structure.

### 3.1.1 Frequency Response Function Method

The Frequency Response Function (FRF) method measures input/output relationships of the structure for use in parameter estimation and is the most common experimental approach in EMA. FRF measurements (Figure 3-1) are performed by exciting the structure with force,  $F(\omega)$ , and measuring the system response,  $X(\omega)$ .

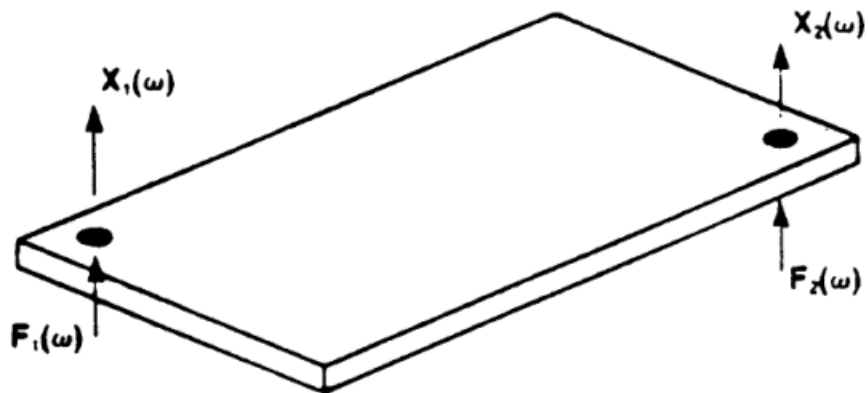


**Figure 3-1: Measurement of the FRF (Allemand R. J., Vibrations III: Experimental Modal Analysis, 1999)**

Modern applications of the FRF method leverage multiple inputs and outputs to the system to form a matrix of FRF measurements. Measurements are typically acquired in the time domain and transformed to the frequency domain via the Fast Fourier Transform (FFT).

#### 3.1.1.1 Relationship to Physical Attributes

The FRF is useful in St-ID because it provides a link between practical measurement quantities (force, acceleration) and the analytical representations of the structure's in-situ state information

(mass, stiffness) via modal models and parameter estimation. Though it is not typically used in this form, the single FRF measurement of a force at DOF  $q$  and response at DOF  $p$ ,  $H_{pq}$ , can be related to of the system state information by the general relationship:

$$H_{pq}(\omega) = \frac{X_p(\omega)}{F_q(\omega)} = \sum_{r=1}^{\infty} \frac{\psi_{pr} \psi_{qr}}{-M_r \omega^2 + C_r j\omega + K_r} \quad \text{3-1}$$

Where the  $M_r$ ,  $C_r$ , and  $K_r$  terms in the denominator refer to the system's modal mass, modal damping, and modal stiffness respectively. Evaluating the above equation along the frequency spectrum, the numerator remains a constant, and the denominator is minimized at areas of resonance (which in turn causes peaks in the FRF). At resonance, the modal mass and stiffness terms cancel and the amplitude of the system response is controlled by the modal damping term.

In the experimental case the modal mass, stiffness, and damping terms are a function of the chosen modal scaling and have no strict physical meaning. To extract modal parameters that are physically meaningful, a combination of estimation models and techniques are used to scale the parameter sets to match the amplitudes of the experimental FRF records. This effectively recovers the system's state information but is difficult in practice. Absolute scaling of the modal model is prone to several errors (i.e. modal truncation, calibration) which are amplified during scaling attempts. Additionally, the peaks in the FRF are controlled largely by damping and, since the actual mechanisms are not well understood, simple mathematical representations are often used which further clouds the extraction of modal scaling. Due to this it is common in St-ID to use the unscaled modal parameters (frequencies, mode shapes) for direct comparison to those determined

by a mechanistic model(s) of the physical structure (e.g. FE model) in order to assess the appropriateness of various modelling assumptions.

### 3.1.1.2 Characteristic Space

The space of all measurements within EMA is referred to as the *characteristic space* and is a function of spatial and temporal information. Two axes of this space represent the spatial locations of the input and output measurements and the third axis represents the temporal information of these DOF sampled in the time or frequency domains. For structural systems that are continuous in terms of mass and stiffness distributions, this space is fundamentally continuous and infinite. The FRF array can be considered the discrete measurement of this space and envisioned as a cube or matrix with rows and columns comprised of the measured outputs and inputs (Figure 3-2). The size of the matrix is determined by the number of output measurements, No, the number of input measurements, Ni, and the number of spectral measurements, Ns.

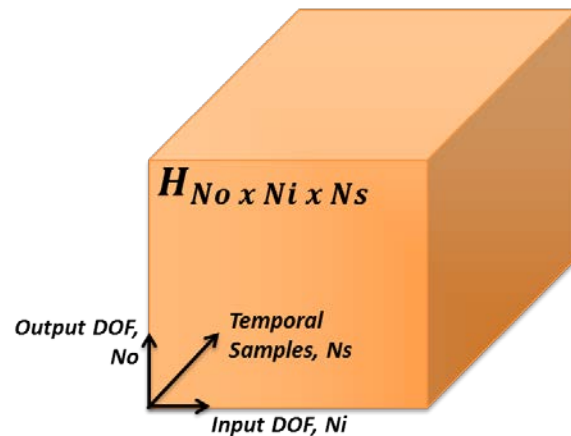


**Figure 3-2: Frequency Response Function and Characteristic Space**

### 3.1.1.3 General Measurement Configurations

Several general experimental approaches used within EMA are presented below based on how the characteristic space of the FRF is measured. Discrete measurement DOF are represented in linear algebra notation and are evaluated throughout the frequency domain. Note that the actual experiment may utilize any combination of these configurations as independent measurements of the FRF matrix can be combined provided the assumption of a linear, time invariant system holds.

#### *Single-input-single-output (SISO):*

Equation 3-1 describes the configuration where the characteristic space is measured by a single input (at point q) and a single output measurement (at point p).

$$X_p = H_{pq} F_q \quad 3-2$$

#### *Single-input-multiple-output (SIMO):*

Equation 3-2 describes the single input (at point q), multiple output (at points 1 through p) configuration.

$$\begin{Bmatrix} X_1 \\ X_2 \\ \vdots \\ X_p \end{Bmatrix} = \begin{Bmatrix} H_{1q} \\ H_{2q} \\ \vdots \\ H_{pq} \end{Bmatrix} F_q \quad 3-3$$

**Multiple-input-single-output (MISO):**

Equation 3-3 describes the multiple input (at points 1 through q), single output (at point p) configuration.

$$\{X_p\} = \{H_{p1} \ H_{p2} \ \dots \ H_{pq}\} \begin{Bmatrix} F_1 \\ F_2 \\ \vdots \\ F_q \end{Bmatrix} \quad 3-4$$

**Multiple-input-multiple-output (MIMO):**

Equation 3-5 describes the multiple input, multiple output configuration.

$$\begin{Bmatrix} X_1 \\ X_2 \\ \vdots \\ X_p \end{Bmatrix}_{No \times 1} = \begin{bmatrix} H_{11} & \dots & H_{1q} \\ \vdots & \ddots & \vdots \\ H_{p1} & \dots & H_{pq} \end{bmatrix}_{No \times Ni} \begin{Bmatrix} F_1 \\ F_2 \\ \vdots \\ F_p \end{Bmatrix}_{Ni \times 1} \quad 3-5$$

### 3.1.2 Analytical Modal Models

FRF models of multiple degree of freedom (MDOF) systems are commonly represented as the linear summation of each individual single degree of freedom (SDOF) modal contribution. The FRF is the Laplace transform of the equation of motion evaluated at  $s = j\omega$  and can be represented as a general partial fraction expansion:

$$[H(\omega)]_{N \times N} = \sum_{r=1}^N \frac{[A_r]_{N \times N}}{j\omega - \lambda_r} + \frac{[A_r]^*_{N \times N}}{j\omega - \lambda_r^*} \quad 3-6$$

The numerator of the above equation is referred to as the residue matrix and is directly related to the modal vectors and absolute modal scaling for each mode by:

$$[A_r] = Q_r \{\psi\}_r \{\psi\}_r^T = Q_r \begin{bmatrix} \psi_1 \psi_1 & \cdots & \psi_1 \psi_N \\ \vdots & \ddots & \vdots \\ \psi_N \psi_1 & \cdots & \psi_N \psi_N \end{bmatrix} \quad 3-7$$

The residue matrices are constant throughout the frequency domain and represent the spatial information of the structure. The temporal information contained in the FRF is represented in the denominator of the partial fraction expansion and is the difference between the discrete complex frequency samples and the roots of the system's characteristic equation. These are often referred to as system poles of the FRF and are a function of the damping factor,  $\sigma_r$ , and the complex natural frequency,  $j\omega_r$ , of each mode:

$$\lambda_r = \sigma_r + j\omega_r \quad 3-8$$

The Impulse Response Function (IRF) is the time domain equivalent of the FRF and can also be expressed by the residues and system poles:

$$[h(t)]_{N \times N} = \sum_{r=1}^N [A_r] e^{\lambda_r t} + [A_r]^* e^{\lambda_r^* t} \quad 3-9$$

### 3.1.3 Parameter Estimation of Modal Models

In the experimental case, the spatial sampling of the FRF is determined by the input and output DOF and represented in the FRF model by explicit notation:

$$[H(\omega)]_{No \times Ni} = \sum_{r=1}^N \frac{[A_r]_{No \times Ni}}{j\omega - \lambda_r} + \frac{[A_r]^*_{No \times Ni}}{j\omega - \lambda_r^*} \quad 3-10$$

Where a single measurement is:

$$H_{pq}(\omega) = \frac{X_p(\omega)}{F_q(\omega)} = \sum_{r=1}^N \frac{A_{pq_r}}{j\omega - \lambda_r} + \frac{A_{pq_r}^*}{j\omega - \lambda_r^*} \quad 3-11$$

The residue matrix is a function of the input/output modal coefficients describing the relative motion of the DOF ( $\psi_p, \psi_q$ ) and modal scale factor,  $Q_r$ , which relates the arbitrary scaling of the mode shapes to the absolute units of the system. For proportionally damped systems, the modal scale factor of a MDOF system is related to the modal mass by:

$$M_r = \frac{1}{2j Q_r \omega_r} \quad 3-12$$

The models used for modal parameter estimation take various forms depending on which system attribute is desired from the actual estimation. Modal models used for parameter estimation typically simplify the measurement space from  $N$  to  $2N$ :

$$[H(\omega)]_{No \times Ni} = \sum_{r=1}^{2N} \frac{[A_r]_{No \times Ni}}{j\omega - \lambda_r} \quad 3-13$$

This generalization makes no assumption regarding the complex conjugate nature of the solution and allows for quality checks by comparing the two solutions found for each mode.

Another general form is found by recognizing that the amplitude of each residue is scaled by the product of the input and output DOF and the modal scale factor constant. Therefore, each column of the residue matrix for mode  $r$  is comprised of the modal vector multiplied by a constant that is proportional to the modal coefficient of the input DOF. When the modal scale factor is paired with the modal coefficient for the input DOF it is referred to as the *modal participation factor* and related to the residues by:

$$\{A\}_{qr} = Q_r \psi_{qr} \{\psi\}_r = L_{qr} \begin{Bmatrix} \psi_1 \\ \vdots \\ \psi_p \end{Bmatrix}_r \quad 3-14$$

Physically, the modal participation factor can be thought of as a relative indication of how well a mode was excited at each input location during the experiment. Multiple reference parameter estimation algorithms compare multiple columns of the FRF and make use of the modal participation factors/vectors to provide the relative scaling necessary to distinguish multiple modes contributing to the measured response at a particular frequency. This allows for multiple modal solutions within a specific frequency band and is useful when the structure exhibits modes that are closely spaced in the frequency domain.

Equation 3-13 can then be represented in terms of the input (modal participation vectors) and output (modal vectors) DOF:

$$[H(\omega)]_{No \times Ni} = [\psi]_{No \times 2N} [\Lambda]_{2N \times 2N} [L]_{2N \times Ni} \quad 3-15$$

Where:

$$[\Lambda]_{2N \times 2N} = \begin{bmatrix} \frac{1}{j\omega - \lambda_1} & \cdots & 0 \\ \vdots & \ddots & \vdots \\ 0 & \cdots & \frac{1}{j\omega - \lambda_{2N}} \end{bmatrix} \quad 3-16$$

### 3.1.3.1 Solution Process

Modal parameter estimation uses numerical techniques to separate and identify the contribution of each mode measured in the FRF. The general partial fraction expansion of the FRF is non-linear in terms of unknown modal parameters. Modal parameter identification algorithms estimate the system's state information through a series of multiple least squares curve fits of the experimental FRF data. Typically this is performed by estimating the numerator (residues) of the FRF in one stage and the denominator (roots) in another, the order of which is determined by the estimation algorithm or chosen approach.

### 3.1.3.2 Model Order

To model a physical system, the structure's continuous mass and stiffness distributions are idealized by a set of discrete measurement points. Analytical models are described by  $N$  DOF and thus have  $N$  modes of vibration with modal vectors of length  $N$  to describe the full system response. In the experimental case, the FRF is described by the number of inputs and the number of outputs and the model order of the estimation models is determined by the shorter of the two.

A single row or column FRF contains representations of the damped natural frequency, modal damping, mode shapes, and modal scaling (mass). SDOF approaches evaluate the frequency bandwidth near each system pole and estimate the modal parameters for each mode on an individual basis. As long as the structure is lightly damped and the modes are well spaced

throughout the frequency spectrum, the measured response is dominated by a single mode and SDOF approaches may yield good approximations of the modal vectors and damped natural frequencies of the system poles.

When the system exhibits frequency bandwidths with even moderate modal density, the solution determined via SDOF approaches will not be able to separate the contribution of each individual mode and *the SDOF residue solution will consist of the linear combination of the contributing modal vectors for each pole*. The size and shape of the measured FRF directly determines the available (and appropriate) parameter estimation approaches. Redundant information of the system is provided by measuring multiple columns of the FRF matrix and can be leveraged by MDOF modal parameter identification approaches to separate the individual contributions of each mode when SDOF assumptions are not valid.

### 3.1.3.3 Shape Estimation

Equation 3-15 is a convenient representation of the FRF as it facilitates the use of the Singular Value Decomposition (SVD). The SVD is the basis of the Complex Mode Indicator Function (CMIF). The CMIF is a spatial domain modal parameter estimation method and is formed by computing the SVD of the FRF at each frequency line:

$$[ H(\omega) ]_{No \times Ni} = [ U(\omega) ]_{No \times 2N} [ \Sigma(\omega) ]_{2N \times 2N} [ V(\omega) ]_{2N \times Ni} \quad 3-17$$

The singular values,  $\Sigma$ , are proportional to the modal scaling of each corresponding mode and are plotted on a log scale as a function of frequency. Each peak of the singular values represents a

location of resonance of the structure and the amplitude is directly related to the dominance of the corresponding mode shape at that frequency. At each frequency line, the left singular vector,  $U$ , is the approximate mode shape of the response DOF, and the right singular vector,  $V$ , is the approximate modal participation vector and represents the modal coefficients of the input DOF. The SVD is particularly useful when multiple columns of the FRF are used as it can detect and decouple multiple modes within a frequency bandwidth. If the SVD is computed with only a single column of the FRF, the summed residue vector for that column will be found at each frequency line. This then effectively reduces to a SDOF estimation approach.

### 3.1.3.4 Pole Estimation

In the CMIF/eFRF approach, the estimated mode shapes are used as a modal filter to condense the number of effective modal solutions for pole estimation. This is done by pre and post multiplying the FRF with each mode shape estimation and relies on the orthogonal properties of each shape (along with adequate sampling of the spatial domain) to enhance each mode's SDOF contribution to the measured MDOF response. This is typically referred to as the enhanced frequency response function (eFRF) and can be represented with the basic model:

$$eFRF_r(\omega) = \frac{Q_r}{(j\omega - \lambda_r)} \quad 3-18$$

The eFRF is then used in a Unified Matrix Polynomial Approach (UMPA) to perform a least squares curve fit of the temporal domain and obtain damping and natural frequency estimates for each mode. The simplified, second order UMPA model is:

$$[[\alpha_2] (j\omega)^2 + [\alpha_1] (j\omega)^1 + [\alpha_0] (j\omega)^0 ] eFRF_r(\omega) = \sum_{k=1}^n [[\beta_k] (j\omega)^k] \quad 3-19$$

### 3.1.3.5 Vector Scaling & Modal Mass

The SVD decouples the output and input modal coefficients of the residue matrices via the right and left singular vectors. The left and right singular vectors are unitary and scaled consistently as a set (but not individually) together with the real valued singular value (Allemand and Brown, 2006). That is, the pair of singular vectors at an area of resonance is proportional to the eigenvector of the system, but the recovered left and right vectors are scaled by different arbitrary constants. When either the full input or output space is measured ( $N_i = N$ , or  $N_o = N$ ), the right or left singular vectors are a full modal vector solution of the measurement DOF. In application, the entirety of the input and output space may not be measured and the size of each respective singular vector is reduced to the subset of measured inputs and outputs. The scaling difference between the left and right vectors must be addressed if a full modal vector of combined input and output DOF is desired.

Driving points refer to the DOF that share input and output measurements and are represented in both the left and right singular vectors. The subset of driving point DOF are typically referred to as the number of references,  $N_{ref}$ , and used to form a modal scaling factor ( $\alpha$ ) to establish consistent scaling between the two estimates of the same modal vector: .

$$\alpha_{cd_r} = \frac{\{\psi_{c_r}\}^H \{\psi_{d_r}\}}{\{\psi_{d_r}\}^H \{\psi_{d_r}\}} \quad 3-20$$

Scaling between the left and right singular vectors must also be corrected if the estimation of modal mass is desired. Once each system pole has been estimated using the eFRF method, modal mass is found in a simple least squares regression analysis around the peaks of each SDOF approximation. When the eFRF is formed using unitary singular vectors, the unit magnitude does not influence the modal scaling estimation. When this is not the case, additional scaling corrections are needed.

The scaling factor between the driving point subset of scaled left,  $\{u_{sc}\}$ , and right,  $\{v\}$ , singular vectors is found by the pseudo inverse:

$$C_3 = \{v\}_{1 \times Nref}^+ \{u_{sc}\}_{Nref \times 1} \quad 3-21$$

The appropriately scaled right singular vector,  $\{v_{sc}\}$ , is then defined as:

$$\{v_{sc}\} = C_3 \{v\} \quad 3-22$$

The scaling corrections for each eFRF are found by computing the Hermitian (squared length) of each vector:

$$\{u_{sc}\}^H \{u_{sc}\} = C_1 \quad \{v_{sc}\}^H \{v_{sc}\} = C_2 \quad 3-23$$

The formulation of the eFRF for mode  $r$  then becomes:

$$eFRF(\omega) = \frac{Q_r}{(j\omega - \lambda_r)} \approx \frac{\{u_{sc}\}^T [ H(\omega) ] \{v_{sc}\}}{C_1 C_2} \quad 3-24$$

### 3.2 Numerical Example – 5DOF Lumped Mass Beam

This section uses a simple numerical model to demonstrate the modal measurement and parameter identification concepts presented above.

#### 3.2.1 Description of Beam

A shear beam with five lumped mass DOF measured in the vertical axis as a function of frequency is shown in Figure 3-3. Each spring stiffness has a value of 6264 in/lb, and each mass is 1.8 lbm. This model was chosen as a relatively easy way to ensure that closely spaced modes existed while keeping the model simple.

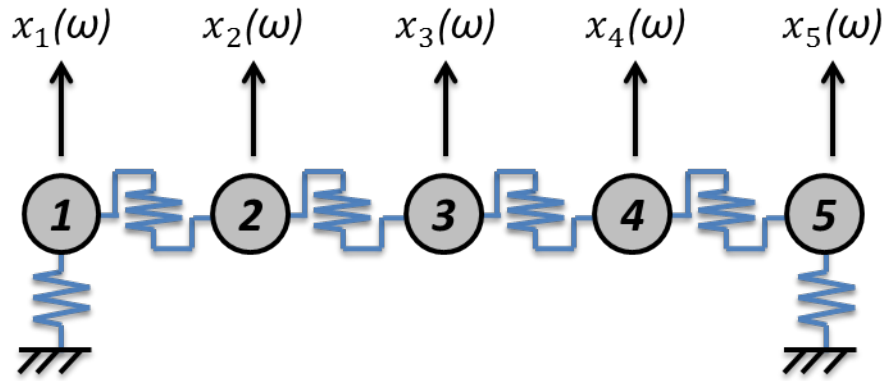


**Figure 3-3: 5DOF Discrete System**

### 3.2.2 Eigenanalysis

Eigenvalues and eigenvectors were found from the mass and stiffness matrices and are an exact solution for the beam. The eigenvectors are the orthonormal, mass normalized mode shapes that decouple the system's mass and stiffness matrices. The undamped natural frequencies found in the eigenanalysis were used with a damping ratio of 5% to calculate the damping factor and the damped natural frequencies (Table 3-1). Using the eigenvectors and modal damping as described creates a modal model with real, normal modes and proportional damping mechanisms. Note that modes three through five are relatively close in the frequency domain.

**Table 3-1: Modal Properties**

Mode	Un-damped Natural Frequency [rad/sec]	Damping Ratio	Damping Factor [rad/sec]	Damped Natural Frequency [rad/sec]	Damped [Hz.]
1	30.52	.05	-1.53	30.56	4.86
2	58.97	.05	-2.95	59.04	9.40
3	83.40	.05	-4.17	83.50	13.29
4	102.14	.05	-5.11	102.27	16.28
5	113.92	.05	-5.69	114.07	18.15

The beam's five eigenvectors are plotted in Figure 3-4 through Figure 3-8:

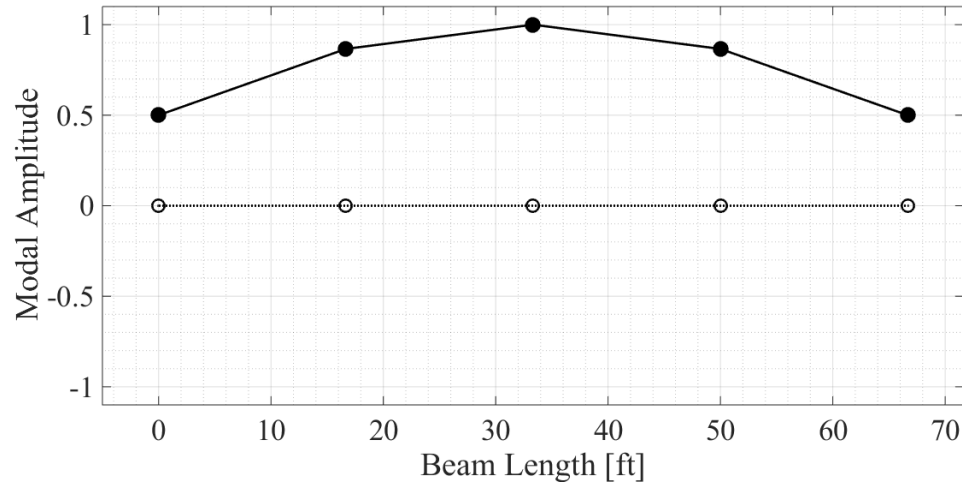


**Figure 3-4: Eigenvector – Mode 1**

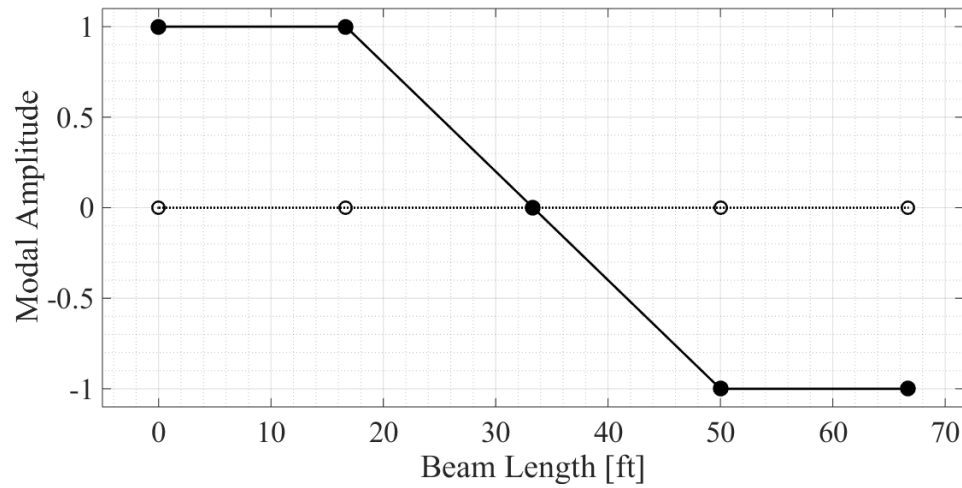


**Figure 3-5: Eigenvector – Mode 2**

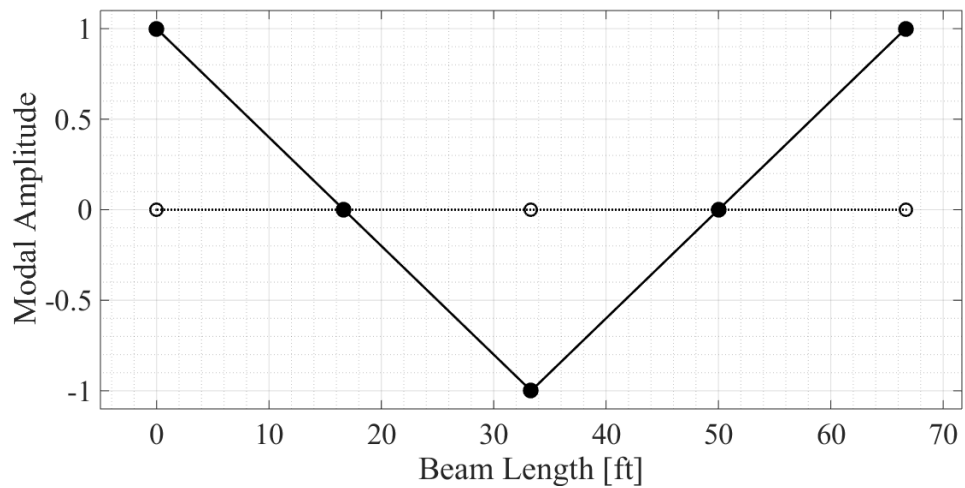


**Figure 3-6: Eigenvector – Mode 3**

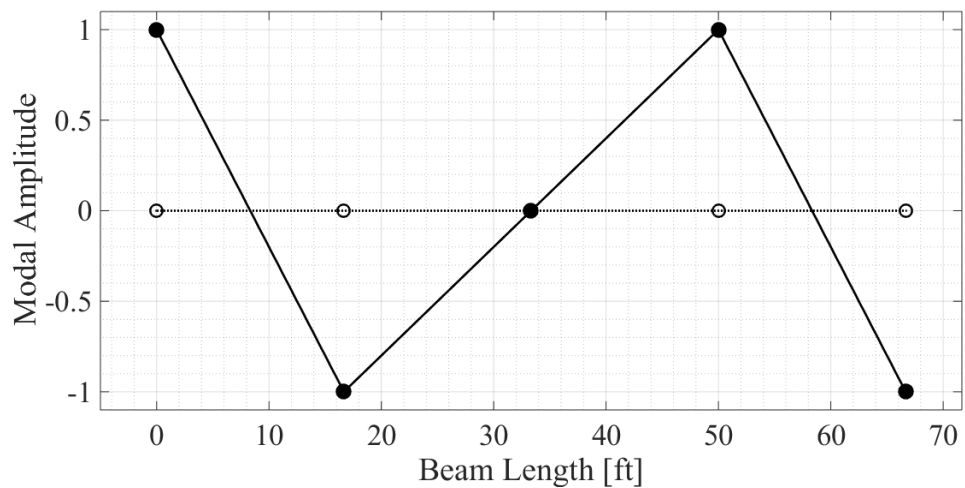


**Figure 3-7: Eigenvector – Mode 4**

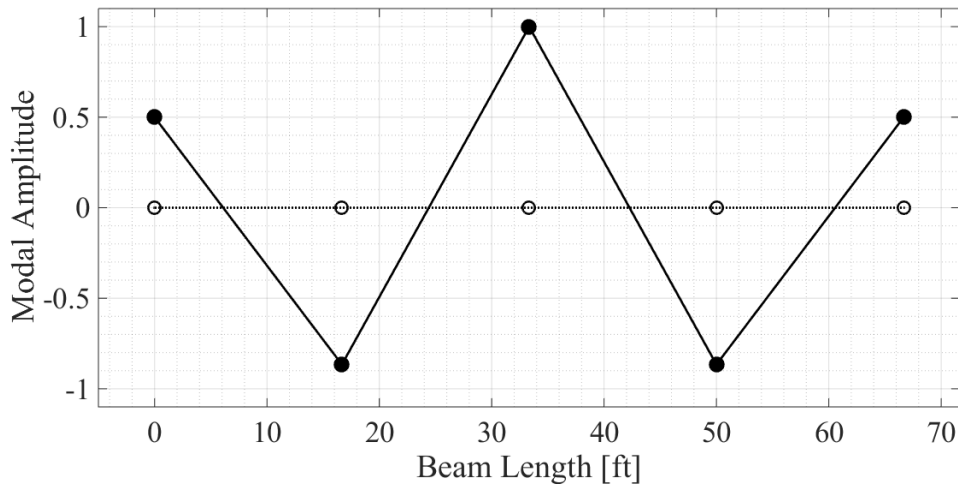


**Figure 3-8: Eigenvector – Mode 5**

### 3.2.3 Simulated FRF Measurements

Using Equation 3-6, the FRF can be formed from the modal parameters determined in the eigenanalysis. The full mass normalized mode shapes and unity modal scale factors were used to develop the residue matrix for each mode. A frequency vector was created over the bandwidth of -150 rad/sec to +150 rad/sec with 512 discrete samples to provide a frequency resolution of .5882 rad/sec. The FRF was evaluated at each of these discrete frequencies to simulate measurement of the temporal domain of the FRF (Figure 3-9). Note that the complex conjugate pairs for each mode are symmetric about the frequency origin due to proportional damping and real, normal modes.

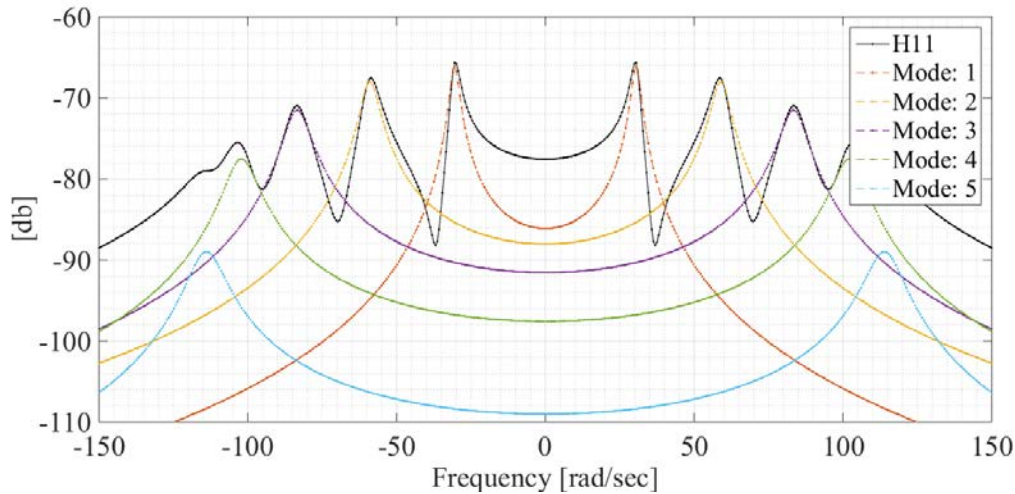


**Figure 3-9: 5DOF – Numerical Example – Mode Contributions**

### 3.2.3.1 Driving Point (SISO) Measurement

Locations containing both input/output measurements are referred to as driving points. The driving point FRF measurement for DOF 3, for example, is analytically equivalent to:

$$H_{33}(\omega) = \sum_{r=1}^5 \frac{Q_r \psi_{3r} \psi_{3r}}{j\omega - \lambda_r} + \frac{Q_r \psi_{3r}^* \psi_{3r}^*}{j\omega - \lambda_r^*} \quad 3-25$$

The positive frequency bandwidth of this measurement is shown in Figure 3-10 as the summation of each individual mode's contribution. The magnitude of the FRF is typically plotted on a log scale and accompanied by the phase diagram to interpret relative orientation of DOF actions. The phase angle for each mode and summed measurement is shown in Figure 3-11.

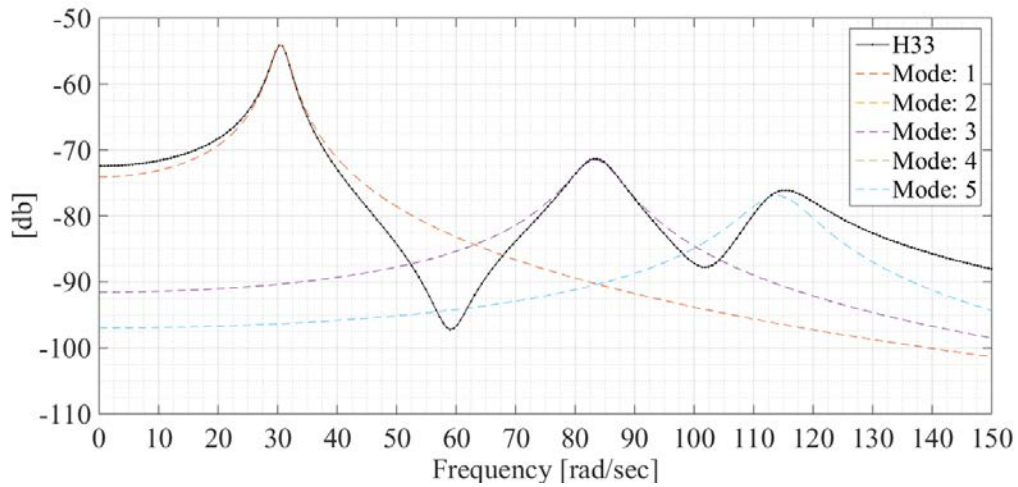


**Figure 3-10: FRF Magnitude – H33**

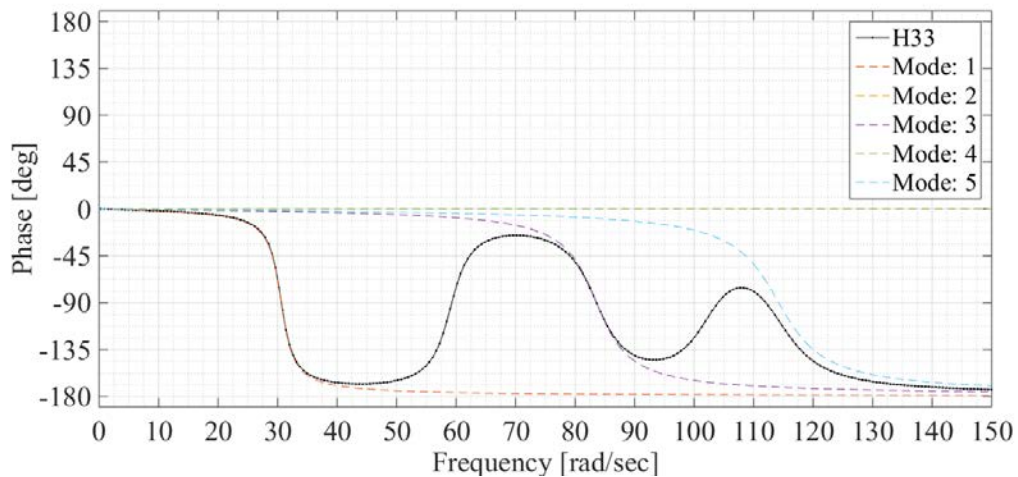


**Figure 3-11: Phase Angle – H33**

Additionally, the phase angle of the driving point DOF remains in the same negative region for all modes (i.e. each modal coefficient is in phase with each other). This is due to the squared modal coefficient in the numerator of the partial fraction expansion and also observed in the IRF

(Figure 3-12). Applying a unit impulse at DOF 3 causes large initial displacements due to the sum of each mode in phase.

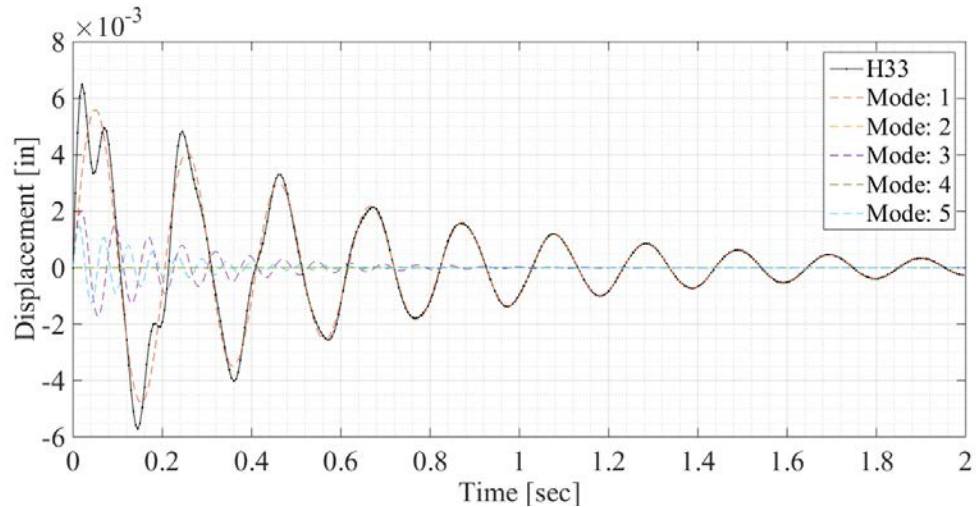


**Figure 3-12: IRF – H33**

### 3.2.3.2 SIMO & MISO Measurements

An input at DOF 1 and response measurement at all DOF represents a column measurement (SIMO). This is represented in analytical form in Equation 3-26 and graphically in Figure 3-13.

$$\begin{Bmatrix} H_{11} \\ H_{21} \\ H_{31} \\ H_{41} \\ H_{51} \end{Bmatrix}(\omega) = \sum_{r=1}^5 \frac{Q_r \psi_{1r} \begin{Bmatrix} \psi_1 \\ \psi_2 \\ \psi_3 \\ \psi_4 \\ \psi_5 \end{Bmatrix}_r}{j\omega - \lambda_r} + \frac{Q_r \psi_{1r}^* \begin{Bmatrix} \psi_1 \\ \psi_2 \\ \psi_3 \\ \psi_4 \\ \psi_5 \end{Bmatrix}_r^*}{j\omega - \lambda_r^*} \quad 3-26$$

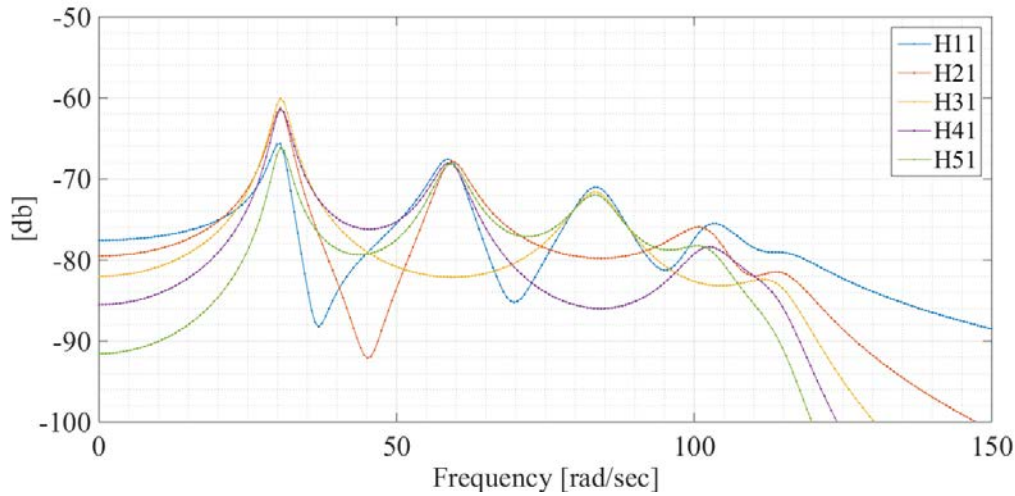


**Figure 3-13: SIMO - Column Measurement – Input at DOF 1**

The measurement of the first row of the FRF (MISO) is performed by input at all DOF and measurement of the output at DOF 1. Applying reciprocity assumptions, the measured rows and columns of the residue matrices are equal and therefore the amplitudes of the FRF are equal as well (Figure 3-14).

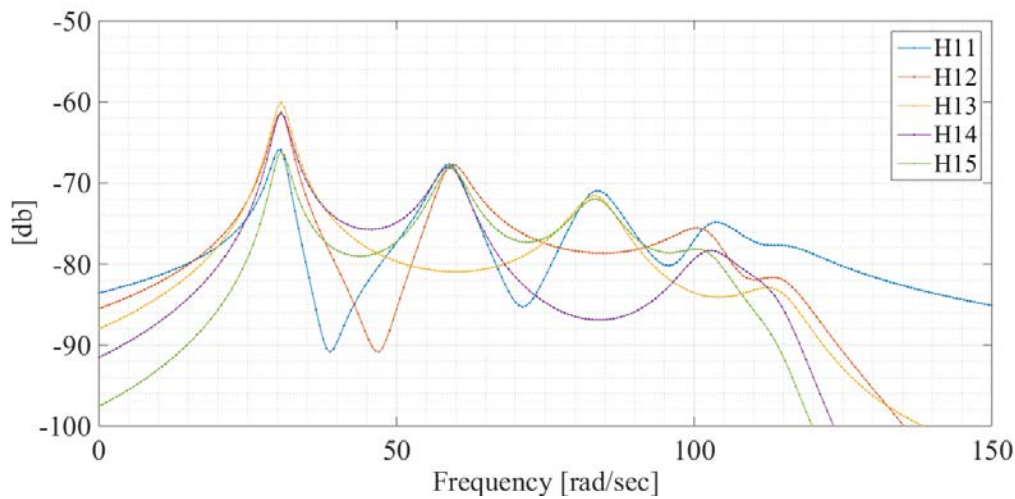


**Figure 3-14: MISO – Row Measurement – Output at DOF 1**

### 3.2.3.3 Spatial Considerations

For each mode, the FRF is a function of the modal scaling and the modal coefficients of the input and output DOF. Referring to the eigenvector plots shown above, the modal amplitude for the first mode at DOF 1 is smaller than the amplitude at DOF 3. This direct affect is observed when comparing the magnitudes of the FRF of each SISO driving point measurement (Figure 3-15).

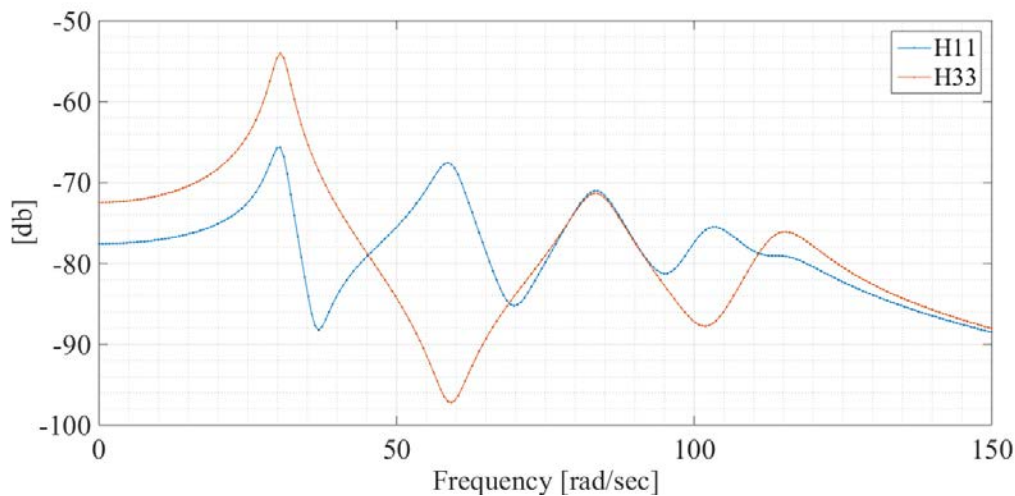


**Figure 3-15: Driving Point Comparison H11 vs H33**

Analytically, this is described by the squared modal coefficient at DOF 3 for the first mode being larger than that of DOF 1. In the context of an experiment, the modal scale factor represents the modal mass of the system and can be thought of physically as the amount of total mass participating in the first mode. Intuitively this is located at the center of the beam for first bending and excitation at this point will best drive the mass participating in the mode. The relative modal amplitudes of each DOF and the participating mass of each mode ultimately drive the total

system response. The implications of this concept dictate the design of the experiment as it is advantageous to seek out larger responses to overcome influences of noise in the measurements.

However, large response levels are not the only spatial consideration in experimental design. The modal amplitude of the second mode at DOF 3 is zero and is referred to as a nodal point. The excitation or response measurement at or near a nodal point of the structure is the equivalent of multiplying the amplitude of the desired signal by zero. In this numerical example, the second mode cannot be measured at this location. This is an important observation as, although larger response measurements are possible by targeting locations with high modal amplitudes for modes of interest, there is a compromise between efficiency (i.e. measuring the complete modal space with each input) and data quality (i.e. high signal to noise ratios).

### **3.2.4 Mode Interaction**

If the system exhibits real, normal modes that are far spaced, the magnitude and phase of the FRF at each system pole are approximately equal to the SDOF response. If the modes are not well spaced, the FRF measurements at areas of resonance will be a combination of contributions from adjacent modes. The FRF measurements at symmetric locations are compared below to present a simple means of tracking the physical interaction between two adjacent mode shapes throughout the frequency spectrum.

DOF pairs 1 and 5 and DOF pairs 2 and 4 are symmetric locations on the beam and therefore share the same modal amplitude for each mode, differentiated only by phase orientation. In each of these plots the unbiased contribution of each SDOF mode is shown in dashed lines and the summation of each is the respective measurement.

The driving point FRF and phase diagram for DOF 1, H11, are shown in Figure 3-16 and Figure 3-17, and the symmetric output measurements at DOF 5, H51, are shown in Figure 3-18 and

Figure 3-19. The driving point FRF and phase diagram for DOF 2, H22, are shown in Figure 3-20 and Figure 3-21, and the symmetric output measurements at DOF 4, H42, are shown in Figure 3-22 and Figure 3-23.

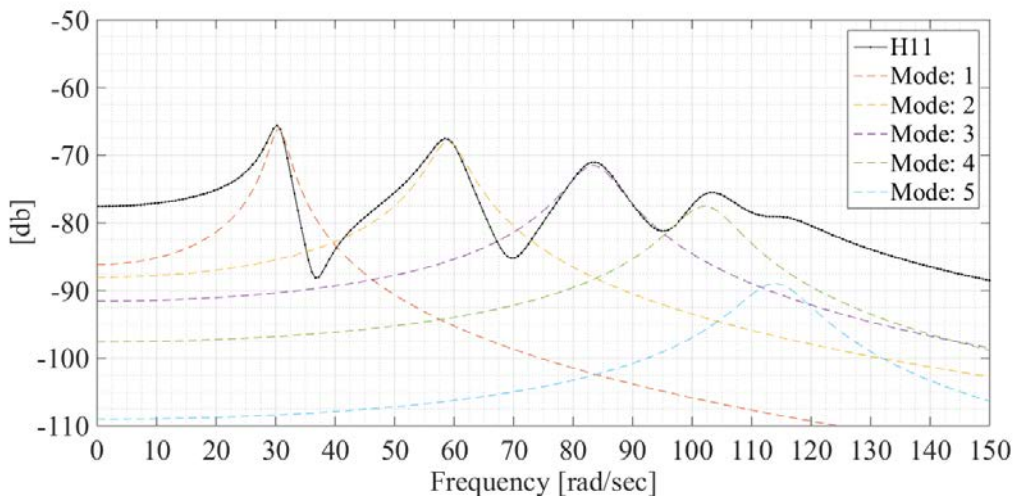


**Figure 3-16: FRF Magnitude – H11**

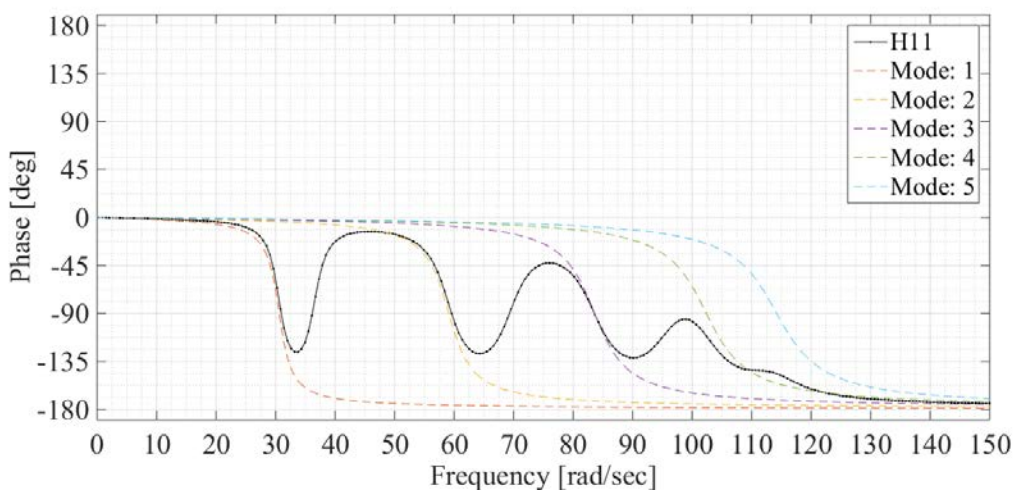


**Figure 3-17: Phase Angle – H11**

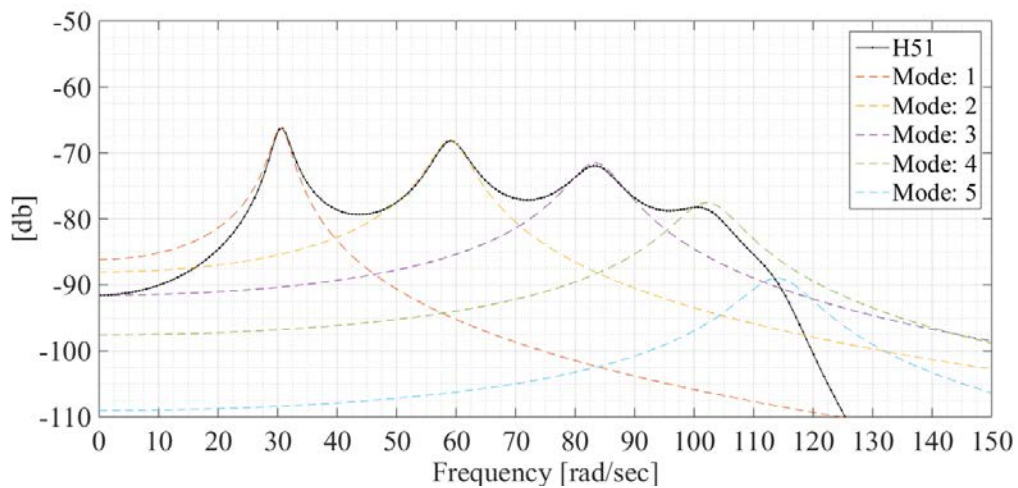


**Figure 3-18: FRF Magnitude – H51**

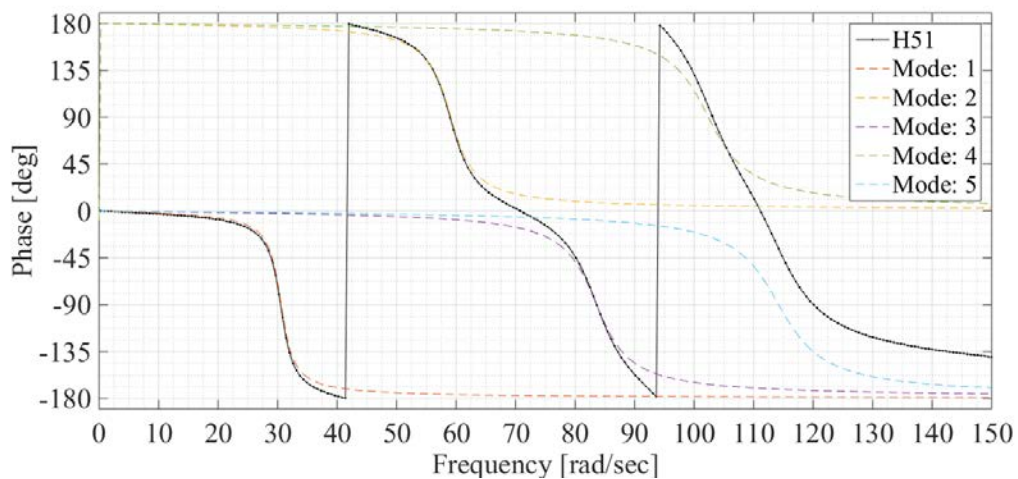


**Figure 3-19: Phase Angle – H51**

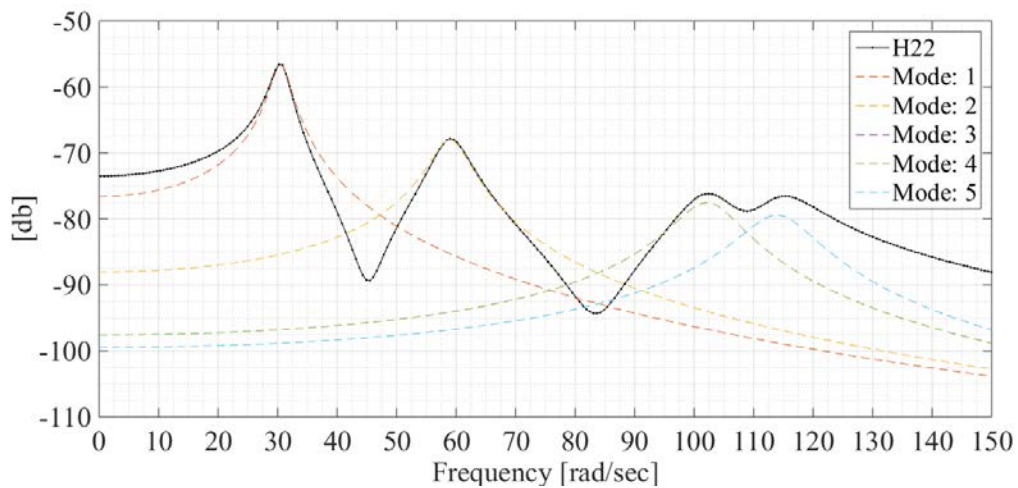


**Figure 3-20: FRF Magnitude – H22**

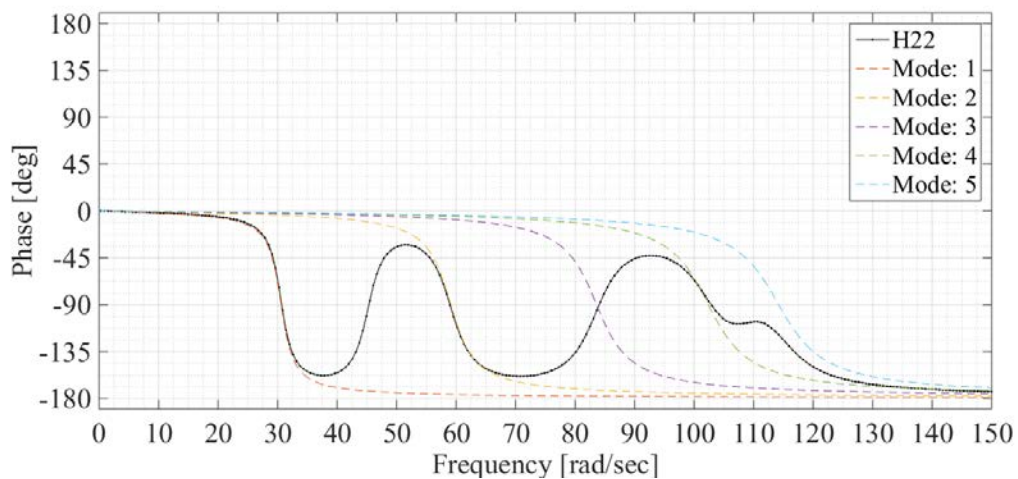


**Figure 3-21: Phase Angle – H22**

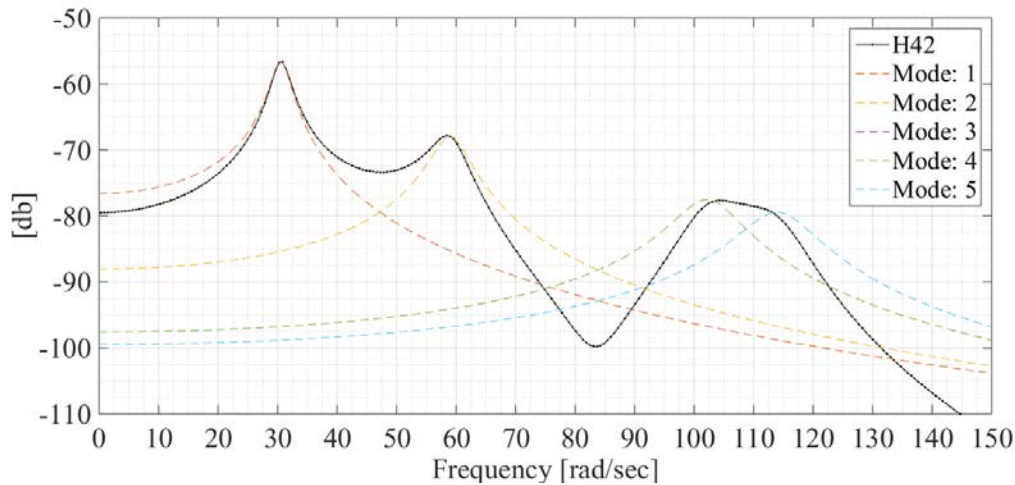


**Figure 3-22: FRF Magnitude – H42**

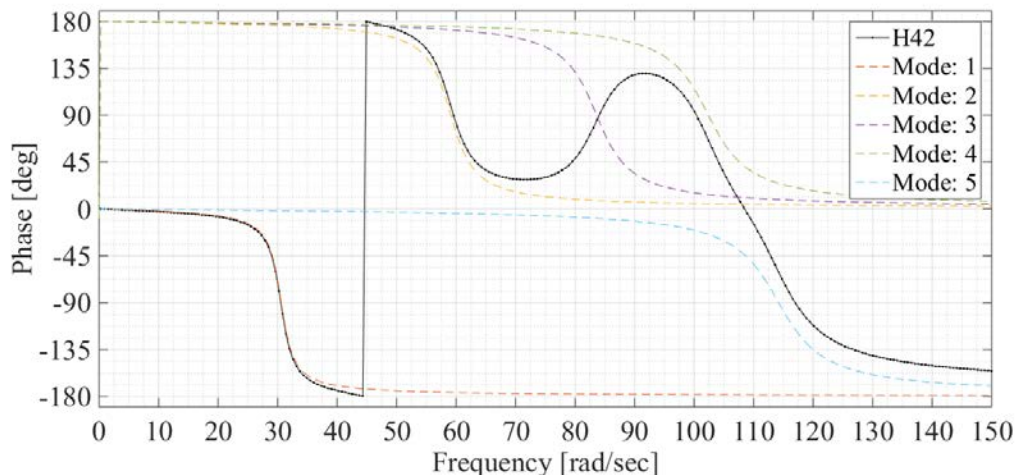


**Figure 3-23: Phase Angle – H42**

Comparing the amplitudes of the FRF measurements to the single DOF contribution shows that the first three modes are reasonably far spaced as the FRF magnitude has approximately the same amplitude and phase angle (i.e. each mode crosses 90 degrees at roughly the same frequency location as each SDOF mode contribution).

Modes four and five are coupled, however, and the effects of this are seen in the frequency band above 95 rad/sec. The driving point measurement H11, for example, shows significant increase in magnitude at the higher frequencies while the amplitude of the H51 measurement significantly decreases at this frequency range. The input at DOF 1 caused the in-phase excitation of all modes at this location, and, due to the modal coupling, the measured response above 95 rad/sec is the addition of the in-phase contributions of modes four and five. The modal coefficients for modes four and five of DOF 5 are out of phase with each other and their summation is a net negative which decreases the total response measurement at this DOF. The same trend of increased amplitude at the driving point and decreased amplitude at the symmetric DOF are observed for DOF pairs 2 and 4.

SDOF assumptions require, among other things, that the measured response within a certain frequency bandwidth be largely dominated by one mode. This is because the solution space for the estimation algorithms is limited by the smallest dimension of the experimental FRF. Therefore, SDOF assumptions are not valid in this frequency bandwidth. A single column (or row) measurement is insufficient to estimate two unique modal vectors as there are simply more unknowns than equations.

### **3.2.5 SDOF Shape Estimates**

To demonstrate the effect of modal coupling in the spatial domain, the first three columns of the FRF were used individually to solve for the SDOF residue of each mode. Each residue was then compared to the true eigenvector of the beam via the Modal Assurance Criterion (MAC). The MAC is a scalar constant that provides a measure of consistency between estimates of modal vectors and is defined as:

$$MAC_{cdr} = \frac{|\{\psi_{cr}\}^H \{\psi_{dr}\}|^2}{\{\psi_{cr}\}^H \{\psi_{cr}\} \{\psi_{dr}\}^H \{\psi_{dr}\}} \quad 3-27$$

The MAC values of the SDOF residue comparisons are shown in Table 3-2. As expected, the first three shapes show strong agreement with the eigenvectors for all unique column measurements. The superposition of the fourth and fifth modes significantly decreases the accuracy of the mode shape estimation from the column measurement due to an input at DOF 1. The resulting mode shape estimates from the first column of the FRF for the fourth and fifth modes are shown in Figure 3-24 and Figure 3-25. These shapes contain significant error when compared to the true eigenvector solution and are not fit for use in the modal model. In fact, referring to the FRF magnitude plot in Figure 3-16, the fourth mode in this measurement is contributing more to the response than the fifth shape is at the fifth system pole. As a result, the fifth shape estimated in Figure 3-25 is more consistent with mode four as it has a higher MAC value of .555.

**Table 3-2: MAC Comparison of SDOF Column Residue Estimation**

Mode	MAC Values		
	{A <sub>1</sub> }	{A <sub>2</sub> }	{A <sub>3</sub> }
1	0.9999	0.9999	0.9999
2	0.9984	0.9998	0
3	0.9978	0	0.9997
4	0.9534	0.9697	0
5	0.2687	0.8395	0.9894

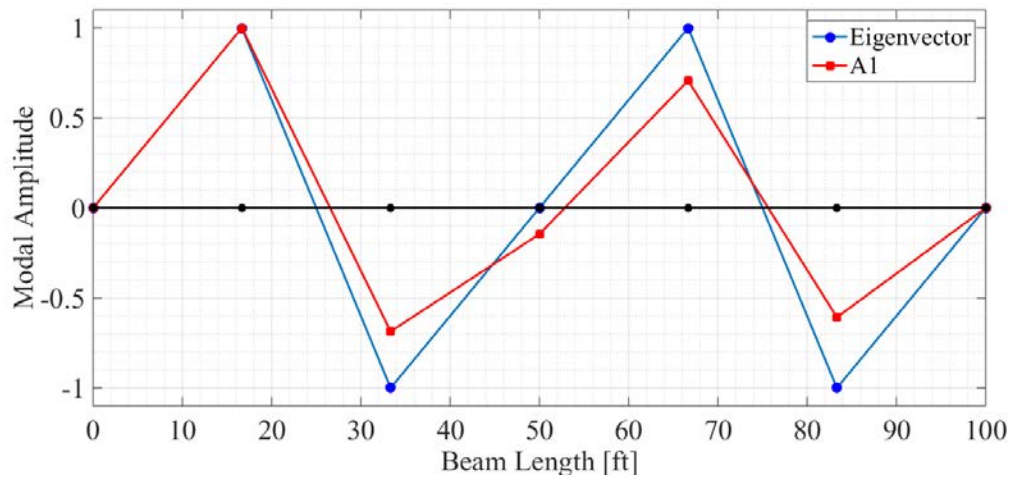


**Figure 3-24: SDOF Residue Estimation – Mode 4 – Input at DOF 1**

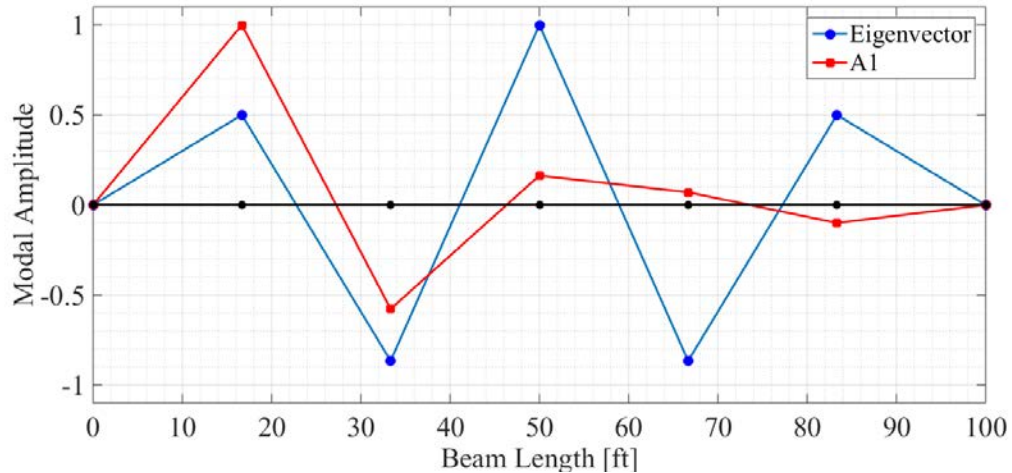


**Figure 3-25: SDOF Residue Estimation – Mode 5 – Input at DOF 1**

In comparison, the fourth mode shape has a nodal point at DOF 3, so using the third column of the FRF for SDOF mode shape estimation of mode 5 yields better results than the other input locations as indicated (Figure 3-26). This approximate mode shape, however, is still influenced by the third mode. From the H33 FRF magnitude and phase plots shown in Figure 3-10 and

Figure 3-11, the third mode slightly increases the amplitude of the residue for the third residue column of the FRF as the third and fifth modes have maximum amplitude at the center of the beam, the location of DOF 3. Even though they are separated by 30.5 rad/sec (5 Hz.), the amplitude of the center DOF for the SDOF estimation shown below is increased by the summation of the in-phase modes 3 and 5.

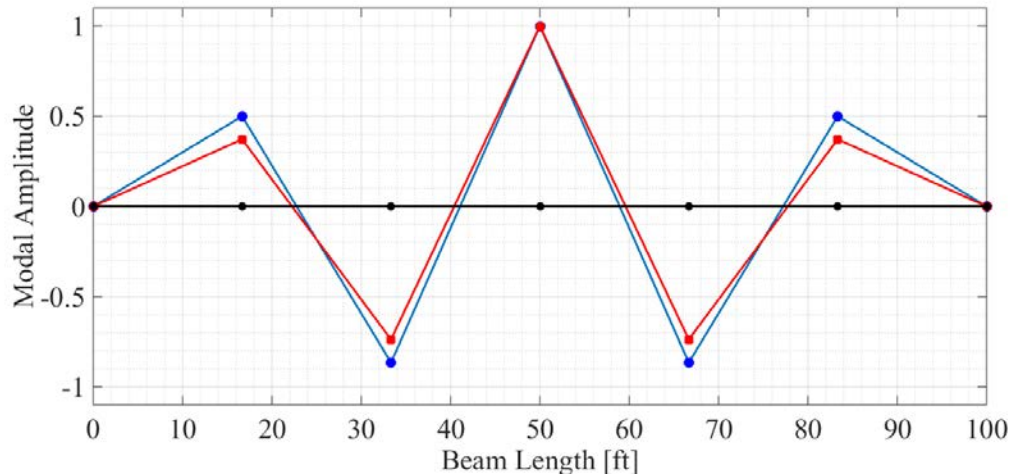


**Figure 3-26: SDOF Residue Estimation – Mode 5 – Input at DOF 3**

### 3.2.6 SDOF Pole Estimates

Spatial domain modal parameter estimation algorithms rely on the estimation of the system's mode shapes to estimate the SDOF contribution of that mode to the measured FRF. The mode shape solution then influences the system's damping and natural frequency estimations. Using each of the SDOF mode shapes presented above, the system poles were estimated using the eFRF method. The system poles are a function of the damping and natural frequencies of the system and each are compared to the true solution. The estimated percent damping values and the percent

error comparisons are shown in Table 3-3 and damped natural frequency values and percent error are shown in Table 3-4.

**Table 3-3: Residue Damping Estimation**

Mode	Eigen Solution	Damping			% Error		
		{A1}	{A2}	{A3}	{A1}	{A2}	{A3}
1	5.00	4.99	4.99	4.99	0.24	0.25	0.25
2	5.00	4.99	4.99	-7.29	0.30	0.29	245.78
3	5.00	4.98	-10.93	4.99	0.49	318.57	0.29
4	5.00	4.90	4.95	-3.07	2.29	1.07	161.32
5	5.00	2.75	4.82	4.96	44.95	3.65	0.75

**Table 3-4: Residue Damped Natural Frequencies Estimation**

Mode	Eigen Solution	Natural Frequency			% Error		
		{A1}	{A2}	{A3}	{A1}	{A2}	{A3}
1	30.56	30.56	30.56	30.56	0.00	0.00	0.00
2	59.04	59.04	59.05	46.66	0.00	0.00	20.98
3	83.50	83.50	84.52	83.50	0.00	-1.22	0.00
4	102.27	102.37	102.14	117.59	-0.10	0.12	-14.98
5	114.07	119.28	114.73	114.08	-4.57	-0.59	-0.02

The largest effect of modal coupling was observed at DOF 1 for modes four and five. Using mode shape estimates from this single residue column, the estimated natural frequencies contained only 0.1% error for the fourth mode and 5% error for the fifth mode. This indicates that any reasonable approximation of the mode shape can be used to estimate the damped natural frequency for that mode. The damping estimates were more sensitive to poor estimations of the mode shape and

showed more deviation from the true solution (2.29% error for the fourth mode and 45% error for the fifth mode).

### **3.2.7 Use of Multiple References**

The spatial sampling of the input space and its effect on the modal parameter solution is investigated in this section. For this deterministic numerical example, the full MIMO FRF provided an exact match to the Eigen solution.

Three of the beam's five modes are well spaced with two modes moderately coupled. Therefore, referencing two independent columns of the FRF allows for two unique modal solutions per frequency line and should yield better approximations of the true Eigen solution compared to the SDOF estimation techniques.

FRFs were formed from nine spatially unique pairs of input DOF. The MDOF modal parameter identification techniques discussed above were used to estimate the system's modal parameters using each set FRF measurement pairs. The discussion is limited to parameter estimation of modes four and five as these modes were most effected by the modal coupling.

Table 3-5 shows MAC value comparisons between the mode shape estimates and the eigenvector solution for each mode, and Table 3-6 shows ranking of the MAC values for each column reference pair from best to worst.

**Table 3-5: Comparison of Mode shape solution as a function of column reference**

## FRF Input DOF Measurement Pairs

<b>2</b>	0.9999	0.9984	0.9997	0.9999	0.9998	0.9999	0.9997	0.9998	0.9984
<b>3</b>	0.9978	0.9994	0.9978	0.9999	0.9997	0.0000	0.9978	0.9997	0.9994
<b>4</b>	0.9689	0.9516	0.9919	0.9987	0.9458	0.9987	0.9919	0.9458	0.9516
<b>5</b>	0.8131	0.9890	0.9734	0.9933	0.9871	0.9999	0.9734	0.9871	0.9890

**Table 3-6: Best to Worst Ranking of MAC Correlations****FRF Input DOF Measurement Pairs**

<b>Mode</b>	<b>1, 2</b>	<b>1, 3</b>	<b>1, 4</b>	<b>1, 5</b>	<b>2, 3</b>	<b>2, 4</b>	<b>2, 5</b>	<b>3, 4</b>	<b>3, 5</b>
1	8	2	6	9	4	1	7	5	3
2	3	8	6	1	4	2	7	5	9
3	6	4	7	1	2	9	8	3	5
4	5	6	3	1	8	2	4	9	7
5	9	3	7	2	5	1	8	6	4

In general, the mode shapes estimated from two columns of the FRF show a much higher correlation to the eigenvectors of the beam, and several spatial considerations are apparent from the comparisons. Using DOF pair one and two as references in the MIMO solution shows a MAC value of 0.8131 for mode five which is a significant increase compared to SDOF approximations. These two DOF are located in close proximity to each other, however, and as a result, the estimated mode shape is still negatively affected by the coupled modes (Figure 3-27). The sampling of the input space was skewed towards DOF one and two which amplified the phase interaction of modes four and five at these DOF. In this case, the skewed spatial sampling did not provide enough information to fully decouple the two modes.

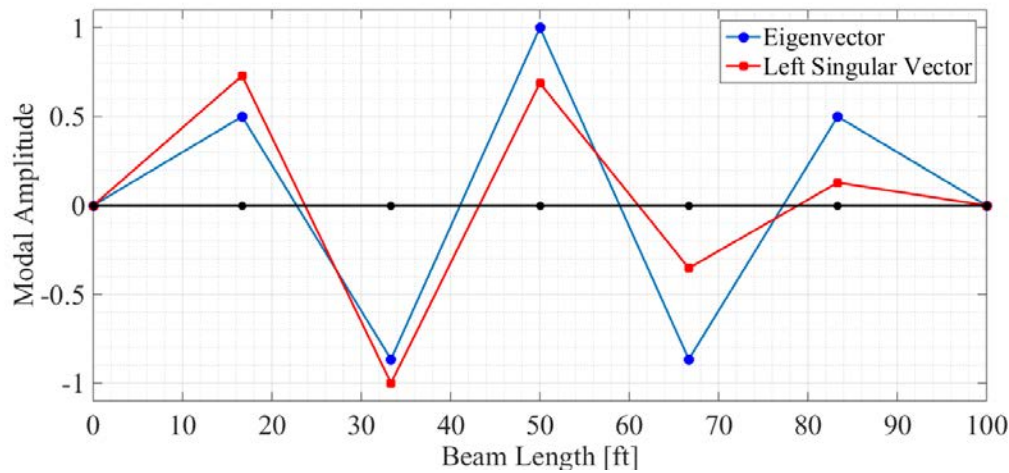


**Figure 3-27: Mode 5 – Eigenvector vs Mode Shape from References 1 & 2**

Using pairs of inputs that have a DOF located at a nodal point of one of the two coupled modes increases the accuracy of the adjacent shape but decreases the accuracy of the mode that contained the nodal point. This behavior is observed in DOF pairs containing the third DOF as it is a nodal point for mode four, and the accuracy of the fifth shape estimations increase while the accuracy of the fourth shape estimations suffer. Targeting nodal points in this way can be beneficial when attempting to decouple closely spaced modes, but can compromise the integrity of other modal solutions.

The best estimations of the fourth and fifth mode shapes were obtained from DOF pairs one & five and two & four as they are the most spatially diverse set of input DOF pairs. The symmetric locations provided a measurement set that sampled both the in-phase and the out-of-phase behavior of each mode. This allowed for the best identification of each mode's contribution and exemplifies the importance of adequately sampling (and understanding the influence of) all three dimensions of the characteristic space of the system.

Table 3-7 shows percent error comparisons between damping estimations obtained from using the MIMO mode shapes and the true solution, and Table 3-8 shows percent error comparisons between the natural frequency estimations obtained from using MIMO mode shapes and the true Eigen solution. The inclusion of a second column reference for shape estimation significantly reduced all previous errors in damping and pole estimation with maximum errors at non nodal points of 5% and 0.8% for damping and natural frequency estimation respectively. This further indicates that the addition of multiple column references greatly increases the accuracy of the identified pole.

**Table 3-7: Damping Estimations – Percent Error**

Mode	Damping - % Error - Values for Column Reference Pairs								
	1, 2	1, 3	1, 4	1, 5	2, 3	2, 4	2, 5	3, 4	3, 5
1	0.25	0.25	0.25	0.25	0.25	0.25	0.25	0.25	0.25
2	0.27	0.30	0.26	0.25	0.29	0.25	0.26	0.29	0.30
3	0.49	0.31	0.49	0.26	0.29	323.47	0.49	0.29	0.31
4	0.92	2.35	0.66	0.34	1.56	0.34	0.66	1.56	2.35
5	4.84	0.58	0.93	-0.51	0.67	0.24	0.93	0.67	0.58

**Table 3-8: Natural Frequency – Percent Error by Input Pairs**

Mode	Natural Frequency - % Error - Values for Column Reference Pairs								
	1, 2	1, 3	1, 4	1, 5	2, 3	2, 4	2, 5	3, 4	3, 5
1	0.00	0.00	0.00	0.00	0.00	0.00	0.00	0.00	0.00
2	0.00	0.00	0.00	0.00	0.00	0.00	0.00	0.00	0.00
3	0.00	0.00	0.00	0.00	0.00	-1.25	0.00	0.00	0.00
4	0.10	-0.11	-0.02	0.00	0.20	0.00	-0.02	0.20	-0.11
5	-0.80	-0.05	-0.08	0.03	-0.07	0.00	-0.08	-0.07	-0.05

### 3.3 Conclusions

As a result of the discussion above, the following conclusions can be drawn regarding the design requirements of the THMPER system test methodology:

- Complete sampling of the structure's characteristic space is required for accurate estimation of modal parameters. Modal parameter identification algorithms cannot account for ineffective or incomplete FRF measurements.
- SDOF assumptions provided inaccurate estimation of the systems modal parameters when the system experienced even light modal coupling from closely spaced or repeated modes.
- The errors within the SDOF mode shape estimates due to the closely spaced modes did not significantly affect estimation pole estimation:
  - ~5% error when using SDOF residues as the modal filter in the eFRF formulation. However, this will not always be the case because as the shapes get closer in the frequency domain, the shape estimations become more super imposed and begin to lose the unique properties of the actual shape that the modal filter relies to decouple the FRF. The filter is then unable to separate the unique contributions of each mode which ultimately results in poor pole estimations.
- Referencing multiple, spatially diverse columns of the experimental FRF permitted MDOF parameter estimation which was more reliable than SDOF approaches. MDOF parameter estimation is a requirement for a robust modal processing framework.

## **CHAPTER 4: TEST METHODOLOGY**

This chapter describes the development of the THMPER system's experimental approach. Typical test scenarios and constraints encountered in EMA applications on civil structures are discussed and, together with theoretical and practical considerations, a general experimental strategy is developed and illustrated through numerical examples. Since the design of the experiment directly affects the scope, strategy, and ultimately the accuracy of the post-processing approach, modal parameter estimation considerations and general processing strategies are discussed as well.

### **4.1 Background**

MRIT on short to medium span highway bridges leverage input/output measurements from a roving excitation source and an array of accelerometers to determine the structure's discrete FRF. Multiple columns of the FRF matrix are measured by impacting in spatially varied locations so that MDOF modal parameter identification techniques may be leveraged for accurate estimations of the modal model. Impact tests are particularly suited for rapid testing due to the relatively short time periods necessary to characterize the structural system - using an impulsive force to excite a structure causes a brief vibration free-decay (on the order of 5-10 seconds for typical highway bridges).

Most dynamic approaches used on short to medium span highway bridges incorporate a fixed array of sensors that are installed on the bridge deck in traffic lanes. A single, dense grid of accelerometers that covers the entirety of the deck has been shown to be an effective means of sampling the structure's characteristic space (Raghavendrachar and Aktan, 1992 & Catbas et al. 2006). All of the desired outputs are measured at once, and set-up and break-down time is minimized. Multiple, staged sensor arrays contained within individual traffic lanes have also been

shown effective on civil infrastructure (Lenett et al. 2000, & Wang et al. 2005). However, in both cases, a full or partial set of fixed sensors is installed prior to testing and remains in place throughout the duration of the test. This causes significant interruptions to traffic and increases the scope and duration of traffic control. It is this requirement for bridge closures or partial closures that the THMPER system aims to remove.

## 4.2 General Approach

The total cost of an experimental effort is largely influenced by the extent and duration of the bridge closure. Closing a traffic lane requires crash truck protection, hired personnel to lay down approach cones (often placed for miles) and supervision throughout the duration of the test. The general approach aims to alleviate the need for extensive traffic control and lane closures by reducing the footprint of the fixed sensors. This is achieved by integrating measurements from a reduced set of fixed DOF with temporary DOF from a roving input/output source. The set of fixed DOF are located out of the way of traffic and the roving excitation provides a safe option for performing modal measurements in the presence of traffic.

The general test configuration for the THMPER system is shown in Figure 4-1. Partial traffic control is used to install stationary sensor grids along the exterior sides of the bridge. The footprint of the fixed sensors must be small and out of the way of traffic so the traffic lanes may remain open during installation and while taking measurements. Measurements in the roadway are acquired during brief traffic slow-downs or temporary single lane closures. If the bridge has sidewalks, traffic control is not needed until measurements are ready to be taken within the traffic lanes. If the bridge does not have sidewalks, some form of traffic control (e.g. cones) on the shoulders is needed to install the reference accelerometers. Typically crash trucks are provided at each shoulder lane to protect personnel during installation, and several cones are left in front of

the glued sensors during the rest of the test. The final arrangement is ultimately dictated by the state DOT, so it is important that the measurement approach remain flexible.

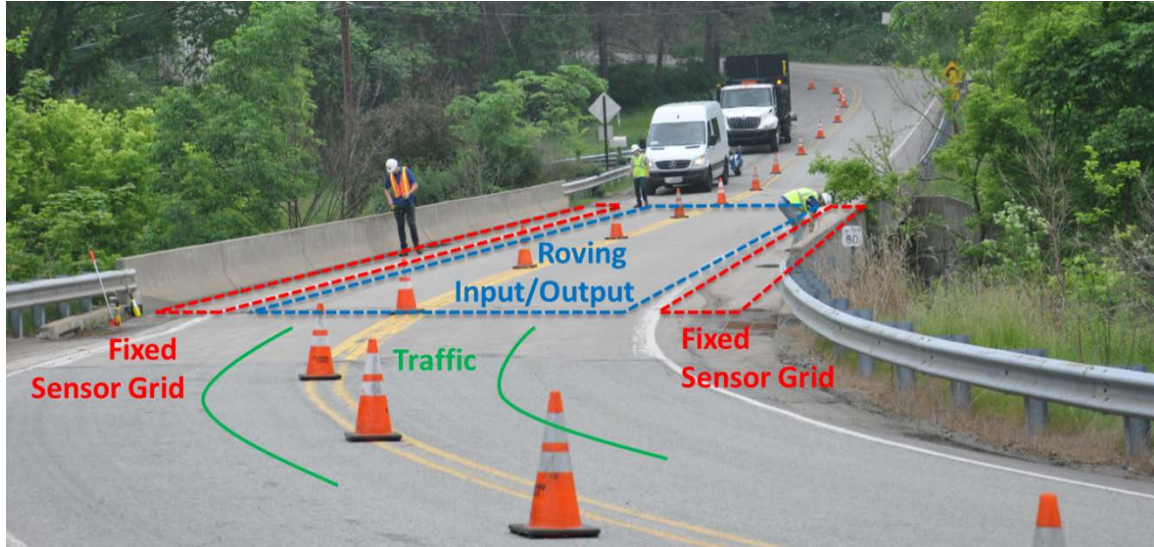


**Figure 4-1: THMPER System – Typical Test Configuration**

### 4.3 FRF Measurements

The experimental approach utilizes a mobile driving point (input/output source) equipped with a local array of accelerometers and a reduced set of stationary sensors to sample the structure's characteristic space and progressively build a complete modal model. Two longitudinal lines of stationary sensors are installed at the start of the test along any available shoulder or sidewalk lanes. These DOF are referred to as stationary references and ideally remain installed throughout the duration of the test. A mobile impact source is used to perform SIMO impact tests and is roved to multiple locations within the traffic lanes until the spatial sampling of the interior lanes is deemed sufficient. The stationary sensors are used as a modal scaling and phase reference and allow each independent local SIMO measurement to be sequentially integrated into a full

multiple-input-multiple-output (MIMO) data set. The result is a mobile, adaptable testing system that can quickly and efficiently obtain reliable FRF measurements of the structure.

This approach allows for two distinct types of FRF measurements. Roving measurements are conducted within traffic lanes (i.e. outside of traffic control). These DOF are required by the concept of operations to be temporary as measurements within the traffic lanes must be able to be removed throughout the duration of the test so that traffic congestion may be alleviated. Roving measurements are performed by driving the local excitation/response system along the traffic lanes of the bridge deck and conducting SIMO impact tests. Responses are measured *synchronously* (to preserve relative phase information) at the stationary references and at each input location.

The second measurement type is contained entirely within the fixed sensor grid. Excitation at these DOF can be performed with the roving excitation source if the references are installed in a shoulder lane or with a hand held instrumented sledge or other impact device if the references are installed on a sidewalk. Ideally the stationary references are represented in both the input and output measurement space but it is not a requirement.

Using the 5DOF shear beam from the previous chapter, Figure 4-2 may represent the cross section of the highway bridge. DOF 1 and 5 represent the stationary references installed along the exterior girders and DOF 2, 3, and 4 represent possible driving point locations of the interior girders.

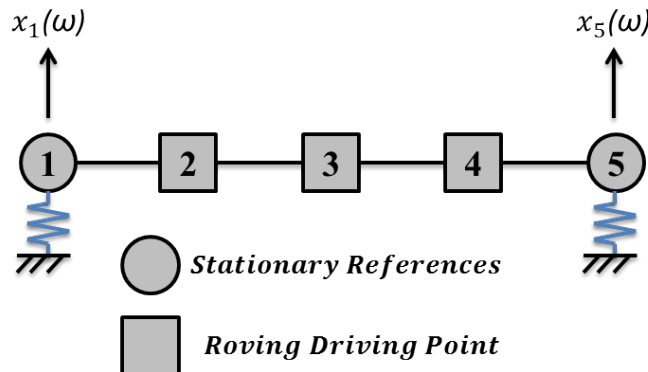


**Figure 4-2: THMPER Measurement Example**

### 4.3.1 Roving Measurements

An example of a roving measurement at DOF 2 is shown in Figure 4-3.

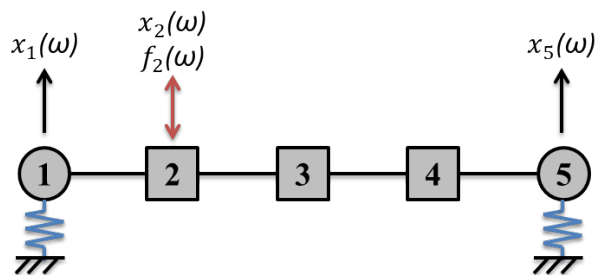


**Figure 4-3: 5DOF Beam – Roving Measurement**

Because the local input/output measurements are roving DOF and only measured temporarily, the reciprocal terms in the FRF are not directly measured and thus not present in the experimental FRF. The following sparse FRF of the system is formed:

$$[H(\omega)]_{N \times N} = \begin{bmatrix} - & H_{12} & H_{13} & H_{14} & - \\ - & H_{22} & - & - & - \\ - & - & H_{33} & - & - \\ - & - & - & H_{44} & - \\ - & H_{52} & H_{52} & H_{52} & - \end{bmatrix} \quad \text{4-1}$$

To leverage the SVD for modal parameter estimation, the sparse FRF must be reduced to:

$$[H(\omega)]_{No \times Ni} = \begin{bmatrix} H_{12} & H_{13} & H_{14} \\ H_{52} & H_{53} & H_{54} \end{bmatrix} \quad \text{4-2}$$

Performing the SVD at each frequency line yields:

$$[H(\omega)] = [U]_{2 \times 2} \left[ \frac{1}{j\omega - \lambda_r} \right]_{2 \times 2} [V]^T_{3 \times 2} \quad \text{4-3}$$

The left singular vector is then comprised of the unscaled modal vectors of the output DOF and the right singular vector is comprised of the unscaled modal vectors of the input DOF:

$$[U]_{No \times N} = \begin{bmatrix} \psi_1 \\ \psi_5 \end{bmatrix}_2 \quad \text{4-4}$$

$$[V]_{Ni \times N} = Q_r \begin{bmatrix} \psi_2 \\ \psi_3 \\ \psi_4 \end{bmatrix}_5 \quad 4-5$$

Provided the modes are far spaced in the frequency domain and each pole is dominated by only one mode, the roving measurements may not require a MDOF solution to provide accurate estimations of the system's mode shapes. If this is the case then the residue columns of the roving measurements can be estimated as SDOF SIMO tests and integrated via a least squares scalar of the driving point DOF in real time. This provides a lower bound in terms of modal parameter robustness and accuracy, however, may still prove useful for increasing the spatial resolution of the estimated mode shapes when the structure exhibits far spaced modes.

$$\{\psi\} = \left\{ \begin{array}{c} \psi_1 \\ \psi_2 \\ \alpha_1 \psi_3 \\ \alpha_2 \psi_4 \\ \psi_5 \end{array} \right\}_r \quad 4-6$$

### 4.3.2 Global Measurements

An example of a global only measurement is shown in Figure 4-4 where DOF1 is excited and the output is measured at DOF1 and DOF5:

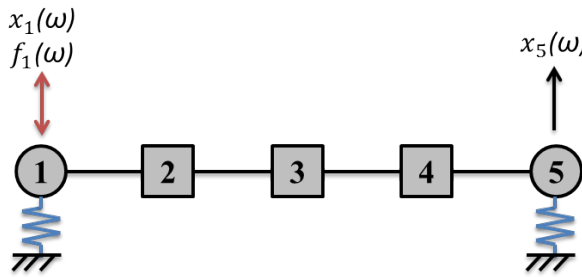


**Figure 4-4: 5DOF Beam – Global Measurement Example**

The full set of the global FRF measurements is:

$$[H(\omega)]_{N \times N} = \begin{bmatrix} H_{11} & - & - & - & H_{15} \\ - & - & - & - & - \\ - & - & - & - & - \\ - & - & - & - & - \\ H_{51} & - & - & - & H_{55} \end{bmatrix} \quad \text{4-7}$$

To leverage the SVD for MDOF modal parameter estimation, the sparse FRF must be reduced to:

$$[H(\omega)]_{No \times Ni} = \begin{bmatrix} H_{11} & H_{15} \\ H_{51} & H_{55} \end{bmatrix} \quad \text{4-8}$$

The left singular vector is then comprised of the unscaled modal vectors of the output DOF:

$$[U]_{No \times N} = \begin{bmatrix} \psi_1 \\ \psi_5 \end{bmatrix}_N \quad 4-9$$

And the right singular vector is comprised of the unscaled modal vectors of the input DOF:

$$[V]_{Ni \times N} = Q_r \begin{bmatrix} \psi_1 \\ \psi_5 \end{bmatrix}_N \quad 4-10$$

### 4.3.1 Combination of Measurements

Combining the full set of possible measurements forms the following FRF matrix:

$$[H(\omega)]_{N \times N} = \begin{bmatrix} H_{11} & H_{12} & H_{13} & H_{14} & H_{15} \\ - & H_{22} & - & - & - \\ - & - & H_{33} & - & - \\ - & - & - & H_{44} & - \\ H_{52} & H_{52} & H_{52} & H_{52} & H_{55} \end{bmatrix} \quad 4-11$$

Note that by sampling the entirety of the input and output space of the stationary references, a direct solution for the global modal vector is available in the MDOF estimation. However, this represents an upper bound in terms of possible spatial sampling and may not always be realistic in application.

#### 4.4 Parameter Identification Considerations

Each set of measurements are not particularly useful on their own, but the combination of the two can be used to form a cumulative FRF that may be estimated by MDOF parameter identification approaches. The measurements inside of the traffic lanes are temporary DOF that are not shared between test locations. The reciprocal terms of the FRF for these DOF are therefore not directly measured and only a sparse representation of the FRF can be formed. Roving measurements have the advantage of spatial resolution of the interior girders but the MDOF modal parameter estimation is constrained to estimation of either the input or output domain of the structure's characteristic space. Global measurements have the advantage of being relatively easy to access but inherently lack the spatial resolution to define the structure's shapes at resonance. However, the spatial sampling of the stationary references can be measured in full with relative ease. And, because they are consistently represented in both measurement sets, can be used to integrate the roving measurements into a more complete modal model.

Figure 4-5 shows the CMIF using only global measurements, Figure 4-6 shows the CMIF using roving only measurements, and Figure 4-7 shows the CMIF using the combination of both measurement sets. For each of these analyses the smallest dimension of the FRF is two and therefore only two modes may be estimated at one time. The combined measurement set then represents the set of MDOF column pair solutions reported in the previous chapter and conceptually represents an upper bound for the method. Note that the drastic under sampling of the spatial domain of the global measurements set causes the fifth mode to change rank. Had SDOF parameter estimation been the only type performed, this mode would likely be missed if global measurements were the only measurement set available.

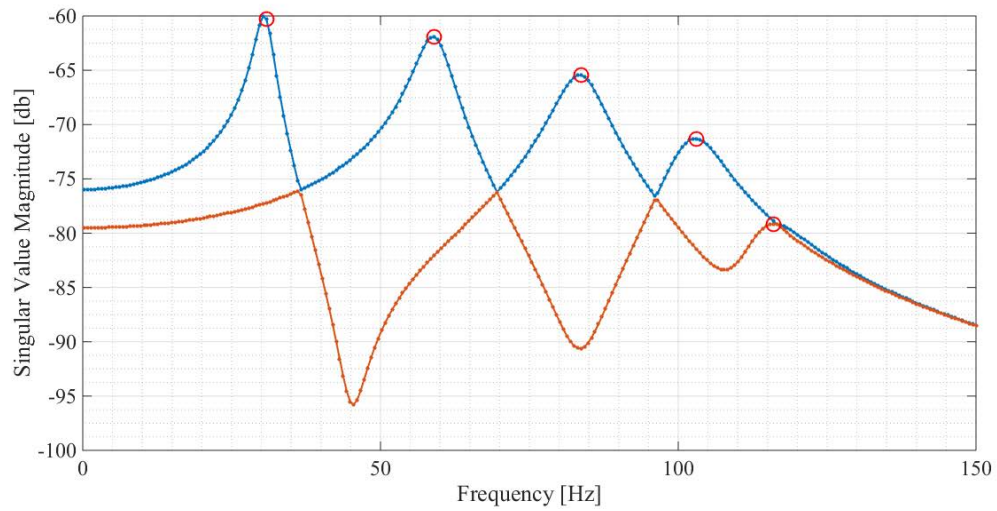


**Figure 4-5: 5DOF Beam - Global DOF – CMIF**

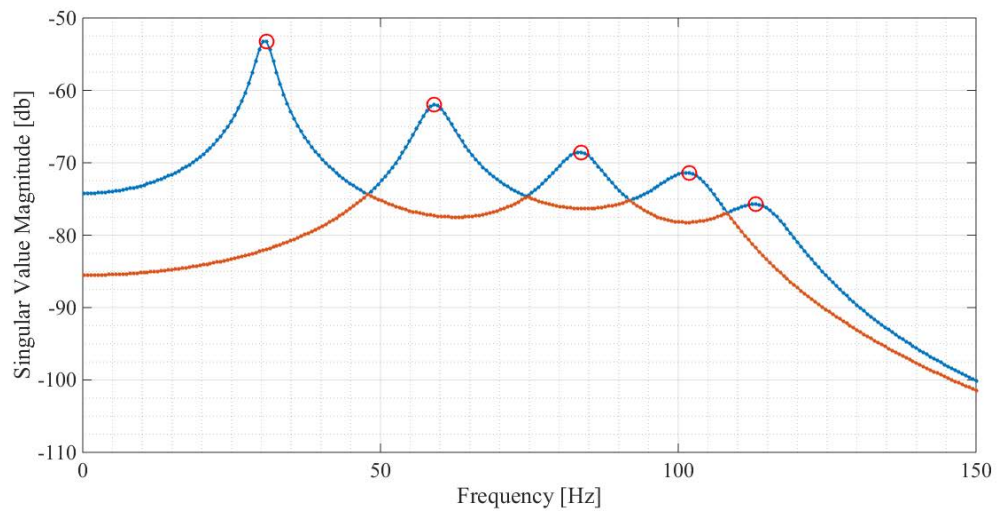


**Figure 4-6: 5DOF Beam – Roving DOF – CMIF**

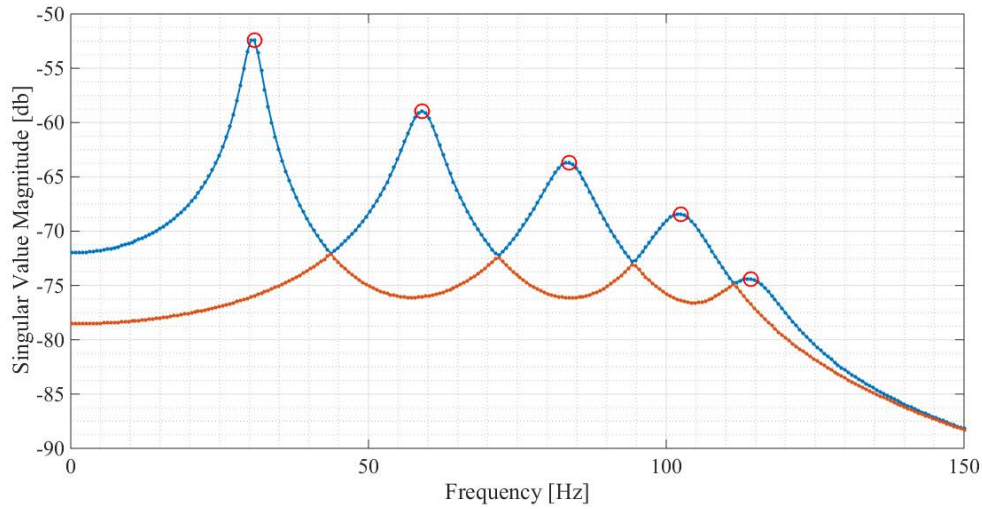


**Figure 4-7: 5DOF Beam – Combined DOF - CMIF**

#### 4.4.1 Shape Estimation

Figure 4-8 through Figure 4-10 and Figure 4-11 Figure 4-13 show the benefits of increasing spatial resolution for modes one and two respectively. The shape approximations from the global measurement set is essentially useless as only the qualitative shape can effectively be used by making drastic assumptions regarding modal order. The MDOF shape solution of the roving only measurements provide a robust modal solution but still suffer from a lack of resolution. For this case, the combination of measurements represents a near exact solution.

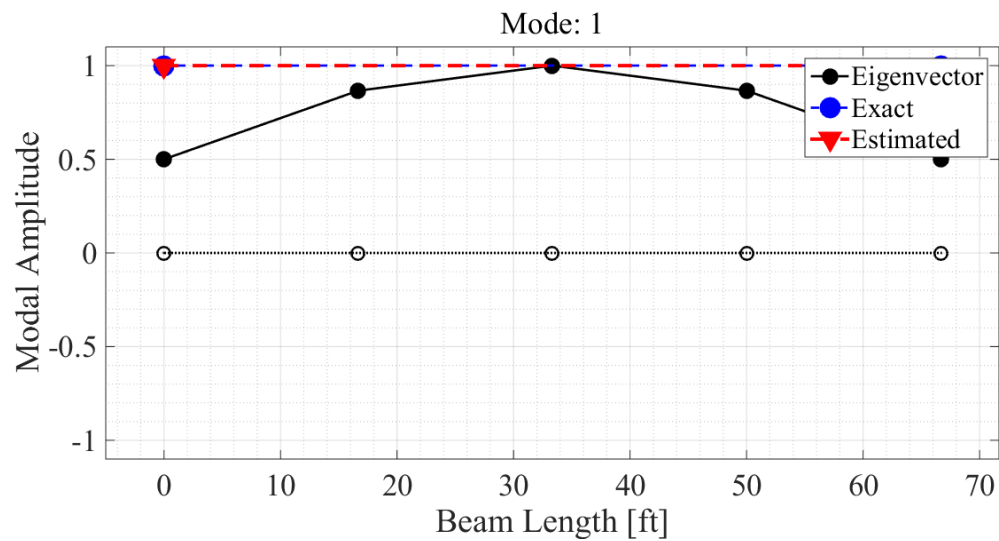


Figure 4-8: 5DOF Beam – Global DOF – Mode 1 - Shape

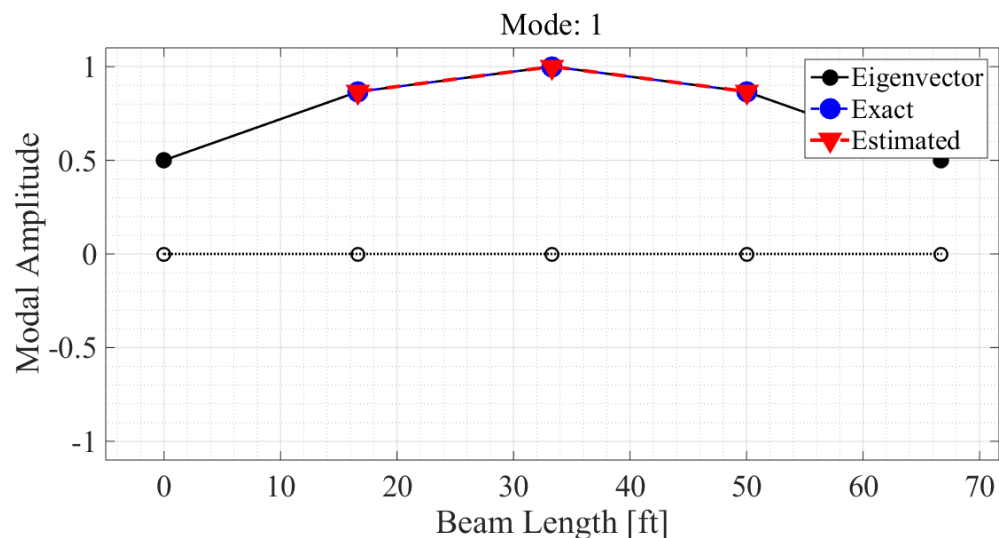
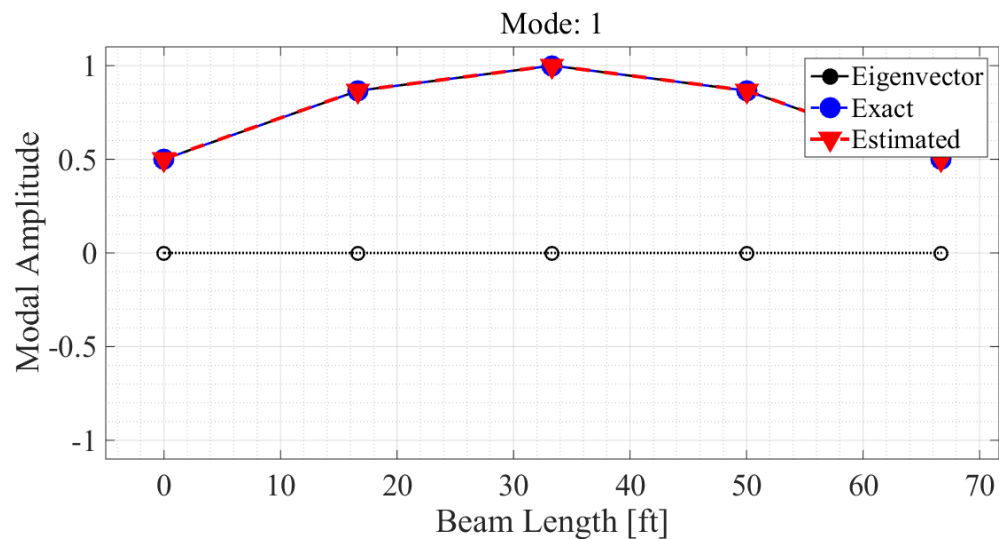
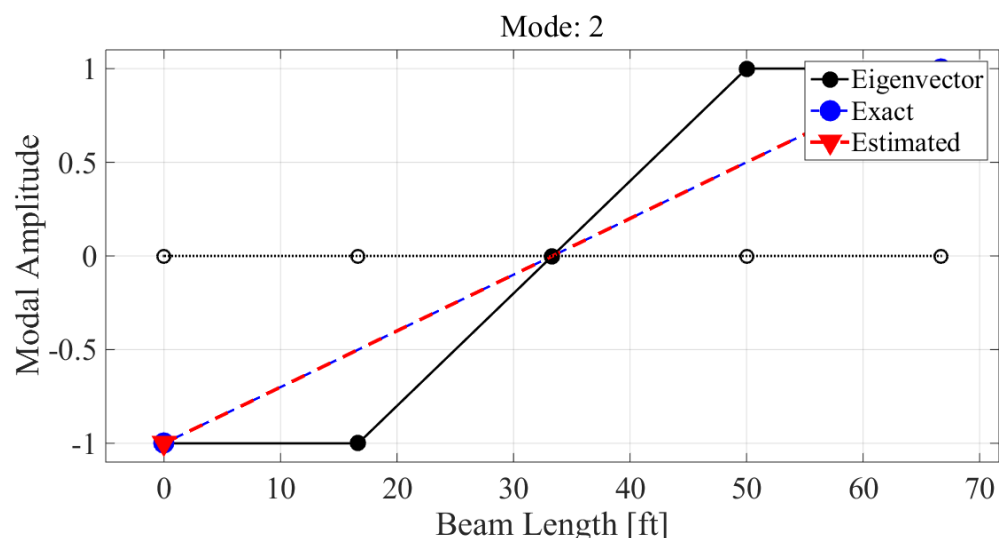


Figure 4-9: 5DOF Beam – Roving DOF – Mode 1 - Shape



**Figure 4-10: 5DOF Beam – Combined DOF – Mode 1 - Shape**



**Figure 4-11: 5DOF Beam – Global DOF – Mode 2 - Shape**

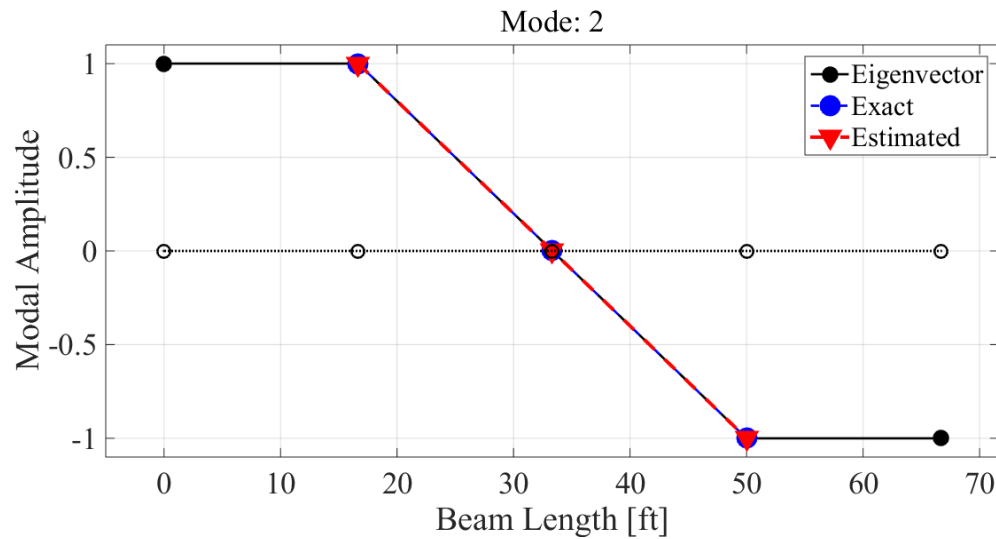


**Figure 4-12: 5DOF Beam – Roving DOF – Mode 2 – Shape**

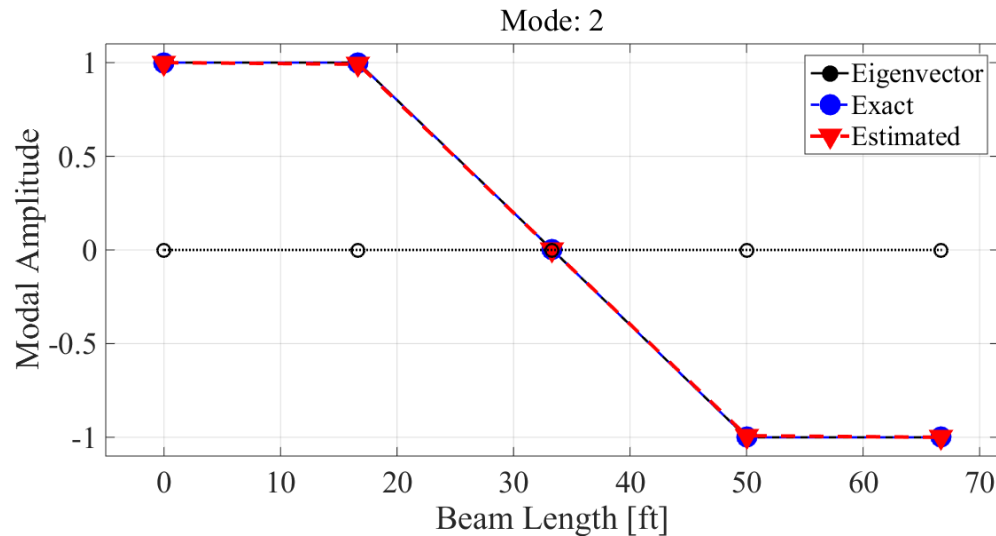


**Figure 4-13: 5DOF Beam – Combined DOF – Mode 2 - Shape**

#### 4.4.2 Pole Estimation

As additional DOF are added to the modal vector, the modal filter becomes more unique and thus more effective at decoupling the MDOF FRF. This is observed in Figure 4-14 through Figure

4-16 which show the corresponding eFRF and resulting curve fits of mode one for each measurement type. Although the global measurements are severely spatially aliased, the pole location is not significantly affected. The spatial aliasing does, however, affect the width and general shape of the peak.

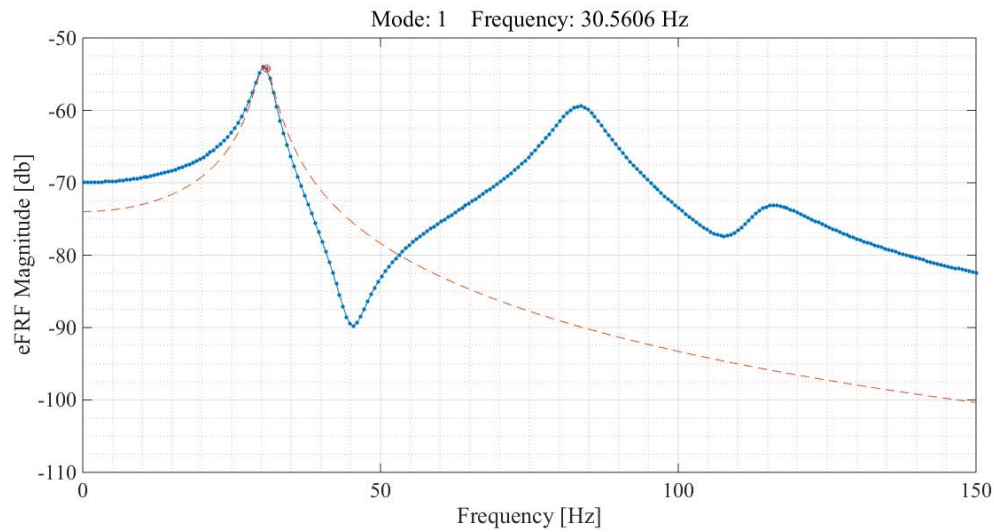


**Figure 4-14: 5DOF Beam – Global DOF – Mode 1 – Pole Fit**

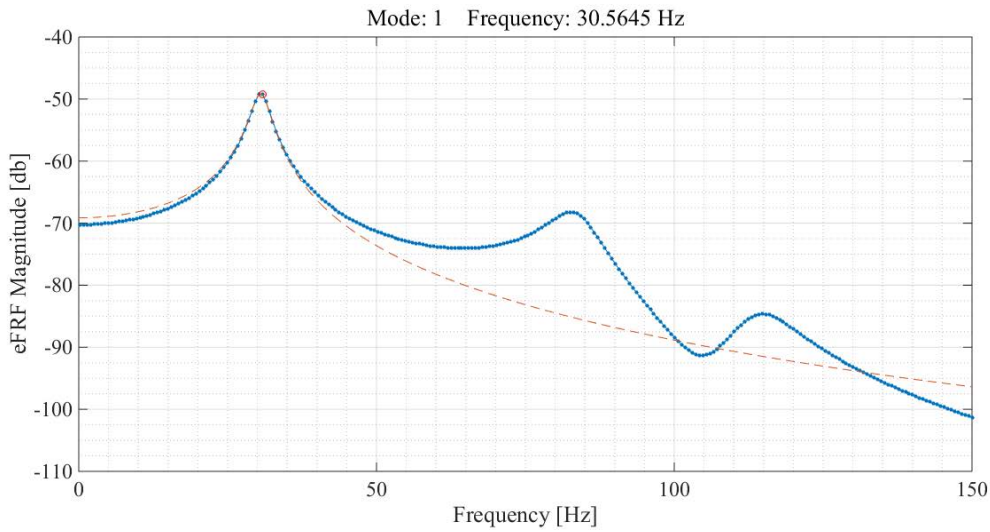


**Figure 4-15: 5DOF Beam – Roving DOF – Mode 1 – Pole Fit**

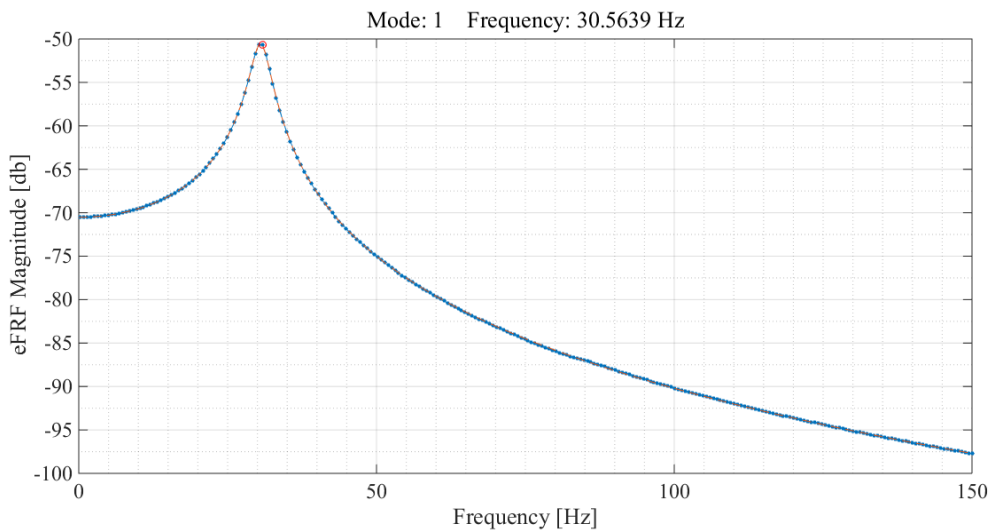


**Figure 4-16: 5DOF – Combined DOF – Mode 1 – Pole Fit**

#### 4.4.3 Conclusions

The maximum number of modes a MDOF parameter identification algorithm can approximate is limited by the minimum dimension of the FRF matrix. The singular vectors found in parameter

identification are modal coefficients of the input and output DOF which presents a problem when the full modal vector of the measurement DOF is desired and the structure's input or output space cannot be sampled in full. However, as we saw earlier, any reasonable approximation of a modal vector can be used to estimate the system pole. In the context of St-Id, the natural frequency predictions of the FE model can be compared to the experimental frequencies with relative confidence as any errors in shape estimations do not have a significant effect on the accuracy of pole estimations. The qualitative or error prone shapes do not necessarily need to be included in the model calibration and solely used to identify and pair modes for calibration. As long as either the left or right singular vectors are spatially complete enough to diagonalize the MAC matrix, the incomplete modal vector approximations can be used to pair the experimental modes to the analytical modes of the FE model and the identified natural frequencies are then the solely used in the objective function residual calculation. This allows for compromise between a full modal solution and one of reduced scope (and with it reduced cost).

#### **4.5 Comparison to MRIT**

The measurement space of the THMPER system and a traditional MRIT is compared in Figure 4-17. Two full columns of the MRIT measurement set represent the full spatial sampling of the output space due to two inputs. The THMPER system instead relies on measuring multiple, partial subsets of the structure's characteristic space and later linearly extrapolating to a full modal solution using the stationary references. The stationary references are the shared DOF between the two measurement subsets and are the crucial link to integrating the partial measurement sets into a full MIMO set.

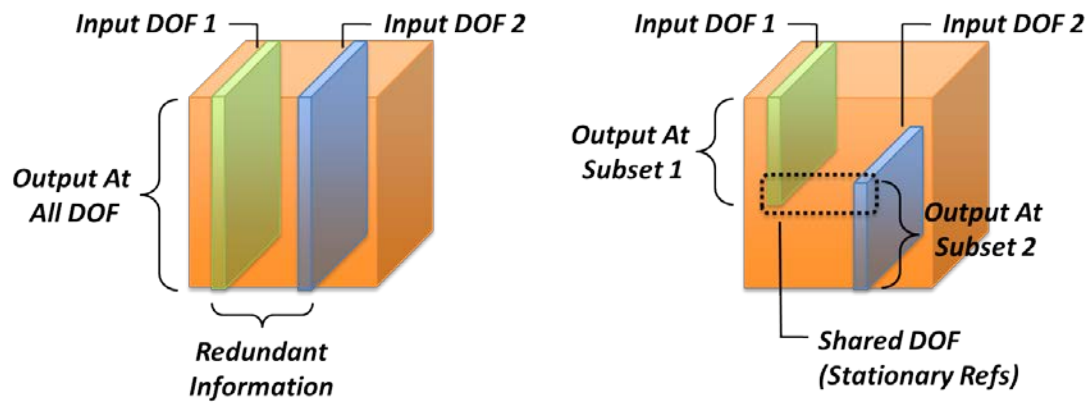


**Figure 4-17: Characteristic Space –Traditional MRIT (Left) vs. THMPER Approach (Right)**

## CHAPTER 5: DESIGN & DEVELOPMENT OF THMPER SYSTEM

The following chapter details the development of the hardware and software systems developed for the THMPER system. The design requirements for the modal test trailer are consistent with the system level goals and established test methodology thus far.

### 5.1 Overview of System Design

The experimental approach detailed in the previous chapter leverages a self-contained modal testing device to perform impact tests within traffic lanes to streamline test execution and reduce the traffic control necessary to safely perform a field test. Modal testing requires a controlled and repeatable excitation source as well as means of measuring the structure's response. The THMPER system experimental strategy involves two distinct measurement types, roving measurements and global, or stationary, measurements.

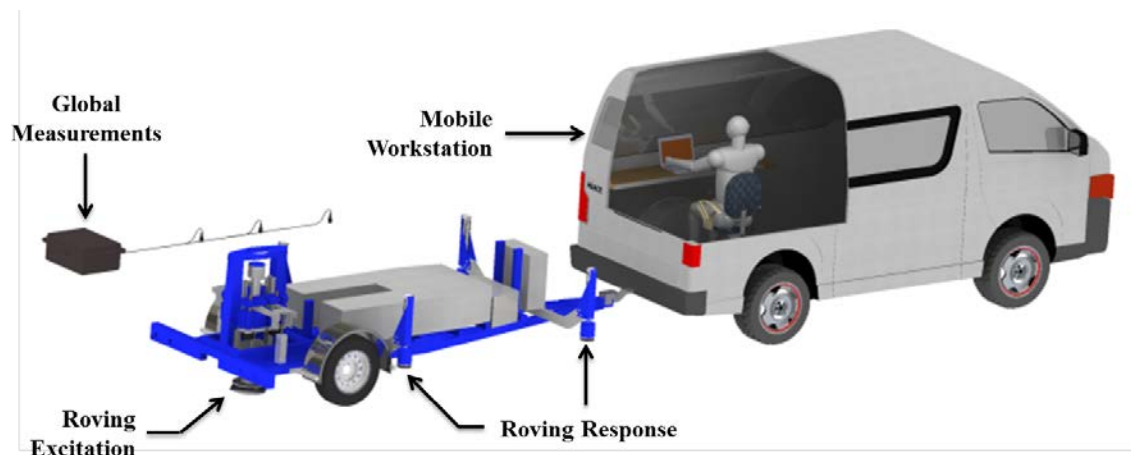


**Figure 5-1: Overview of THMPER System**

## 5.2 Excitation Source

The impact method is a type of forced vibration test that uses a transient impulsive force as excitation measure the resulting vibration free-decay. Due to the transient nature of the excitation, impact testing has two distinct advantages when compared to other forced vibration testing methods – each impact typically excites a broad frequency range of the structure, and each excitation/response record can be measured in a relatively short duration of time. Also, the free-decay response is typically on the order of 5 to 10 seconds.

First a simple numerical example is used to demonstrate the effect of varying the stiffness, mass, and drop height of a falling mass system. Second, the signal characteristics of several impact devices are determined via a field test on a simply supported steel stringer highway bridge. The characteristics are reported and used to influence the final design decisions regarding the THMPER system excitation source design requirements.

### 5.2.1 Review of Impact from Falling Mass

The falling mass system leverages the gravitational pull of the earth to convert potential energy of a raised mass to kinetic energy as the mass makes contact with an impact surface. The drop height, mass of the impact body, and stiffness of the impact tip can all be adjusted to provide varying input characteristics to the system. Figure 5-2 presents a simple, idealized model of a falling mass system where a known mass is raised (1) to an initial height ( $H_0$ ). The mass then falls and impacts a spring (2) with initial velocity ( $V_0$ ) and spring stiffness ( $K$ ). The spring then displaces during the impact (3). The velocity of the mass ( $V(t)$ ) and displacement of the spring ( $D(t)$ ) throughout the duration of the impact may then be solved using simple energy balance and kinematic relationships. To provide a physical relationship between the system properties (mass,

drop height, and impact tip stiffness), multiple combinations of these parameters are discussed below.

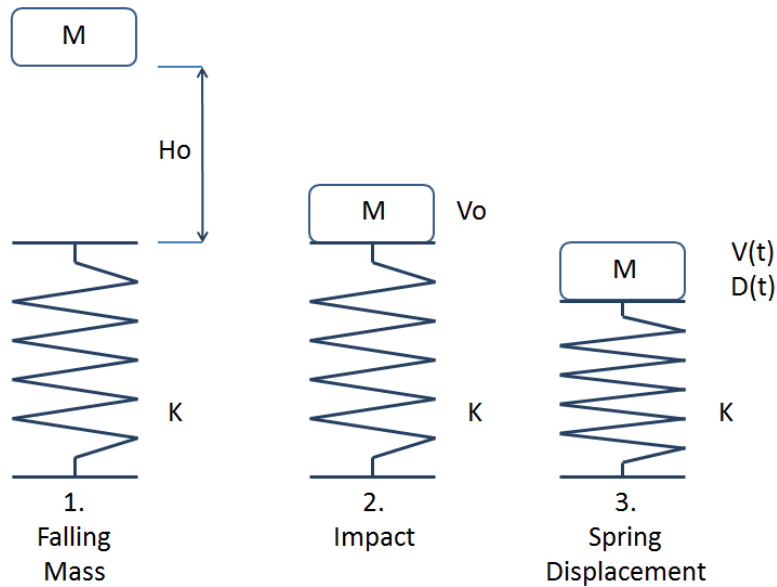


**Figure 5-2: Impact Numerical Analysis**

Four combinations of system properties are presented below in which the drop height, mass, and stiffness parameters of the system were varied (Table 5-1) to provide a physical relationship between the system properties and resulting excitation characteristics. Case A simulates a 100lb mass dropping 24 inches onto a spring of stiffness 50,000lb/in and is the base case for this numerical experiment. Case B decreases the original drop height from 24 inches to 12 inches, Case C increases the original mass from 100lbs to 200lbs, and Case D decreases the original spring stiffness from 50,000lb/in to 25,000lb/in.

**Table 5-1: Impact Numerical Analysis Variable Definitions**

<b>Case</b>	<b>K [lb/in]</b>	<b>Ho [in]</b>	<b>Mass [lb/g]</b>	<b>PE_o [lb*in]</b>	<b>Vo [in/sec]</b>	<b>D_max [in]</b>	<b>Delta_t [sec]</b>
A	50000	24	0.259	2400	136.118	0.310	0.00001
B	50000	12	0.259	1200	96.246	0.219	0.00001
C	50000	24	0.518	4800	136.118	0.438	0.00001
D	25000	24	.259	2400	136.118	0.438	0.00001

The effects of the variation of these parameters on the input force signal in both the time and frequency domains are presented in Figure 5-3. Case A produces a ~15,500lb impact force with a duration of .007 seconds resulting in a usable frequency band of ~0-150Hz. Decreasing the drop height in Case B causes the impact force to drop to ~11,000lbs, however, the width of the impulse remains the same. This results in the same excitation bandwidth as Case A but the amplitude of the signal in both time and frequency domains becomes slightly decreased. Increasing the mass in Case C causes a much larger ~22,000lb impact force but causes the duration of the impact to increase as well. This results in a decrease of frequency band input, causing the usable frequency content to reduce to ~0-100Hz. Decreasing the spring stiffness in Case D causes a reduction of force levels in both the time and frequency domains similar to that of Case B, however, the width of the impulse signal remains the same and results in similar frequency content but at a decreased amplitude.

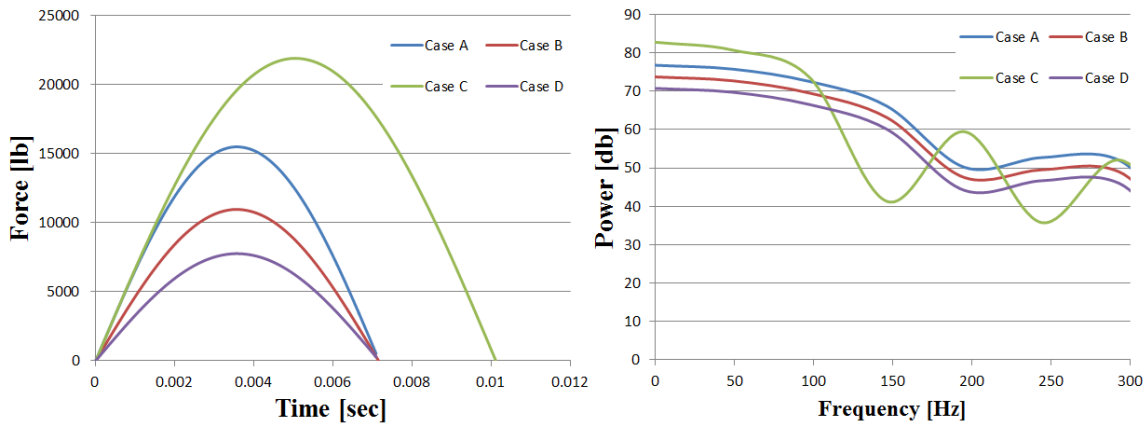


**Figure 5-3: Impact Numerical Analysis Results**

The results of this simple numerical experiment show how varying the mass, stiffness, and drop height of an impact system varies the characteristics of the impulse signal in both the time and frequency domains. Thus, an opportunity is present to vary the mass, stiffness, and drop height of the test trailer's impact carriage and tune the impulse signal to excite specific frequencies of interest.

### 5.2.2 Review of Impact Devices

Several impact devices were used to perform MRIT on a typical steel stringer highway bridge to investigate the characteristics of several commercially available impact devices (Figure 5-4). An instrumented sledge hammer, damped drop hammer, non-damped drop hammer, and rebound controlled drop hammer were utilized for modal testing of the Pennsauken Creek Bridge in Palmyra, New Jersey.



**Figure 5-4: Impact Devices used for PCB Tests**

The Pennsauken Creek Bridge (Figure 5-5) is a three span, simply supported steel stringer structure that is representative of the most common bridge type found throughout the U.S. It consists of three spans, each approximately 50' and carries two lanes of traffic in each direction. Each span consists of a reinforced concrete deck on simply supported rolled steel I-beams with partial-length welded bottom flange cover plates.



**Figure 5-5: Pennsauken Creek Bridge in Palmyra, New Jersey – Elevation View**

### 5.2.2.1 Instrumented Sledge

A model 086D50 instrumented sledge hammer was purchased from PCB Piezotronics, Inc. and utilized in the Pennsauken Creek Bridge tests. The sledge weighs 12.1lbs and is instrumented with a quartz dynamic load cell which has a linear measurement range from 0-5,000lbs. Typical force signals were observed between 3,000-5,000lbs with usable frequency content from ~0-350Hz. (Figure 5-6). The impact caused typical driving point accelerations up to 1g.

Being hand held the sledge's primary advantage is ease of use and transportability. This convenience comes at the price of lower force levels as the relatively low mass of the sledge cannot *drive* the mass of the bridge.

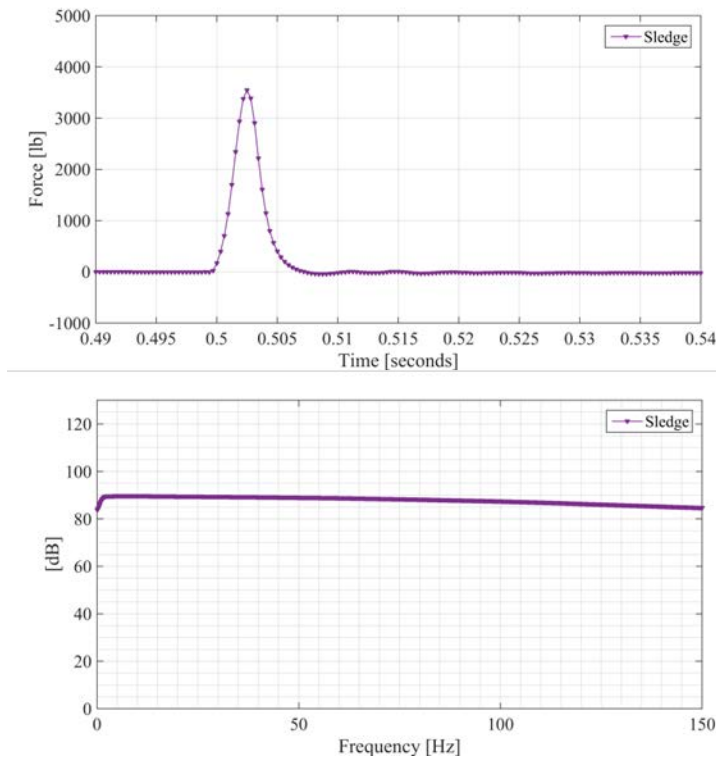


**Figure 5-6: Impact Force Characteristics – Instrumented Sledge**

### 5.2.2.2 The Modal Shop Drop Hammer

The Modal Shop (TMS) drop hammer was once considered the state-of-the-art in civil infrastructure impact devices and was rented from PCB Piezotronics, Inc. for testing on the Pennsauken Creek Bridge. The TMS hammer's impact carriage weighs approximately 75lbs and is capable of dropping 1-2 feet. The impact tip has an adjustable stiffness and contains a dynamic load cell. Additionally, the impact carriage contains a damping mechanism to prevent the carriage from impacting the bridge deck multiple times. The TMS drop hammer delivered typical force levels up to ~1,000-2,500lbs with usable frequency content from ~0-35Hz (Figure 5-7). Typical driving point accelerations were observed up to .05g-1g.

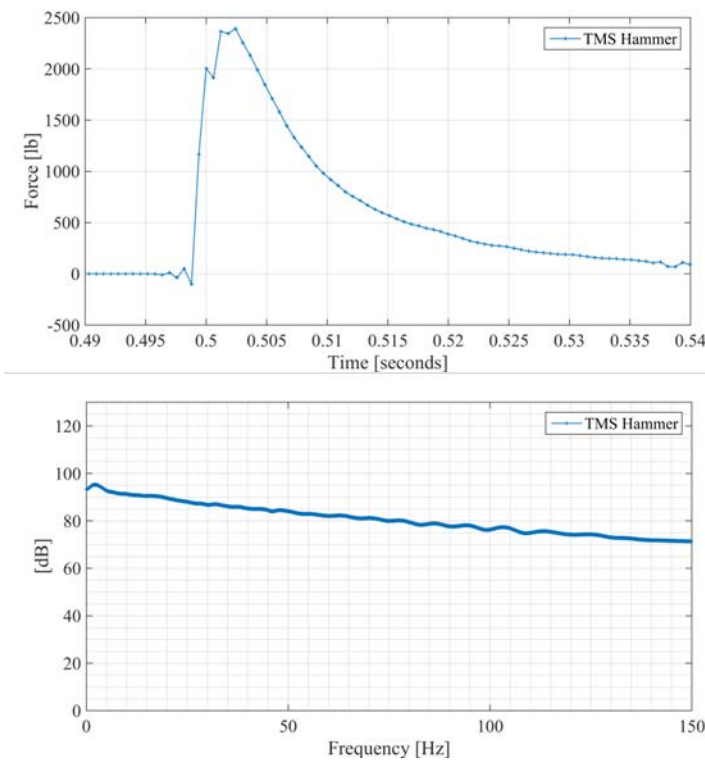


**Figure 5-7: Impact Force Characteristics – Damped Drop Hammer**

### 5.2.2.3 Drexel Drop Hammer – Proto 1

The original Drexel Drop Hammer was designed and manufactured in house at Drexel University. It consists of a ~100lb impact carriage that has a 2 foot vertical travel and an adjustable stiffness impact tip. In between the moving mass and the impact tip is a PCB model 200C50 dynamic load cell. Typical force levels were observed up to 18,000lbs (Figure 5-8). Typical driving points reached +1.5g's which resulted in good excitation of all global modes. However, due to the lack of a rebound mitigation system, multiple rebounds were captured within each time window. This violates the harmonic assumption of the FFT and causes errors in the frequency content. The device was ultimately deemed un-reliable for frequency response function development.

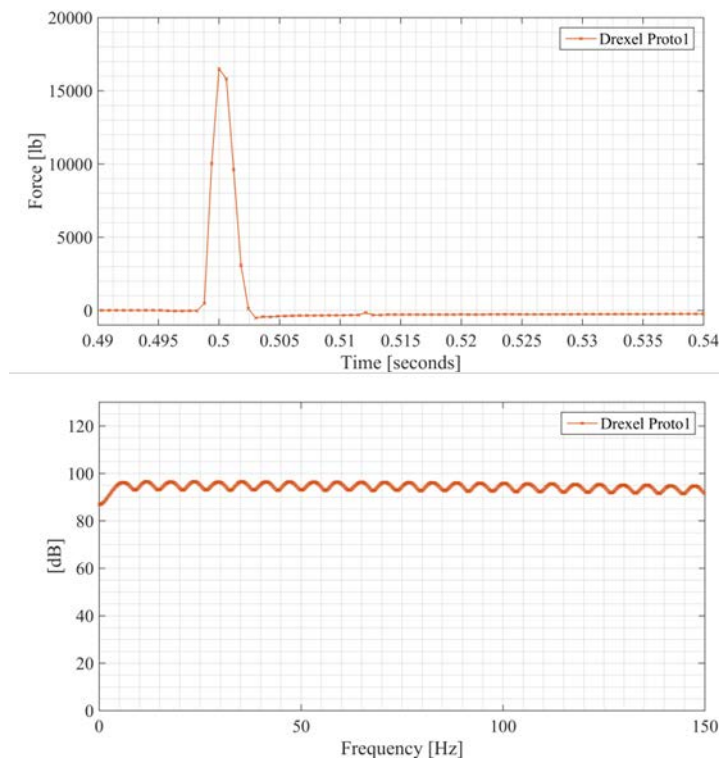


**Figure 5-8: Impact Force Characteristics – Drexel Drop Hammer Proto1**

#### 5.2.2.4 Drexel Drop Hammer – Proto 2

Following the December, 2010 Pennsauken Creek Bridge test, the original Drexel Drop Hammer was revised with additional mass and outfitted with a rebound mitigation system. The rebound control system is depicted in (Figure 5-9) and consists of a mechanical brake system and a sensing/control system. The brake system includes precision THK linear motion rails paired with ball bearing guides and Nexen Group pneumatic brakes. The brakes are spring engaged and air released in order to obtain a maximum response time of .05s. This quick response time is necessary to ensure the moving mass is at a near zero velocity upon catch initiation. To release, the brakes accept an air pressure of 80psi from a computer controlled 3-way valve. Upon detection of zero velocity at the apex of the first rebound, the 3-way valve receives a signal from the controller and switches off allowing a drop of 2-3psi in the soft air connection tubing. This then initiates two quick exhaust valves (mounted on the drop hammer) which rapidly purge the brakes of air pressure, engaging the brake's friction pads and halting the moving mass. The sensing and control system includes a National Instruments cRIO data acquisition system that interfaces with an Acuity AR700 laser distance gauge. The cRIO controller reads an analog input module (NI9205) to acquire and process distance measurements of the impact carriage. An analog output module (NI9269) provides control signals to the mechanical 3-way valves.

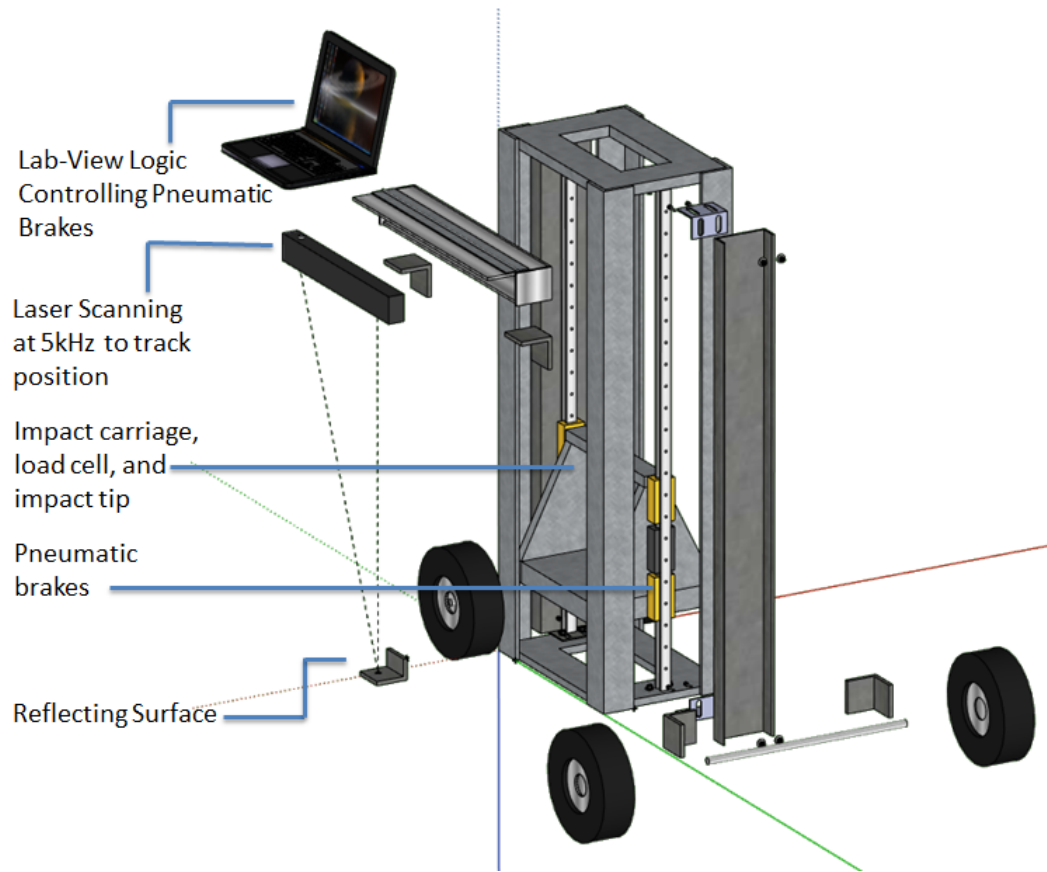


**Figure 5-9: Drexel Drop Hammer with Rebound Control**

The revised Drexel Drop Hammer with rebound control was utilized in May, 2011 for additional modal testing of the Pennsauken Creek Bridge (Figure 5-10). The addition of over 50lbs of steel to the impact carriage and smoother guide rails resulted in typical force input levels being raised to 20,000-27,000lbs. The rebound control system provided a single unit impulse which resulted in excellent characterization of the force signal in the frequency domain with usable frequency content from ~0-125Hz. Driving point accelerations of the bridge deck were observed up to 2-3g's and excellent excitation of global modes was achieved.

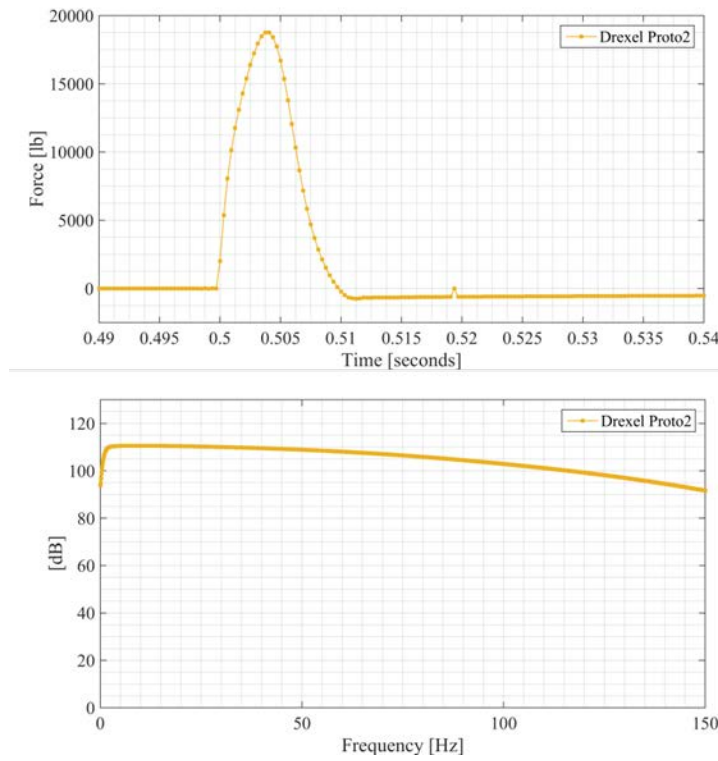


**Figure 5-10: Impact Force Characteristics – Drexel Drop Hammer Proto2**

### 5.2.2.5 Summary & Design Considerations

The instrumented sledge performed adequately in exciting global modes of the bridge, however, suffers from having relatively low mass and thus spreads excessive energy throughout a broad and inefficient frequency band for civil infrastructure applications. The Modal Shop drop hammer performed sub-par in exciting global modes of the bridge. Additionally, due to the increased duration of the force time history resulting from the use of a damper to obviate the rebound of the impact mass, this approach it is not feasible to achieve the desired impact characteristics for the test trailer. The original Drexel Drop Hammer showed promise in delivering large impact forces within lower focused frequency bands which resulted in large acceleration levels; however, frequency content of the input signal became un-reliable due to multiple rebounds of the impact carriage.

### 5.2.3 Development & Component Testing

#### 5.2.3.1 FWD Impact Device

The THMPER system is based upon a modified Falling Weight Deflectometer (FWD) which is a common pavement assessment tool owned operated by most DOTs. Previous research investigating the FWD as a structural condition assessment tool has had limited success. Hoadley & Gomez et al (1996) used a standard FWD to directly extract displacement coefficients of a highway bridge but reported significant error when comparing the displacements to FEM analysis and traditional static results. Catbas et al (2004) introduce the concept of using the FWD as a modal impact trailer for recovery of modal flexibility coefficients, citing speed and ease of execution as major benefits. Grummlesman et al (2013) used a standard FWD and fixed array of sensors to conduct impact tests on a truss bridge and compared impulse characteristics and extracted modal parameters of the FWD with an instrumented sledge hammer. The authors determined the FWD is an effective excitation device for impact testing of bridges and found good agreement between resonant frequencies and mode shapes extracted from each device.



**Figure 5-11: Original FWD Trailer Purchased in June, 2011**

The final impact device of the modal test trailer (Figure 5-12) consists of a hydraulic lift that remotely raises an impact carriage of steel weights (weighing approximately 500lbs) which is then dropped from an adjustable height of approximately 1-2 feet onto a strike plate. Four to six rubber bumpers impact the strike plate which in turn transmits the impulse to the bridge surface. In series with the strike plate system are three dynamic force ring load cells capable of capturing the large impact force. The mass and stiffness of the impact carriage are adjustable to control the magnitude and frequency band of the impact. However, as the testing system is expected to perform in the presence of traffic (to eliminate the need for costly traffic control) the impact must be large enough to overcome this traffic and thus determined to be on the order of 20-30kips. The mass and stiffness properties were also tuned to ensure the adequate excitation of all global modes of interest (typically up to 50 to 75 Hz for highway bridges). Additionally, to provide a strict unit impulse and thus preserve proper characterization of the impulse in the frequency domain as well as preserve the ability to directly calculate modal mass (or modal flexibility) a single unit impulse is achieved through the use of a pneumatic rebound control system.

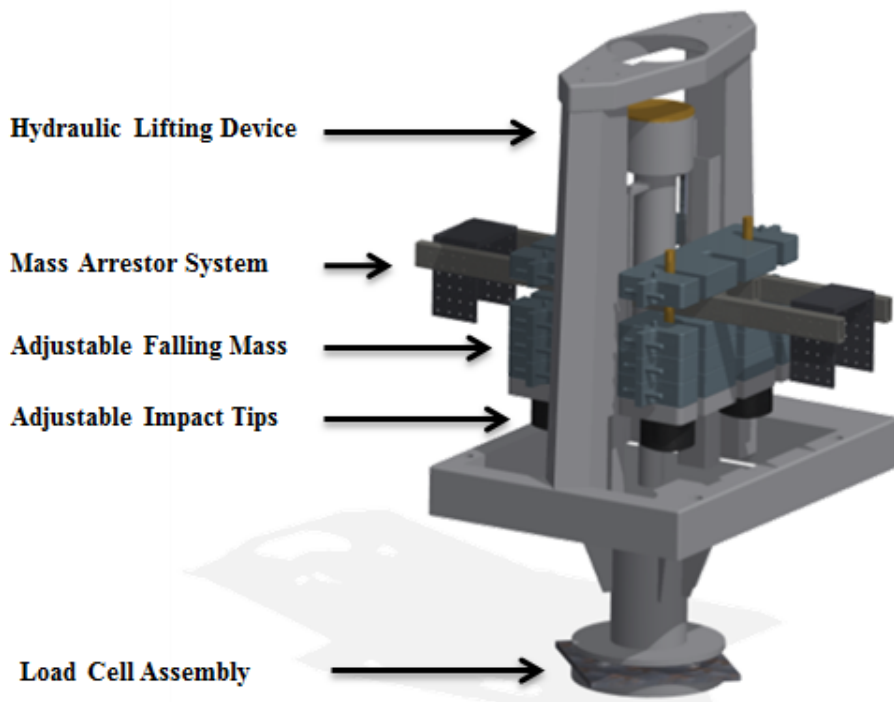


**Figure 5-12: Excitation Source - A Modified FWD Impact Device**

### 5.2.3.2 Load Cell Assembly

The original FWD obtained from Dynatest contained a proprietary load cell that was found to be nonoperational. This load cell has a unique geometry and fits above the circular strike surface in a type of ball-and-socket joint. To mitigate the issue the load cell retrofit depicted in Figure 5-13, was implemented. Three PCB Model 203B force ring load cells were installed in parallel, connecting the strike plate stem to the roadway contact surface. The load cells are designed to measure dynamic impact forces and have a linear measurement range of 10-20,000lbs each.



**Figure 5-13: Falling Weight Deflectometer Load Cell Installation**

Additionally, due to the force ring design each load cell must be pre-loaded with 1,000lbs of compression using a beryllium-copper stud (Figure 5-14). This not only provides a mounting solution for the trailer but also allows for flexibility in accurately capturing forces due to off axis loading not strictly applied in the axial direction.

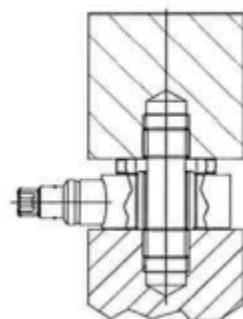


**Figure 5-14: Force Ring Load Cell**

### 5.2.3.2.1 Benchmark Experiment

Since each load cell is recorded independently, the three raw impact time histories must be summed to realize the total drop force. To ensure this arrangement provides accurate measurements of the force signal, a benchmark was performed using a calibrated PCB Model 200C50 dynamic load cell. The experimental setup is shown in Figure 5-15.



**Figure 5-15: Load Cell Assembly – Benchmark Test**

Multiple impacts at various heights were recorded and compared. The three raw input signals from a typical test are shown in Figure 5-16. The sum of each summation is then compared to the reference load cell – the time domain representation is shown in Figure 5-17 and the equivalent frequency domain representation is shown in Figure 5-18. The load cell assembly shows good agreement to the reference load cell, with some minor differences that may be attributed to calibration errors. The results indicate the load cell assembly does not influence the force measurements and vets it for use on the trailer.

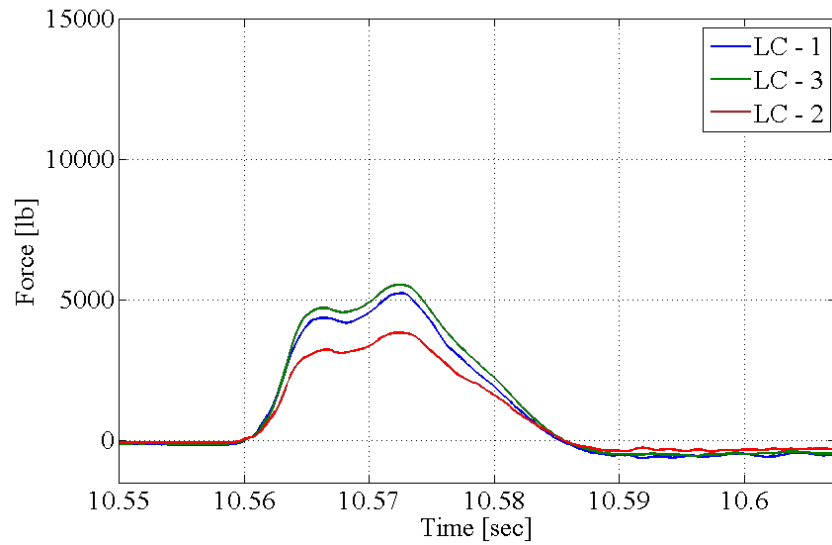


**Figure 5-16: Load Cell Assembly – Benchmark Test – Load Cell Individual Force Record**

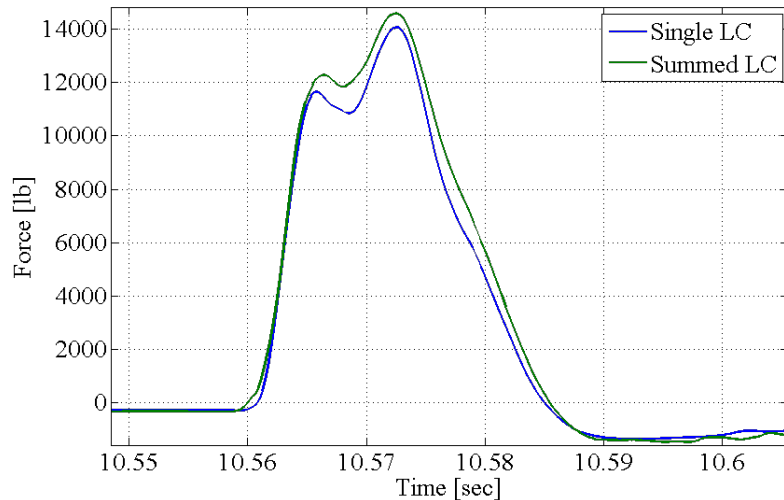


**Figure 5-17: Load Cell Assembly – Benchmark – Comparison of Forces – Time Domain**

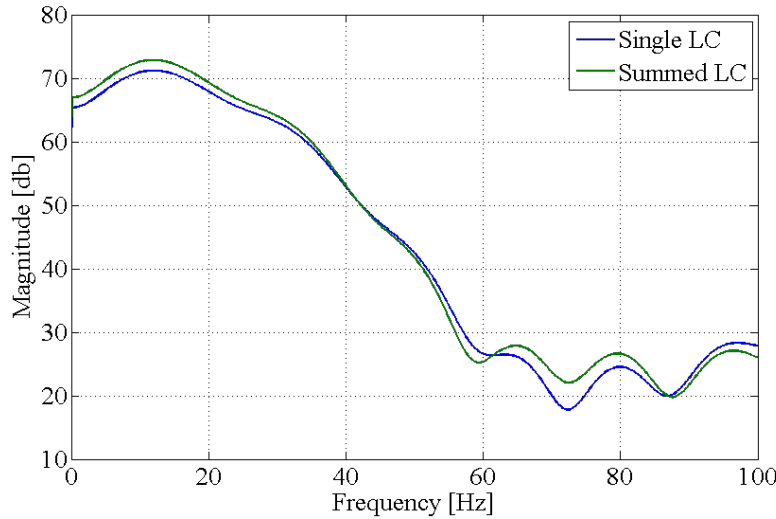


**Figure 5-18: Load Cell Assembly Laboratory Benchmark – Frequency Comparison**

### 5.2.3.3 Rebound Mitigation System

The trailer's rebound mitigation system (Figure 5-19) is comprised of two fast acting Norgren Series 90000 compact actuators, two Parker 3-way valves, a compressed air system, a Hamlin sinking gate hall sensor, and an NI cRIO controller. The cRIO controller provides power for the system and continuously polls the output voltage of a hall sensor located on the strike surface of the impact device. During a drop sequence the mass enters free fall and accelerates towards the strike surface. Once the mass contacts the strike surface the output voltage of the hall sensor drops to zero which informs the cRIO of an impact. The cRIO then initiates the rebound control sequence activating each 3-way valve. This releases 100psi of air pressure to the actuators causing them to rapidly extend upwards and follow the rebounding mass (Figure 5-20). The extended actuator rods meet the impact carriages halting the mass at apex. The mass is then held at apex for 10 seconds to allow acquisition of the bridge free-decay vibrations without subsequent input. The 3-way valves are returned to their original position bleeding the actuators and completing the rebound control sequence.

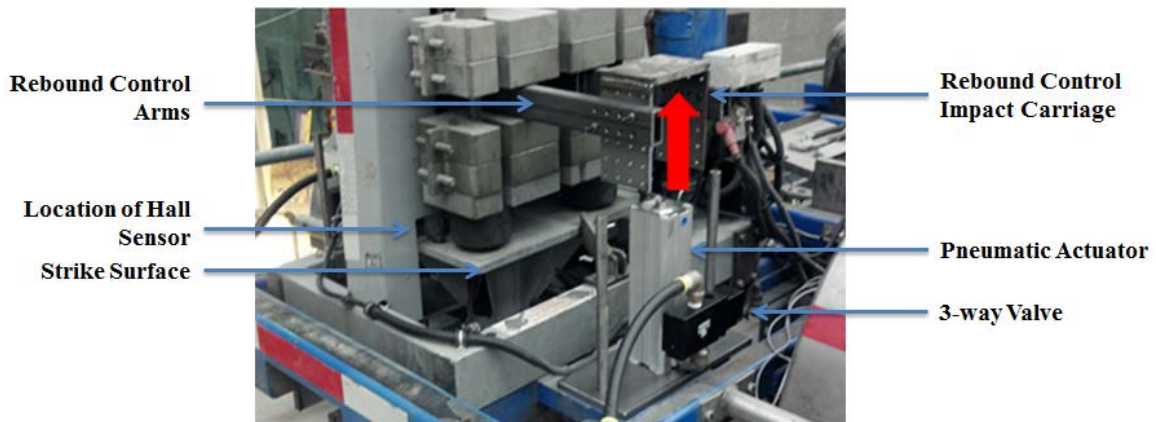


Figure 5-19: Rebound Mitigation System

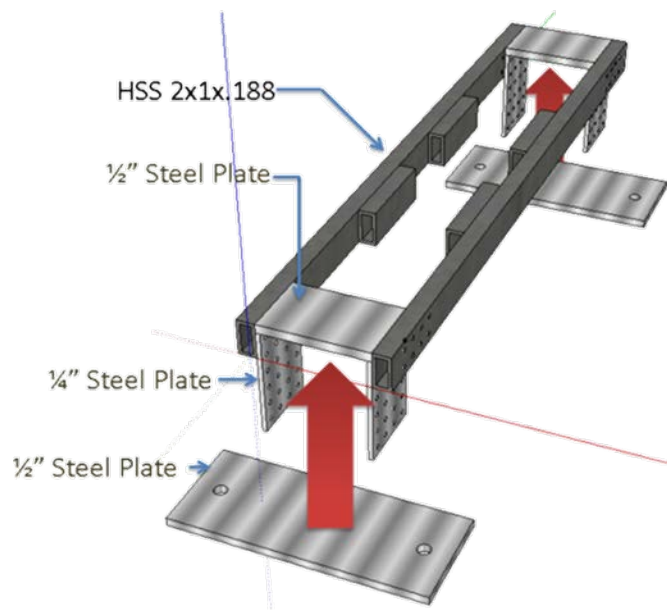


Figure 5-20: Impact Carriage Schematic

### 5.2.3.4 Comparison to Existing Impact Devices

A summary of the impact device comparison is shown in Table 5-2. The comparison of the input signals in the time domain is shown in Figure 5-21, and the equivalent representation of the input signal in the frequency domain is shown in Figure 5-22.

**Table 5-2: Summary of Impact Device Comparison**

Impact Device	Weight [lbf]	Drop Height [ft]	Peak Force [lb]	Frequency Bandwidth [Hz]	Peak DP Acceleration [g]
Sledge	12.1	N/A	5,000 lb	0 - 235 Hz	0.42 g
TMS Drop Hammer	75	1-2 ft	2,500 lb	0 - 35 Hz	0.21 g
Drexel Drop Hammer - Proto1	35	1-2 ft	15,000lb	0 - 400 Hz	1.75 g
Drexel Drop Hammer - Proto2	150	1-2 ft	20,000 lb	0 - 150 Hz	2.25 g
THMPER System	500	1-2 ft	25,000 lb	0 - 75 Hz	3.5 g

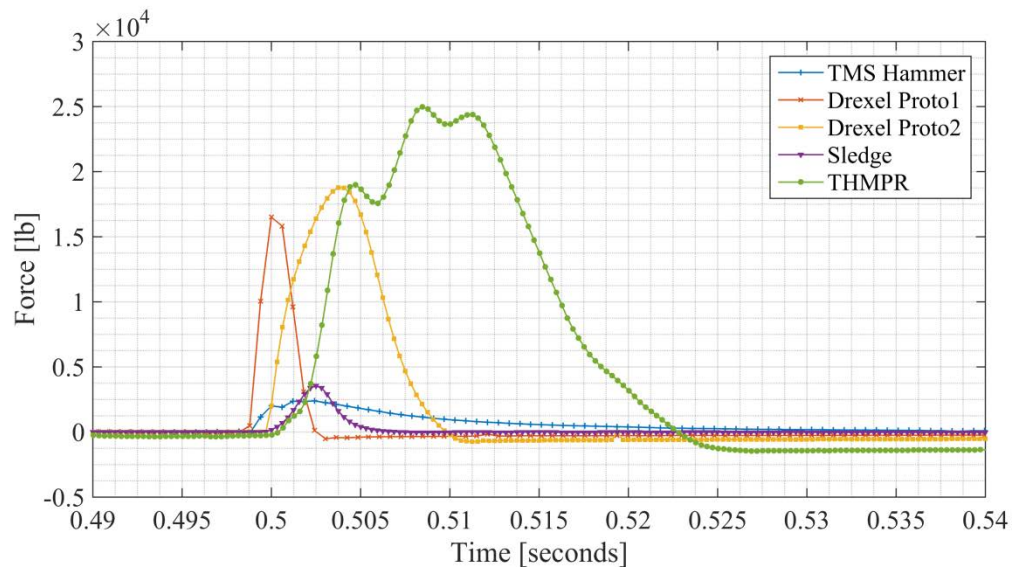


**Figure 5-21: Comparison of Impact Devices – Time Domain**

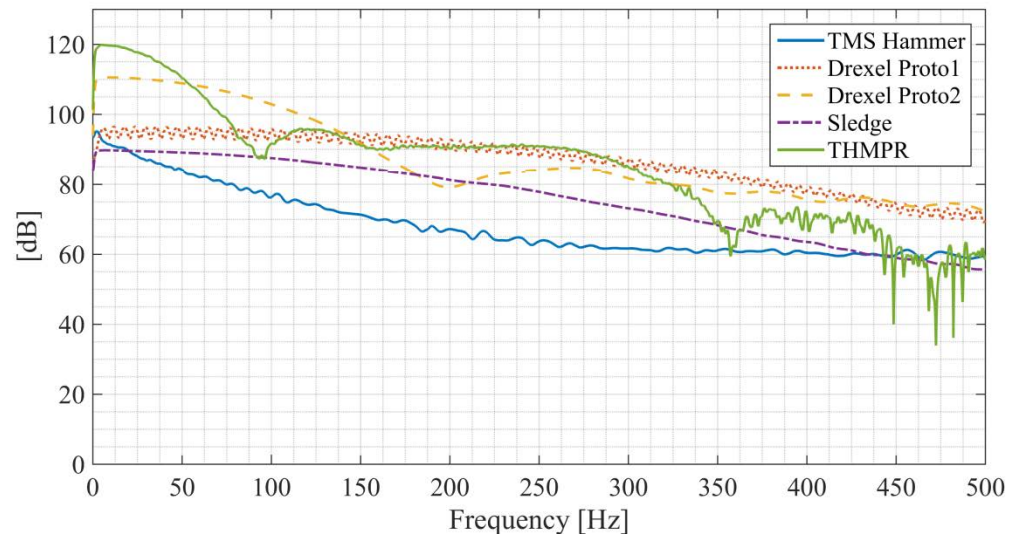


**Figure 5-22: Comparison of Impact Devices – Frequency Domain**

### 5.2.3.5 THMPER Comparison to Sledge during Traffic

The input signals and resulting FRFs between THMPER system and instrumented sledge were compared using clean and traffic polluted records. This was done to compare each impact device's ability to overcome noise pollution by a passing vehicle. The instrumented sledge was used as a baseline for a performance comparison as it is currently the standard commercially available impact device.

Ideal data records were recorded for both impact devices without the presence of traffic as well as polluted data records which included erroneous input from vehicle traffic in each data record. Frequency response functions were formed from the clean and polluted signals for both the instrumented sledge and the THMPER system (Figure 5-23). Two non-polluted time signals were used to compute the FRF and coherence for each impact device. A third record was later included in the FRF formulation that captured a ~0.025 g noise influence for two seconds for each impact device.

The benefit of the THMPER system's focused frequency band and large force levels can clearly be seen in the results FRF and coherence values when compared to the sledge results. The THMPER system was able to overwhelm most of the erroneous influence of passing traffic with negligible effects to both the FRF and coherence values. In contrast, the instrumented sledge induced relatively small force levels compared to traffic and, due to its low mass and high tip stiffness, spread this energy throughout a broader frequency band. As a result, the FRF and coherence values obtained by the sledge are negatively affected.

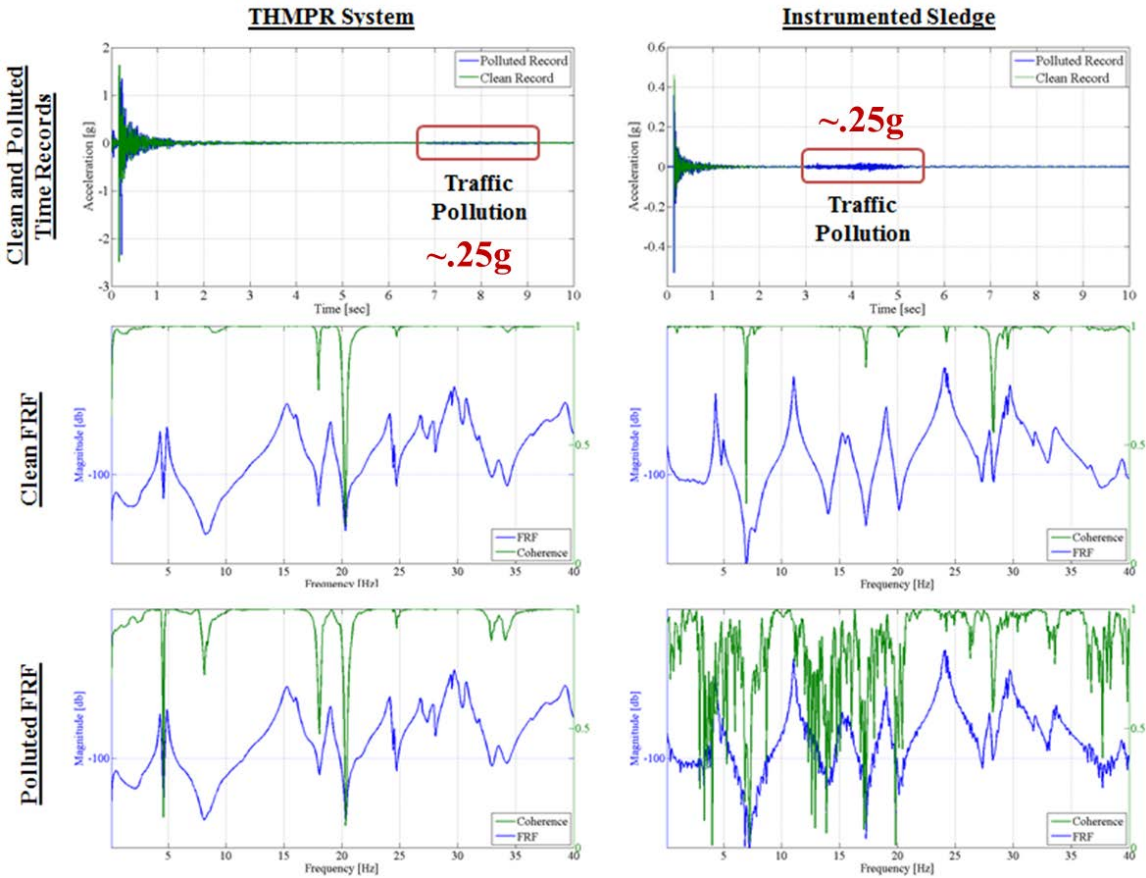


**Figure 5-23: THMPER vs Sledge – FRF Comparison in Traffic**

### 5.3 Response Measurements

#### 5.3.1 Mobile Sensor Array

Design of the mobile sensing array contained the following criteria: (1) capture the pure global vibrations of a test bridge without influence, (2) contain a dense grid of local degree-of-freedom (DOF) to ensure good spatial resolution in local mode shapes, (3) rapidly deploy and retract to reduce the amount of testing time required for execution at each location as well as maintain driving safety during travel, and (4) stay within a single lane to facilitate testing in the presence of traffic.

A total of six PCB 393A03 accelerometers in a spread pattern (Figure 5-24) were chosen to ensure practical yet adequate spatial resolution. The accelerometers have a measurement range of +/-5g. This is beneficial because the local sensors that are attached to the trailer are in close proximity to a very large impact that regularly generates driving point accelerations of +4g's. The sensors have a broadband resolution of 0.00001g Root Mean Squared (RMS), a resonant frequency from 0.5 to 2,000 Hz, and are hermetically sealed. The accelerometers are locally cabled through conduit mounted to the trailer frame and terminate at the front of the trailer, inside of the mounted electrical enclosure.

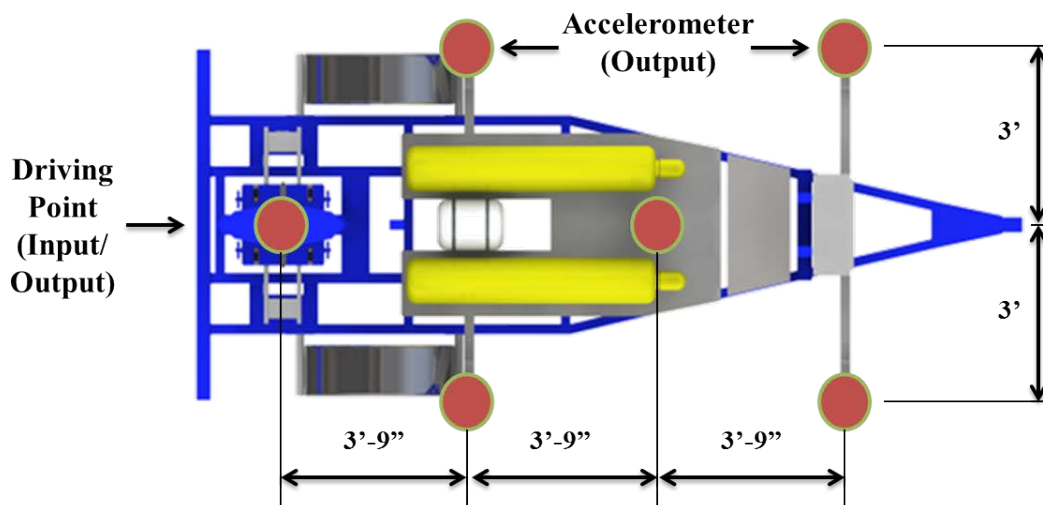


**Figure 5-24: THMPER System Sensor Footprint**

### 5.3.1.1 Accelerometer Housing

The sensors must also be autonomously deployed from the trailer. To accomplish this, a pneumatic actuator system is used to press a sensor assembly onto the bridge surface. Each sensor

assembly contains an inner, spring loaded accelerometer housing. The accelerometer housing and deployment mechanism are shown in Figure 5-25.

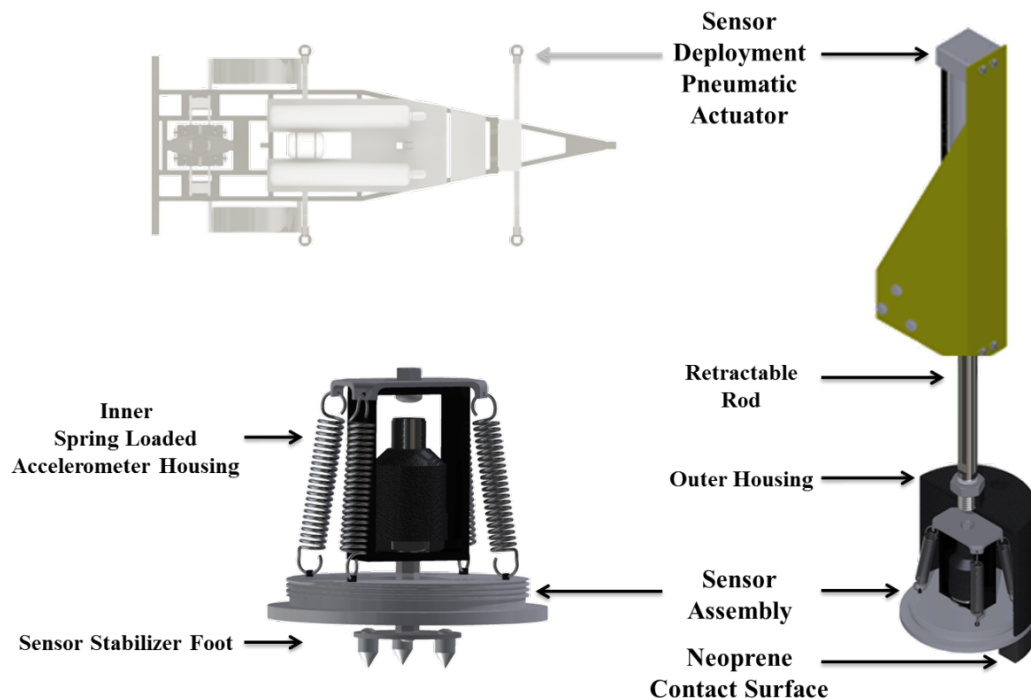


**Figure 5-25: Mobile Sensor Array – Pneumatic Deployment & Sensor Housing Details**

As the sensor assembly is pressed onto the bridge deck, the stabilizer foot is the first to contact. The foot has three-prongs which stabilize the accelerometer and keep it oriented perpendicular to the bridge surface. After roughly half an inch of travel, an outer ring of neoprene secured to the bottom of the outer assembly makes contact with the deck and prevents further travel of the inner housing. The displacement of the inner housing causes the springs to extend which isolates the accelerometer from the trailer and helps reduce extraneous noise propagating from the hydraulic motor, the engine of the towing vehicle, etc. The displacement also causes a pre-load on each accelerometer from the spring extension. This essentially utilizes the trailer as a reactionary mass

which prevents the entire sensor assembly from lifting off of the bridge when accelerations larger than 1g are experienced.

Determining an appropriate temporary accelerometer installation method was an iterative process.

Figure 5-26 shows several prototypes that were developed throughout the process.



**Figure 5-26: Sensor Housing Prototypes**

### **5.3.1.1 Numerical Benchmark**

The simplified model shown in Figure 5-27 was used to evaluate the accelerometer housing concept. The model was developed using the Strand7 and the analysis was done using the linear transient dynamic solver. A nominal cross section was chosen for the aluminum stabilizer rod and the stabilizer foot was ignored. The spring forces of the four inner springs were summed and an initial nodal displacement of .5 inches was used to create the pre-stressing force onto the point mass of the accelerometer. A beam element was used to model the stabilizer rod and was fixed at its base.

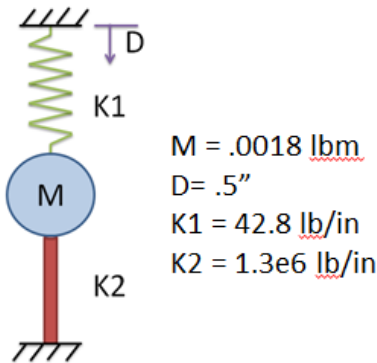


**Figure 5-27: Numerical Benchmark Model**

A typical driving point acceleration record (Figure 5-28) was applied at the base node of the model and a linear transient analysis was performed. The axial force of the beam element was monitored to ensure that the initial compression in the aluminum rod did not transition into a net tension. This would indicate possible lift off of the accelerometer housing. This did not occur and the rod remained in compression throughout the time window.

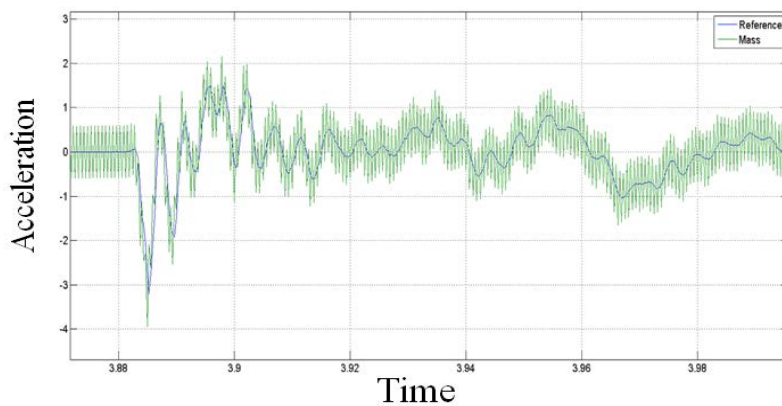


**Figure 5-28: Numerical Benchmark – Acceleration Record**

No significant influence was observed on the frequency content of the sensor acceleration within the frequency bandwidth of interest (Figure 5-29). Note the 1,100 Hz resonance is due to the axial mode of the aluminum rod.

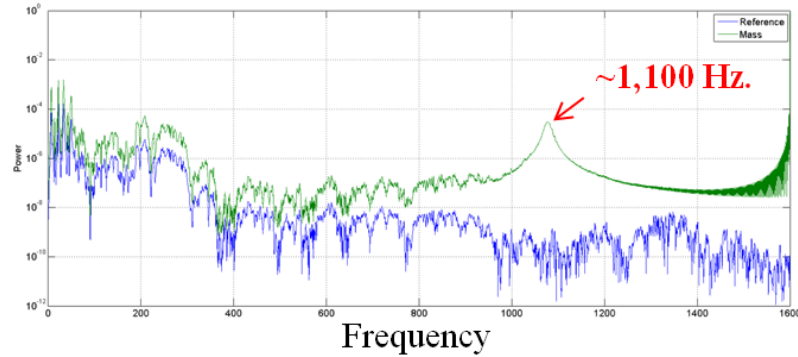


**Figure 5-29: Numerical Benchmark – Frequency Content**

### 5.3.1.1.2 Experimental Benchmark

During several field tests reference accelerometers were temporarily glued to the bridge deck in close proximity to the local deployed sensor housings (Figure 5-30). Figure 5-31 shows the time domain comparison of the THMPER system driving point and its glued reference. At first glance the THMPER system acceleration seems to be polluted with large amounts of noise. Figure 5-32 and Figure 5-33 examines the frequency content of each signal and confirm that the noise is mostly high frequency noise and has little effect on the relevant signal properties EMA attempts to recover.

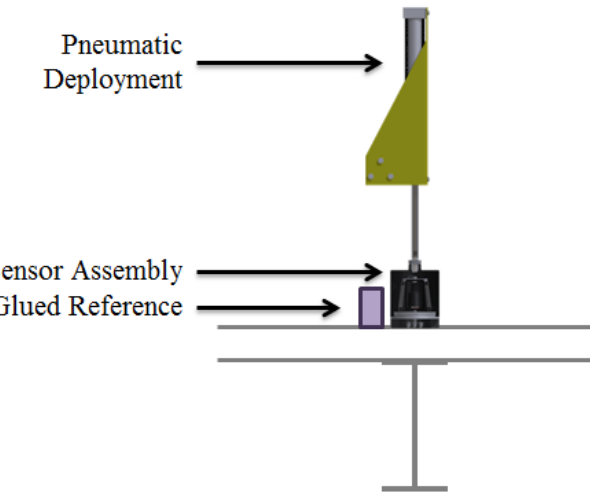


**Figure 5-30: Accelerometer Housing – Experimental Benchmark Setup**

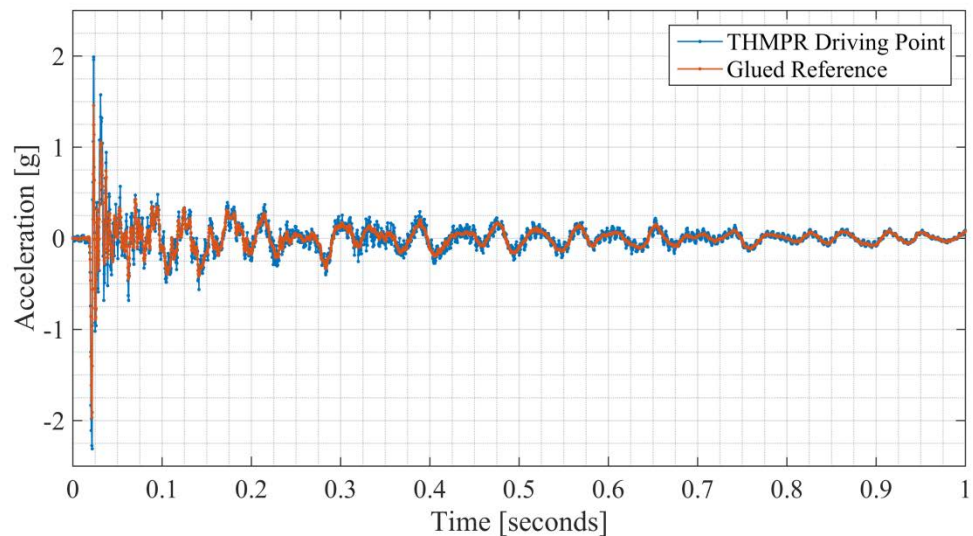


**Figure 5-31: Experimental Benchmark – Time Domain Comparison**

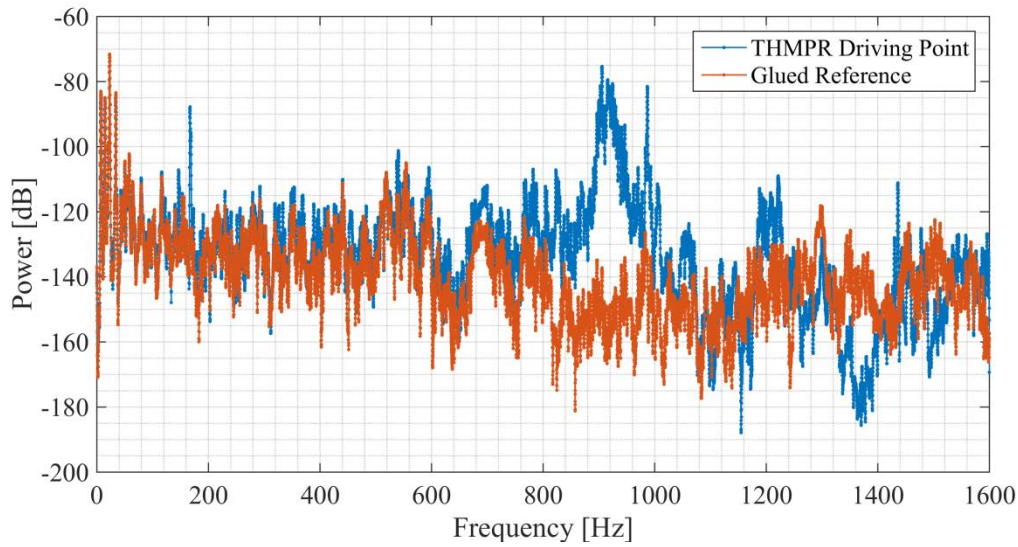


**Figure 5-32: Experimental Benchmark – Frequency Domain Comparison 1**

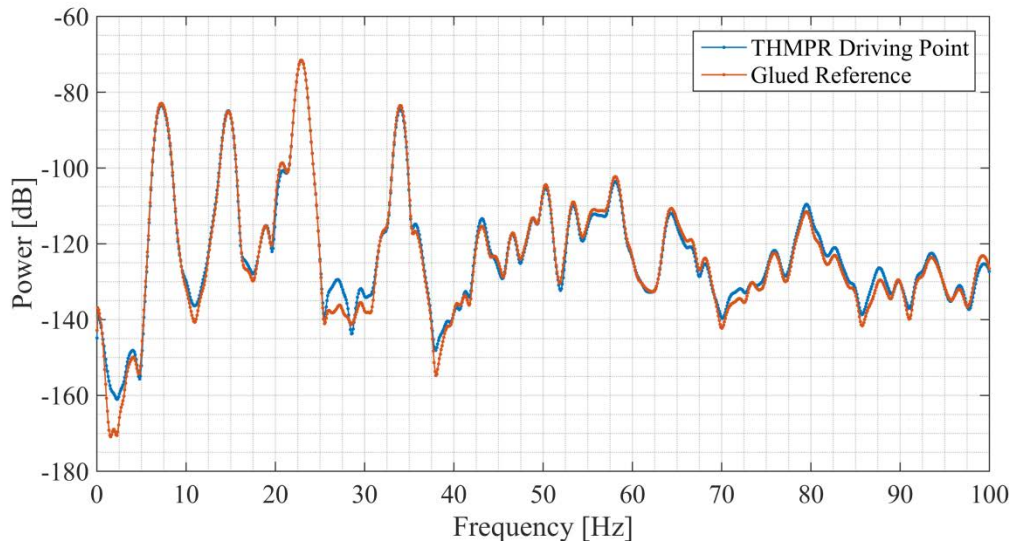


**Figure 5-33: Experimental Benchmark – Frequency Domain Comparison 2**

To accentuate this point, the high frequency noise can be filtered out to show a more representative comparison in the time domain. The filter shown in Figure 5-34 is a Butterworth

filter with a pass band of 75 Hz and a stop band of 150 Hz. It has an allowable passband ripple of 3dB and the attenuation in the stop bad was set to 50 dB.

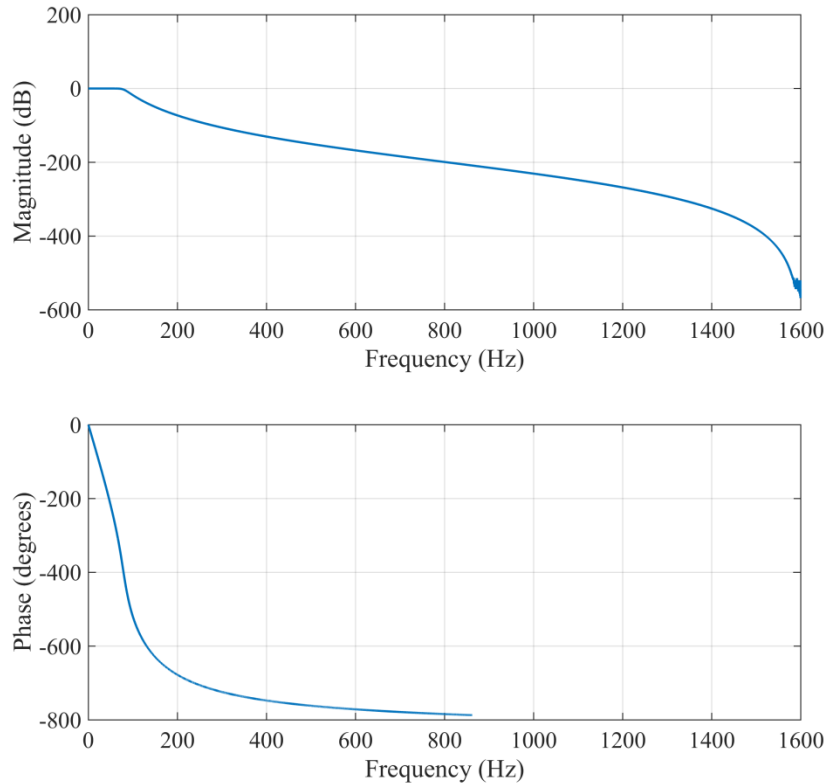


**Figure 5-34: Filter Design**

Figure 5-35 shows a comparison of the filtered THMPER driving point signal and the glued reference. Removing the high frequency noise pollution with a low pass filter shows a more agreeable comparison between the driving point and glued reference time signals. This is confirmed in Table 5-3 which compares the percent difference between the two signal's RMS.

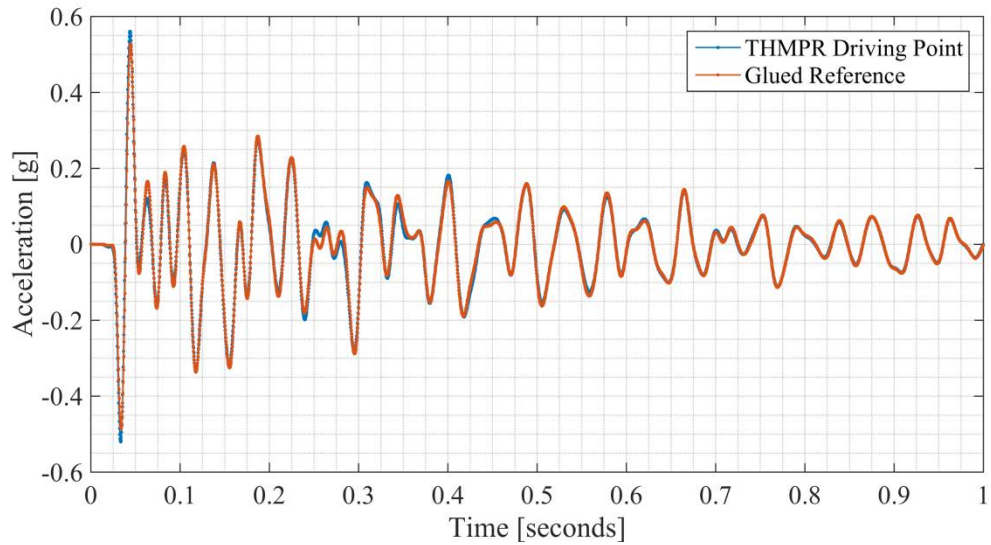


**Figure 5-35: Driving Point Comparison – Post Filter**

**Table 5-3: Accelerometer Benchmark – Root Mean Square Comparison**

	THMPER Driving Point	Glued Reference	% Difference
No Filter, 0-1s	.1767g	.1501g	17.73%
No Filter, 0-10s	.0768g	.0529g	45.08%
Filter, 0-1s	.1100g	.1091g	0.81%
Filter, 0-10s	.0381g	.0380g	0.032%

Note that although it appears that a filter is necessary, it actually has little effect in the frequency bandwidth of interest. This is by design. Figure 5-36 shows a plot of the pre and post filter

frequency content and confirms this. Therefore it will also have negligible effect when using frequency based modal parameter estimation techniques. As a result it is rarely performed and the raw experimental data is pre-processed as little as possible to preserve data integrity.

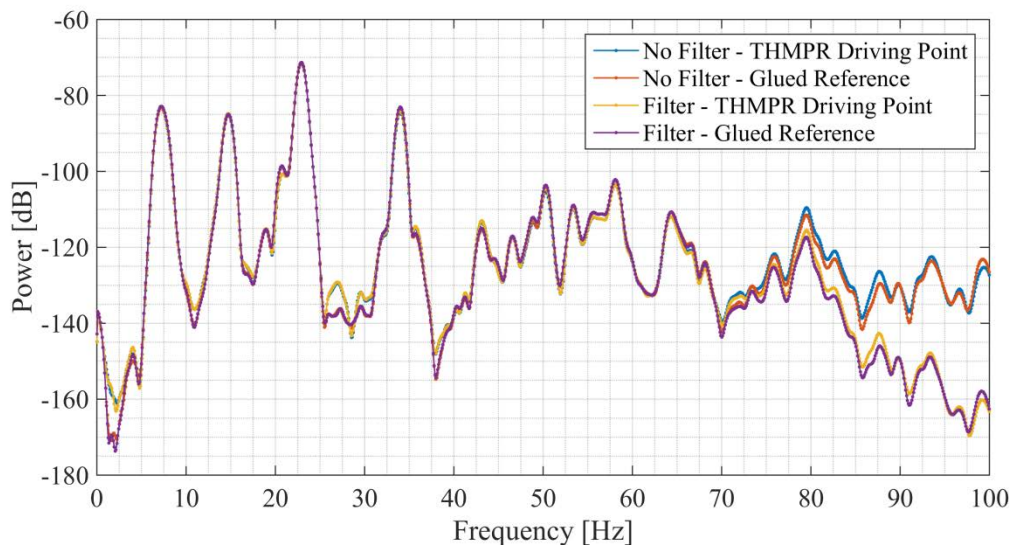


**Figure 5-36: THMPER Driving Point Benchmark – Filtered Vs. Non-Filtered Response**

### 5.3.1.2 Integrated Data Acquisition & Control

Custom data acquisition code and hydraulic and pneumatic control code is required to remotely operate the mobile trailer and record the induced global vibrations. Autonomous control is important in accelerating the speed at which each SIMO test is conducted as well as maintaining safe conditions for the operating engineer (namely, the ability to operate the trailer without being subjected to passing vehicles). The data acquisition must be able to record each desired input and response channel synchronously, sample at a rate large enough to adequately describe the input force characteristics, and store large enough data records to provide adequate frequency resolution (on the order on 10 seconds).

A National Instruments (NI) CompactRIO (cRIO) controller provides both the control and data acquisition. Using the programming environment of Labview, the operator is resides in the towing vehicle throughout the test. Using a dedicated PC connected to the NI cRIO via Ethernet to remotely deploy the accelerometers, operate the impact hydraulic lift, and record the global response of the bridge. The cRIO is mounted in an environmentally sealed enclosure (Figure 5-37) and uses 24-bit resolution NI9234 modules for acquisition of the dynamic data. All cables are run through internal conduit which is mounted to the frame of the trailer. A series of relays is used to interface with the existing hydraulic controls of the original FWD trailer. The pneumatic control and rebound mitigation control schematic is shown in Figure 5-38.

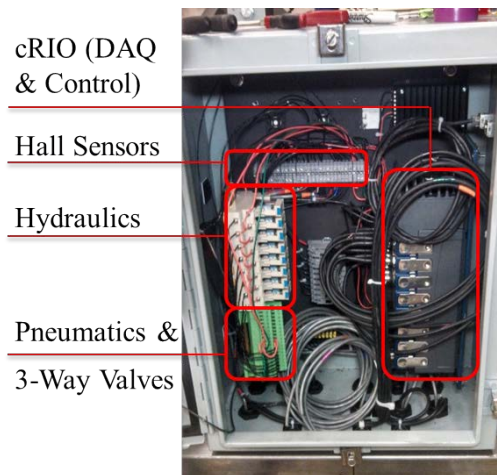


**Figure 5-37: Trailer Mounted Data Acquisition & Control**

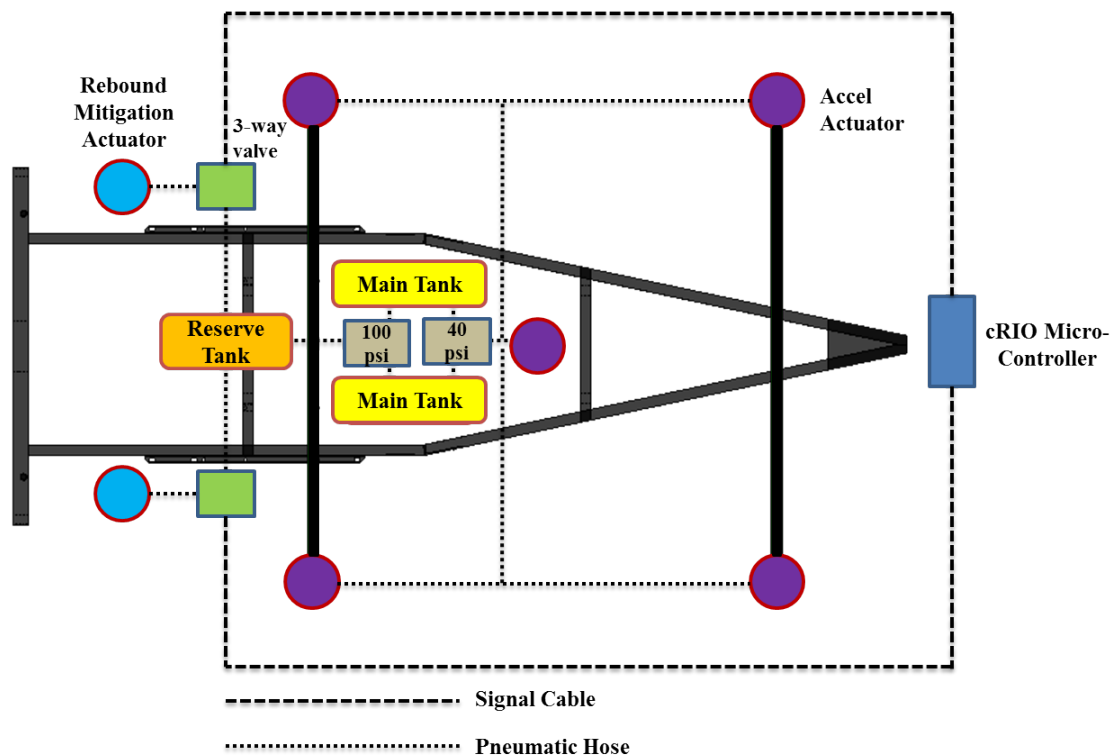


**Figure 5-38: Data Acquisition & Control Schematic**

### 5.3.2 Wireless Stationary Reference Sensors

Wireless stationary references are required to provide relative phase and magnitude information between local tests to permit the integration of the roving and stationary measurement types. The stationary references must be recorded synchronously with the roving trailer measurements. To accomplish this, an independent data acquisition system similar to the one equipped on the trailer was developed.

#### 5.3.2.1 Distributed Data Acquisitions

The distributed data acquisition (DAQ) system of the THMPER system contains a battery power NI cRIO mounted in an environmentally protected case. Each remote DAQ has network capability and is configured to continuously attempt connection to an access point that is housed

in the roving mobile workstation. Once the stationary references sensors are installed data is continuously recorded (typically at a sampling frequency of 3,200 Hz.) and stored locally in 500MB blocks by default. This is a safety precaution so that no data is lost during interruptions to the network stream. The internal storage of each cRIO was expanded from 2 to 30GB using a USB to account for the large amount of anticipated data. The remote DAQ systems published a stream of one second data blocks to a WLAN that allows real time viewing and access to the data using standard TCP/IP communication.

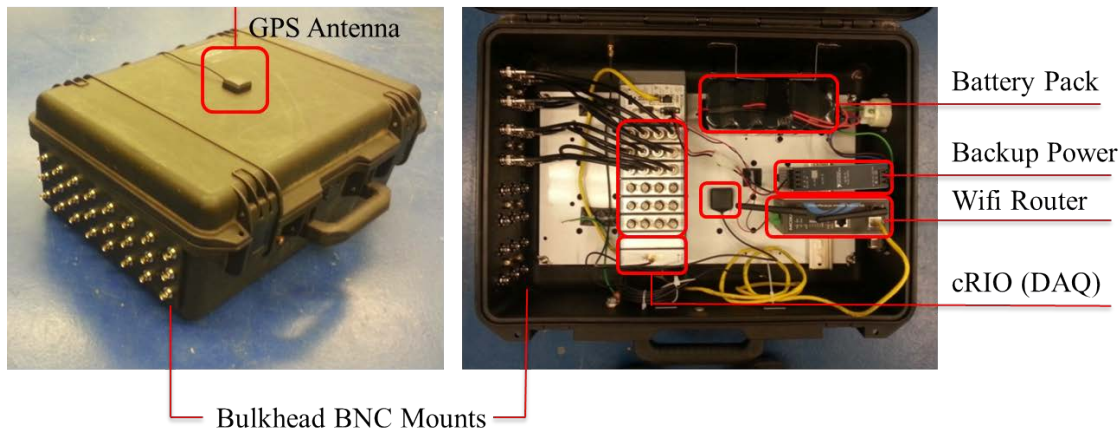


**Figure 5-39: Distributed Data Acquisition Module**

### 5.3.2.2 GPS Synchronization

Time synchronization between the multiple distributed DAQ systems is achieved at the hardware clock level using NI9467 module and the FPGA timekeeper library. The synchronization concept is shown in Figure 5-40. The clock of each cRIO is synchronized using PPS broadcasts from multiple satellites and set to timestamp each acquisition tick in absolute time (UTC standard). PPS accuracy is +/- 99 ns with >99% accuracy typical.

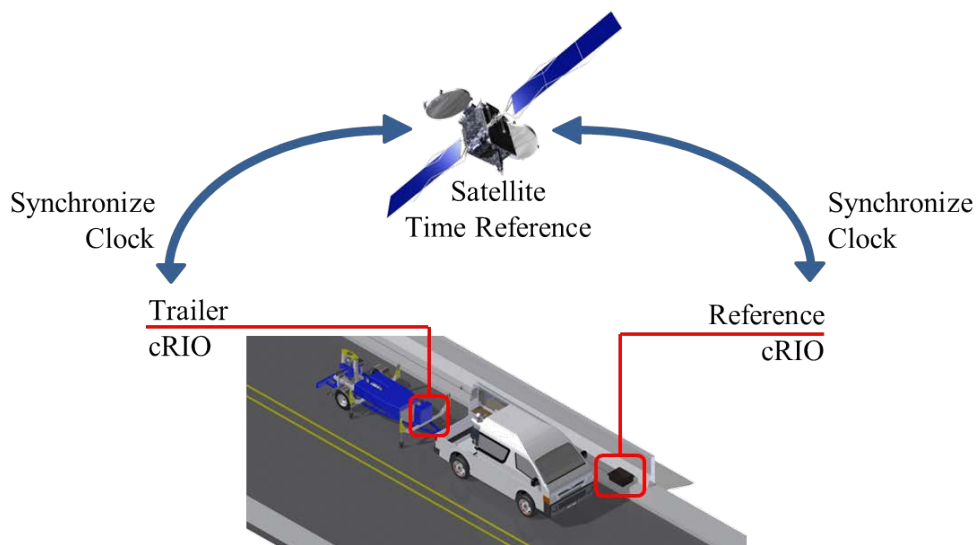


**Figure 5-40: GPS Synchronization Concept**

Per the NI9467 reference manual: After a self-survey, the GPS module uses the known location (computed once on power on) and satellite signals to generate accurate timing signals. Like all GPS receivers, the NI 9467 requires GPS satellite ephemeris and almanac data to compute accurate time and location. The ephemeris is detailed orbital information about each satellite (where each is expected to be at a given time). The almanac data describes the general health of each satellite (for example, the receiver won't use signals from satellites marked as unhealthy) and contains coarse orbit information. The GPS satellites broadcast the ephemeris and almanac data every 30 seconds. Therefore, it usually takes around 30 seconds for it to receive the ephemeris and almanac data and start computing location and timing fixes. The antennas require direct line of site in all directions (360 degrees) down to an imaginary line making a 30 degree angle to the ground. Synchronization performance increases with the number of satellites. During testing +10 are typically located.

### 5.3.2.2.1 Synchronization Benchmark

Two independent remote data acquisition systems were used to benchmark the time synchronization. Once each timekeeper was locked each cRIO was set to run at 3,200 Hz. for ~20 minutes. A third cRIO was used to produce a raw voltage. This voltage was mechanically split and routed to the NI9234 input of each cRIO. Figure 5-41 shows a macro scale of the synchronized signals and Figure 5-42 shows a zoomed in plot of the signal. Each plot was created by plotting the independent time vector saved locally on each cRIO. That is, each signal was plotted with its own, independent variable and not with a shared set of time bins.

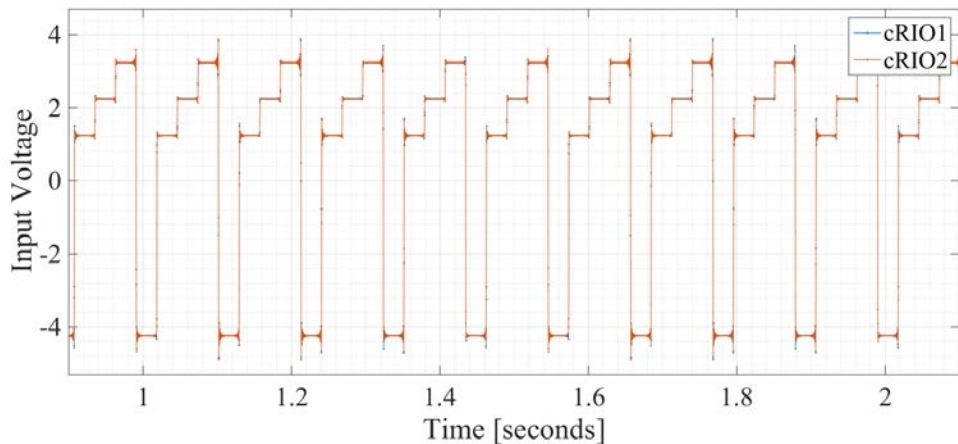


**Figure 5-41: GPS Synchronization – Signal Comparison**

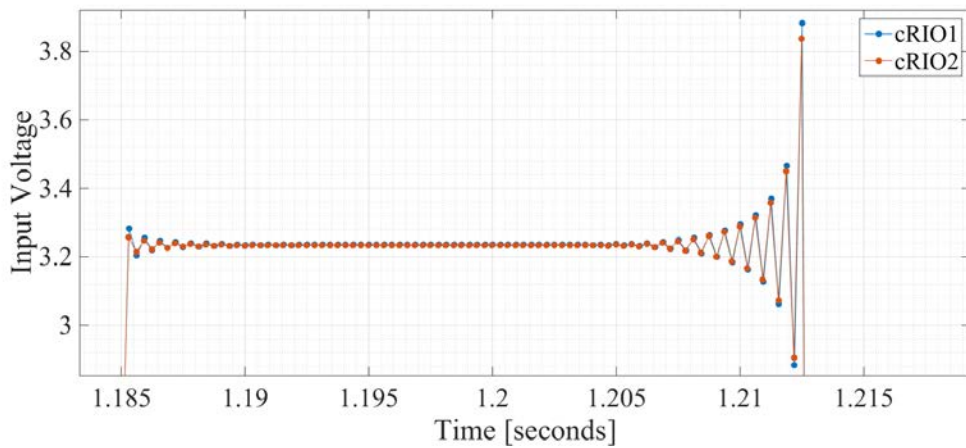


**Figure 5-42: GPS Synchronization – Zoomed Signal Comparison**

Figure 5-43 is a plot of the relative drift between the two cRIOS. The y-scale is plotted in terms of number of samples. The internal clocks drifted at a steady rate of approximately one time step every 240 seconds. When acquiring data at a rate of 3200Hz, this means that (for this benchmark setup and acquisition software version) the sampling between the two cRIOS will differ by 0.0003125 seconds roughly every four minutes. This is not a significant drift over the duration of the short time windows used for impact testing and was deemed acceptable.

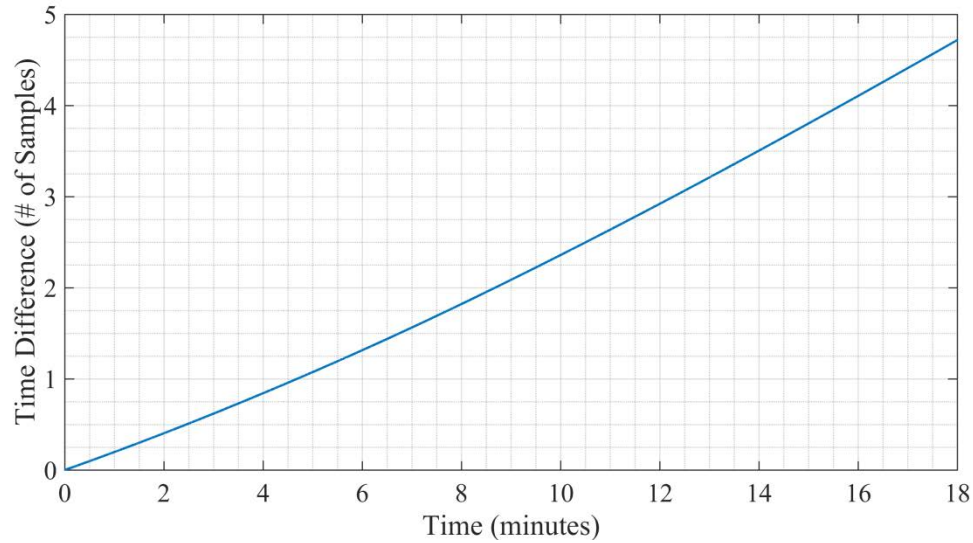


**Figure 5-43: GPS Synchronization – Relative Drift**

## 5.4 Software Systems

The software system of the test trailer has three main tasks:

- Control: The software must interface with the hardware system and provide smooth, reliable operation of the impact source and sensor deployment systems trailer.
- Data Acquisition: The software must be able to acquire experimental vibration measurements. The measurements must be synchronous and the software design consistent (i.e. scalable) for distributed systems application.
- Signal Analysis: Once the data is acquired, the software must have the signal processing and modal parameter identification tools to reduce the experimental data to actionable metrics.

### **5.4.1 Data Acquisition & Controls**

Custom data acquisition code and hydraulic and pneumatic control code is required to remotely operate the mobile trailer and record the induced global vibrations. Autonomous and intuitive control and data acquisition has a key role in accelerating the speed each SIMO test is conducted as well as maintaining safe conditions for the operating engineer (namely, the ability to operate the trailer without being subjected to passing vehicles).

The THMPER system data acquisition and hydraulic and pneumatic control is performed through National Instruments LabVIEW FPGA environment, shown in Figure 5-44. The user selects the sampling frequency, block size, and file name (B1) for each data record at each impact location. The user is then able to stream the data to disk locally in binary format (which is later converted to standard ASCII text format) while operating the trailer. Semi-automated control (B2) consists of the ability to raise and lower both the local sensor array and the impact carriage. Additionally, the mass is raised a variable 12"-18", dropped and autonomously caught by a rebound control system. The mass is then held at apex at apex for 10 seconds to allow an uninterrupted time window. The local six accelerometers, three load cells, and global stationary reference accelerometers are continuously read and displayed (B3) for complete situational awareness for the user.

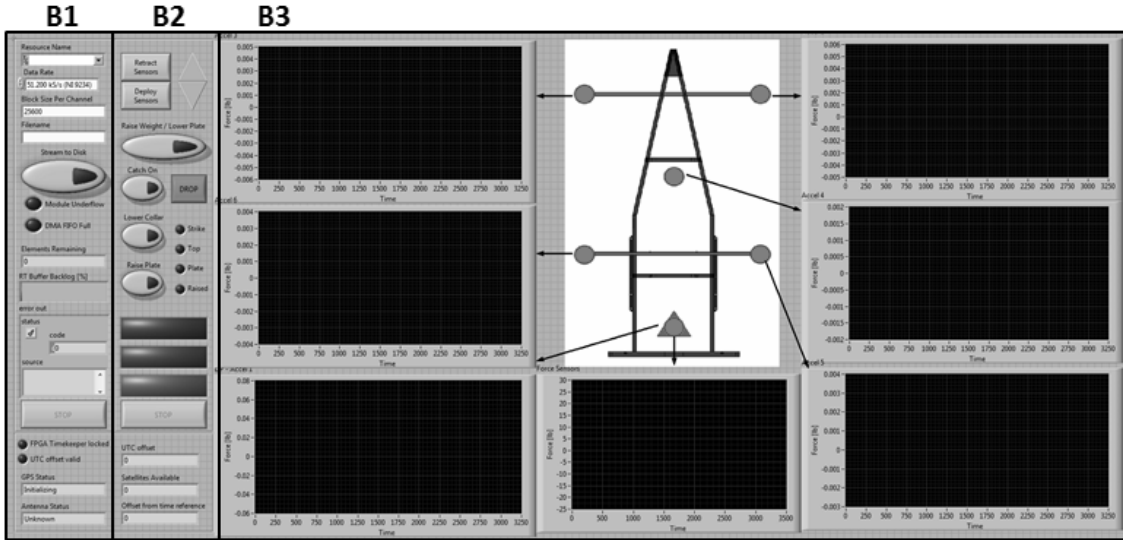


**Figure 5-44: Data Acquisition & Control User Interface Panel**

### 5.4.2 Modal Analysis Tools

Visual Modal Analysis (VMA) is a Graphical User Interface (GUI) program written in Matlab. It is used to perform Experimental Modal Analysis (EMA) signal processing tasks and aims to encapsulate the inner workings of the actual analysis so that the user may focus on interpretation.

#### 5.4.2.1 FE Model Integration

Prior to conducting a test, a series of Matlab/Strand7 API functions are run to extract preliminary information from the Finite Element model. Seen in Figure 5-45, the user selects the file name and path of the Strand 7 model (A1) and selects either the frequency bandwidth or the maximum number of natural frequencies to solve (A2). Once this information is entered, a natural frequency analysis is performed on the model file and displayed (A5). The user may then scroll through the solved modes (A3) which is displayed in scalable (A4) 3d, plan and elevation views (A5). A Modal Assurance Criterion (MAC) analysis is performed on the a priori modal vectors and displayed for the user as well (A6). Additionally, the deck nodal coordinates and unique Strand 7

nodal ID are extracted from the model and saved within the VMA workspace to be used throughout the test. These global model nodes are then used as a master set for all spatial parameters input throughout the testing. THMPER impact locations, local sensor locations, stationary reference sensor locations may then be ‘snapped’ to the FE model nodes to ensure seamless interaction between the experiment and modelling.

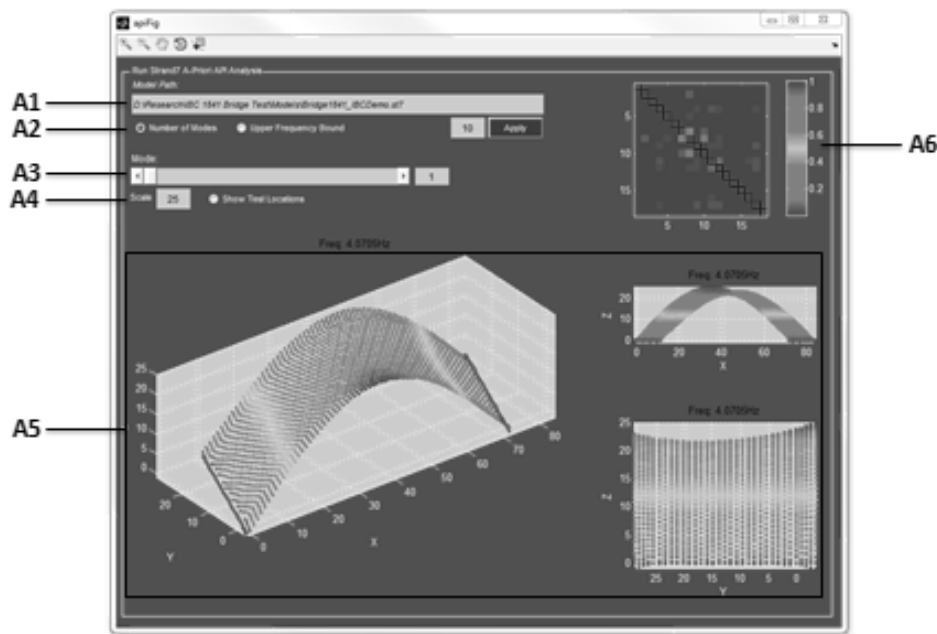


**Figure 5-45: Matlab/Strand7 API Panel**

#### 5.4.2.2 Data Import

The raw data collected at each impact location is then import into VMA (Figure 5-46). The nodal coordinates of the test bridge and all impact locations are continuously displayed (C1) for the user. The coordinates of the local sensor array of the trailer is displayed (C2) and graphed (C3) for the user. Although these coordinates are fixed, this table is editable in case situational

adjustments must be made in the field. This table of local coordinates is then used to snap the orientation and local coordinates of the THMPER to the global coordinates of the test bridge for each impact location. This is entered by the user (C5) in which the driving point measurement on the trailer is the point of reference. Information regarding the stationary global references is input once by the user (C6) and contains a user friendly format for labelling and saving each sensor coordinate a global x and y coordinate, unique degree-of-freedom number and contains orientation and channel information for ease in data import. Data files are then selected by the user (C4) and loaded into the VMA workspace using tables C5, and C6 to pair temporal data with spatial data.

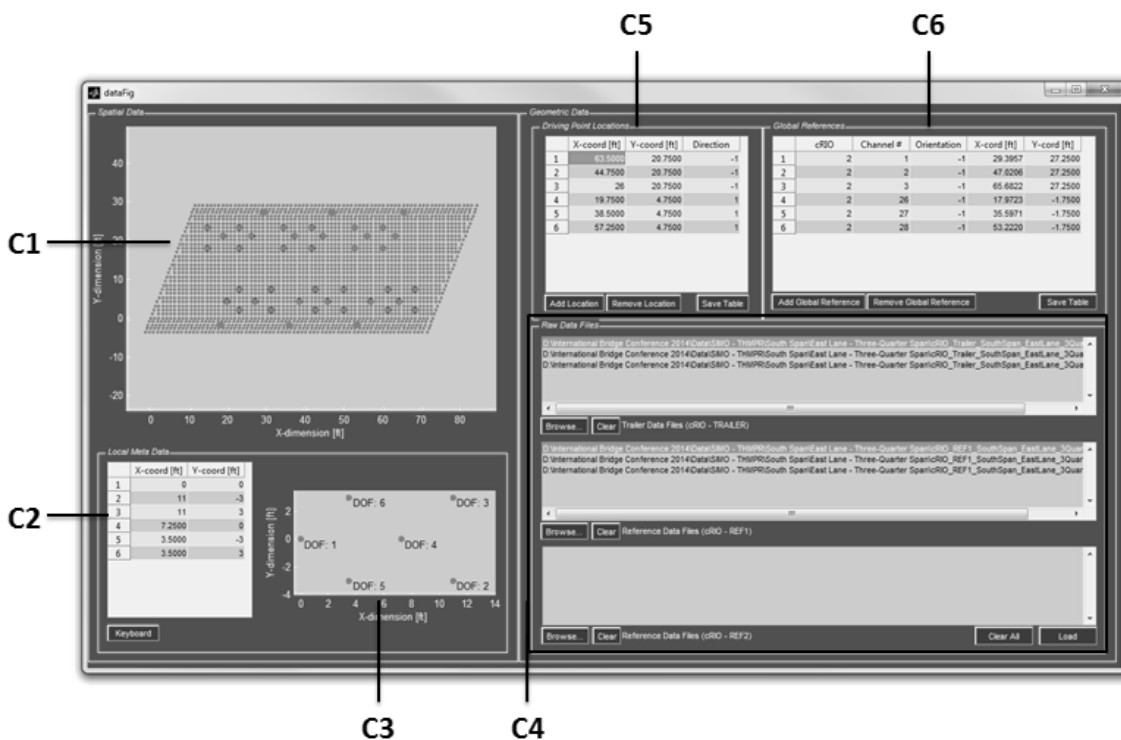


Figure 5-46: VMA File IO Panel

### 5.4.2.3 Semi-Automated Signal Pre-Processing

Upon successful data acquisition at an impact location, the custom software first performs automated data quality checks to vet the data records use for further processing before the trailer is moved to another location. This includes checking for excessive erroneous noise, dropped channels, overloading of the load cells, and proper time synchronization of the independent data acquisitions. Using the pre-processing panel shown in Figure 5-47, the user is then able to navigate the data for each impact location (D1), average number (D2), and sensor number (D3). The time and frequency force information (D6), response time and frequency information (D7) and spatial information (D5) for each selection is displayed for the user. Next, a series of automated filtering and windowing algorithms (D4) can be applied following the current best practice approaches.

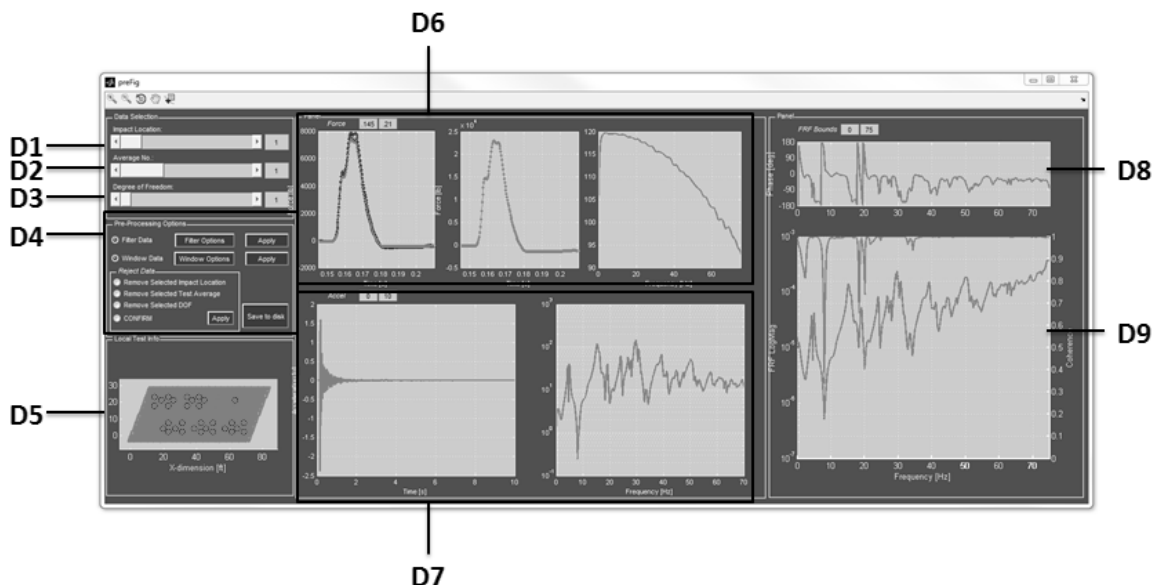
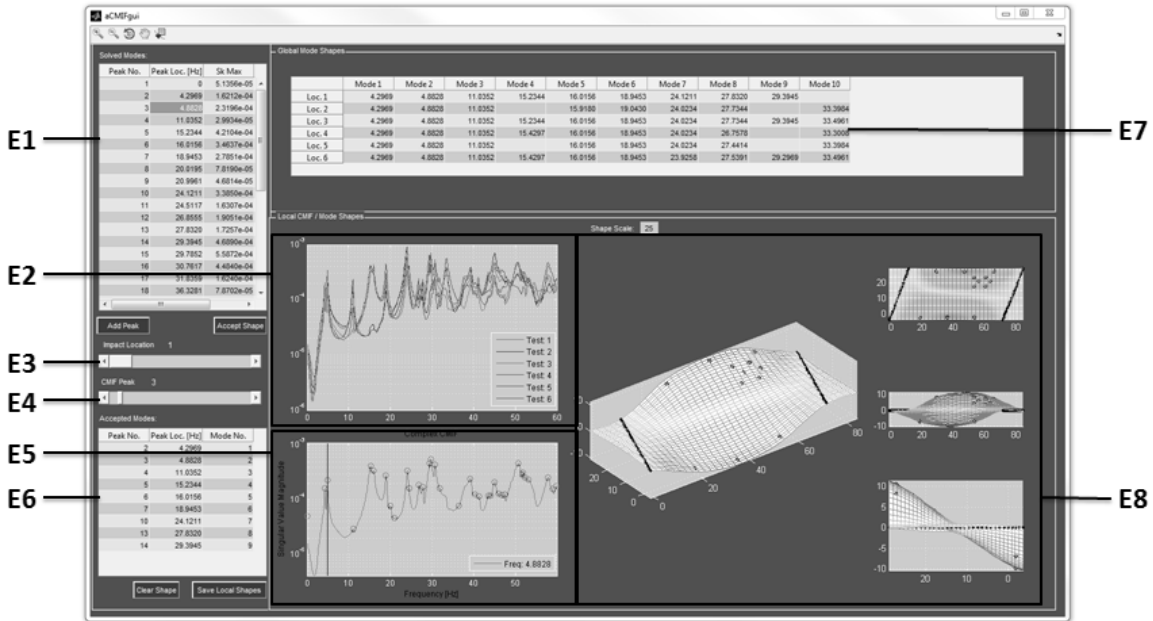


Figure 5-47: VMA – Pre-Processing Panel

The filtering and windowing options are configurable. Filtering typically includes the use of a low-pass Butterworth filter as these filters have low ripple effects within the pass-band. Automated windowing is then performed including a rectangular window on the force signal (utilizing 1/16th cosine taper at the ends of the signal while keeping unity during impact) and an exponential window on the response signals to prevent leakage errors by ensuring the free-decay vibration signal approaches zero at the end of each record. The Frequency Response Function, coherence, and phase (D8/D9) is then autonomously developed and displayed for each degree of freedom (DOF) utilizing the H1 method (as this realistically assumes the majority of noise introduced into the system occurs at the response channels).

#### **5.4.2.4 Semi-Automated Modal Parameter Identification**

Semi-automated modal identification is performed for each impact location via the Complex Mode Indicator Function (CMIF) to extract approximate pole location and mode shapes. CMIF is a spatial domain method typically used for Multi Reference Impact Testing, or multiple-input-multiple-output (MIMO) testing. It is based upon the Expansion Theorem in that it assumes that, at every frequency, the long dimension of the FRF matrix is made up of a summation of modal vectors. The Singular Value Decomposition (SVD) is then utilized to estimate the modal vectors (mode shapes) at each frequency line for each available impact location. The resulting singular values are a measure of dominance of the corresponding modal vector/shape at each frequency line and displayed for each impact location (E2) as well as the selected impact location (E5) with identified candidate peaks. An automated peak picking algorithm identifies and indexes candidate pole locations and corresponding mode shapes. The candidate peak locations are displayed for the user (E1) who is able to scroll through each impact location (E3) and each candidate peak (E4) to display the peak's mode shapes in 3d, plan, and elevations (E8). The user then selects a final set of local pole locations (E6) and assigns global modal rank (E7).



**Figure 5-48: Modal Parameter Identification – CMIF – Shape Selection Panel**

The approximate pole locations are then passed to an Enhanced Frequency Response Function (eFRF) module. The eFRF is a virtual measurement which uses a single degree of freedom model to identify temporal information (poles and scaling) from the spatial information (mode shapes/modal vectors) for each mode identified in the CMIF. The eFRF is formed by pre and post multiplying the FRF by left and right singular vectors respectively for each mode. This is commonly referred to as performing a ‘modal filter’ and enhances a particular mode of vibration. A second order Unified Matrix Polynomial Approach is then used to perform a SDOF least squares fit for each mode and accompanying eFRF. This provides a solution to the damped natural frequencies and modal mass of each synthesized SDOF. Each candidate pole location is displayed (G1) where the user can choose the number of shapes to average (G2), the pole average range (G3), and the number of beta terms (G4). The combination of these parameters produces a synthesized eFRF for each mode which is overlaid with the experimentally measured eFRF in real time (G7). Throughout the analysis the full set (for each mode) of eFRF’s is displayed to the

user for reference (G6). The final set of extracted modal parameters for the master SIMO location is then displayed to the user for final confirmation (G5).

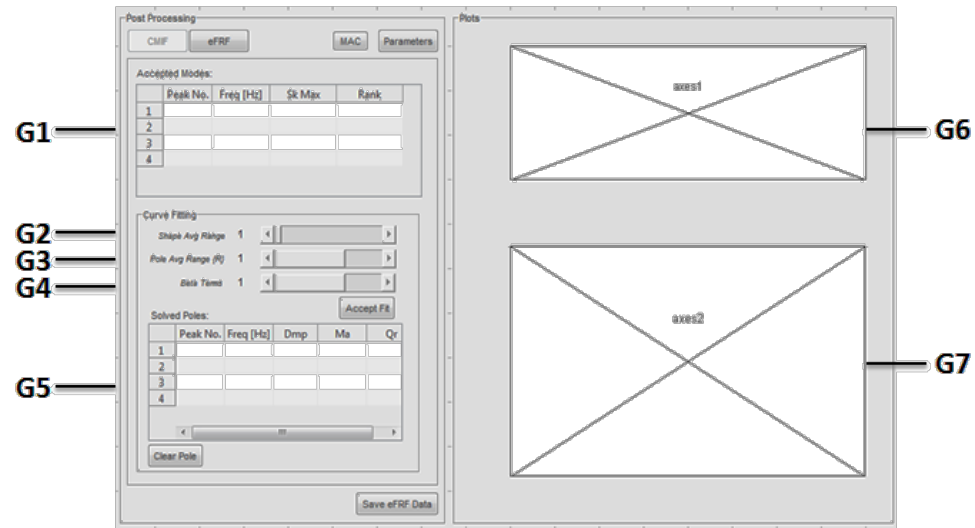


**Figure 5-49: Modal Parameter Identification – CMIF / eFRF – Pole Selection**

## 5.5 Summary of Completed System

A schematic of the prototype THMPER trailer is presented in Figure 5-50. Utilizing an NI cRIO micro-controller and pneumatic actuators, a local sensor array presses spring loaded accelerometer housings onto the bridge deck. A hydraulic lift system then raises an impact carriage with configurable mass and stiffness. The impact carriage is dropped, impacts the bridge deck and rebounds upwards. A sensing/control system utilizing hall sensors detects the impact and triggers fast acting pneumatic actuators which extend upwards to catch the mass, preventing subsequent rebounds. The impact causes a 25,000 – 30,000lb unit impulse force with frequency content between 50 – 65 Hz. During testing, an independent data acquisition system utilizing GPS synchronized records acquires several stationary accelerometers to use as spatial and modal references for post processing analysis. Several impact sequences are performed in a rapid succession at each location for averaging during FRF development and, once completed, the mobile sensing array is raised and the trailer is towed to a new location on the bridge deck.

The primary components of the test trailer consist of:

- A single, repeatable impact device with focused frequency band
- A robust, mobile, rapidly deployable sensing array
- An integrated data acquisition and machine control system
- A wireless, GPS synchronized remote sensing and data acquisition system

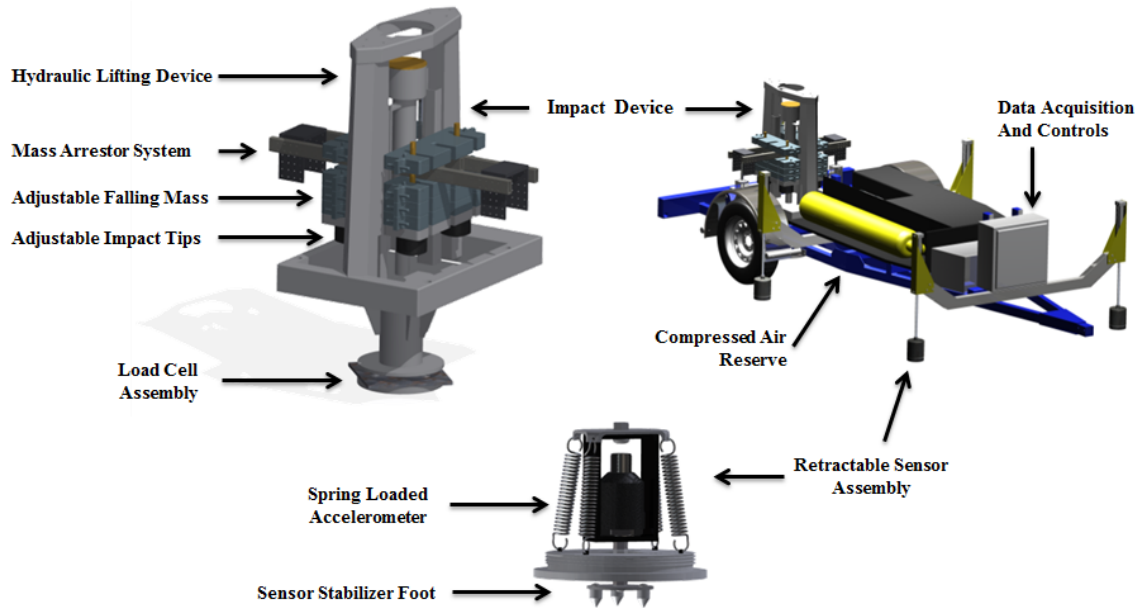


Figure 5-50: THMPER System – Trailer Subsystem Components

## CHAPTER 6: Overview of Field Validation Case Study

### 6.1 Introduction

The previous chapters detail the system design and component level verification. Verification of each system and subsystem design requirements only ensures that the design specifications were met. It does explicitly guarantee that the produced system effectively meets the intended purpose.

The system validation plan, outlined in the ConOps, was used to guide the experimental design of the Mossy Creek Bridge tests. Field test objectives included:

- ***MRIT for EMA benchmark*** – The system validation plan requires the THMPER system be evaluated against the current ‘best practices’ in forced vibration. The instrumented sledge is used as this benchmark and the estimated modal parameters recovered from each experimental and analytical method are compared.
- ***Assessment of travel capabilities*** - Bridge is located far away. THMPER to be driven to the bridge and an assessment on the durability performed on arrival.
- ***Assessment of system operation***- The THMPER system experiment and analysis will be compared to a traditional ‘best practices MRIT’ using the following measures:
  - *Durability*
  - *Test time*
  - *Instrumentation Effort*
  - *Test Execution Effort*
  - *Data Quality/Completeness*

- ***MRIT Benchmark Comparison*** – MRIT will be used as the benchmark comparison as it represents the standard excitation method used for impact tests performed on highway bridges.
- ***Obtain Field Calibrated Load Rating*** – A field calibrated load rating is desired. Since the translation between dynamic testing and static load predictions is still a research endeavor, a static truck load test shall be used as the ‘ground truth’. The modal parameters of each dynamic testing method will be used to correlate a FE model. The FE models will be used to predict the displacements of the known truck wheel loads which will be compared to the ground truth measurements.
- ***Recommendations for future tests*** – Get feedback regarding operations and maintenance, changes and upgrades (hardware and software), and assess the system’s capabilities and applicable improvements.

## 6.2 Description of Bridge

The Mossy Interchange Bridge is located in Mossy, West Virginia. It was built in 1954 and at the time of testing, the structure was posted for load and recorded as being structurally deficient. The bridge carries local route 612 across Paint Creek. The 2013 NBI database lists an ADT of 2100. In addition, the bridge is a key link, connecting numerous mines to the turnpike. As such, it sees considerable heavy truck traffic that is transporting mined material.



**Figure 6-1: Load Posting**

Mossy Interchange Bridge is located in Mossy, West Virginia, just off the West Virginia Turnpike (I-77). The structure is a 3-span, simply supported steel stringer bridge with a cast-in-place composite concrete deck. The spans are comprised of five girders spaced at 8'-0" and have zero skew. The center span is approximately 52 feet long with 2 rows of internal diaphragms spaced at 17'-2" and oriented perpendicular to the girders. The two external spans are approximately 20 feet long and have diaphragms only at the supports.

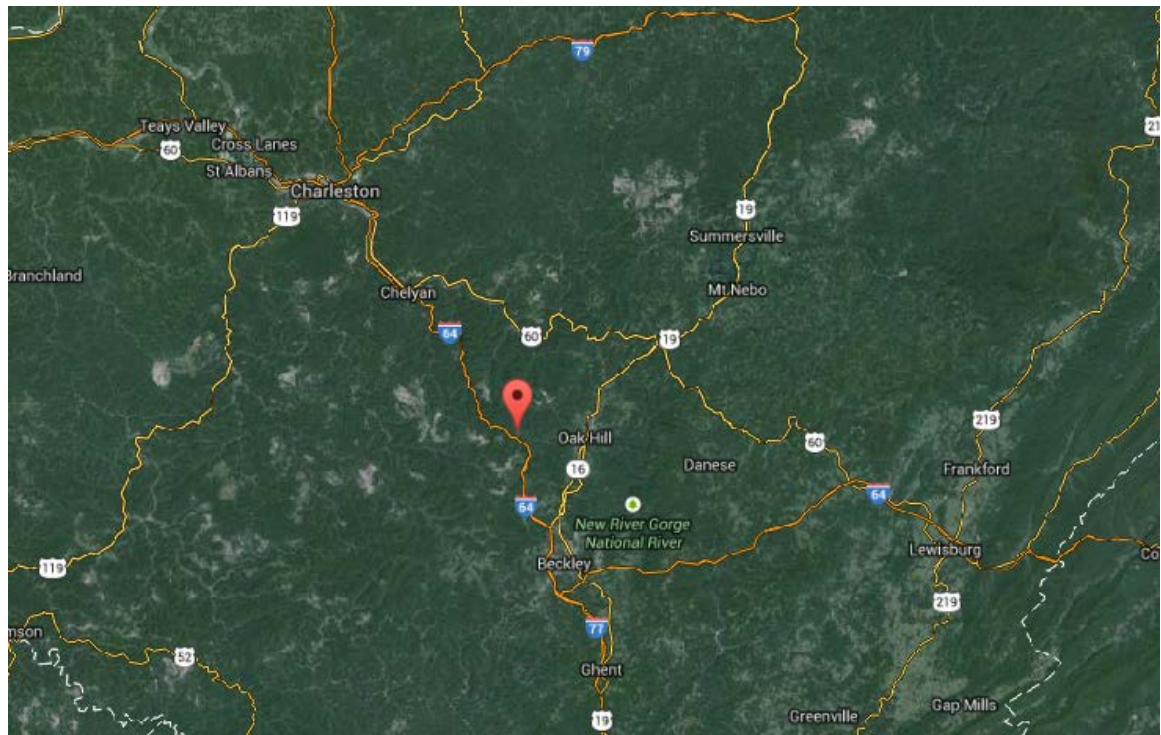


Figure 6-2: Regional Location of Test Site

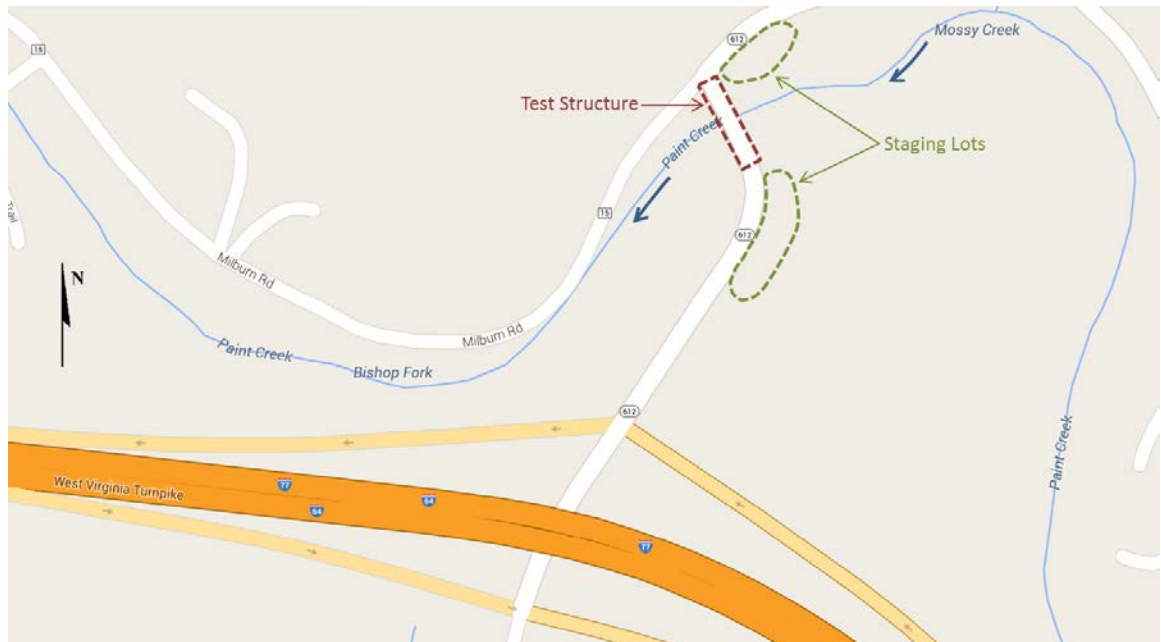


Figure 6-3: Position of Test Structure and Staging Zones



**Figure 6-4: Bridge Topside**



**Figure 6-5: Bridge Underside**

### 6.3 On-site Observations

Figure 6-6 shows the typical deterioration found on the deck of the center span. The photograph was taken at the pinned side of the center span, above Pier 2. Several portions of the deck have exposed rebar that was likely the result of punch through from heavy trucks. The plans specify a deck thickness of 7" with no overlay specified. The inspection reports indicate the presence of an LMC overlay which is not specified in the original plans. However, the exposed rebar reveals that this was most likely an error in the inspection report as it is not at the appropriate depth.

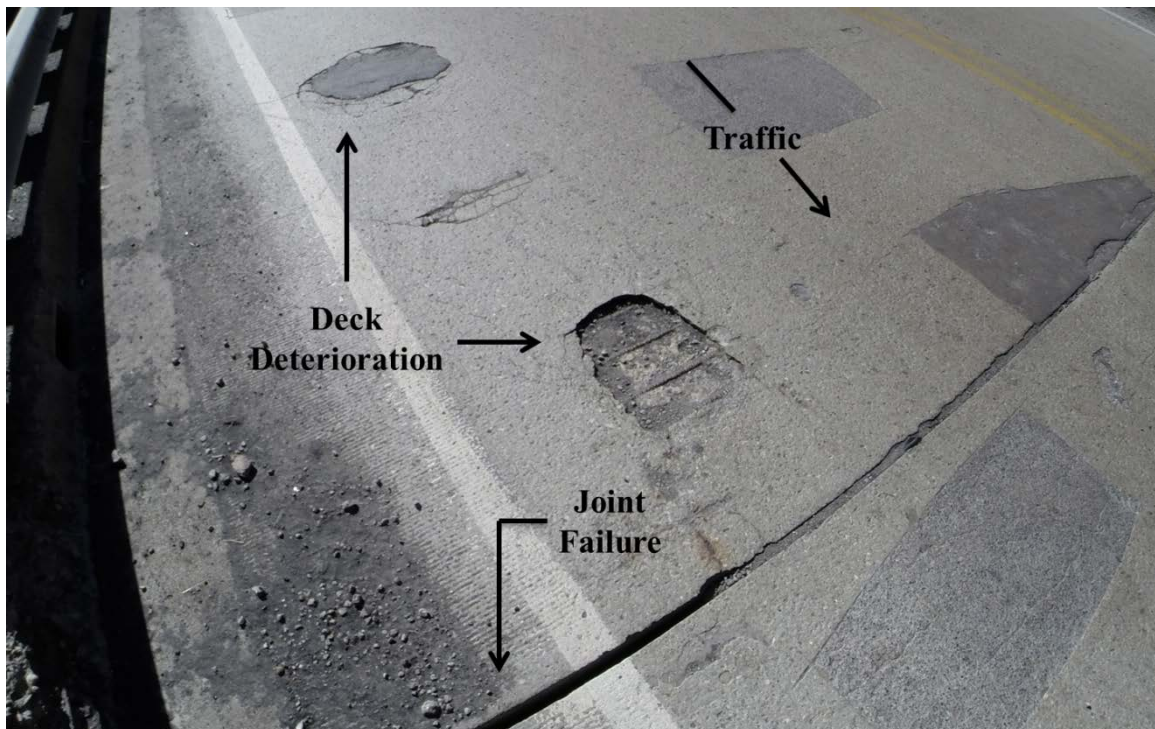


**Figure 6-6: Center Span Deck Deterioration**

The southern end of the center span rests on steel rocker bearings, while the northern end rests on pinned bearings. These bearings are supported by reinforced concrete hammerhead piers. Several

bearings were heavily corroded (Figure 6-8, Figure 6-9) while others were in relatively good condition (Figure 6-7). The corrosion is likely due to the failure of deck seals in the expansion joints. Furthermore, a bearing on the norther exterior span over the pier was observed to have lost connection to the superstructure. While this “floating” bearing is not a threat to bridge integrity, it is indicative of the significant corrosion present.



**Figure 6-7: Expansion Bearing at Interior Girder – Pier 1**



**Figure 6-8: Deterioration of Exterior Expansion Bearings at Pier 1**



**Figure 6-9: Center Span (Far) and Side Span (Near) Exterior Expansion Bearings at Pier 2**

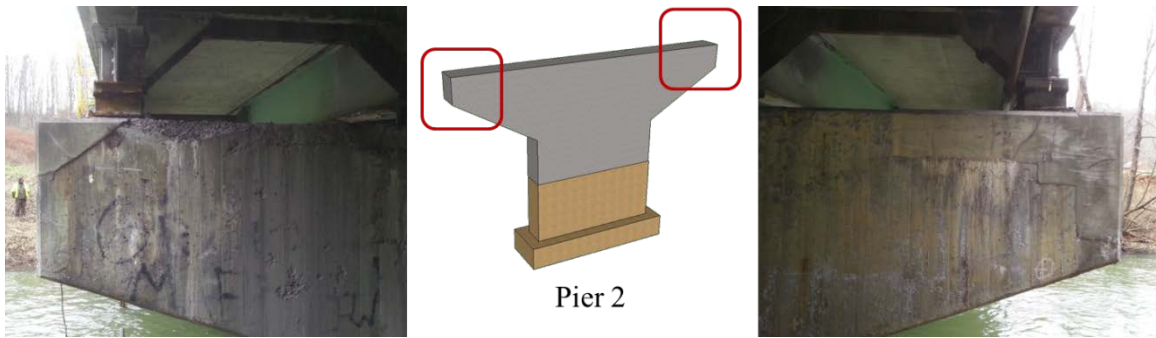


**Figure 6-10: Repairs at Pinned Bearing Pier**

## 6.4 A Priori Modeling

### 6.4.1 RAMPS Overview

The RAMPS (Rapid Automated Modeling and Performance of Structures) software includes three main modules packaged within a single graphical user interface that leverage the application programming interface between Matlab (computational tool) and Strand7 (FE modeling software) for model creation and calibration. The first module provides assistance to the user in the semi-automatic creation of an FEM bridge model. Given the somewhat regular and symmetric geometries of common highway bridges, details such as roadway geometry, girder type and spacing, cross-bracing configuration, and bearing type may be used to create a 3D geometric FE model using shell and beam elements and rigid links. The second module provides users simplified model-experiment calibration of various uncertain parameters. Because of the close integration of the THMPER and RAMPS systems, uncertain parameters may be efficiently updated using natural frequencies and mode shapes. The Third module provides the user with the ability to simulate dead load and truck live loads and extract bridge responses. These responses are used to produce a refined AASHTO Load and Resistance Factor Rating (LRFR) of the structure which may then be compared to its counterpart line-girder rating also produced through the software.

#### 6.4.2 FE Model Creation

A finite element model of the bridge was created utilizing the RAMPS software that is part of the THMPER system. Figure 6-11 illustrates the general element-level model construction. Prior to the test, Drexel University received plans of the test structure. Using these plans and the RAMPS GUI, an element-level FEM model of the bridge was created. Upon arrival on site, the model dimensions and plans were checked against *in situ measurements*; no changes to the model were required.

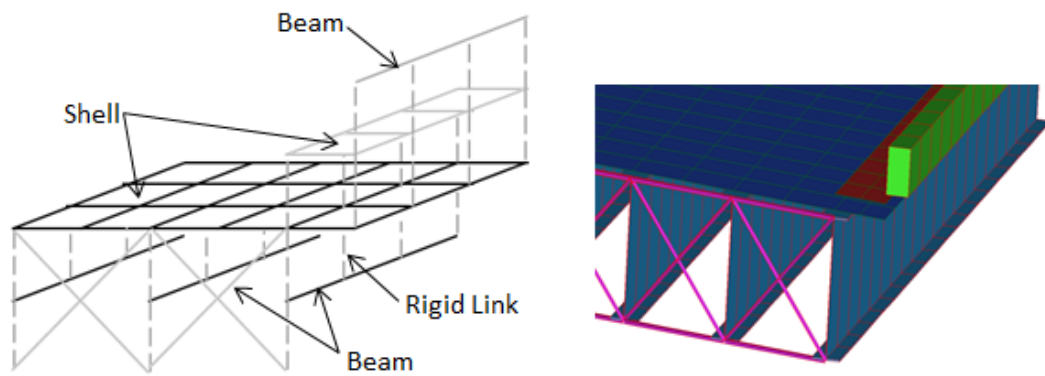


Figure 6-11: Schematic of FEM Bridge Model Developed with RAMPS

## CHAPTER 7: MOSSY INTERCHANGE BRIDGE TESTS

This chapter presents the system validation case study where two forced vibration tests and one static truck load test were used to perform St-Id on a steel stringer bridge located in West Virginia.

### 7.1 Forced Vibration Tests

Two dynamic tests were performed on December 6<sup>th</sup> and 7<sup>th</sup>, 2014. The tests consisted of a traditional MRIT using an instrumented sledge hammer and the THMPER system. The distributed data acquisition (DAQ) system developed for the THMPER system was used for both vibration tests. The THMPER system used a combination of the two remote distributed DAQs, and a single, cabled DAQ was used during the sledge MRIT.

#### 7.1.1 MRIT Benchmark

##### 7.1.1.1 Instrumentation Plan

The MRIT benchmark test was performed using a PCB model 086D50 instrumented sledge hammer and 25 PCB 393A03 accelerometers. A total of twenty-five accelerometers were installed along the underside of the center span. A Hydra Platform truck (Figure 7-60) was required to access the underside of the bridge as local rain storms had caused significant flooding of the creek below. Using the hydra platform, five accelerometers were installed along each girder using magnets and the cables were routed longitudinally to Pier 1 where a battery powered, distributed data acquisition (DAQ) system was located. The DOF were equally spaced at 8'-7" and are shown in Figure 7-1. The impact locations were chosen at areas of high modal amplitude for all modes of interest, ensuring preservation of data quality and signal to noise ratios.

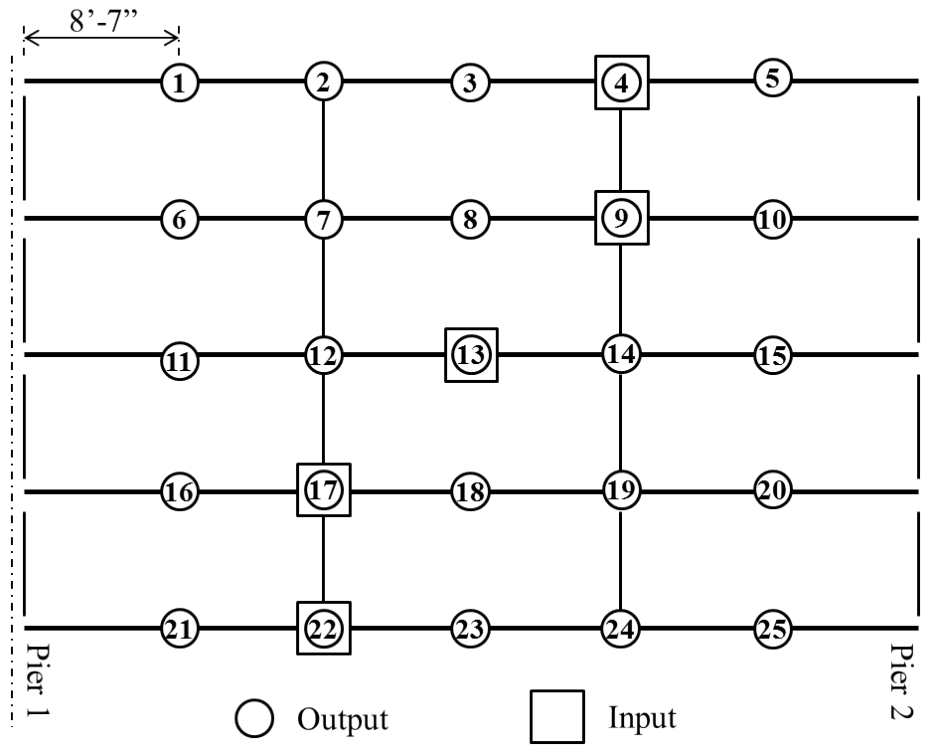


**Figure 7-1: Benchmark MRIT – Instrumentation Plan**

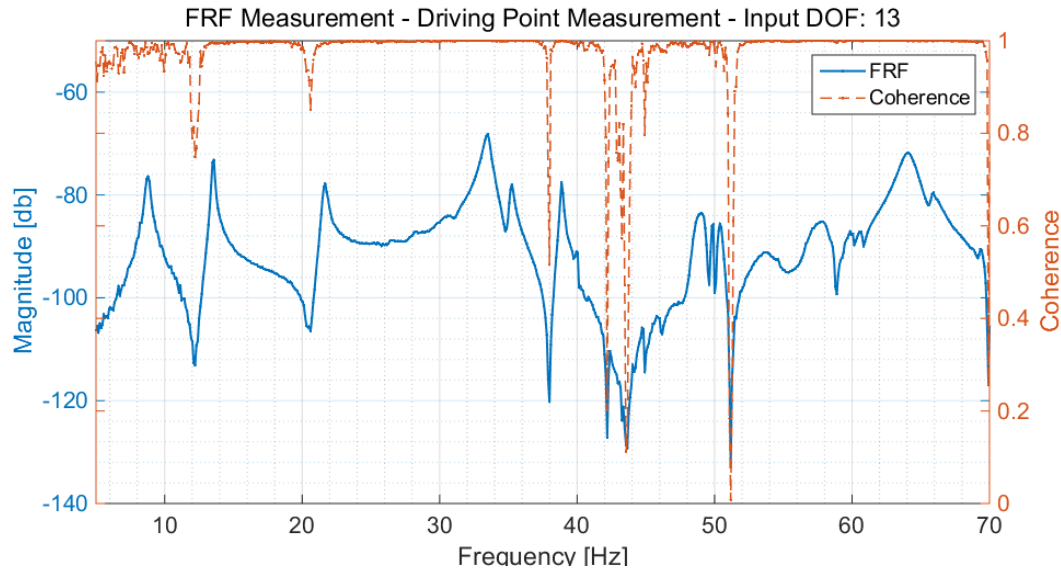
### 7.1.1.2 Test Execution

The sledge was used to excite the bridge at five, spatially varied input locations. Data was sampled at a frequency of 3,200 Hz. and time windows were acquired for ten seconds post impact. A minimum of three impacts were performed at each input location for averaging during FRF estimation.

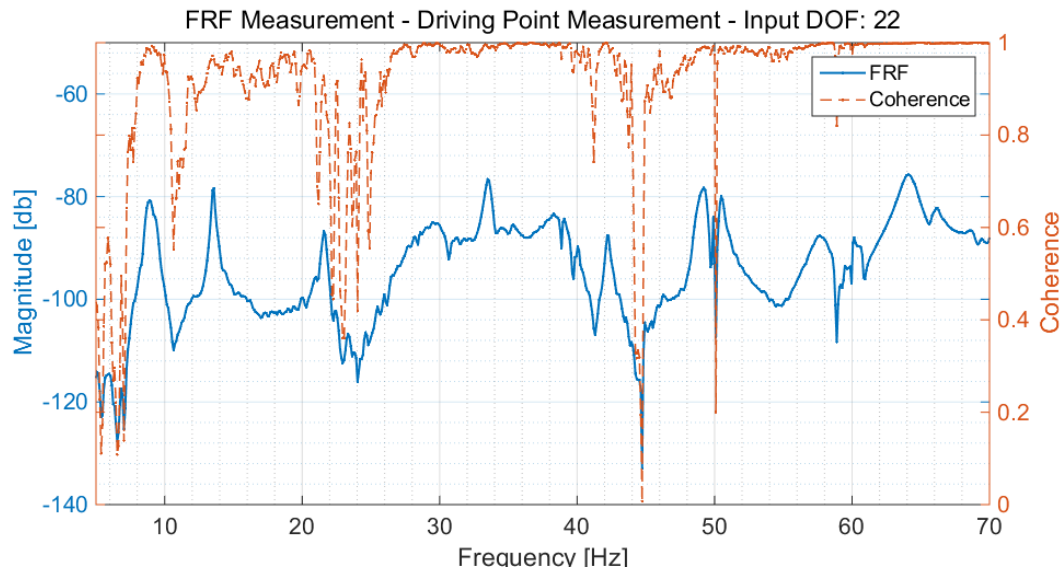
### 7.1.1.3 FRF Measurements

Figure 7-2 shows the FRF measurement of the center span, center girder (DOF 13) driving point measurement with Coherence plotted as a function of frequency. Figure 7-3 shows the same plot for the DOF 22 driving point records. In general, the sledge excited all modes of interested, and due to the number of averages used erroneous noise was significantly reduced as can be seen in

the Coherence levels at areas of resonance. The FRFs show clear, smooth peaks of resonance indicating proper sampling of the structure's characteristic space.



**Figure 7-2: Sledge MRIT – FRF – Driving Point at DOF 13**



**Figure 7-3: Sledge MRIT – FRF – Driving Point at DOF 22**

Figure 7-4 shows the reciprocity of input/output at DOF 9 and DOF 17, and Figure 7-5 shows the reciprocity of input/output at DOF 4 and DOF 22. There were several abnormalities in the data (e.g. miss matched amplitudes at several frequencies) that is likely attributed to input from the side spans or substructure. However in general the structure generally exhibited linear behavior throughout the sledge MRIT testing.

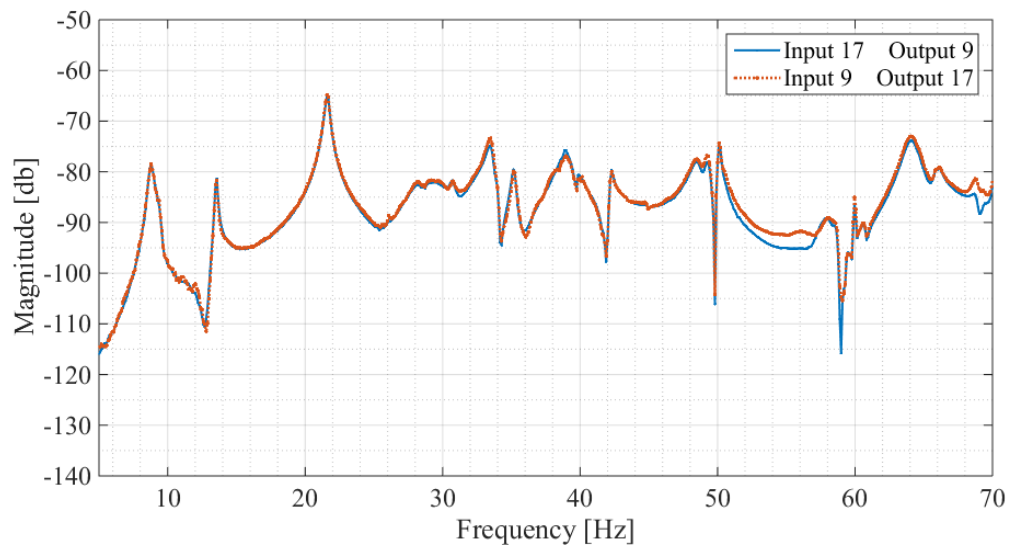


**Figure 7-4: Sledge MRIT – Reciprocity – DOF 9 & 17**

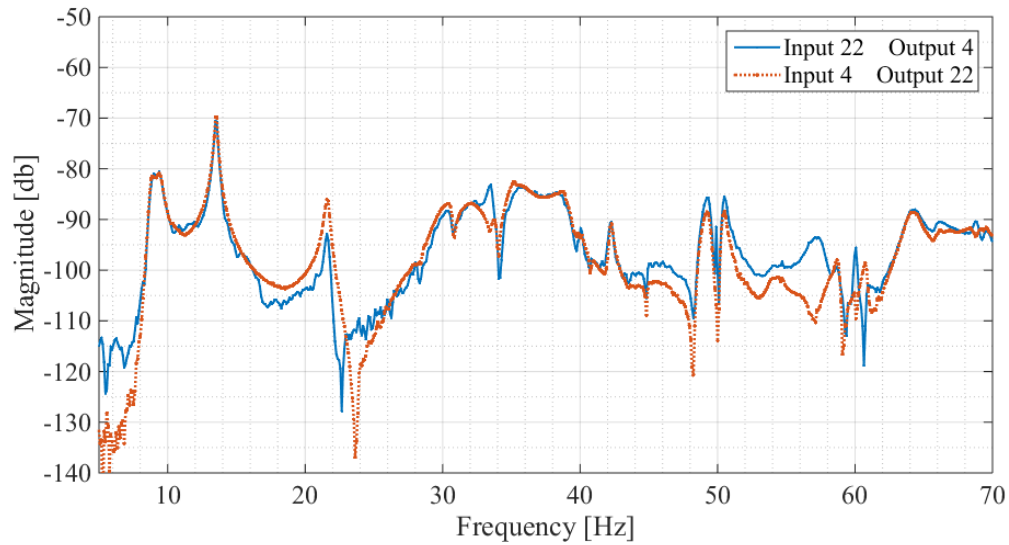


**Figure 7-5: Sledge MRIT – Reciprocity – DOF 4 & 22**

#### 7.1.1.4 Parameter Identification

The smallest dimension of FRF determines the number of available solutions at each frequency line. The left singular vector consists of the twenty five output DOF, and the right singular vector consists of the five input DOF. The CMIF is the plot of the five singular values as a function of frequency. The CMIF for the MRIT Sledge benchmark is shown in Figure 7-6. The peaks of the CMIF indicate resonance and the candidate poles are indicated in red. Note that not all peaks are due to resonance.

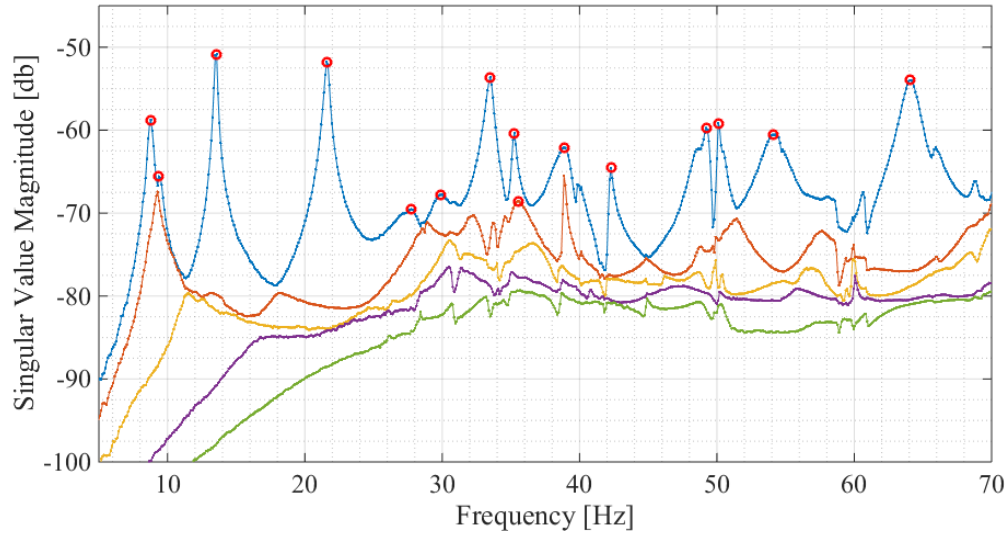


**Figure 7-6: Sledge – MRIT – CMIF**

#### 7.1.1.4.1 Shape Estimation

The first eight global mode shapes were selected from the left singular vectors of fifteen candidate peaks identified in the CMIF and are shown in Figure 7-7 through Figure 7-14. The shapes appear symmetric and do not indicate any major superposition pollution from adjacent modes.

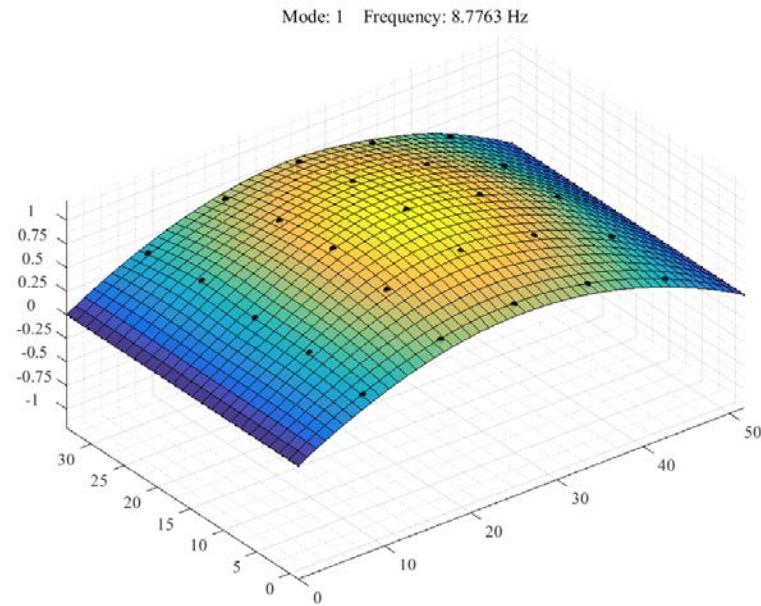


**Figure 7-7: Sledge MRIT – Mode 1**

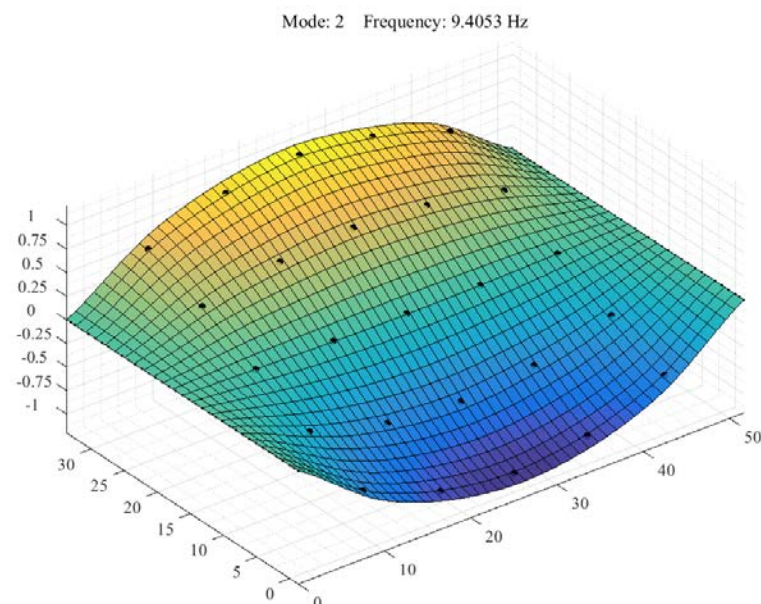


**Figure 7-8: Sledge MRIT – Mode 2**

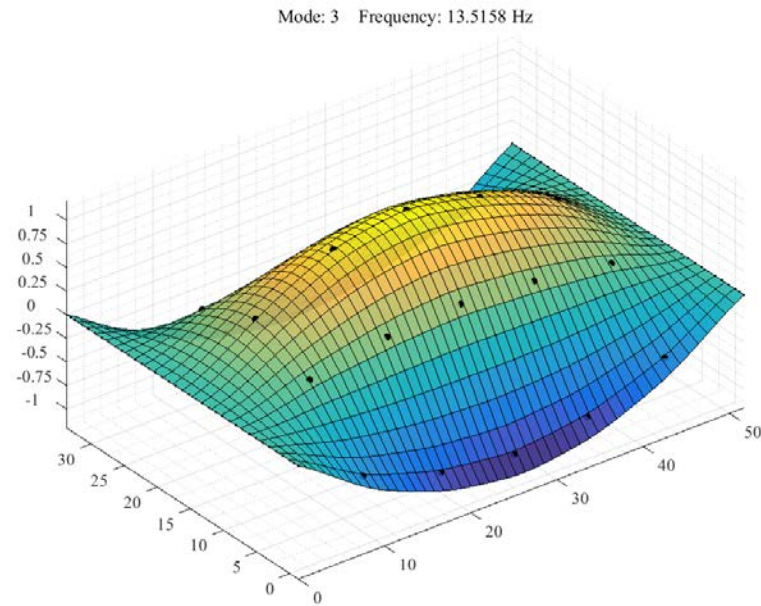


**Figure 7-9: Sledge MRIT - Mode 3**

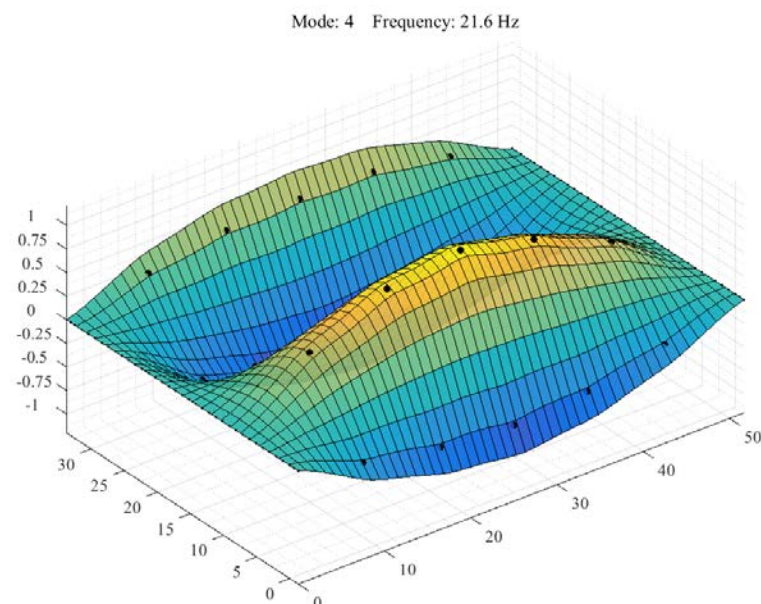


**Figure 7-10: Sledge MRIT – Mode 4**

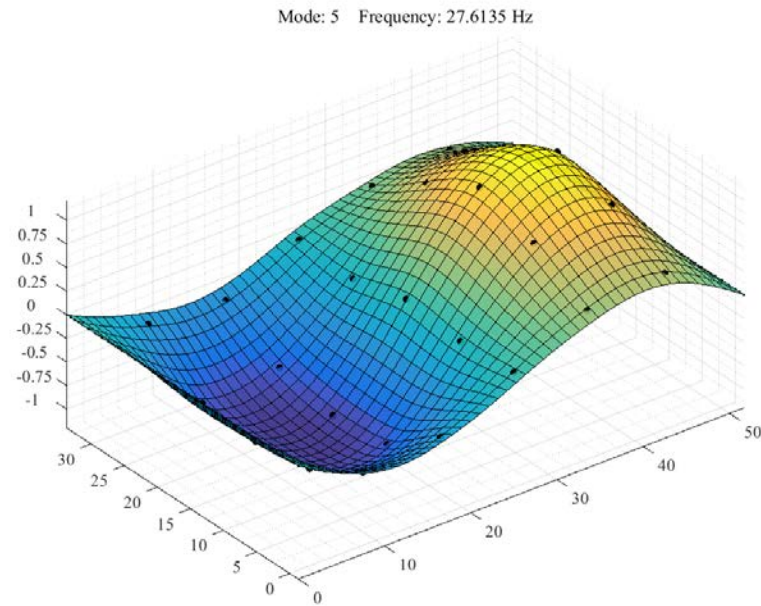


**Figure 7-11: Sledge MRIT - Mode 5**

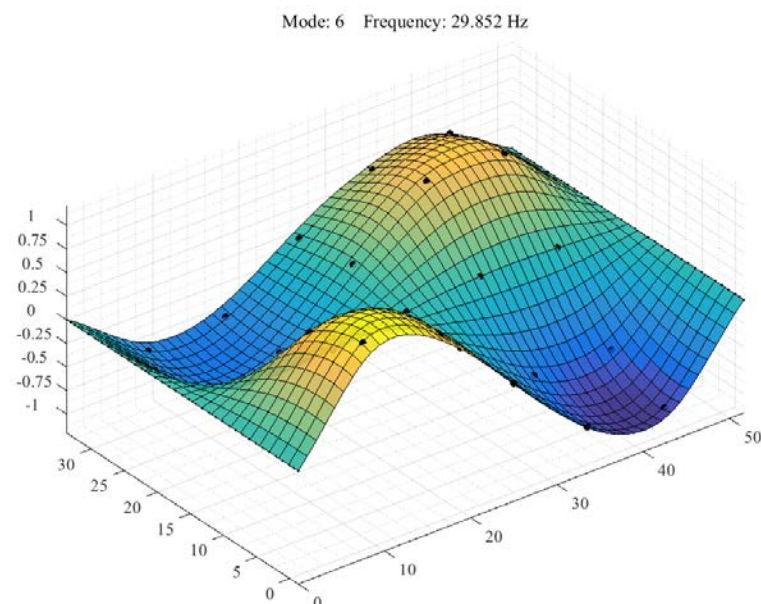


**Figure 7-12: Sledge MRIT – Mode 6**

Mode: 7 Frequency: 33.442 Hz

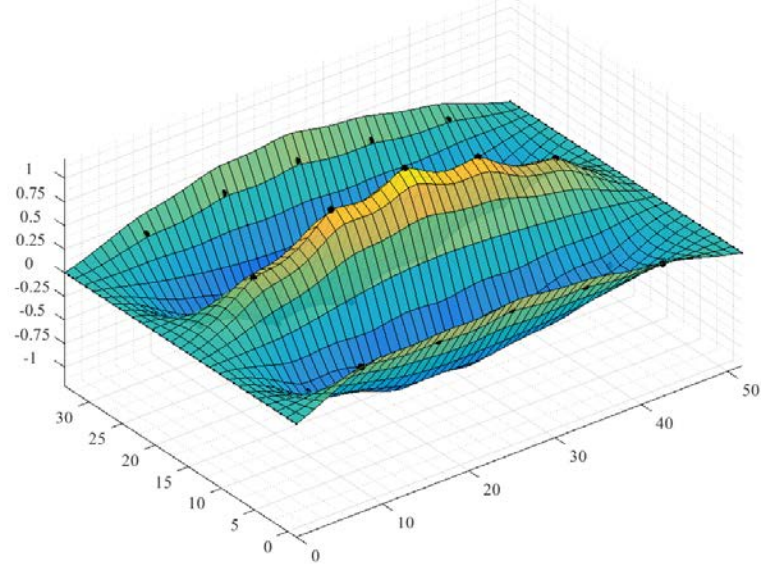


**Figure 7-13: Sledge MRIT – Mode 7**

Mode: 9 Frequency: 35.6183 Hz

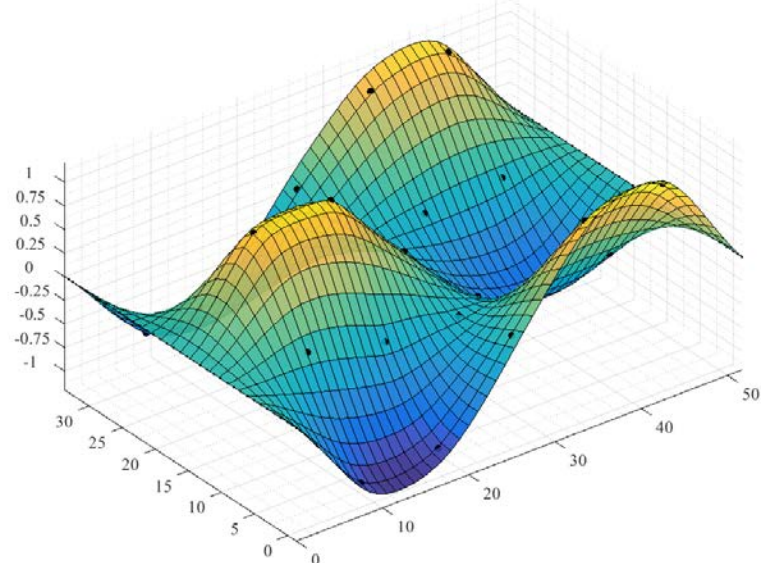


**Figure 7-14: Sledge – MRIT – Mode 8**

The MAC values for the first eight modes are shown in Figure 7-15 and Table 7-1. The shapes are unique and demonstrate orthogonal properties to one another indicating adequate spatial resolution.

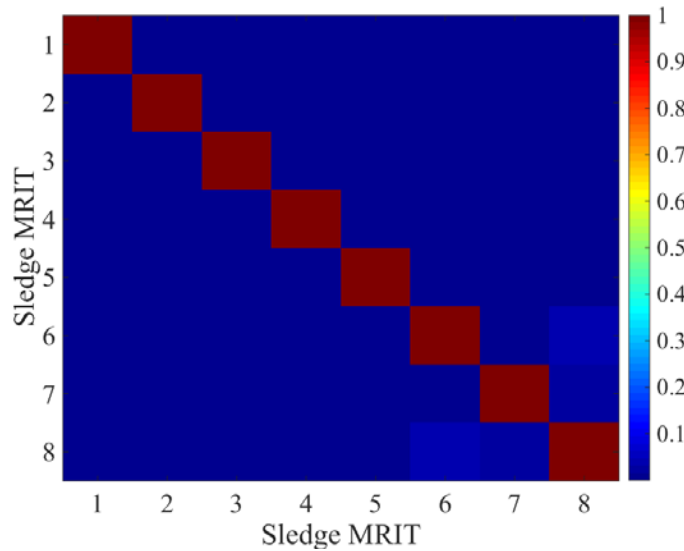


**Figure 7-15: Sledge MRIT – MAC Values**

**Table 7-1: Sledge MRIT – MAC Values**

<b>Mode</b>	<b>1</b>	<b>2</b>	<b>3</b>	<b>4</b>	<b>5</b>	<b>6</b>	<b>7</b>	<b>8</b>
<b>1</b>	1.0000	0.0054	0.0110	0.0002	0.0012	0.0000	0.0012	0.0003
<b>2</b>	0.0054	1.0000	0.0000	0.0030	0.0019	0.0001	0.0003	0.0000
<b>3</b>	0.0110	0.0000	1.0000	0.0012	0.0007	0.0001	0.0002	0.0001
<b>4</b>	0.0002	0.0030	0.0012	1.0000	0.0000	0.0005	0.0053	0.0007
<b>5</b>	0.0012	0.0019	0.0007	0.0000	1.0000	0.0109	0.0056	0.0015
<b>6</b>	0.0000	0.0001	0.0001	0.0005	0.0109	1.0000	0.0023	0.0387

<b>Mode</b>	<b>1</b>	<b>2</b>	<b>3</b>	<b>4</b>	<b>5</b>	<b>6</b>	<b>7</b>	<b>8</b>
<b>7</b>	0.0012	0.0003	0.0002	0.0053	0.0056	0.0023	1.0000	0.0210
<b>8</b>	0.0003	0.0000	0.0001	0.0007	0.0015	0.0387	0.0210	1.0000

#### 7.1.1.4.2 Pole Estimation

The left and right singular vectors for the eight modes identified from the CMIF were used as a modal filter for the formulation of the eFRF. The eFRF for each mode was then curve fit using a second order unified matrix polynomial approach. The estimated natural frequencies and percent critical damping are summarized in Table 7-2.

**Table 7-2: Sledge MRIT – Natural Frequencies and Damping**

<b>Mode</b>	<b>Frequency [Hz]</b>	<b>Damping [% critical]</b>	<b>Mode Shape Type</b>
1	8.78	2.17	1st Bending
2	9.41	3.77	1st Torsion
3	13.52	0.71	1st Butterfly
4	21.60	0.84	2nd Transverse Bending
5	27.61	4.83	2nd Bending
6	29.85	3.68	2nd Torsion
7	33.44	0.85	3rd Transverse Bending

8	35.62	3.25	2nd Butterfly
---	-------	------	---------------

The eFRF estimates for the first four modes is shown in Figure 7-16. The first and second mode are highly coupled and closely spaced, only ~6 frequency bins apart. However, the spatial resolution of the left and right singular vectors was sufficient in decoupling each modes SDOF contribution to the FRF. The individual eFRF curve fits for the first four modes are shown in Figure 7-17 through Figure 7-20. From these plots it is evident that the spatial resolution of the left and right singular vectors as well as the curve was sufficient in decoupling each modes contribution to the FRF into SDOF components.

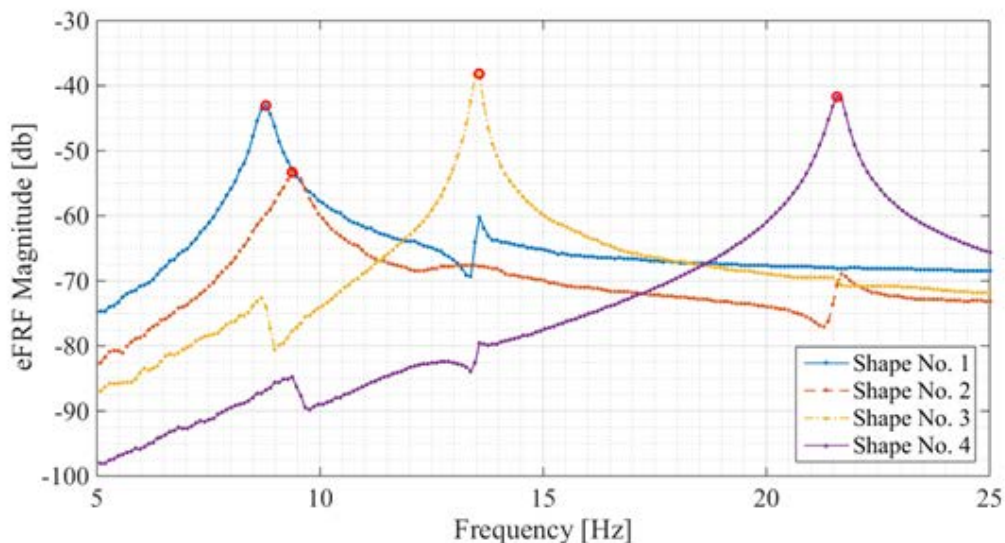


**Figure 7-16: Sledge MRIT – eFRF Estimates for Modes 1 - 4**

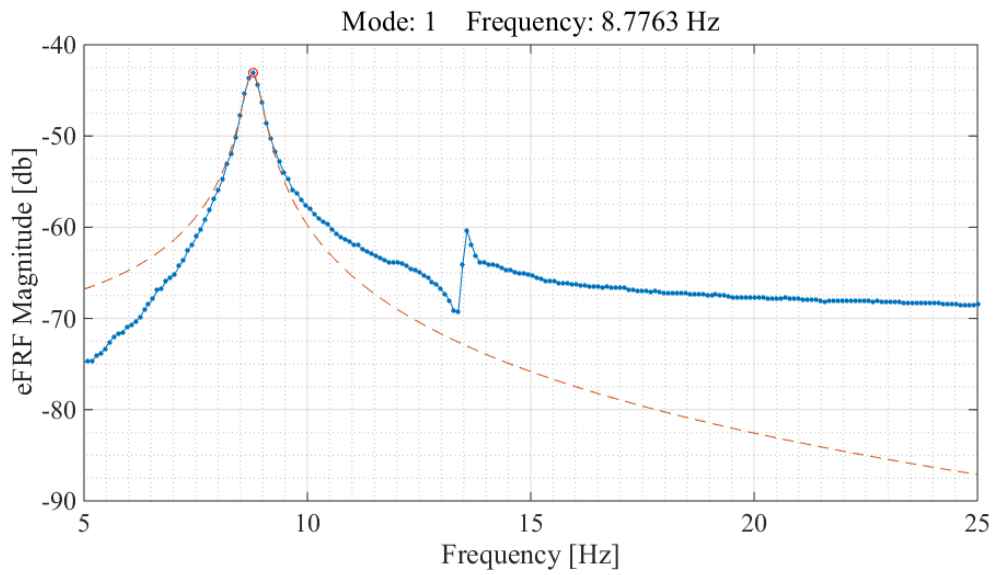


**Figure 7-17: Sledge MRIT – eFRF Fit – Mode 1**

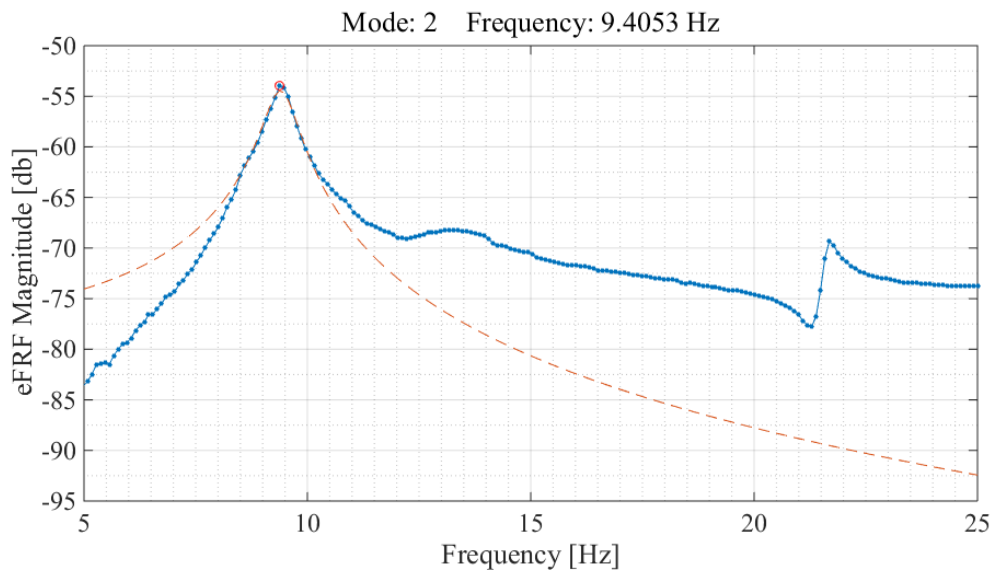


**Figure 7-18: Sledge MRIT – eFRF Fit – Mode 2**

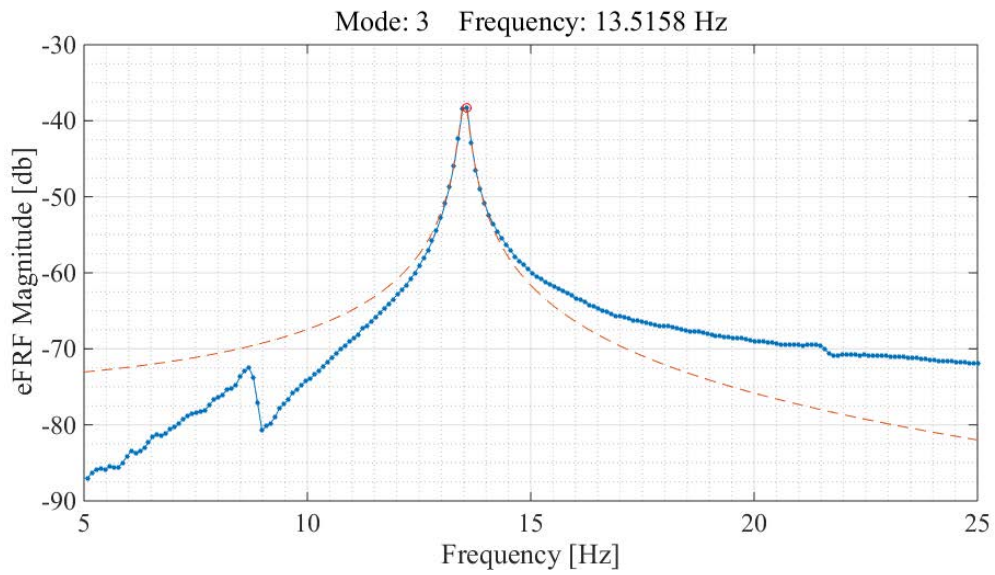


**Figure 7-19: Sledge MRIT – eFRF Fit – Mode 3**

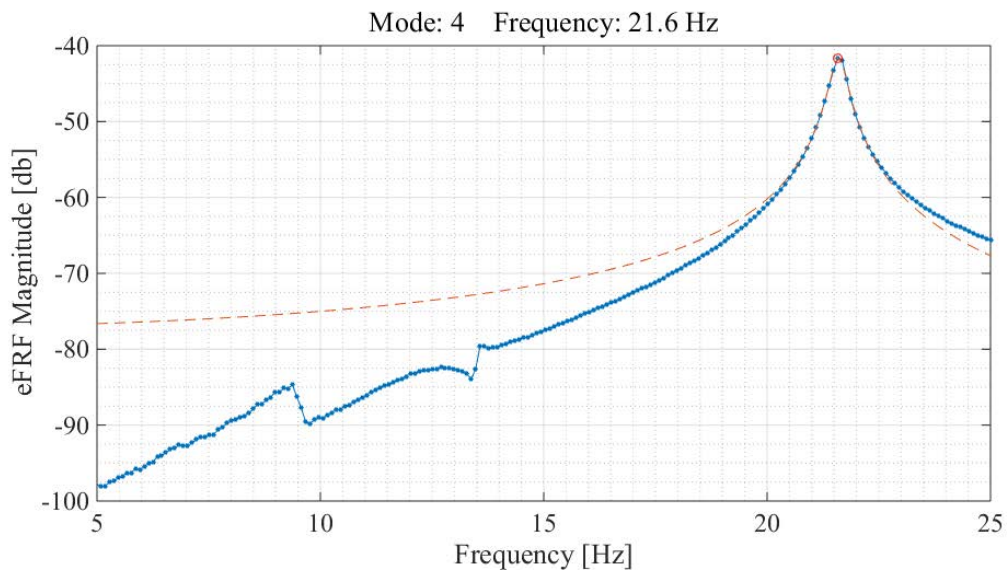


**Figure 7-20: Sledge MRIT – eFRF Fit – Mode 4**

### 7.1.1.5 Modal Scaling

Modal scaling was also estimated in the eFRF curve fits. Using the complex poles, complex modal scaling, and mode shape solutions, the modal model was used to reproduce several FRF measurements. Figure 7-21 shows the FRF synthesis of an input at DOF 17 and input at DOF 9, and Figure 7-22 shows the FRF synthesis of an input at DOF 22 and output at DOF 4. Both plots show the contribution of each mode to the summed system response the measured DOF. From these plots, good agreement is observed between the modal model and the measured data. This indicates that the modal model built from the sledge MRIT test represents the structural system and thus serves as a good benchmark comparison to evaluate THMPER system performance.

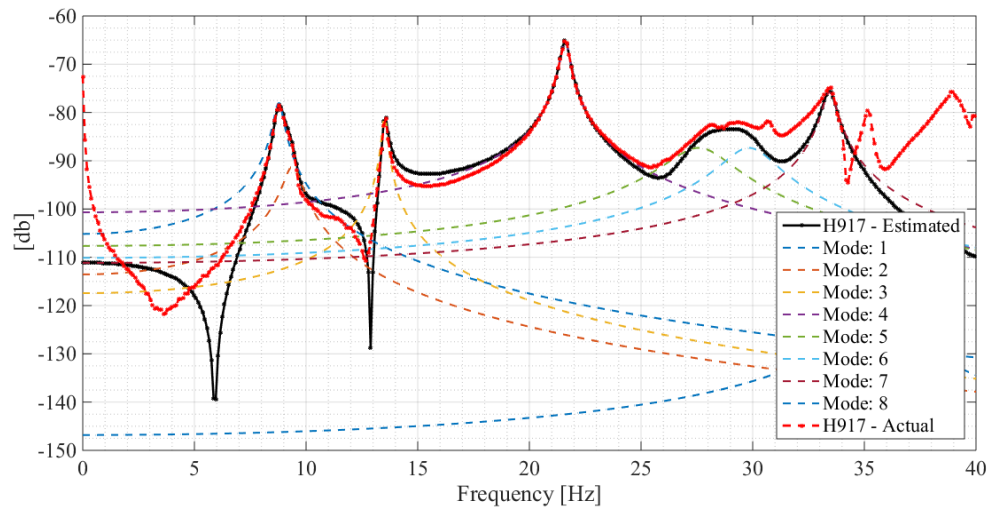


**Figure 7-21: Sledge MRIT – FRF Synthesis – Input at DOF 17, Output at DOF 9**

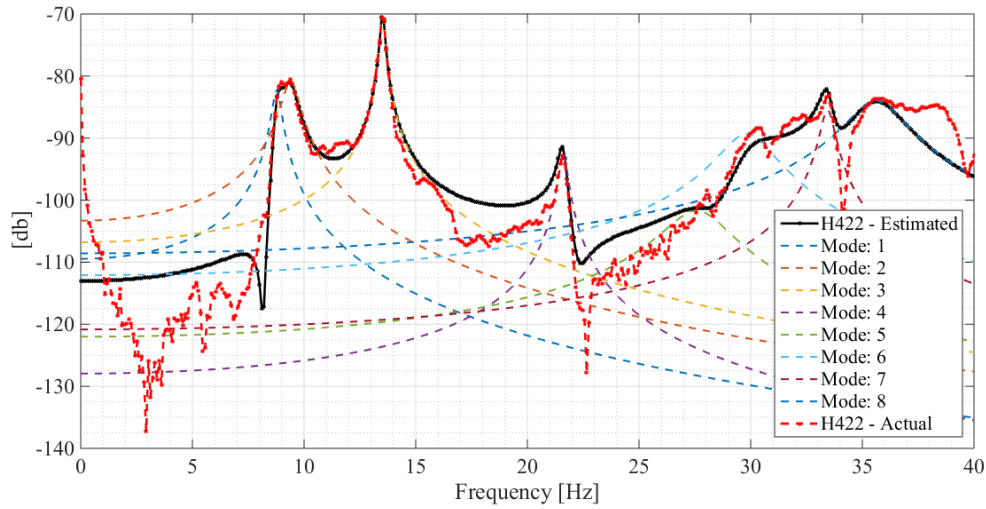


**Figure 7-22: Sledge MRIT - FRF Synthesis – Input at DOF 22, Output at DOF 4**

### 7.1.2 THMPER System

Testing was conducted on December 6<sup>th</sup> and 7<sup>th</sup>, 2014. During brief traffic closures, the THMPER system was driven across each girder-line and used to perform a minimum of three impact tests at each input location. The testing required a total of three traffic closures. The roving input/output measurements were recorded locally on the THMPER system trailer and the stationary response measurements were stored on the distributed data acquisition system located at Pier 1, and streamed wirelessly over a WLAN to inspect in real-time.



**Figure 7-23: THMPER System Test on Mossy Interchange Bridge**

### **7.1.2.1 Instrumentation**

The instrumentation plan, shown in Figure 7-24, consisted of a total of ten stationary accelerometers (locations 1-10) and a total of nine roving impact locations (locations 11-16). Three impact locations were selected at the quarter span, mid span, and three-quarter span of each interior girder and were measured and marked along the bridge deck prior to testing. The impact locations were chosen to (1) provide adequate spatial resolution of the interior girders, (2) reduce the extend and duration of traffic control, and (3) excite the structure at areas of high modal amplitude for all modes of interest to ensure a high signal to noise ratio.

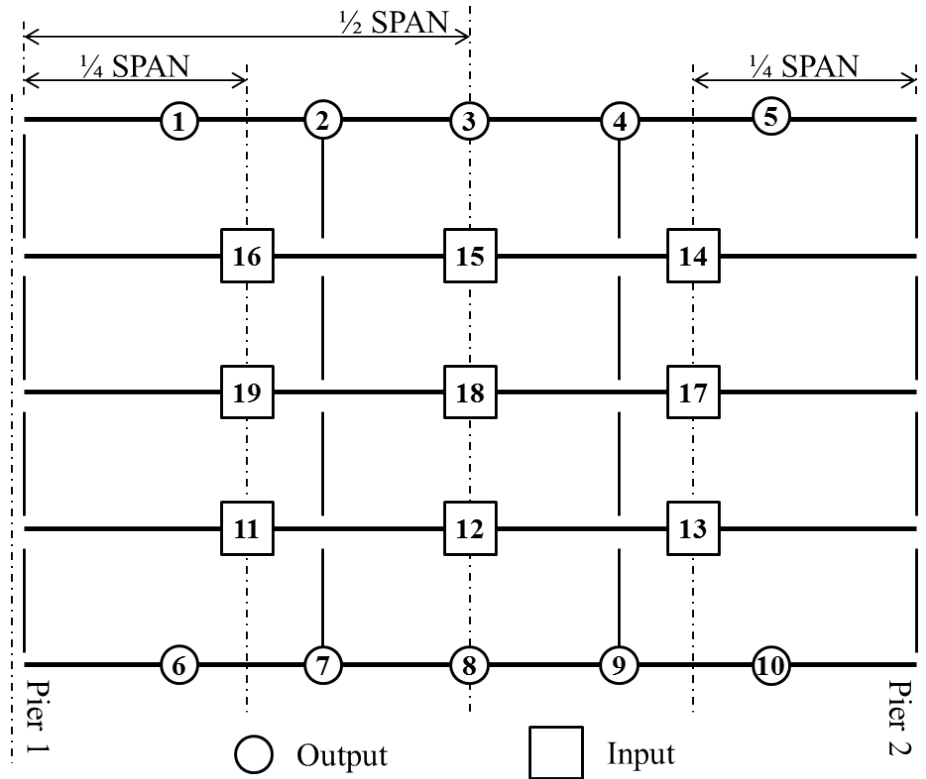


**Figure 7-24: THMPER Instrumentation Plan**

### 7.1.2.2 Data Quality

Data was recorded at a sampling rate of 3,200 Hz. In order to accurately define the shape of the impulse signal and allow for good characterization of the signal's frequency content. Typical force levels were observed above 25,000 lbs (Figure 7-25) which delivered typical frequency content (defined here as 20db roll-off) between ~0-65 Hz. (Figure 7-26) and caused typical driving point accelerations up to +/-3g's (Figure 7-27).

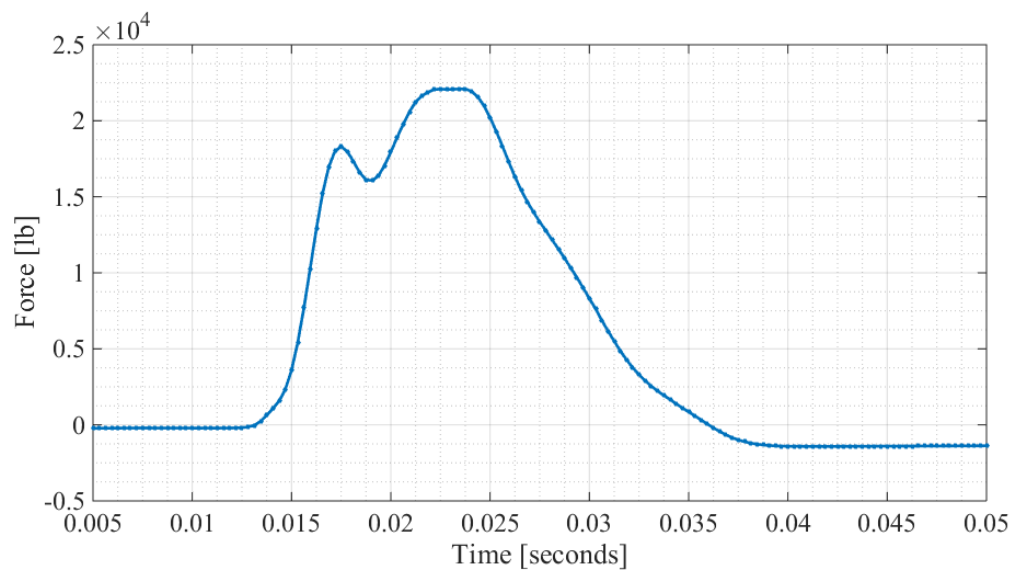


**Figure 7-25: THMPER – Force – Time Signal**

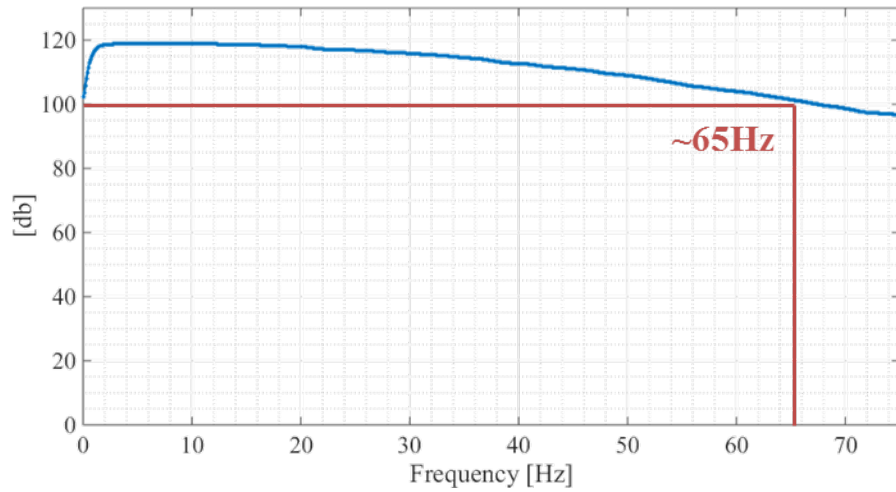


**Figure 7-26: THMPER – Force – Frequency Content**

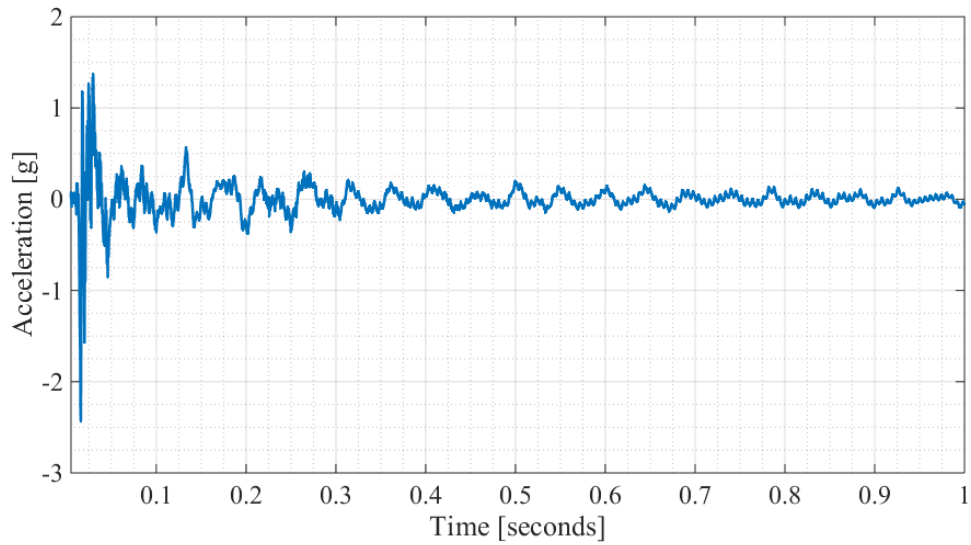


**Figure 7-27: THMPER – Typical Driving Point Acceleration**

### 7.1.2.3 FRF Measurements

Figure 7-28 shows the FRF measurement of the center span, center girder (DOF 13) driving point measurement with Coherence plotted as a function of frequency. In general, the THMPER system excited all modes of interest and due to the number of averages had minimal noise in each record as can be seen in the Coherence levels at areas of resonance. The FRFs show clear, smooth peaks of resonance indicating proper sampling of the structure's characteristic space.

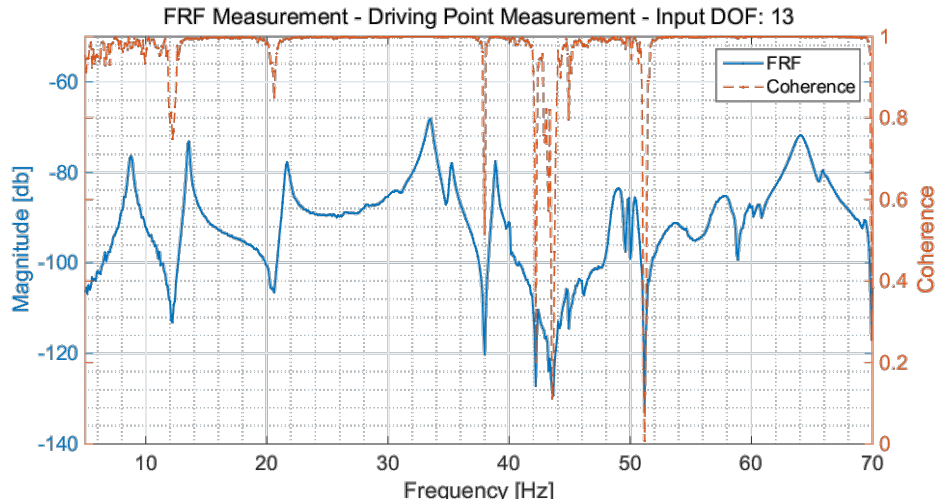


**Figure 7-28: THMPER – FRF Measurement and Coherence**

Without a set of DOF shared between the input and output spaces of the modal solution reciprocity cannot be found. This would require an impact to be performed with a secondary impact device at one of references while the local sensor array was engaged at a roving impact location. Even still this would not be a direct one to one reciprocity comparison unless an impact device of similar mass and stiffness was used. Due to a lack of time this was not able to be performed during testing window. However, the THMPER system FRF's were directly compared to those obtained by the sledge MRIT. Comparing the shape, magnitude, and location of the peaks it was determined that the dynamic properties of the bridge did not change due to the higher load levels experienced by the THMPER system's excitation device and the bridge was assumed to remain linear throughout both dynamic tests.

#### 7.1.2.4 Parameter Identification

The smallest dimension of FRF determines the number of available solutions at each frequency line. The left singular vector formed from the THMPER data set consists of the ten stationary output DOF, and the right singular vector consists of the nine interior input DOF. The CMIF is the plot of the nine singular values as a function of frequency. The CMIF for the THMPER system is shown in Figure 7-29. The peaks of the CMIF indicate resonance and the candidate poles are indicated in red. Note that not all peaks shown below are due to resonance and represent global modes.

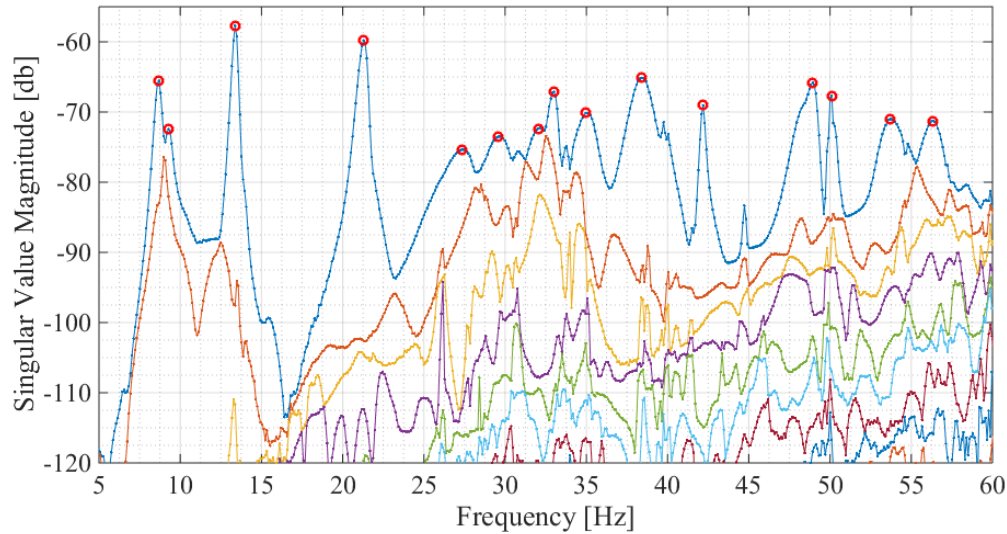


**Figure 7-29: THMPER – CMIF**

##### 7.1.2.4.1 Shape Estimation

To obtain a full set of global modal DOF, local SDOF residue estimations obtained from the roving input locations were integrated within the MDOF mode shape estimations of the stationary

references. For each unique peak identified in the CMIF, the stationary references served as a master set of modal coefficients to which the roving locations were slaved to. The local mode shapes extracted from the roving locations were linearly combined or ‘stitched’ together using the least squares method described in Chapter 5. Impact locations occurring at nodal points for a particular mode were discarded ad not used for incorporation within the global modal parameter set. The first eight global mode shapes are shown in Figure 7-30 through Figure 7-37.

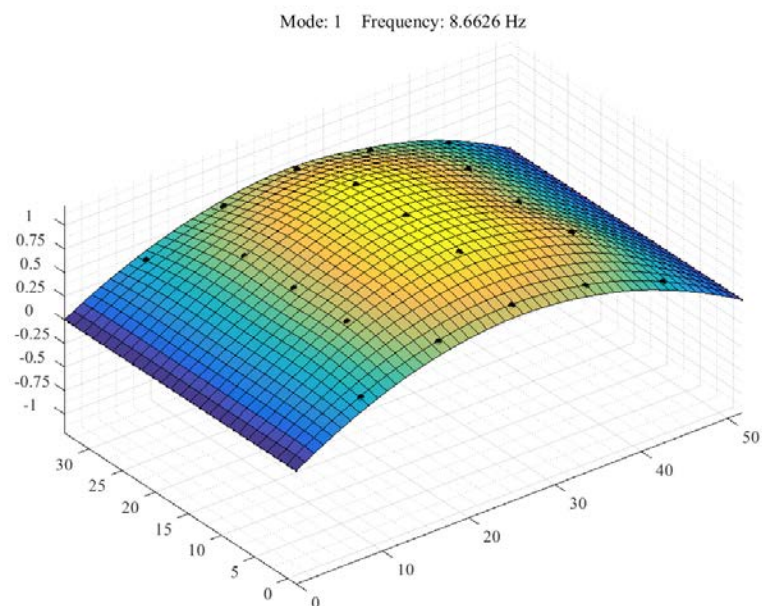


**Figure 7-30: THMPER – Mode 1**

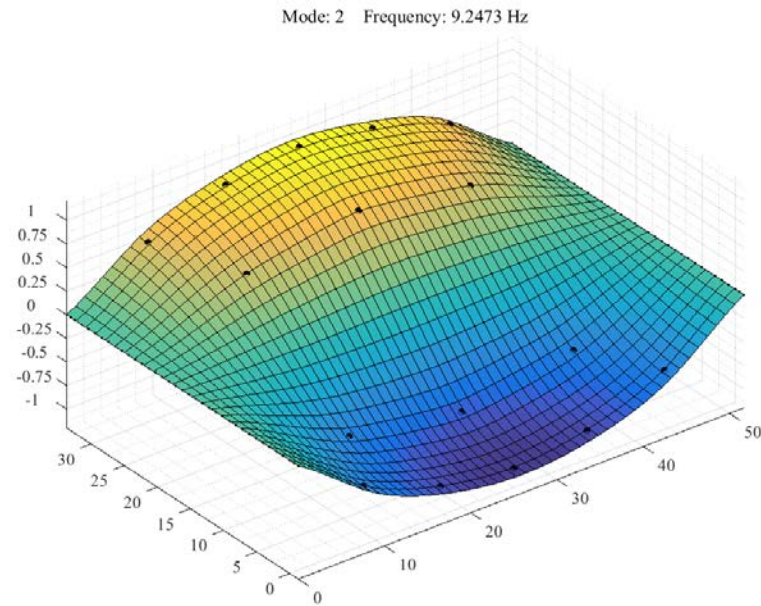


**Figure 7-31: THMPER – Mode 2**

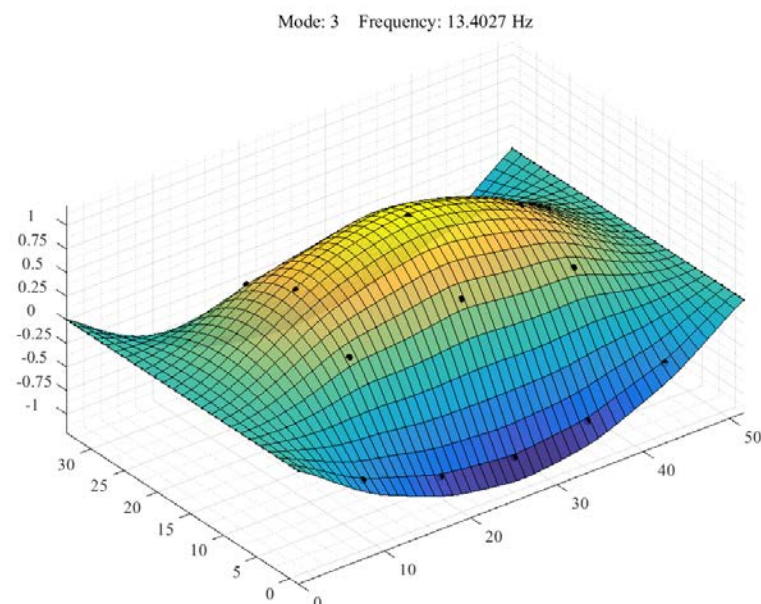


**Figure 7-32: THMPER – Mode 3**

Mode: 4 Frequency: 21.3626 Hz

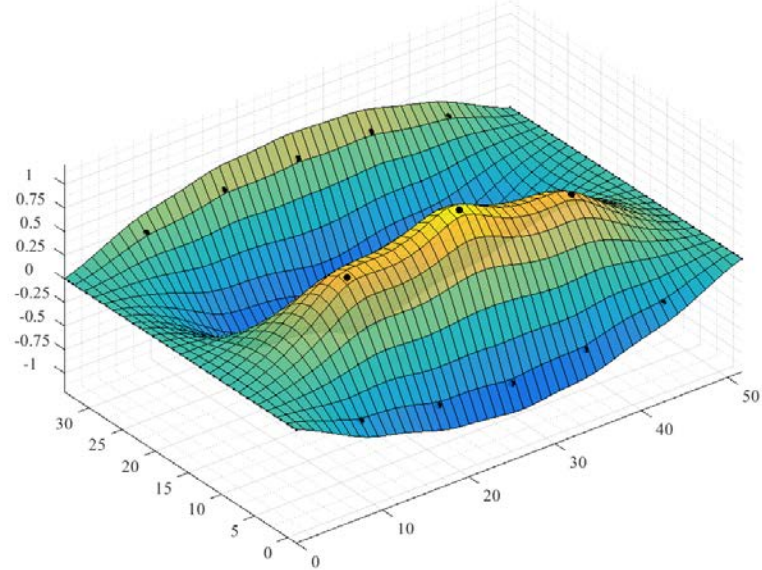


Figure 7-33: THMPER – Mode 4

Mode: 5 Frequency: 27.9228 Hz

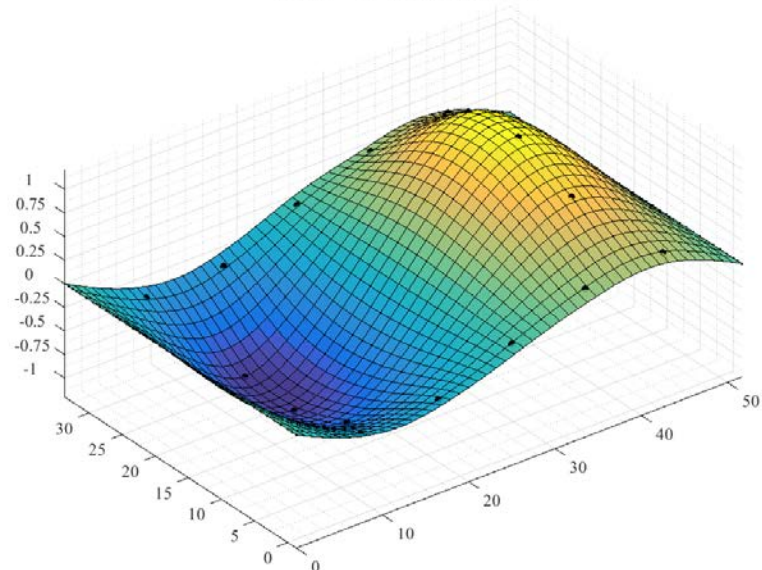
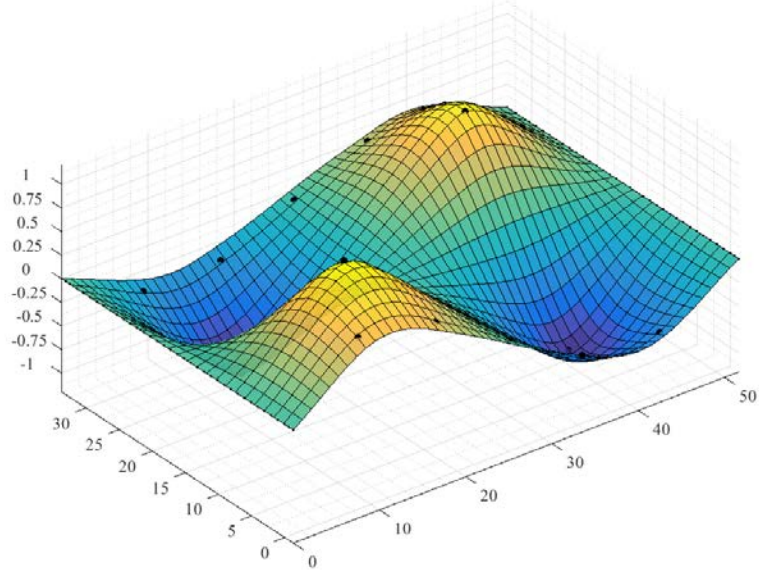
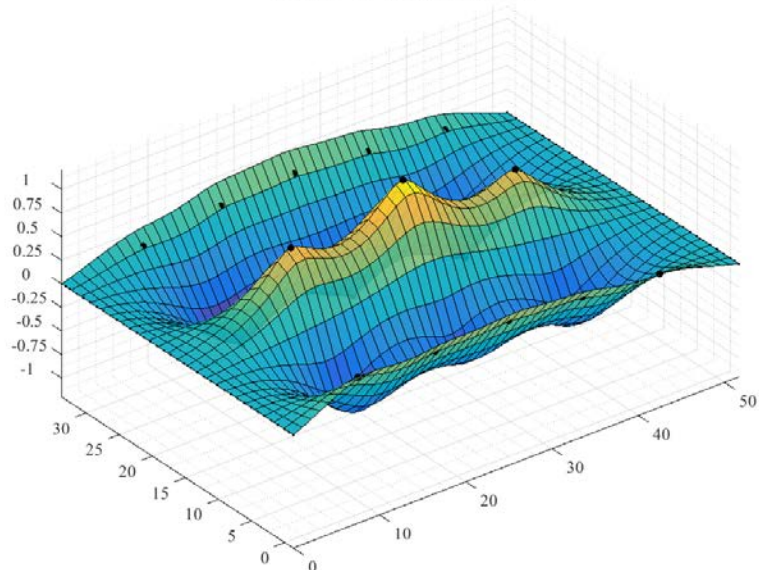


Figure 7-34: THMPER – Mode 5

Mode: 6 Frequency: 29.7529 Hz

**Figure 7-35: THMPER – Mode 6**

Mode: 8 Frequency: 33.0463 Hz

**Figure 7-36: THMPER – Mode 7**

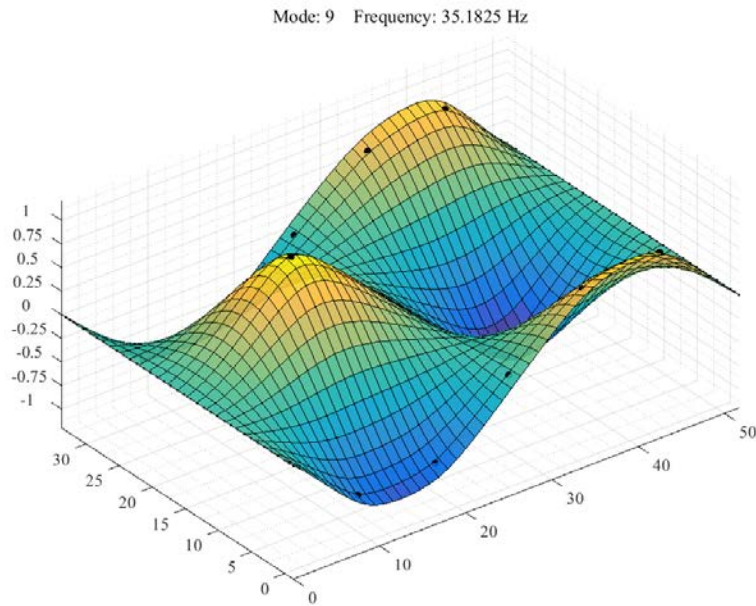


**Figure 7-37: THMPER – Mode 8**

#### 7.1.2.4.2 Pole Estimation

The eFRF method was used for estimation of the structure's complex poles. The eFRF method utilizes known spatial information (mode shapes) as a filter to condense the coupled MDOF FRF measurements to a series of multiple, SDOF contributions. The orthogonal properties of the mode shapes enhance each mode and, given adequate spatial resolution, allow for SDOF curve fitting techniques to be used regardless of the modal density in the desired frequency band. The first eight system poles found from the THMPER data set are shown in Table 7-3.

**Table 7-3: Sledge MRIT – Natural Frequencies and Damping**

Mode	Frequency [Hz]	Damping [% critical]	Mode Shape Type
------	-------------------	-------------------------	-----------------

Mode	Frequency [Hz]	Damping [% critical]	Mode Shape Type
1	8.70	2.98	1st Bending
2	9.25	4.07	1st Torsion
3	13.39	1.27	1st Butterfly
4	21.30	1.32	2nd Transverse Bending
5	27.92	4.52	2nd Bending
6	29.84	4.09	2nd Torsion
7	32.96	1.14	3rd Transverse Bending
8	35.22	2.29	2nd Butterfly

Because there is no overlap between the input and output space (e.g. no stationary driving points) in this scenario, it is not possible to obtain a reliable estimate of the modal scaling (modal mass). However, the spatial sampling of the THMPER system's test still provides enough resolution to decouple each modes SDOF contribution within the vicinity of each peak and provides a MDOF estimation of the complex roots (system poles). An example of the eFRF curve fits for the first four poles are shown in Figure 7-38 through Figure 7-41.

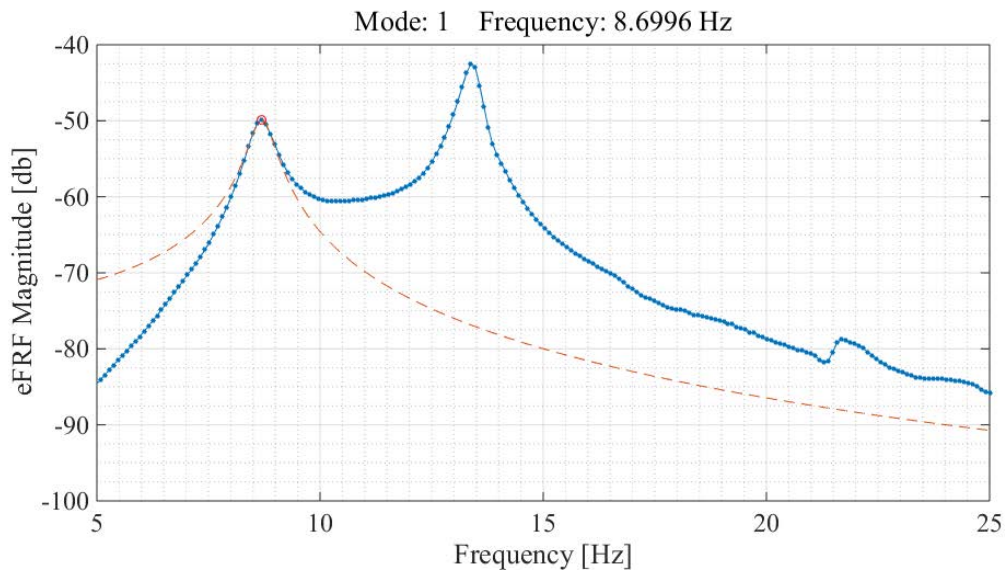


**Figure 7-38: THMPER – eFRF Fit – Mode 1**

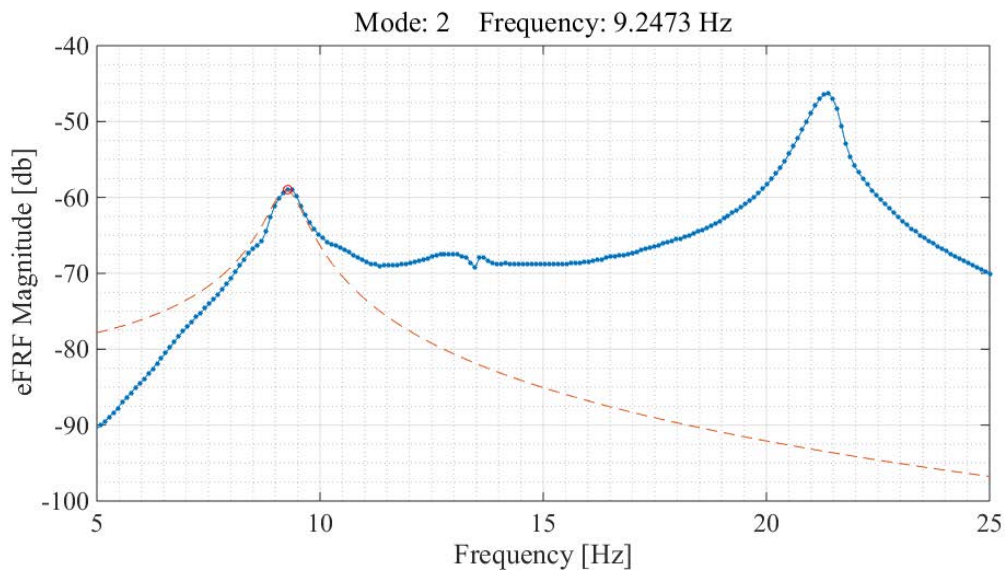


**Figure 7-39: THMPER – eFRF Fit – Mode 2**

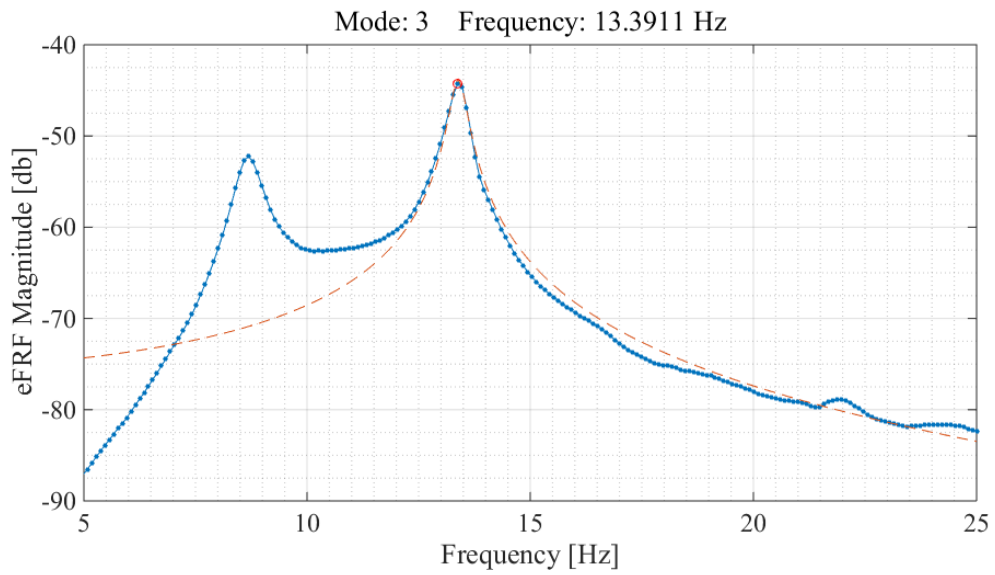


**Figure 7-40: THMPER – eFRF Fit – Mode 3**

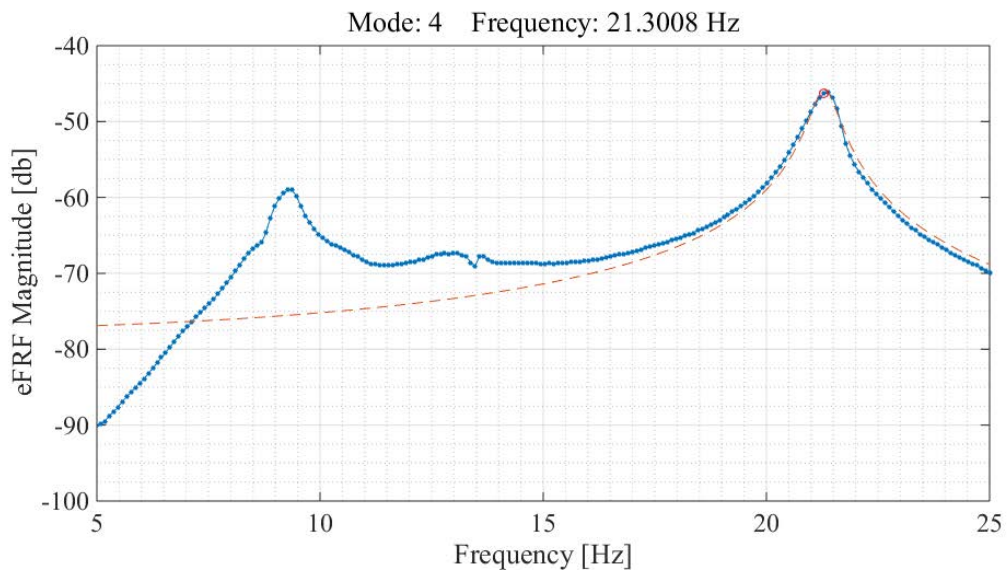


**Figure 7-41: THMPER – eFRF Fit – Mode 4**

### 7.1.3 Comparison of Modal Parameters

#### 7.1.3.1 Mode Shapes

A direct comparison between the modal DOF of each forced vibration test is not possible as the only shared spatial locations between the two tests were at the stationary references. Instead, the mode shapes were extrapolated to 10 equally spaced DOF per girder line using a cubic-spline method. The MAC values were then computed to determine the correlation between the two shapes. Figure 7-42 shows a graphical depiction of this comparison, Table 7-4 shows the individual results listed by mode, and Table 7-5 reports the statistical summary. The MAC values between the sledge MRIT benchmark and the THMPER system were greater than 0.9 for the first eight modes identified.

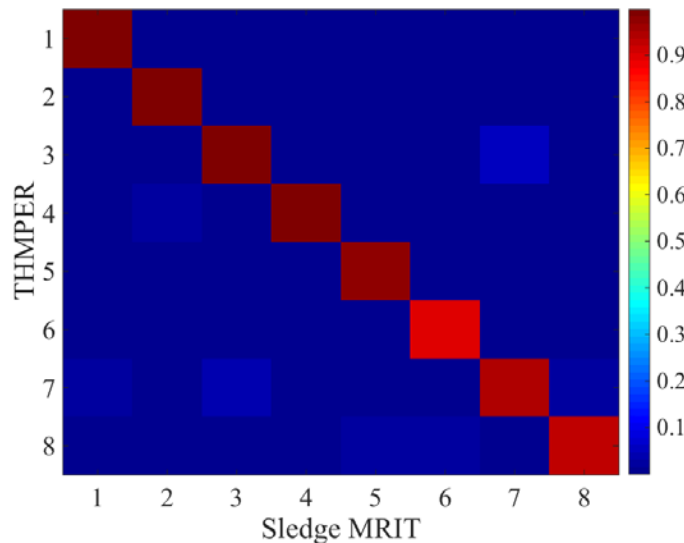


**Figure 7-42: THMPER vs. Sledge – Mode Shape Comparison – MAC Values**

**Table 7-4: THMPER vs. Sledge – MAC Values**

<b>Mode</b>	<b>MAC</b>
1	0.998
2	0.986
3	0.994
4	0.994
5	0.982
6	0.901
7	0.946
8	0.931

**Table 7-5: THMPER vs. Sledge – MAC Value Statistics**

<b>Average</b>	0.966
<b>Min</b>	0.901
<b>Max</b>	0.998

Comparing the first two modes in more detail reveals some minor errors in the THMPER system mode shapes. Figure 7-43 shows the details regarding the mode shape discrepancies between the THMPER and sledge for mode 1 and Figure 7-44 for mode 2. The mode shapes estimated from the THMPER system were obtained using least squares scaling estimations to combine each driving point measurement into the global modal parameter set. This is inherently a SDOF method and as such cannot fully account for the modal coupling observed between modes 1 and 2. Since system response at the driving point DOF is a result of that modal coefficient squared (e.g. all modes are in phase at the initial instance of impact), the contribution of multiple modes is

additive. This causes discrepancies between the exterior stationary references and the interior driving points which could possibly be mistaken for artificial stiffness of the exterior girders.

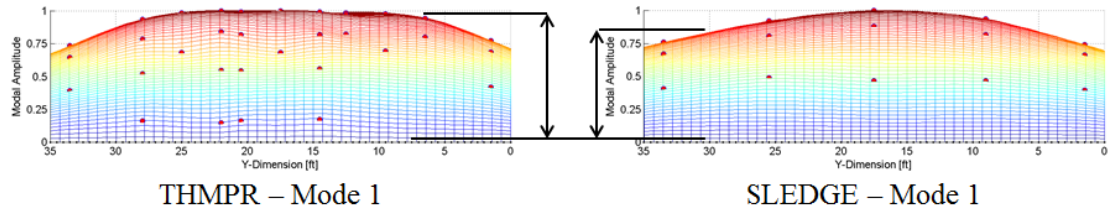


**Figure 7-43: Mode Superposition Errors – Mode 1**

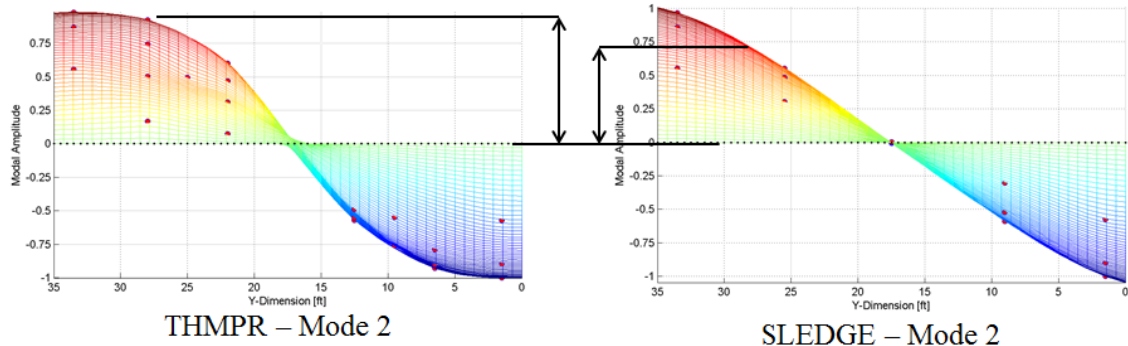


**Figure 7-44: mode Superposition Errors – Mode 2**

### 7.1.3.2 System Poles

The complex roots pole estimations were compared using a percent error calculation. Percent error comparisons between estimated natural frequencies and percent critical damping are presented in Table 7-6. The average, minimum and maximum for each comparison is presented in Table 7-7. Good agreement between the natural frequency estimations was found, however, the damping estimations contained significant errors.

**Table 7-6: Pole Estimation Percent Error**

<b>Mode</b>	<b>Frequency [Hz]</b>	<b>Damping [% critical]</b>
1	-0.87%	37.01%
2	-1.68%	7.85%
3	-0.92%	79.10%
4	-1.39%	57.87%
5	1.12%	-6.53%
6	-0.04%	11.14%
7	-1.45%	33.69%
8	-1.11%	-29.35%

**Table 7-7: Pole Estimation Comparison – Statistics**

	<b>Frequency [Hz]</b>	<b>Damping [% critical]</b>
<b>Average</b>	1.07%	32.82%
<b>Min</b>	0.04%	6.53%
<b>Max</b>	1.68%	79.10%

## 7.2 Static Truck Load Test

Load testing of a structure involves the direct measurement of global structural responses due to the application of a known load(s). Load testing is often employed as a part of advanced load rating procedures, whereby a structure's capacity is estimated.

In the case of Mossy Interchange Bridge, previous load ratings based on single-line girder analysis had indicated that the structure had insufficient capacity to accommodate all legal trucks and was thus posted for load. The load test performed on the Mossy Interchange Bridge served two purposes: it served as a means to experimentally determine the true load carrying capacity of the bridge, and it also provided “ground truth” global responses.

### 7.2.1 Instrumentation Plan

The underside of the center span was instrumented as established in Figure 7-45 through Figure 7-48. The instrumentation primarily consisted of transverse sensor lines located at quarter, mid, and three-quarter span lengths. A total of 15 displacement transducers and 36 strain gauges were installed on the superstructure. Table 7-8 provides a further breakdown of the number and type of sensor at each location.

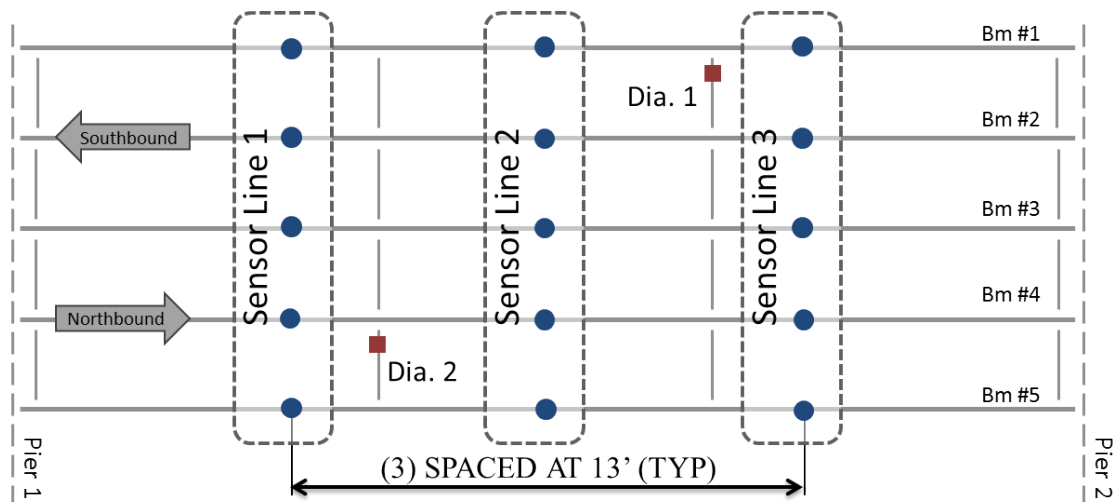


**Figure 7-45: Superstructure Instrumentation Layout**

**Table 7-8: Truck Test Instrumentation Schedule**

	<b>Line 1</b>	<b>Line 2</b>	<b>Line 3</b>
<b>Beam 1</b>	SP SG(2)	SP SG(4)	SP SG(1)
<b>Beam 2</b>	SP SG(1)	SP SG(4)	SP SG(1)
<b>Beam 3</b>	SP SG(1)	SP SG(4)	SP SG(1)
<b>Beam 4</b>	SP SG(2)	SP SG(4)	SP SG(2)
<b>Beam 5</b>	SP SG(2)	SP SG(4)	SP SG(3)

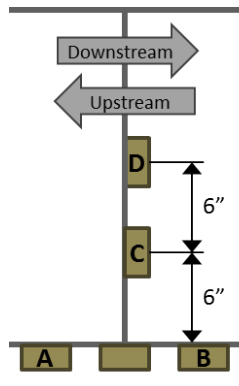


**Figure 7-46: Strain Gage Position**

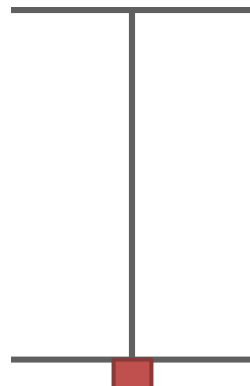


**Figure 7-47: String Pot Position**

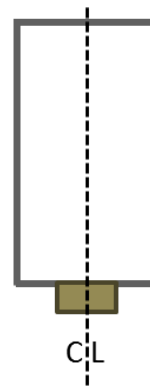


**Figure 7-48: Diaphragm Strain Gage Position**

## 7.2.2 Test Execution

The truck load tests were performed on December 7<sup>th</sup>, 2014. West Virginia DOT supplied six trucks that were used in a total of eight loading stages using single, tandem and four truck configurations (Table 7-9). The trucks were filled with materials from a nearby coal mine to produce three load levels for each truck – empty, half, and fully loaded. The varied load levels were chosen to examine the linearity of response, and the ~300kip proof load level was chosen to provide maximum flexural response of the girders and compressive strain in the piers. Intercomp LP600 wheel load scales were used to determine the weight of each truck by sequentially measuring the set of wheel loads for each of the three axles. The wheel load scales have a linear measurement range up to 30 kips and an accuracy of +/-1%.

At the conclusion of the final load case (tandem crawl test), two trucks drove in tandem at operational speed onto the bridge and braked to stop in an effort to impart longitudinal forces to the piers. The responses from this test were not substantial.

**Table 7-9: Load Test – Truck Configurations & Applied Loads**

Load Case	Truck Configuration	Load Level	Total Weight [lb.]
1	Single	Empty	33,580
2	Single	Half	37,280
3	Single	Full	78,520
4	Tandem	Empty	69,400
5	Tandem	Half	113,000
6	Tandem	Full	147,420
7	Proof Loading – 4 Trucks	Full	299,120
8	Crawl Test – Tandem	Full	147,420

### 7.2.2.1 Displacement Measurements

Global displacements were measured using Celeesco PT8510 cable-extension transducers, or string pots. The string pots are a very versatile sensor as they can be read with standard quarter bridge completion modules and operate on an unregulated voltage between 14.5-40 VDC. The string pots have internal signal conditioning which produces a 0-5VDC output signal that is linearly proportional to the physical distance traveled. The sensors have a full 5" linear stroke however the string pots are typically installed at the middle of this range to avoid possible overload or other electrical issues.

The string pots were mounted upside down on the bottom flange at each sensor line using a combination of c-clamps and magnets mounted to the sensor housing (Figure 7-49). The external reference was provided by sign posts that were driven into the stream bed Figure 7-50. Braided fishing line was used to attach the string pots to the driven sign posts.



**Figure 7-49: Typical String Pot Installation**



**Figure 7-50: Installation of String Pot Displacement Sensors**

### 7.2.2.2 Strain Measurements

Geokon 2" vibrating wire strain gauges and Hi-Tec weldable quarter-bridge strain gauges were used for the truck tests. All locations had at least a single 2" vibrating wire strain gauge on the bottom flange to capture maximum strains induced by the truck loads. Along sensor line 2, two strain gauges were placed on the bottom of each flange to determine the magnitude of out-of-

plane bending. Furthermore, at sensor line 2 every girder also had two strain gauges on the web of the girder to locate the neutral axis (Figure 7-51). Because of the poor apparent roadway condition, strain gages were also placed in the webs of beams 4 and 5 at the other sensor lines to investigate the degree of composite action at these areas as well.

Each strain gauge installed onto the superstructure was done so with a micro dot spot welder using the following procedure:

- The longitudinal location along each girder line was determined using laser distance measurements
- An angle grinder was used to remove paint at each location
- The gauge was positioned and welded onto the girder with a micro dot welder
- The cable was strain-relieved
- The area of exposed steel was painted over to prevent corrosion



**Figure 7-51: Strain Gauge Web Installation – Web**

### **7.2.3 Summary of Results**

#### **7.2.3.1 Peak Responses**

The peak responses were measured during the proof load test. The proof load test consisted of four fully loaded trucks positioned rear-to-rear and with the third (middle) axle down. This was done to apply the largest load possible towards the center of the span. A photograph of the truck positioning for the proof load test is shown in Figure 7-52 and a plan view schematic is shown in Figure 7-53 for clarification.



**Figure 7-52: Positioning Trucks during Proof Loading**

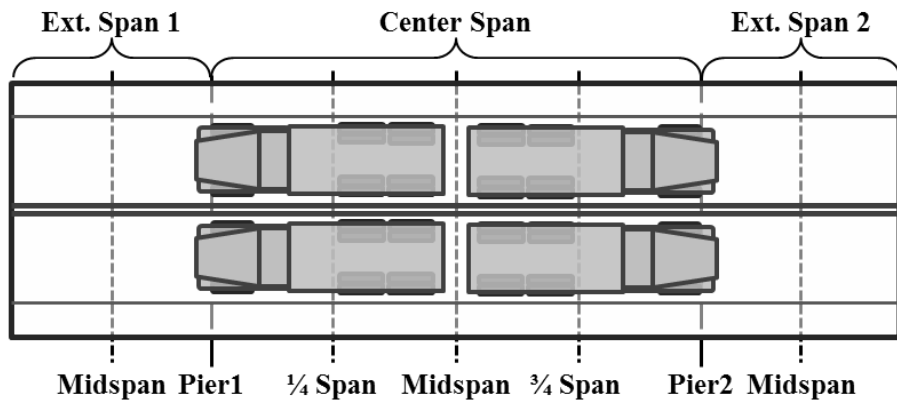


**Figure 7-53: Proof Load Truck Positions**

The displacements of each girder due to this load case are shown in Figure 7-54, and the corresponding strain responses are shown in Figure 7-55. The proof loading caused both peak strain and peak displacement responses at the center span of the center girder (girder 3). At this location a displacement of -0.289 inches and a strain of  $206.7\mu\varepsilon$  (in the bottom flange) were

measured. This strain corresponds to an approximate bottom flange stress of 6.0 ksi. The peak strain and displacement responses at each sensor location are shown in Table 7-10.

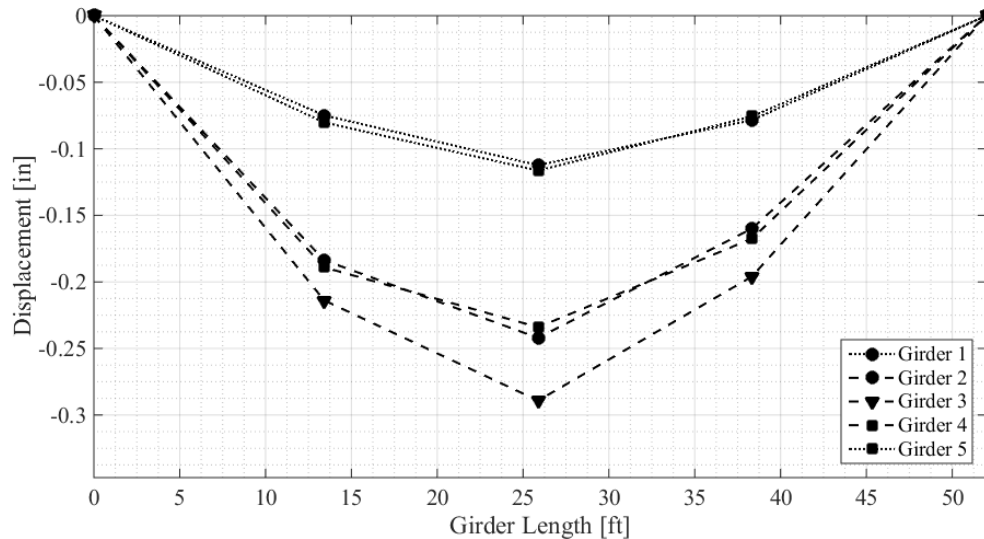


**Figure 7-54: Proof Load Test – Peak Displacements**

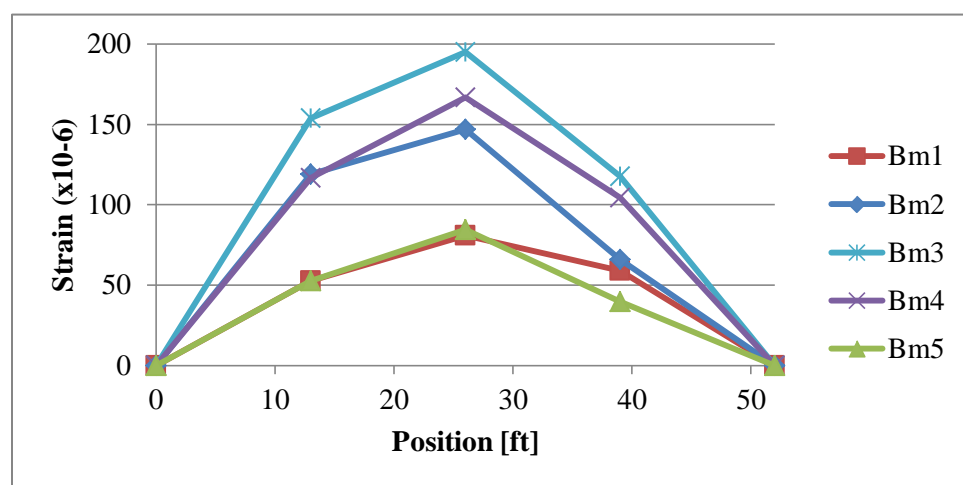


**Figure 7-55: Proof Load Test – Strain Responses**

**Table 7-10: Peak Strain and Displacement**

Location Girder-Line	Strain [us]	Displacement [in.]
1-1	53.3	-0.075
1-2	92.2	-0.112
1-3	58.9	-0.078
2-1	119.0	-0.184
2-2	163.2	-0.242
2-3	66.0	-0.160
3-1	153.9	-0.214
3-2	206.7	-0.289
3-3	117.6	-0.196
4-1	116.8	-0.189
4-2	188.1	-0.234
4-3	104.4	-0.168
5-1	52.6	-0.080
5-2	98.3	-0.116
5-3	60.7	-0.076

### 7.2.3.2 Linearity Checks

Three load levels were used to estimate the degree of linearity that was exhibited by the structure during testing by comparing the measured displacements against incrementing load levels. The center span displacement at each of the five girders is plotted versus the three center span loading locations for the three tandem truck configurations. Quarterspan loading is shown in Figure 7-56, mid span loading is shown in Figure 7-57, and three-quarter span loading is shown in Figure 7-58.

Girders 1 and 2 show consistent minor stiffening at higher load levels (i.e. the measurement displacement at these locations increases non-uniformly with the applied load levels). This is likely attributed to an increase in load transfer through mechanisms that were only engaged under high level loads. Although there appears to be some minor load re-distribution (e.g. minor

apparent stiffening/softening) between the girders, the structure generally exhibits a strong degree of linearity. Though not shown here, the force vs strain relationship was checked in the same manner and it exhibited the same general trends discussed above.

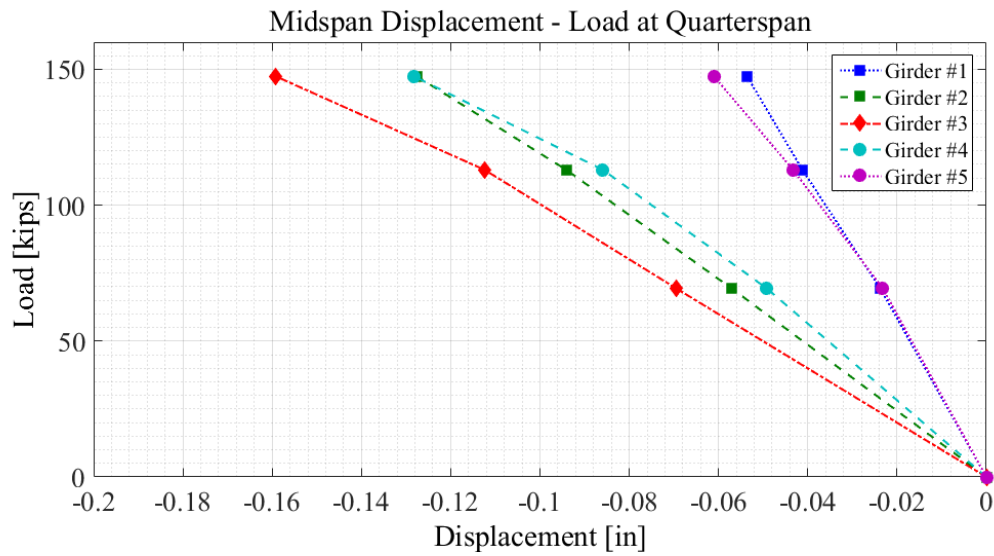


**Figure 7-56: Midspan Displacement vs Quarterspan Load**

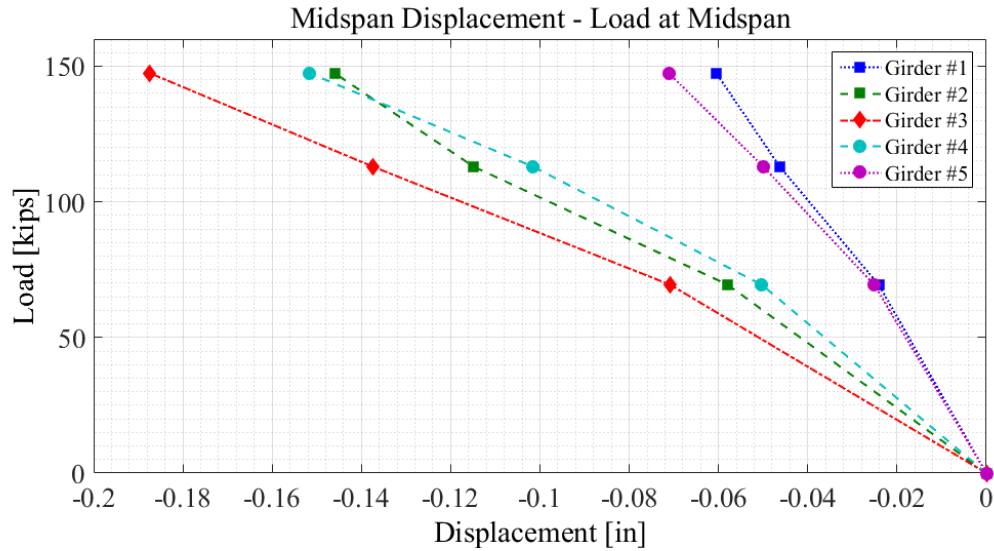


**Figure 7-57: Midspan Displacement vs Midspan Load**

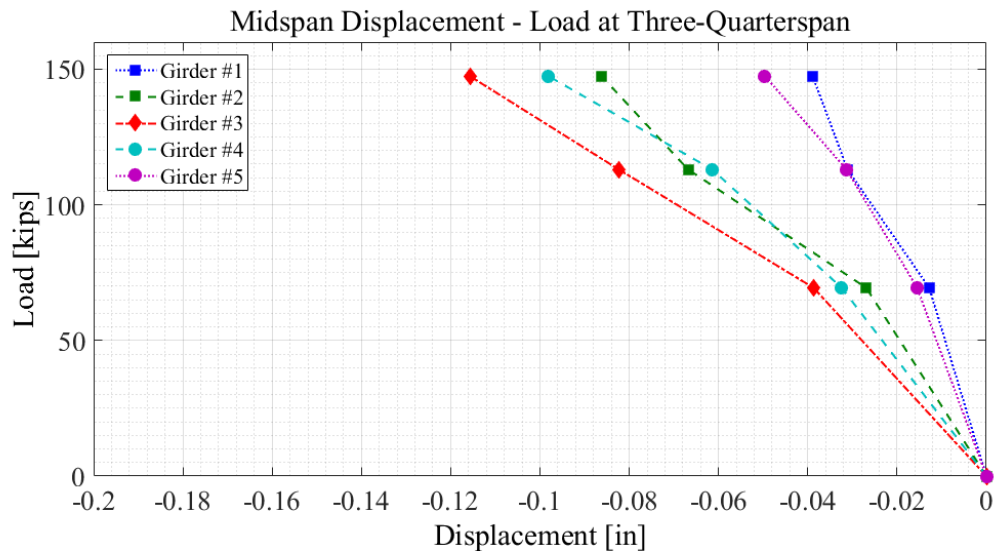


**Figure 7-58: Midspan Displacement vs Three-Quarterspan Load**

Note that the reduction of observed response at the three-quarter span loading location is likely due to the front wheels of the trucks extending off of the center span. Positioning the rear axle of the tandem trucks at the three quarter span location caused the front wheels of each truck to

extend out and onto the far side span. Thus, the full load level was not actually reached at this location.

### **7.2.3.3 Composite Action**

At several locations, strain gauges were installed on the web of the girders in addition to the bottom flange, permitting the location of the neutral axis to be determined. This provides an indication of whether the span is acting compositely with the deck.

The theoretical composite neutral axis was calculated to be 33.5" above the bottom of the bottom flange. Table 7-11 lists the experimental neutral axis at several locations due to the proof load case.

**Table 7-11: Neutral Axis Locations**

Sensor <b>Girder-Line)</b>	<b>NA location</b> [in.]
2-2	<b>50.76</b>
3-2	<b>25.28</b>
4-1	35.47
4-2	<b>29.24</b>
4-3	37.17
5-1	46.31
5-2	<b>25.78</b>

Some deviation is expected due to material assumptions and effective width calculations. Even considering this, some shifting of the neutral axis toward non-composite is observed at a few locations (e.g. the distance to the neutral axis is less than the calculated value). The values are still well above the value of 18" corresponding to completely non-composite behavior, and therefore it can be concluded that the sections at these locations are acting predominately composite.

In one location (midspan of Girder 2) the computed value of the neutral axis is considerably higher than the calculated composite neutral axis. This value is not the true location of the neutral axis of the section and is likely the result of having a considerable amount of axial compression in the member in addition to the bending stress.

Estimations of the neutral axis due to the varied truck load combinations are plotted in Figure 7-59. A moderate amount of variability is observed at the lower load levels that may be due to localized non-linearities (e.g. local stick-slip mechanisms) turbulent stresses from localized effects. Application of larger loads appears to redistribute the localized effects on the section to converge at a linearized global response.

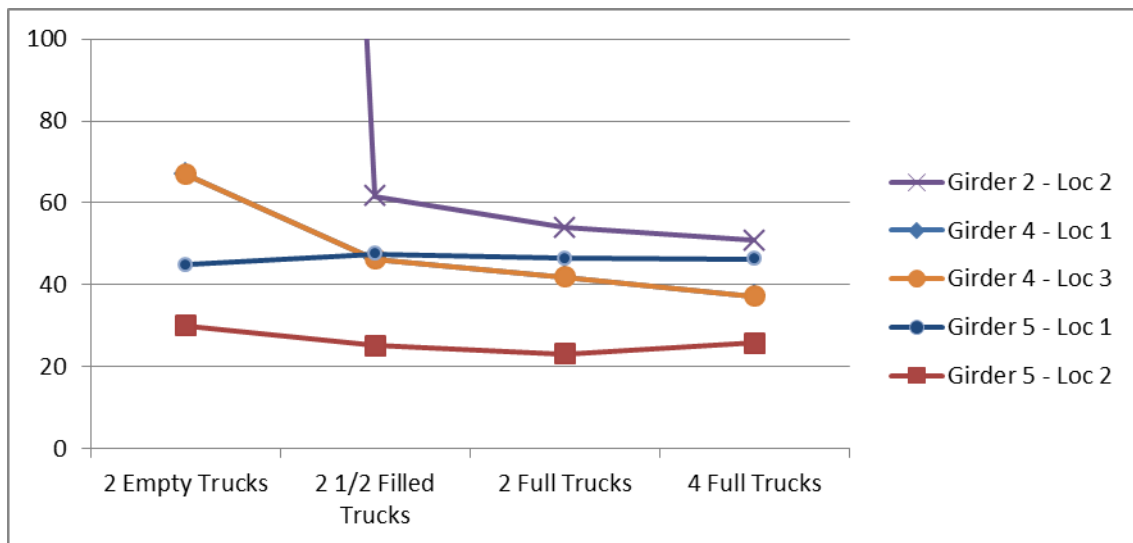


**Figure 7-59: Variability of Neutral Axis Due to Load Levels**

#### 7.2.4 Summary of Constraints

The tests took place in December of 2014. The local area was cold, wet, and had reduced daylight hours. Obtaining light sources was necessary to work past sunset. Due to the nature of underside installations and the necessity to remain on schedule for the planned traffic closures, this meant using portable head lamps as the sole source of illumination for large portions of the installation.

The center span is over water which made the underside difficult to access and required a large preparation effort to obtain global displacement measurements. Due to the need for an external reference, a hand held pneumatic post driver was used to drive sign posts into the creek bed. The post driver was operated from the Hydra platform which needed to be continually adjusted during the three day installation effort.

Underside access was constrained due to the geometry of the intersection at the far end. Accessing the far end required partial or sometimes full obstruction of traffic entering the

roadway which periodically caused delays for the coal trucks and other passing traffic (as well as the engineers). This was compounded by the Hydra platforms size and difficulty to reposition. Additionally, the maximum extension of the underside catwalk was only able to reach three girders at each sensor line. This added a significant amount of installation time due to the additional Hydra truck positioning.



**Figure 7-60: Underside Installation with Hydra Platform**

Large amounts of rain caused the creek bed to rise which significantly increased the effort and time required to install each displacement sensor. At times, the flow rate of the creek was deemed too dangerous to enter with waders and a Hydra truck was required to access the string pot measurement lines.

The rain affected access to the roadway during portions of the instrumented sledge testing which caused minor delays. No delays were caused by rain during THMPER testing as the operation of

the system is performed from inside the mobile work station Sprinter van and personnel are not directly exposed to traffic.

The cold weather ultimately caused problems using the micro-dot welder which lengthened the installation time required for each strain gauge. Generally, epoxy is the preferred method to attach vibrating wire strain gauges onto a girder as it is quicker and less tedious than using a micro-dot welder. But because the epoxies available were not rated for the anticipated temperatures (due to cure time), the micro-dot welders were an inconvenient necessity. Consequently, the cold weather ultimately drove selection of the specific sensor type as the 2" vibrating wire gauges were the largest weldable gauges available.

### **7.2.5 Additional Measurements**

Though not reported in this writing, several other measurements from the superstructure and substructure were acquired during the testing. Two exterior diaphragms on the superstructure were instrumented with strain gages as indicated in the above schematic of the superstructure. The relative longitudinal displacements at each exterior bearing along each span were monitored using TML displacement transducers. The TMLs were mounted with angles and c-clamps and were installed in an effort to determine the behavior of the expansion joints as well as possibly quantify substructure attributes based on pier movement due to the heavy loads.

Impact testing was performed on Pier 2 during the several days prior to the load test while superstructure instrumentation was being installed. In addition to the accelerometers used in the forced vibration test of the pier, a combination of tilt meters and strain gauges were also used for instrumentation. The pier responses were very low, however. Substructure tilt, for example, was measured with Geokon vibrating wire tilt meters. Despite these meters having a resolution of ~.01 degrees, negligible tilt was measured during all truck load levels and configurations.

## CHAPTER 8: Model-Experiment Correlation

The FE model was calibrated using modal parameters obtained from THMPER and the sledge MRIT tests. The first six modes were used for the updating process. The following parameters were updated using the RAMPS FEM software:

- Deck ( $f'c$ )
- Sidewalk & Barrier ( $f'c$ )
- Diaphragm (E(ksi))
- Composite Action ( $I_x$ )
- Bearing Rotational Stiffness

The *a-priori* model had these parameters set at base values as prescribed by AASHTO. The concrete compressive strength was set at 2500 psi, the diaphragms modulus of elasticity was set to 29000 ksi, the deck was modeled fully composite, and there was no rotational stiffness applied at the bearing locations.

These values were permitted to vary within bounds acquired through sensitivity studies. The optimization function used for calibration was run several times for each model from different starting points to reduce the likelihood of settling within a local minimum. The calibrated model that most accurately predicted the dynamic results for each respective test was chosen as the presentative model for this structure.

## 8.1 Modal Properties

Table 8-1 displays the natural frequencies from the THMPER and sledge tests and those predicted by the calibrated model. Table 8-2 displays the percent error of each model's natural frequency predictions.

**Table 8-1: Comparison of Experimental and Predicted Natural Frequencies**

Mode	Sledge	THMPER	FEM
1	8.78	8.7	8.58
2	9.41	9.25	9.51
3	13.52	13.39	14.2
4	21.6	21.3	20.01
5	27.61	27.92	28.04
6	29.85	29.84	28.56
7	33.44	32.96	31.56
8	35.62	35.22	33.01

**Table 8-2: Comparison of Experimental and Predicted Natural Frequencies - Percent Error**

Mode	Sledge	THMPER
1	2.33%	1.40%
2	-1.05%	-2.73%
3	-4.79%	-5.70%
4	7.95%	6.45%
5	-1.53%	-0.43%
6	4.52%	4.48%
7	5.96%	4.44%
8	7.91%	6.69%

## 8.2 Displacement Predictions

The calibrated model was analyzed under the proof level load. The truck loading was simulated by placing point loads on the deck elements at locations corresponding to the locations of the truck tires as measured during the test and equal to the measured weights.

The percent error of the displacement predictions obtained from each model is shown in Table 8-3 and summarized in Table 8-4.

**Table 8-3: Displacement Predictions – Percent Error**

<b>Beam</b>	<b>X [ft.]</b>	<b>Y [ft.]</b>	<b>A Priori</b>	<b>Sledge</b>	<b>THMPER</b>
1	13.42	32.42	-16.30%	0.98%	-7.09%
1	25.88	32.42	-9.55%	6.64%	-1.22%
1	38.33	32.42	-20.28%	-1.09%	-11.49%
2	13.42	24.31	8.34%	15.58%	11.12%
2	25.88	24.31	4.96%	11.32%	8.07%
2	38.33	24.31	-3.06%	4.14%	0.26%
3	13.42	16.21	12.50%	17.98%	14.29%
3	25.88	16.21	11.39%	15.45%	13.36%
3	38.33	16.21	7.62%	12.55%	10.05%
4	13.42	8.10	11.07%	18.20%	13.79%
4	25.88	8.10	1.38%	7.99%	4.63%
4	38.33	8.10	1.14%	8.04%	4.35%
5	13.42	0.00	-9.55%	7.06%	-0.83%
5	25.88	0.00	-7.77%	8.14%	0.37%
5	38.33	0.00	-28.07%	-7.98%	-18.81%

**Table 8-4: Displacement Predictions – Percent Error Statistics**

	<b>A Priori</b>	<b>Sledge</b>	<b>THMPER</b>
<b>Average</b>	10.20%	9.54%	7.98%
<b>Min</b>	1.14%	0.98%	0.26%
<b>Max</b>	28.07%	18.20%	18.81%

Figure 8-1 shows the displacement of each girder as predicted by the three models. Figure 8-2, Figure 8-3, and Figure 8-4 show the displacement cross-section at each sensor line. The measured experimental displacements are represented as well. Note that some of the wheel loads from the truck load testing were not contained within the center span. The side spans were not modeled and therefore their interaction with the center span is not represented.

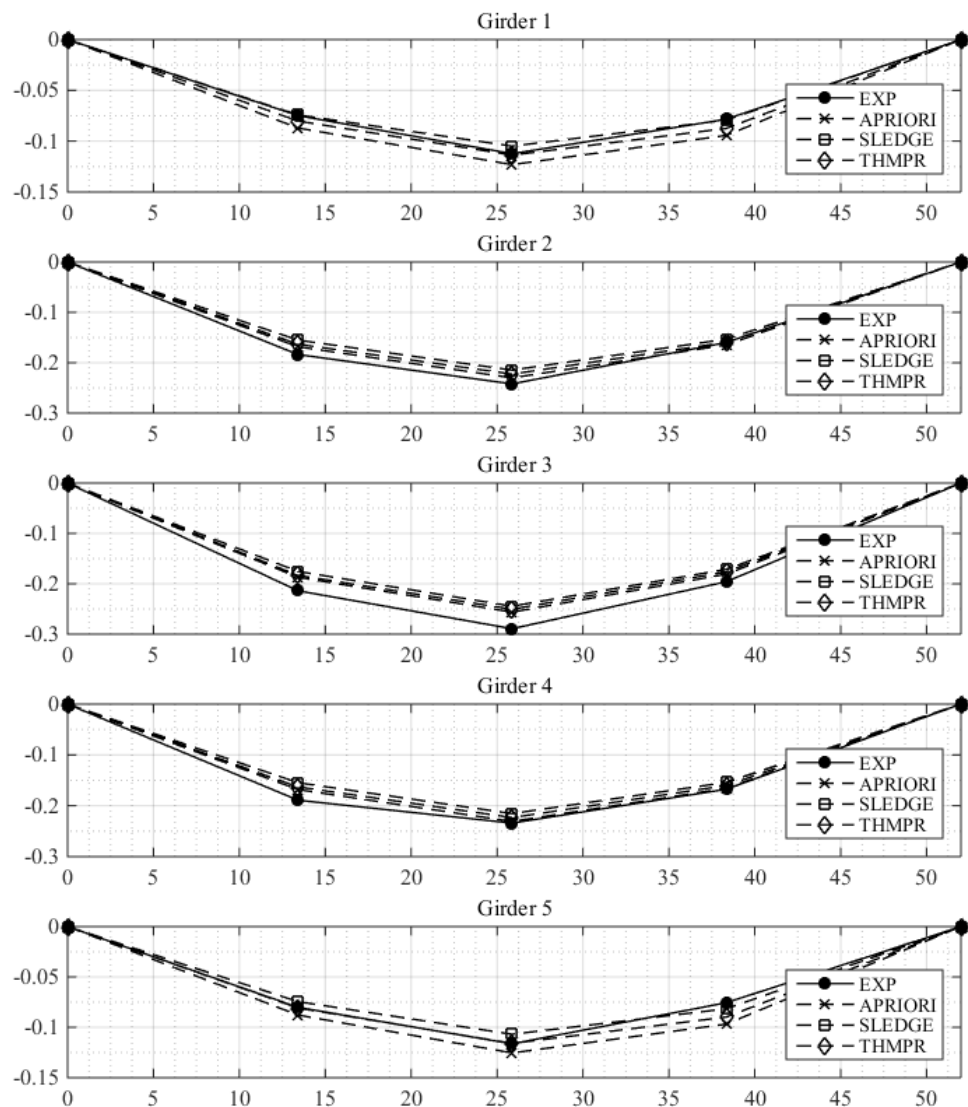


**Figure 8-1: Comparison of Predicted Displacements – Elevation View**

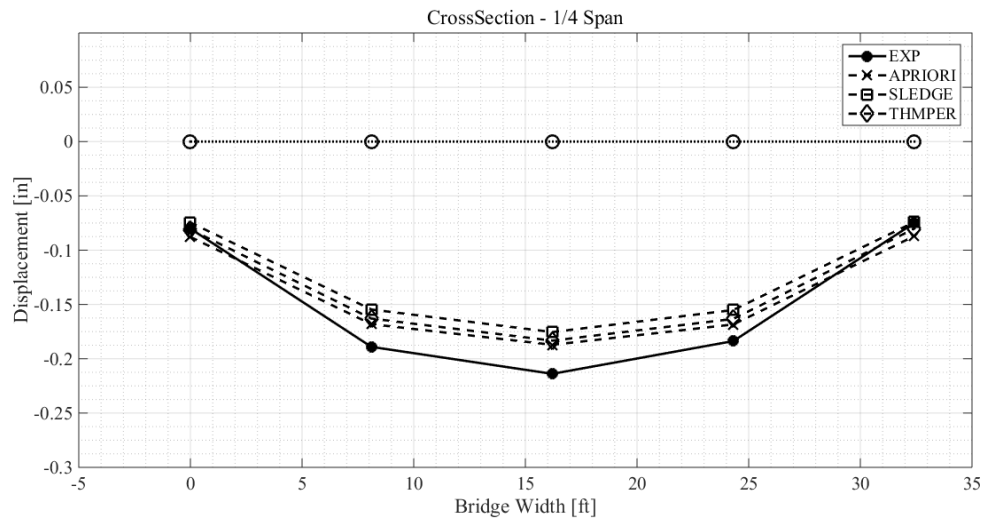


**Figure 8-2: Cross-section Displacement – Proof Load Test – Quarter Span**

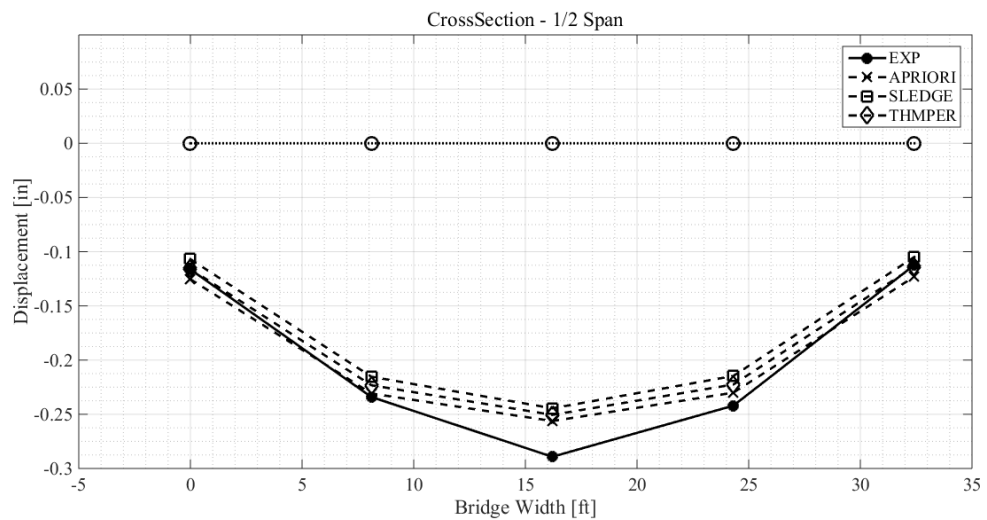


**Figure 8-3: Cross-section Displacement – Proof Load Test – Mid Span**

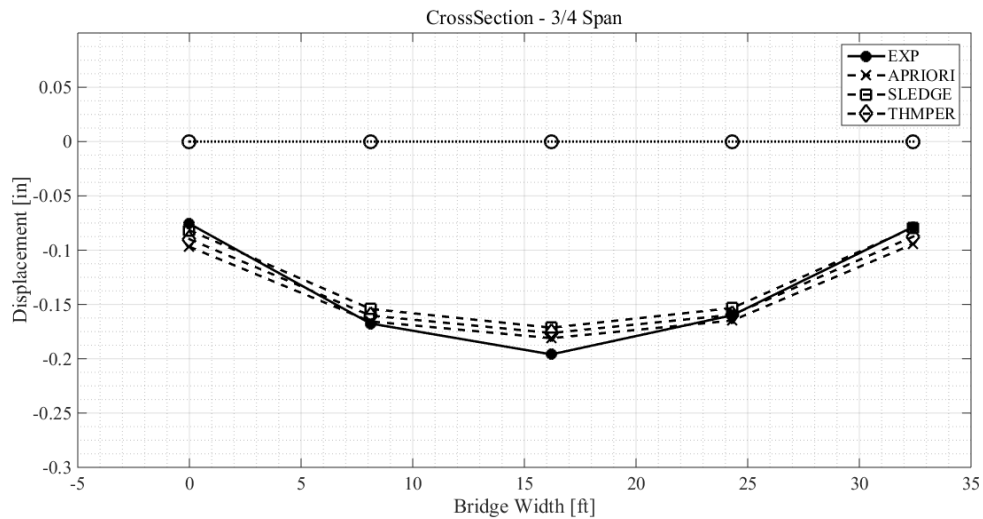


**Figure 8-4: Cross-section Displacement – Proof Load Test – Three-Quarter Span**

The sledge and THMPER models exhibited the same general trends during the updating process. The model predictions differ by no more than 20% and less than 10% at most locations. The majority of this difference is likely due to the inherent error in measurements of wheel weights and locations. Furthermore, the model was calibrated with dynamic responses for which the bridge experienced far less load levels than when under four fully loaded trucks. It is expected that the degree to which many load distribution mechanisms are engaged will vary under these very different load levels. The linearity plots previously presented show that minor stiffening and softening occurred during the several stages of the load test. Therefore it is expected that a model calibrated with dynamic results will be unable to perfectly represent the structural responses under proof level loads.

However, in spite of this, the model is still capable of adequately representing the structure under proof level loads and for the purposes of load rating, as evidenced by the agreement between measured and predicted displacements.

### 8.3 Load Rating

The bridge was load rating using both traditional AASHTO single-line girder model methods and with a finite element model. Both methods employ the Load and Resistance Factor Rating (LRFR) method for determining structural capacity. Any rotational stiffness in the model as a result of the calibration process was removed before computing the ratings, as this mechanism may diminish or disappear under large load conditions or as the bridge ages. The controlling LRFR ratings under HL-93 loading for interior and exterior girders are summarized in Table 8-5.

**Table 8-5: LRFR Load Rating Factors**

	Inventory				Operating			
	Strength I		Service II		Strength I		Service II	
	Int	Ext	Int	Ext	Int	Ext	Int	Ext
SLG	1.75	2.20	1.57	2.00	2.27	2.85	2.04	2.60
A-Priori	2.43	3.24	2.23	3.15	3.16	4.21	2.90	4.10
THMPER	2.41	3.31	2.24	3.31	3.12	4.29	2.91	4.30
Sledge	2.36	3.20	2.53	3.15	3.06	4.15	3.28	4.10

Both the sledge and THMPER models differed very little from the *a-priori* model. Because Drexel had access to construction drawings, and a fair estimate of material properties, the *a-priori* model was able to reliably estimate the structure for the purposes of load rating. The rating factors changed less than 10% as a result of updating the model.

The rating factors obtained from the updated model were determined using conservative assumptions. Mechanisms contributing to structural capacity that may not be reliable long term (i.e. rotational restraint at the bearings) were removed. However, deterioration and changing site conditions may cause changes to the global behavior of the structure and affect the load carrying

capacity. Thus the rating factors reported offer no guarantee of predicting structural capacity at a future date.

## CHAPTER 9: SUMMARY OF MID-ATLANTIC CLUSTER THMPER TESTS

The following is an overview of the THMPER system tests performed as part of the LTBP Mid Atlantic Cluster NDE effort.

### 9.1 Overview of THMPER Tests

The LTBP Program is a research effort to collect scientific performance field data from a representative sample of bridges nationwide. The THMPER system was used to perform EMA on a total of eleven bridges of the Mid-Atlantic Cluster. Tests were performed throughout the summer of 2015.

**Table 9-1: Overview of THMPER Mid-Atlantic Cluster Tests**

	<b>Structure Type</b>	<b>Spans</b>	<b>Continuity</b>	<b>Length</b>	<b>Width</b>	<b>Skew</b>
<b>DE 1</b>	Prestressed	1	simple	900	720	22
<b>DE 2</b>	Steel Stringer	2	continuous	-	679	
<b>DE 3</b>	Steel Stringer	1	simple	780	610	0
<b>MD 1</b>	Steel Stringer	2	simple	508	570	15
<b>MD 2</b>	Prestressed	2	simple	1200	488	0
<b>NJ 1</b>	Steel Stringer	1	simple	1189	-	50.9
<b>NJ 2</b>	Prestressed	2	non-continuous	1160	474	0
<b>NJ 3</b>	Prestressed	2	non-continuous	976	550.75	7.58
<b>PA 1</b>	Steel Stringer	2	continuous	1404	576	0
<b>PA 2</b>	Prestressed	2	non-continuous	916	576	5
<b>PA 3</b>	Prestressed	1	simple	1632	552	0

#### 9.1.1 Traffic Control

In general, one to two days were allocated per bridge test. Traffic control began setting up between 8-9AM and typically finished lane closure(s) within one to two hours, depending on the level of traffic. Details of each traffic control plan were dictated by the specific testing conditions

as well as state DOT preferences. However, the general traffic control configuration consisted of multiple, single lane closures that were staged throughout the day. Prior to closing the lane, traffic cones were placed in the roadway leading up to and past the lane closure to alert and route drivers as well as contain the working personnel. To establish the closure, traffic was slowed and crash trucks were positioned between oncoming traffic and the bridge.

### **9.1.2 Test Execution**

Once on the test span, field measurements were recorded and used to mark the roving impact locations and reference sensor locations. For each test, typically three to five reference sensors were installed along each shoulder of each span. Tests on two-span bridges required placing the remote data acquisition at the center of the two spans to avoid extending the 100ft PCB cables. Roving input locations were typically chosen at quarter points in each lane resulting in three equally spaced inputs per accessible lane. At each roved location +3 impacts were performed and used for signal averaging.

The references were installed in each accessible shoulder lane at the start of the test and set to record continuously until the test was completed. The distributed data acquisition (DAQ) system of the THMPER system contains a battery power NI cRIO mounted in an environmentally protected case. Each remote DAQ system is GPS synchronized (using PPS broadcasts from multiple satellites) and set to timestamp every acquisition tick in absolute time (UTC standard). Once the reference sensors were installed, data was continuously recorded at a sampling frequency of 3,200 Hz and stored locally in 500MB blocks. The internal storage of each cRIO was expanded from 2 to 30GB using a USB to account for the large amount of acquired data. The remote DAQ systems also published a stream of one second data blocks to a WLAN that allowed viewing and access to the data in real time.

## 9.2 Overview of Results

### 9.2.1 Data Quality

Reviewing the impulse records shows typical force levels of +25 kips and frequency content +50Hz. Tests performed during heavy traffic were not significantly affected and generally retained high coherence values. This is a result of the large excitation force levels and frequency content of the impact as well as the signal pre-processing approach (averaging, force/response windows).

The frequency resolution obtained from the impact records was typically .09 Hz which was adequate for characterizing the frequency content for the majority of test bridges. Some of the larger bridges contained closely spaced modes within the lower frequency bands that caused challenges in identifying the shapes contributing to system response (discussed further below). This issue was accentuated for multi-span bridges and records containing traffic pollution. An increased drop height increases the force levels and the addition of mass to the drop weight would increase the width of the impulse signal, focusing excitation to a lower frequency band. Both changes would obtain a finer frequency resolution by amplifying the response and lengthening the free-decay acquisition windows. Nevertheless, even on the larger bridges that were subjected to moderate-severe traffic, the system generated FRF measurements with acceptable signal/noise thresholds and frequency content to characterize the first 6 modes for most of the single span bridges and +12 modes for most of the multiple spans.

### 9.2.2 Parameter Estimation

The first step of the estimation strategy was the formulation of the MDOF CMIF using the reference FRF measurements. The modal density of the test bridge throughout the frequency domain was identified and approximate pole locations were used to extract mode shape

estimations of the stationary and roving DOF from the left and right singular vectors respectively. The stationary shapes provide the spatial resolution for the exterior lanes of the structure and the roving shapes provide the spatial resolution of the interior lanes of the structure. Both sets of shapes were used as the modal filter for the eFRF estimation of system poles. Global shapes were obtained by scaling the SDOF residue estimation of each roving driving point measurement to the MDOF shapes estimated in the MDOF CMIF.

The two-span analyses were particularly challenging. For each two-span analysis, the modal parameters indicated a high degree of continuity between spans, regardless of the continuity details. The two spans become highly coupled throughout the frequency domain. Areas of resonance appear as single poles but are actually two distinct resonances with unique shapes. The mode shape pairs at each pseudo repeated root contain the same shape estimation and are differentiated only by relative phase between the two spans.

#### **9.2.2.1 Example of Modal Coupling of Multiple Spans**

The structure consists of two simply supported pre-stressed concrete spans with seven girders. Each span is 96.5 ft. long and 34.5 ft. wide (Figure 9-1). The spans bear on expansion bearings at each abutment and pinned bearings at the center pier. There is a 1" joint between the two spans that contains a preformed elastic joint sealer (Figure 9-2).

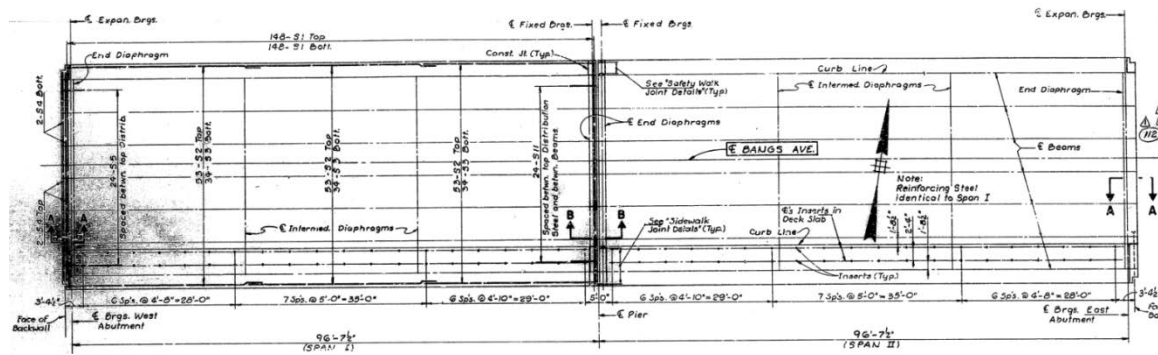


Figure 9-1: Two Span Example – Plans

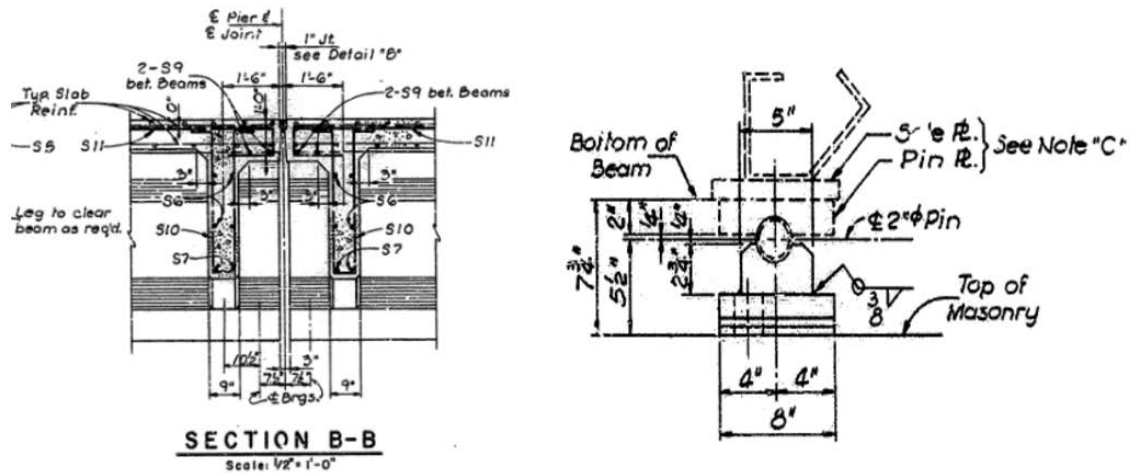
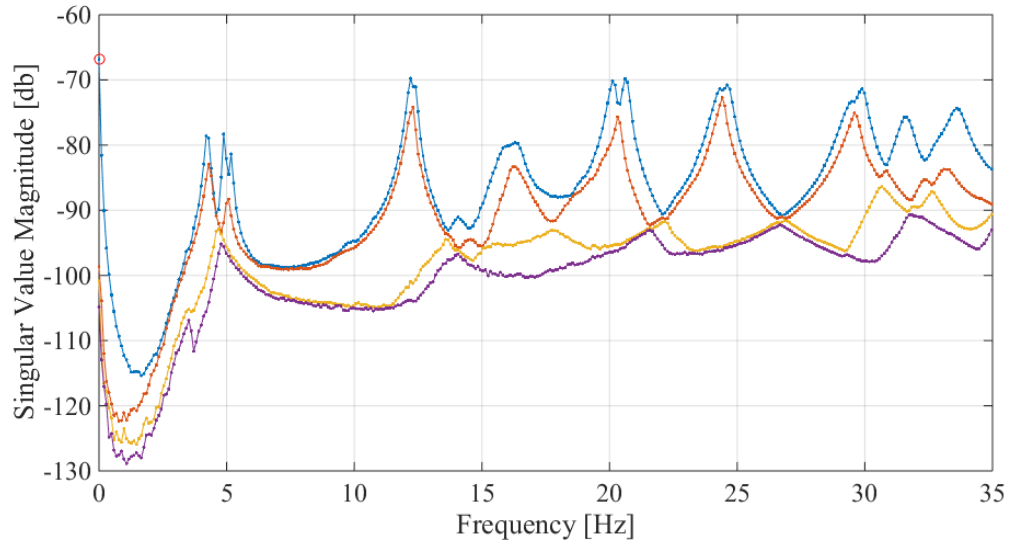


Figure 9-2: Two Span Example – Bearing Details

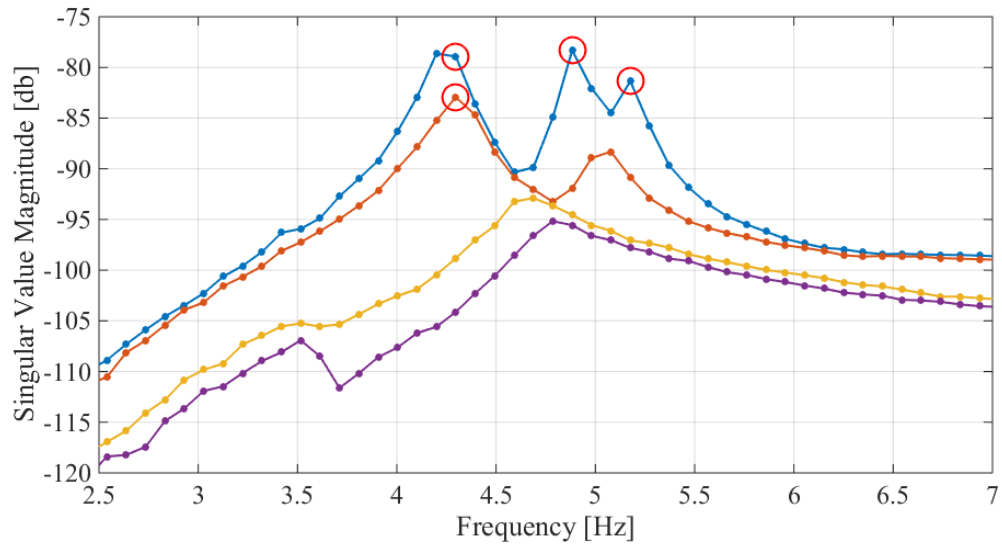
Given the lack of continuity between the two spans, most static analysis scenarios would simplify the problem and consider the two non-continuous spans as independent structures. From a vibrations standpoint this may not always be a valid assumption. The two spans of the bridge were found to resonate as a single structure for the majority of the recovered fundamental modes.

Inspection of the CMIF (Figure 9-3) shows that the first seven pole locations appear as closely spaced modes and repeated roots. Many of these closely spaced modes would likely have been misinterpreted as single poles had MDOF parameter identification techniques not been used.

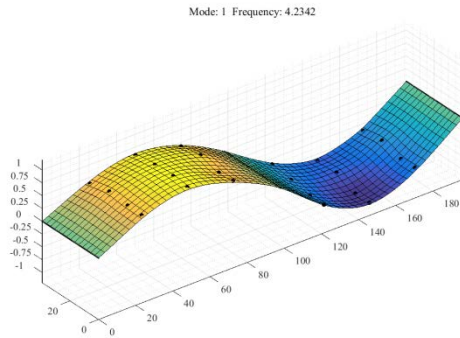
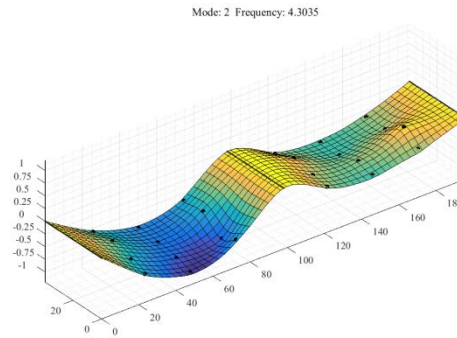
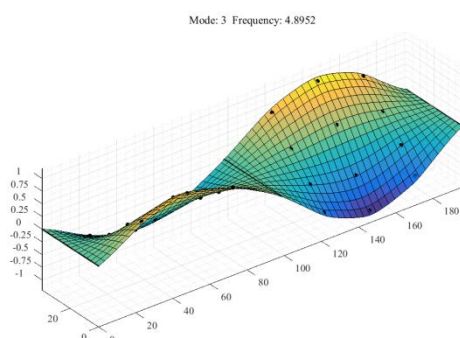
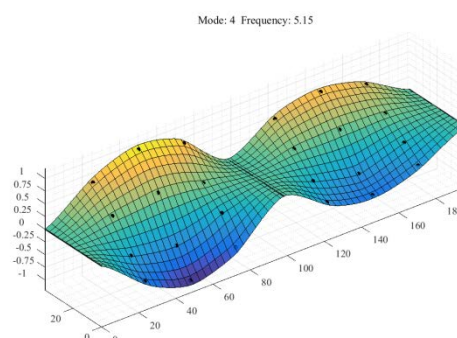


**Figure 9-3: CMIF of NJ Bridge**

Due to the coupling between spans and the compounding resolution error in the lower frequency ranges, the first two modes appear as a true repeated root when in reality these poles are just very close in frequency and require MDOF identification techniques to successfully estimate. This is shown in Figure 9-4 and is the left most two peaks. The two distinct shapes were recovered for each set of closely spaced modes. Modes 1 and 2 are shown in Figure 9-5 and Figure 9-6 b and Modes 3 and 4 are shown in Figure 9-7 and Figure 9-8. Although a reasonable estimate of each shape was recovered, the effects of the modal coupling can be seen in Mode 2 as the out of phase contributions of the first mode are superimposed onto the second.

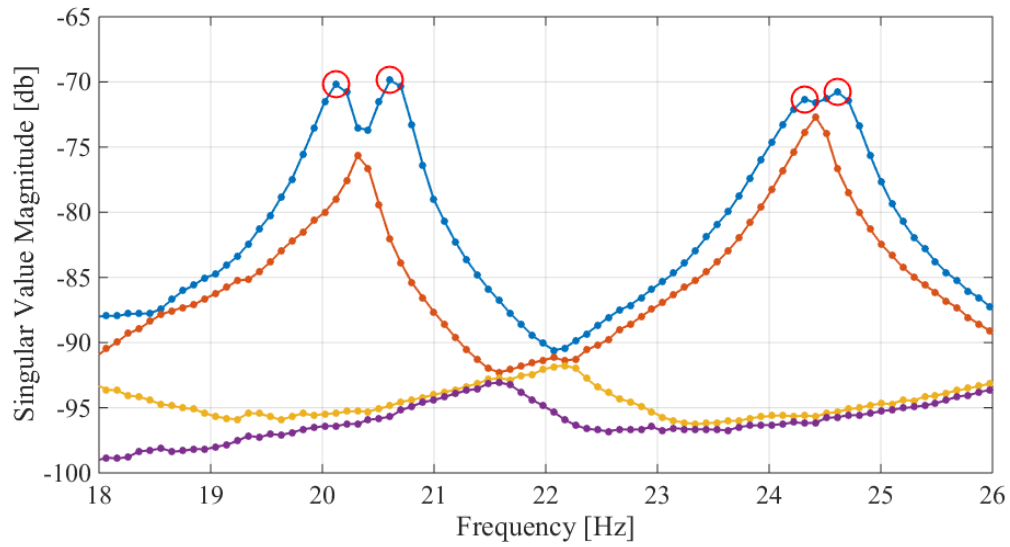


**Figure 9-4: CMIF – Low Frequency Band**

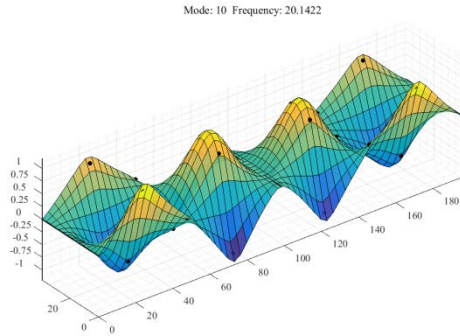
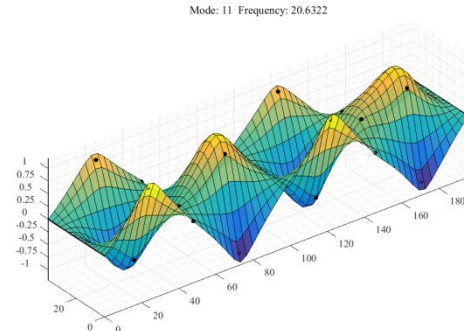
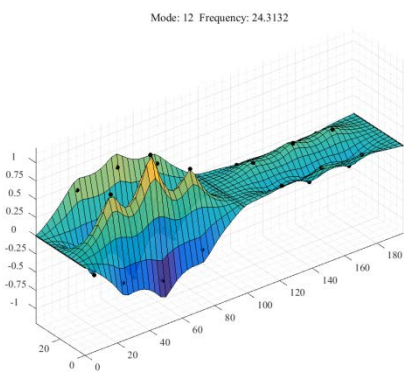
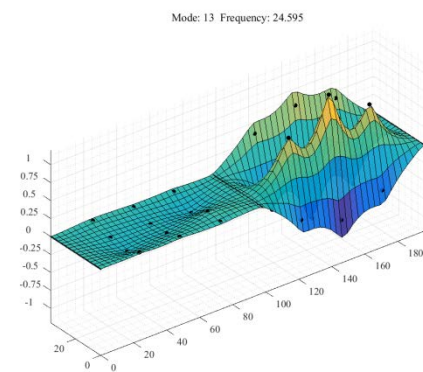
**Figure 9-5: Mode 1****Figure 9-6: Mode 2****Figure 9-7: Mode 3****Figure 9-8: Mode 4**

The global mode shapes for six of the seven in and out of phase mode shape pairs contained roughly equal contributions from each span the global shape (i.e. the modal amplitudes of each span were approximately equal). Modes 12 and 13 were the only exception. Figure 9-9 through

Figure 9-13 show the mode shape contribution of Modes 10, 11, 12, and 13 in the frequency bandwidth of 18 to 26 Hz. Modes 10 and 11 exhibit typical contributions from each span for while Modes 12 and 13 show poles that are clearly dominated by a single span. These two modes appear to resonate independently and were the only pair of shapes under 35 Hz that exhibited this behavior.



**Figure 9-9: CMIF – Frequency Band 2**

**Figure 9-10: Mode 10****Figure 9-11: Mode 11****Figure 9-12: Mode 12****Figure 9-13: Mode 13**

### 9.3 Summary of Constraints

The following constraints were encountered during the LTBP Mid Atlantic Cluster THMPER testing.

***Traffic Control:***

- Access to references - Crash trucks were required at the entrance of all lanes occupied by personnel. This required two crash trucks be present to fully install both fixed lines of global reference sensors as well as an additional vehicle to cross open traffic lanes.
- Changing Closed Lanes - Depending on the bridge, cones could be placed for several miles before and after the structure. This made changing lane closures and access to the references difficult and time consuming, especially during heavy traffic. This presented challenges, particularly during the later stages of the test as it was not uncommon for traffic to accumulate throughout the day as a result of the lane closure. Despite the difficulties, THMPER system had access to the entire top side of most structures at some point during the test.

#### **9.4 Summary of System Limitations**

The following system limitations were encountered:

***Functional Performance:***

- Operation & Maintenance - The current prototype required significant maintenance to minimize operational failures and retain a high level of data quality. Small operational issues can pollute the data with erroneous noise and have a detrimental impact on the signal quality. Keeping the system operational was by far the largest challenge. Being so close to the road, the pneumatic actuators of the catch system and sensor housing locks needed to be cleaned.
- Banked Roadways & Missed Timing of Drop/Catch - The drop weight has two vertical rails that guide the mass in the vertical direction during free-fall. The rails are the original

to the FWD and have a relatively large tolerance that can allow the mass to move rather excessively when the alignment is not perfectly vertical. This is accentuated on heavily banked roadways and often caused awkward impacts with missed timing of the impact bumpers and/or the catch actuators.

- Pneumatic Control System - The pneumatic controls raise and lower the local accelerometer housings and extend the catch actuators during an impact. Compressed air was used originally but was ultimately too temperature dependent. When tests were conducted in the cold, the sensor deployment and catch sequence would perform sluggish which caused missed catches.
- Data Acquisition Equipment - The trailer mounted BNC connections required cleaning after any extended drive. The bulkhead connectors are not waterproof and if water is present the signal will not ground properly. The connection can be cleaned out fairly easily with compressed air from the trailer mounted tanks or hand held cans.

***Test Execution:***

- Data Pre-screening - An RMS coherence check helped to screen the data and identify issues such as signal drops, sensor over-ranges, and high noise levels. An RMS coherence of .6 was typical for over-ranged or dropped signals.

## CHAPTER 10: CONCLUSIONS, RECOMMENDATIONS AND FUTURE WORK

### 10.1 Summary of Research Objectives and Scope

The research reported herein aimed to develop a quantitative bridge structural assessment tool which disrupts the conventional cost/benefit paradigm, and offers a rapid and cost-effective approach to informing decisions that require a reliable and quantitative understanding of structural performance. To meet this overarching goal and help structure the entire research effort, the following four specific research objectives were defined and adopted.

- (1) Develop a rapid structural assessment concept and establish its feasibility through (a) documenting logistical constraints associated with the field testing of bridges, (b) examining a suite of candidate assessment approaches and mapping their technical requirements against the identified logistical constraints, (c) establishing the feasibility of each candidate assessment approach to support rapid structural assessment, and (d) selection of the most promising technique and development of both a concept of operations and a set of system requirements.
- (2) Develop and validate the necessary theoretical methodologies to extend the selected candidate approach to serve as the basis for the envisioned rapid structural assessment tool, which entails accommodating the identified logistical and technical constraints, and updating the concept of operations and system requirements accordingly.
- (3) Design, develop, and integrate the necessary hardware and software systems required to realize the concept of operations and meet the identified system requirements
- (4) Establish the performance of the developed systems through (a) validation of the system components through comparison of performance with the identified requirements, (b)

validation of the system performance through comparison with best practice structural assessment approaches, and (c) field implementation on a suite of operating bridges to validate and/or refine the concept of operations.

To satisfy these objectives, the research scope adopted the systems engineering process outlined in Figure 1-1 below. A more detailed description of the scope is provided in Section 1.4 and Section 1.5.

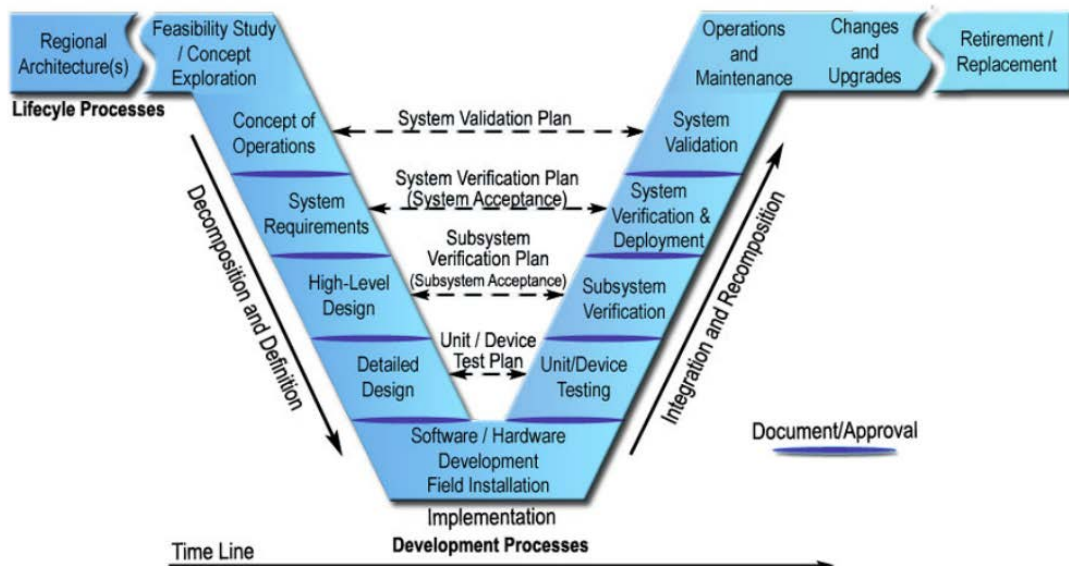


**Figure 10-1: Systems Engineering “V” Model (National ITS Architecture Team, 2007)**

## 10.2 Conclusions

The following conclusions are drawn from the work presented herein, and were organized based on the four primary objectives.

### **10.2.1 Conclusions Related to Objective 1 – Development of Rapid Structural Assessment Concept**

- To realize the concept of the envisioned rapid structural assessment tool the requirements for both underside access (which requires lifts, snoopers, etc.) and fixed topside access (which requires lane closures) must be minimized. Although some topside access will be required for all of the techniques considered, the goal should be to limit the duration of topside access windows such that traffic slow-downs as opposed to lane closures can be used.
- Based on a mapping of static and crawl-speed truck load testing approaches against the constraints identified above, it is concluded that these procedures are currently incompatible with the envisioned rapid structural assessment tool due primarily to the required underside access. It is acknowledged that the development of non-contact sensing approaches may relax (or remove) the requirement for underside access in the future.
- Dynamic testing approaches, particularly impact testing, appear to be a feasible basis for the envisioned rapid structural assessment tool as it (a) does not require any underside access, and (b) requires only relatively small, discrete windows of topside access, which may be accommodated through traffic slowdowns.
- To realize the concept of operations detailed in Section 3.4, it was determined that the system must have the following key requirements: (a) an impact source capable of exciting the structural modes (i.e. lower modes) of common bridge types, and the ability to drown-out ambient vibrations caused by operating traffic, (b) an impact source that can be roved across the bridge deck to induce spatially distributed impacts within discrete, short time window, and (c) the ability to capture spatially distributed response

data in order to ensure proper mode shape characterization and the identification of closely-spaced modes. A full list of all system requirements can be found in Section 3.5.

### **10.2.2 Conclusions Related to Objective 2 – Theoretical Development**

- To realize the concept of operations outlined in Section 3.4. the modal testing approach must deliver impacts and capture driving point responses to the central portion of the bridge through roving measurements; however, a set of fixed sensors may be installed along the shoulders or sidewalks of the bridge. This type of modal testing (i.e. the integration of a fixed array of sensors together with a roving impact source and driving point response measurement) is not currently addressed in the modal testing literature.
- Three approaches to addressing this particular type of modal testing were identified. These approaches may be considered a set of Pareto optimal solutions as they successively provide additional benefits (i.e. more reliable mode shape estimation) while simultaneously demanding additional costs (i.e. more impact locations).
- The least costly but least reliable method developed treats each impact location as an independent test, and then uses an ‘ad hoc’ stitching approach to generate estimates of global mode shapes. More specifically, the different impact locations are processed individually as SIMO tests and then stitched together by estimating the scaling and phase information from the fixed references. This method provides accurate frequency predictions, but is unable to reliably decouple mode shapes and produces “operating” mode shapes (which amount to a superposition of various modes at closely spaced poles). Although such shapes cannot reliably be used within the objective function to update an FE model, they will generally be sufficient to pair modes and permit the updating of an FE model based only on frequencies.

- The second method (intermediate cost, intermediate reliability) involves performing additional SIMO measurements at the stationary references to link a subset of the input/output domains of the structure's characteristic space and increase the resolution of the modal model. This method requires performing additional impacts at the references which adds to the time and access requirements of each test, and thus adds to the total cost of the evaluation. However, by linking the input/output space, this method is capable of providing a more robust and spatially complete MDOF estimate of the structure's modal vectors, especially in the presence of closely spaced modes. This method may be somewhat restrictive as (a) an additional means of excitation may be required when the large, vehicle mounted trailer is not able to be positioned to the desired reference, and (b) if the references selected for impacts are located near nodal points of certain modes, scaling errors will be introduced and the shape estimation for these modes may be skewed.
- The third method represents the upper bound of the modal solution, as well as the upper bound in terms of total cost and time for execution as it involves impacting at every reference in addition to the roving impact locations within the interior lanes. By sampling the entirety of the input domain of the structure's characteristic space, a full MDOF modal vector solution can be obtained with a relatively straight forward analysis procedure. Ad hoc stitching or least squares scaling (to link the phase and magnitude of the input/output DOF) are not needed as the full solution is provided from the right singular vector itself. The primary advantage of this approach is that it provides reliable mode shape information, which may be included within the objective function to update an FE model.

### 10.2.3 Conclusions Related to Objective 3 - System Design, Development and Integration

The Targeted Hits for Modal Parameter Estimation and Rating (THMPER) system developed as part of this research (Figure 10-2). THMPER is comprised of a self-contained modal testing trailer, a mobile work station, and streamlined data processing software to extract modal parameters (natural frequencies and mode shapes) of a structure in an efficient manner.



**Figure 10-2: The Targeted Hits for Modal Parameter Estimation and Rating (THMPER) System**

The modal testing trailer is comprised of a Falling Weight Deflectometer (FWD) that was significantly reconfigured to (1) provide a single, large (~30kip) broadband impact source, and (2) collect the resulting free-decay response of the bridge's surface at the impact location. In addition, the system also contains a set of accelerometers which can serve as fixed references and are sampled by an independent data acquisition system. This independent data acquisition system streams the data from the reference accelerometers wirelessly to the modal testing trailer. All data

acquisition within the THMPER system are GPS synchronized to permit the seamless integration of reference and driving point measurements.

Once collected, the data is ported to Visual Modal Analysis (VMA), which is a semi-automated modal processing software developed as part of this research. This software contains three primary systems that focus on (1) data quality checks (2) frequency response function development, and (3) modal parameter estimation.

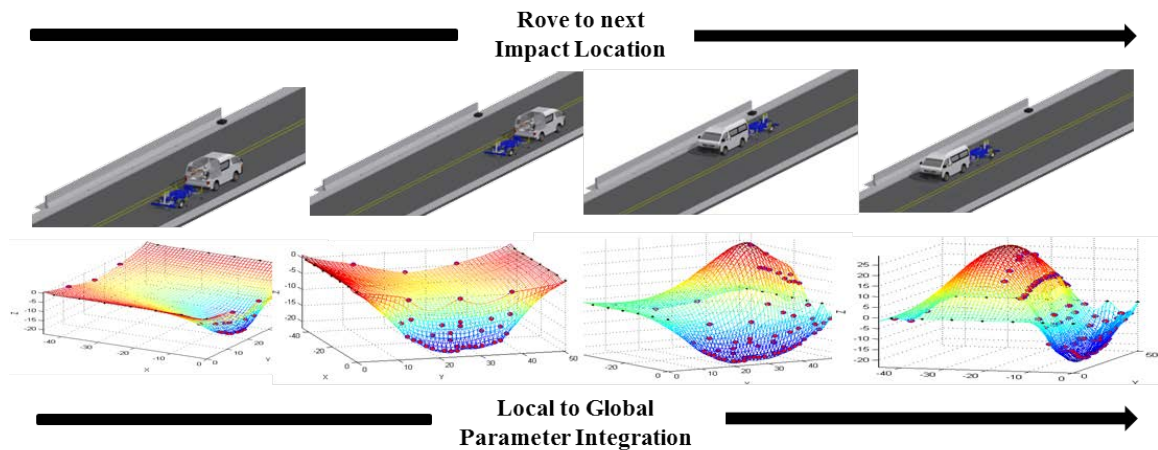


**Figure 10-3: THMPER System Test Methodology**

#### 10.2.4 Conclusions Related to Objective 4a - Component Validation

- The impact source of an\_FWD with standard bumpers/weights was able to meet the requirements for both force level (approximately 25 kips) and usable frequency content (~0-50 Hz). In addition, this impact source was capable of routinely inducing driving point accelerations of 2.5 g, which was able to overwhelm the vibrations due to traffic in adjacent lanes (see Chapter 6 for details).

- The spring loaded accelerometer mounts designed and integrated with the THMPER System were shown to accurately capture the vibrations of the deck surface following an impact. This was validated through comparison with independent, glued sensors and there was less than 1% difference in RMS values of the filtered signals.
- The GPS synchronization/wireless distributed data acquisition systems were shown to work and function appropriately. The synchronization between the three cRIO chassis differed in the nanosecond range and was shown to have a negligible effect on the modal results.

#### **10.2.5 Conclusions Related to Objective 4b - System Validation**

To validate the developed THMPER System, it was compared against two ‘best practices’ structural assessment approaches using an operating highway bridge as a test specimen. First, comparison was done with a multi-reference impact test (MRIT) that employed a fixed sensor array. Second, a comparison to a static truck load test was carried out. To permit this comparison, an FE model was updated using the THMPER test results and used to ‘predict’ the results of the static truck load test. From these comparisons the following conclusions are drawn.

- The identified natural frequencies showed good agreement between the sledge MRIT benchmark and the THMPER system indicating negligible loading errors and bias due to the developed testing method. Specifically, for the first eight modes identified, the average percent error was **1.07%**, the minimum was **0.04%**, and the maximum was **1.68%**.
- The identified damping estimations showed poor agreement between the sledge MRIT and the THMPER system. Specifically, the average percent error was **32.82%**, the minimum was **6.53%**, and the maximum was **79.10%**. Although this may be due to the

large differences in force levels between these two tests, the reader is cautioned that the estimation of damping through modal testing is notoriously variable.

- The identified modal vectors showed good agreement between the sledge MRIT benchmark and the THMPER system indicating negligible loading errors and bias due to the developed testing method. Specifically, the average MAC value was **0.966**, the minimum was **0.901**, and the maximum was **0.998**.
- The displacements predicted from FE models updated using the THMPER testing results were in good agreement with the displacements measured during the static load test. Specifically, the average displacement error was **7.98%**, the minimum error was **0.26%**, and the maximum error was **18.81%**. The observed errors may have been due to the differences in spatial resolutions of the two testing approaches as well as differences in force level.

#### **10.2.6 Conclusions Related to Objective 4c - Field Implementation**

To examine the validity of the envisioned concept of operations, the THMPER system was deployed as part of the FHWA Long-Term Bridge Performance (LTBP) Program to test 11 bridges within the Mid-Atlantic Clusters. The analysis is still ongoing. However, based on this field implementation and analysis thus far, the following conclusions are drawn:

- The THMPER system provided a reasonable means of efficiently testing highway bridges at a large scale. Although the system suffered from minor maintenance issues throughout the duration of testing, the system did not experience a complete failure and was able to complete each of the 11 bridge tests. At least the first 2-3 global modes of each structure were found, with some of the two span structures reaching +15 estimated modes.

- Several of the two span non-continuous prestressed bridges experienced a high degree of modal coupling between the two spans. From an analytical standpoint these bridges appeared to be fully continuous despite a 1" expansion joint between the two spans.
- Bridges with significant vertical curves or super-elevation caused problems with the drop weight and catch systems. A more robust guide rail and rebound mitigation mechanism should be investigated

### **10.3 Future Work**

The work presented in this thesis served as the groundwork for establishing a rapid testing system and methods for large scale highway bridge condition assessment. The following are suggestions for the continuation of this work:

- The input/output spatial sampling is still skewed towards the exterior girders (i.e. the stationary reference measurements are weighted more heavily). Incorporating a suitable excitation source within the stationary reference locations would provide an unbiased spatial sampling and make sure any down time during lane closure switches.
- Local positioning system – The system currently lacks any local positioning system. The current process of marking the impact and reference locations with chalk prior to the test has worked fine thus far. This is partly because verifying plans and dimensions was part of the scope and topside access was generally not an issue.

## List of References

- AASHTO. (2011). *The manual for bridge evaluation*. Washington, DC: American Association of State Highway and Transportation Officials.
- Aktan, A. E., Catbas, N. F., Turer, A., & Zhang, F. Z. (1998). Structural Identification: Analytical Aspects. *Journal of Structural Engineering*, 817-829.
- Aktan, A. E., Farhey, D. N., Brown, D. L., Dalal, V., Helmicki, A. J., Hunt, V. J., et al. (1996). Condition Assessment for Bridge Management. *Journal of Infrastructure Systems*, 108-117.
- Aktan, A. E., Farhey, D. N., Helmicki, A. J., Brown, D. L., Hunt, V. J., Lee, K. L., et al. (1997). Structural Identification for Condition Assessment: Experimental Arts. *Journal of Structural Engineering*, 1674-1684.
- Allemang, R. J. (1999). *Vibrations II: Analytical And Experimental Modal Analysis*. Cincinnati, Ohio: University of Cincinnati.
- Allemang, R. J. (1999). *Vibrations III: Experimental Modal Analysis*. Cincinnati, Ohio: University of Cincinnati.
- Allemang, R. J. (2003). The Modal Assurance Criterion - Twenty Years of Use and Abuse. *Sound and Vibration*.
- Allemang, R. J., & Brown, D. L. (2006). A complete Review of the Complex Mode Indicator Function (CMIF) with Applications. *International Conference on Noise and Vibration Engineering*. Heverlee, Belgium: Curran Associates, Inc.

- Buckle, I. G. (1866). Field Tests of a Curved Box Girder Bridge Using Simulated Earthquake Loads. *Preceedings of hte 8th European Conference on Earthquake Engineering*, 1-8.
- Catbas, F. N. (1996). Modal Analysis of Multireference Impact Test Data for Steel Stringer Bridges. *Proceedings of the 15th International Modal Analysis Conference (IMAC 15)*, 381-389.
- Catbas, N. F., & Aktan, A. E. (2002). Condition and Damage Assessment: Issues and Some Promising Indices. *Journal of Structural Engineering*, 1026-1036.
- Catbas, N. F., Brown, D. L., & Aktan, A. E. (2004). Parameter Estimation for Multiple-Input Multiple-Output Modal Analysis of Large Structures. *Journal of Engineering Mechanics*, 921-930.
- Catbas, N. F., Brown, D. L., & Aktan, A. E. (2006). Use of Modal Flexibility for Damage Detection and Condition Assessment: Case Studies and Demonstrations on Large Structures. *Journal of Structural Engineering*, 1699-1712.
- Douglas, B. M., & Reid, W. H. (1982). Dynamic Testing and System Identification of Bridges. *Journal of Structural Engineering*, 2295-2312.
- Fernstrom, E. V., Carreiro, J. L., Rawn, J. D., & Grummelsman, K. A. (2013). Dynamic Characterization of a Truss Bridge by Falling Weight Deflectometer. *Journal of the Transportation Research Board*, 81-89.
- Halvorsen, W. G., & Brown, D. L. (1977). Impulse Technique for Structural Frequency Resopnse Testing. *Sound and Vibration*, 8-21.

- Hearn, G. (2014). *State Bridge Load Posting Processes and Practices*. Washington, DC: National Cooperative Highway Research Program.
- Hoadley, P., & Gomez, J. P. (1996). *Structural Stiffness Identification of Bridge Superstructures*. Technical Reoprt for Virginia Military. NTIS Issue Number: 199613.
- Lenett, M. S., Brown, D. L., Hunt, V. J., & Helmicki, A. J. (2000). Performing Bridge Condition Assessment with Spliced Multi-Reference Impact Data. *Conference: 2000 IMAC XVIII - 18th International Modal Analysis Conference*, (pp. 1307-1312).
- Masceri, D. (2015). *Examination of Bridge Performance through the Extension fo Simulation Modeling and Structural Identification to Large Populations of Structures*. Doctoral dissertation, Drexel University.
- Moon, F. L. (2006). Impacts of Epistemic (Bias) Uncertainty on Structural Identification of Constructed (Civil) Systems. *The Shock and Vibration Digest*, 399-420.
- Morassi, A., & Tonon, S. (2008). Dynamic Testing for Structural Identification of a Bridge. *Journal of Bridge Engineering*, 573-585.
- NASA. (2007). *NASA Systems Engineering Handbook*. Maryland 21076: NASA Center for AeroSpace Information.
- National Instruments. (2008). *CompactRIO Developers Guide*.
- National ITS Architecture Team. (2007). *Systems Engineering for Intelligent Transportation Systems*. Washington, DC 20590: Department of Transportation.

- Phares, B. M., Washer, G. A., Rolander, D. D., Graybeal, B. A., & Moore, M. (2004). Routine Highway Bridge Inspection Condition Documentation Accuracy and Reliability. *Journal of Bridge Engineering*, 403-413.
- Prader, J. (2012). *Rapid Impact Modal Testing for Bridge Flexibility: Towards Objective Evaluation of Infrastructures*. Doctoral Dissertation, Drexel University.
- Raghavendrachar, M., & Aktan, A. E. (1992). Flexibility by Multireference Impact Testing for Bridge Diagnostics. *Journal of Structural Engineering*, 2186-2203.
- Ramsey, K. A. (1975). Effective Measurements for Structural Dynamics Testing. *Sound and Vibration*, 24-35.
- Sandwell, D. T. (1987). Biharmonic Spline Interpolation of GEOS-3 and SEASAT Altimeter Data. *Geophysical Research Letters*, 139-142.
- Smith, B. (2005). *Developing and Using a Concept of Operations in Transportation Management Systems*. Washington, DC 20590: Operations Office of Transportation Management, FHWA.
- Teughels, A. (2004). Structural damage identification of the highway bridge Z24 by FE model updating. *Journal of Sound and Vibration*, 589-610.
- Wang, X., Kangas, S., Padur, D., Lui, L., Swanson, J., Helmicki, A., et al. (2005). Overview of a Modal-Based Condition Assessment Procedure. *Journal of Bridge Engineering*, 460-467.
- Weidner, J. (2012). *Structural Identification of a Complex Structure using both Conventional and Multiple Model Approaches*. Doctoral Dissertation, Drexel University.

Zhou, Y., Prader, J., DeVitis, J., Deal, A., Zhang, J., Moon, F., et al. (2011). Rapid Impact Testing for Quantitative Assessment of Large Populations of Bridges. *Nondestructive Characterization for Composite Materials, Aerospace Engineering, Civil Infrastructure, and Homeland Security 2011*. San Diego, California: SPIE.

## Vita

John DeVitis was born in Philadelphia, PA on April 11, 1986. He graduated from Upper Darby High school in 2004 and attended Delaware County Community College where he began to study secondary education, focusing in mathematics. It was there that he fell in love with engineering and decided to enroll as a civil engineer at Drexel University. He completed his undergraduate degree in 2010 and returned to Drexel to begin a doctorate in Structural Engineering, focused on structural dynamics and experimental evaluation techniques. He defended his research in December, 2015 and after graduation he plans to continue working in bridge condition assessment.